# HIGH $T_c$ SUPERCONDUCTOR, FERROELECTRIC THIN FILMS AND MICROWAVE DEVICES

**TAN CHIN YAW**

*(B.Sc.(Hons.), NUS)*

A THESIS SUBMITTED FOR THE DEGREE OF

DOCTORATE OF PHILOSOPHY

DEPARTMENT OF PHYSICS

NATIONAL UNIVERSITY OF SINGAPORE

2005

## ACKNOWLEDGEMENTS

I am very fortunate and thankful to have Prof. Ong Chong Kim as my thesis supervisor. I am very grateful to him for accepting me into his research centre, Centre of Superconducting and Magnetic Materials (CSMM), and for allowing me to pursue my own research ideas while providing the proper guidance. Prof. Ong is truly concerned for the well-being of his students and works tirelessly to make their research possible.

I would to thank Dr. Lu Jian, Dr. Chen Linfeng and Dr. Rao Xuesong for their introduction to microwave theories, the many helpful advices and discussions, and their friendship.

I would also like to thank Dr. Chen Ping for his introduction on the pulsed laser deposition technique; Miss Lee Wai Fong for her introduction on photolithography and wet etching; Dr. Li Jie and Dr. Yan Lei who had helped me with the fabrication of ferroelectric thin films.

I am also very grateful to Dr. Xu Shengyong and Mr. Li Hongping, who had pioneered the development of many experimental setups at CSMM; Mr. Tan Choon Wah and his team of staff at the machine workshop, Department of Physics, who had help me fabricated many of the items required in my work.

I would also like to thanks my friends at CSMM, who have made my time there so enjoyable. These people are Mr. Ong Peng Chuan, Mr. Goh Wei Chuan, Miss Liu Yan, Mr. Liu Huajun and Mr. Wang Peng.

Lastly, I would like to thank my parents for their unfailing love and support. This work is dedicated to them.

This research was supported in part by DSO National Laboratories (DSO/C/99100/L) and Defence Science and Technology Agency (MINDEF-NUS-DIRP/2001/POD0103047).

## TABLE OF CONTENTS

## SUMMARY

This thesis presents a study on the high $T_c$ superconductor (HTS) $YBa_2Cu_3O_{7-\delta}$ (YBCO) thin films, ferroelectric $Ba_{0.1}Sr_{0.9}TiO_3$ thin films and their applications in passive microwave devices.

YBCO, $Ba_{0.1}Sr_{0.9}TiO_3$ and multilayer YBCO/$Ba_{0.1}Sr_{0.9}TiO_3$ thin films were fabricated using the pulsed laser deposition (PLD) technique. The PLD experimental setup incorporated a silicon radiation heater and a laser beam scanning system for the fabrication of large-area double-sided YBCO thin films suitable for the production of microstrip HTS microwave devices. Considerable efforts were spend on the optimization of the PLD experimental setup and procedures to produce high quality thin films. The crystalline structure and surface morphology of the thin films were examined using X-ray diffraction, scanning electron microscopy and atomic force microscopy. The dc electrical properties of the YBCO thin films were examined using four-wire measurements and the microwave surface resistance was examined using a dielectric resonator method. A dual-resonator planar circuit measurement method was also developed to examine the microwave complex permittivity of the ferroelectric thin films.

The applications of HTS thin films in the fabrication of high quality factor microstrip resonators were studied. A novel type of miniaturized microstrip resonator based on the dual-spiral geometry was developed. The dual-spiral resonators were found to have quality factors much higher than straight half-wavelength resonator. The dual-spiral resonators were also found to be highly suitable for the design of cross-coupled filters, as inter-resonator coupling with suitable phase shift and coupling coefficient can be easily achieved using the dual-spiral resonator pairs. A

highly-compact cascaded quadruplet bandpass filter with enhanced selectivity was developed using the dual-spiral resonators.

The application of HTS/ferroelectric thin films for planar tunable microwave devices was studied using YBCO/$Ba_{0.1}Sr_{0.9}TiO_3$ multilayer thin films. A process for the fabrication of patterned ferroelectric was developed. The fabrication process for patterned ferroelectric thin film enabled the development of tunable planar HTS/ferroelectric devices with better performance as unnecessary loss and unwanted tuning were eliminated. Tunable YBCO microstrip resonator and filter with patterned $Ba_{0.1}Sr_{0.9}TiO_3$ thin films fabricated by the process were found to have improved performance.

As HTS thin film can be easily damaged by improper handling, the fabrication process of the YBCO thin film microwave devices was carefully designed to avoid damaging the thin film during the device fabrication process. Packaging designs with good performance and reliability was also developed for the HTS microstrip devices.

## LIST OF FIGURES

## LIST OF SELECTED SYMBOLS AND ABBREVIATIONS

| | |
|---|---|
| Dielectric constant | $\varepsilon_r$ |
| Permeability | $\mu$ |
| Permeability of vacuum | $\mu_0$ |
| Electrical conductivity | $\sigma$ |
| Angular frequency | $\omega$ |
| Atomic Force Microscopy | AFM |
| Magnetic field or magnetic flux density | **B** |
| Centre for Superconducting and Magnetic Materials | CSMM |
| direct current | dc |
| Electric field | **E** |
| Frequency | $f$ |
| Resonant frequency | $f_0$ |
| Full-Width at Half-Maximum | FWHM |
| Magnetic field or magnetic field intensity | $H$ |
| High $T_c$ Superconductor | HTS |
| Prefix used to indicate an imaginary number | $j$ |
| Superconducting critical current density | $J_c$ |
| $LaAlO_3$ | LAO |
| Pulsed Laser Deposition | PLD |
| Loaded Q factor | $Q_l$ |
| Unloaded Q factor | $Q_u$ |
| radio frequency | rf |
| Surface resistance | $R_s$ |
| Reflection S-parameter | $S_{11}$ |
| Transmission S-parameter | $S_{21}$ |
| Scanning Electron Microscopy | SEM |
| Loss tangent | tan $\delta$ |
| Superconducting critical transition temperature | $T_c$ |
| Surface temperature of heater | $T_h$ |
| X-Ray Diffraction | XRD |
| $YBa_2Cu_3O_{7-\delta}$ | YBCO |

# CHAPTER 1:
# INTRODUCTION TO SUPERCONDUCTORS AND ITS MICROWAVE APPLICATIONS

Superconductivity was discovered by Heike Kamerlingh Onnes in 1911. Onnes was investigating the resistivity of mercury cooled to liquid helium temperature when it was observed that the resistivity dropped abruptly to zero at a temperature of about 4 K.

In 1933, Walter Meissner and Robert Ochsenfeld discovered that when a superconductor was cooled to the superconducting state in a magnetic field, the magnetic field would be expelled from the interior of the superconductor. This discovery clearly differentiated superconductivity from perfect conductivity.

Since the discovery of superconductivity by Onnes, many other superconducting metals, alloys and compounds were discovered. Up until 1985, the material with the highest known critical temperature was a niobium germanium alloy ($Nb_3Ge$), which was discovered in 1973 to have a critical temperature of 23.2 K [1].

In 1986, J. G. Bednorz and K. A. Müller announced the discovery of a superconducting La-Ba-Cu-O compound with critical temperature of around 35 K [2]. This discovery generated tremendous interests and efforts to discover other superconductors with higher critical temperature.

In 1987, Paul C. W. Chu and Maw Kuen Wu substituted lanthanum with yttrium and discovered that $YBa_2Cu_3O_{7-\delta}$ (YBCO) has a critical temperature of around 90 K [3]. This was a landmark discovery since this critical temperature could be easily attained using liquid nitrogen which has a boiling point of 77 K. Prior to this discovery, superconductivity could only be achieved using costly and complex

refrigeration techniques or by using liquid helium as the cryogenic refrigerant. Liquid helium with boiling point of 4.2 K, is rare and expensive, as well as difficult to handle and store. Unlike liquid helium, liquid nitrogen is a relatively cheap and readily available cryogenic refrigerant. Furthermore, temperature of around 90 K is relatively easy to attain and maintain with commercially available closed-cycle cryocooler, making widespread research and commercial applications of superconductivity possible.

Many other superconductors with higher critical temperature had since been discovered. These new superconductors with relatively high critical temperature are often referred to as High $T_c$ Superconductor (HTS) while the superconductors discovered before 1986 are referred as Low $T_c$ Superconductor (LTS). Although $La_{1.85}Ba_{0.15}CuO_4$ with critical temperature of around 35 K is generally considered to be the first HTS material, there is no formal temperature definition differentiating HTS and LTS.

## 1.1 Basic characterization parameters of superconductor

The temperature at which a material transforms into a superconducting state is called the critical temperature ($T_c$). The sharp drop of electrical resistance to zero occurs over a temperature range. A narrower transition temperature range usually indicates a sample with higher phase purity.

If a superconductor is exposed to sufficiently strong magnetic field, the superconductor will revert to a non-superconducting state. The minimum field that will disrupt the superconducting state is called the critical magnetic field ($H_c$).

Superconductors can be classified as type I or type II. A type I superconductor completely expels magnetic flux from its interior, and completely lose its

superconductivity if the applied magnetic field exceeds $H_c$. A type II superconductor has two critical fields: $H_{c1}$, when small localized magnetic flux can exist within its interior (and partially suppressing the superconductivity) and $H_{c2}$, when it completely loses its superconductivity. Type I and II superconductors are described in greater details in section 1.2.1. A superconductor will also lose its superconductivity when it carries an electrical current with current density exceeding the critical current density ($J_c$).

Superconductivity is strongly influenced by temperature, magnetic field and electrical current density. $J_c$ and $H_c$ are temperature dependent and will increase with decreasing temperature. $T_c$ and $J_c$ will decrease with increasing applied magnetic field, while $H_c$ and $T_c$ will decrease when a superconductor is carrying more electrical current.

## 1.2 Superconductivity at microwave frequencies

In 1957, John Bardeen, Leon Cooper and Robert Schrieffer proposed the first widely accepted theory on the mechanism of superconductivity, now commonly referred to as the BCS theory [4]. In this theory, superconductivity is due to phonon mediated coupling between electron pair with opposite spin, leading to the superconducting Bose condensation state. The paired electrons, called “Cooper pair”, can travel without the collisions and interactions present in normal conductor that leads to resistance. This pairing can only occur when the temperature is lower than $T_c$ so that the ordinary thermal induced motions of the electrons are sufficiently reduced.

While BCS theory can explain superconductivity in LTS very well, it cannot fully explain several features found in HTS. Up till now, there is still no theory that is

able to fully explain the superconductivity in HTS satisfactorily. Fortunately, for passive HTS microwave devices, the phenomenological theory based on the London equations and the two-fluid theory provide an adequate basic theoretical understanding and a microscopic theory of superconductivity in HTS materials is not necessary [5,6].

### 1.2.1 Meissner effect and London equations

Meissner effect refers to the exclusion of magnetic field within the interior of superconductors. Meissner effect can be represented using the first London equation:

$$\Lambda \frac{\partial \mathbf{J}_s}{\partial t} - \mathbf{E} = 0 , \tag{1.1}$$

and the second London equation:

$$\Lambda \nabla \times \mathbf{J}_s + \mathbf{B} = 0 . \tag{1.2}$$

$\Lambda$ is the London parameter given by

$$\Lambda = \frac{m_s}{n_s q_s^2} , \tag{1.3}$$

where $m_s$, $n_s$ and $q_s$ are the effective mass, density and electrical charge of the superconducting carriers respectively. $\mathbf{J}_s$ is the superconducting current density given by

$$\mathbf{J}_s = n_s q_s \mathbf{v}_s , \tag{1.4}$$

where $\mathbf{v}_s$ is the velocity of the superconducting carriers. **E** and **B** are the electrical field and magnetic field respectively.

Using equation (1.1) and the Maxwell equations, it can be derived that

$$\nabla^2 \mathbf{B} - \frac{1}{\lambda_L^{\,2}} \mathbf{B} = 0, \tag{1.5}$$

where $\lambda_L$ is the London penetration depth given by

$$\lambda_L = \sqrt{\frac{\Lambda}{\mu}} = \sqrt{\frac{m_s}{\mu n_s q_s^2}}, \tag{1.6}$$

where $\mu$ is the permeability. The one-dimension solution of equation (1.5) is

$$B(x) = B(0) e^{-\frac{x}{\lambda_L}}. \tag{1.7}$$

Equation (1.7) shows that the magnetic field inside a superconductor decreases exponentially from the surface with a decay length of $\lambda_L$.

The Meissner effect and London equations are subject to some limitations because of the relative length scales involved. In BCS theory, the Cooper pair interacts over a length called the superconducting coherence length, which is given by

$$\xi = \frac{ahv_F}{k_B T_c}, \tag{1.8}$$

where $h$ is the Plank's constant, $v_F$ is the electron velocity at the Fermi surface, $k_B$ is the Boltzmann's constant, and $a$ is a numerical constant of unity order.

The coherence length of a type I superconductor is greater than its London penetration depth. For type I superconductors, complete exclusion of magnetic flux occurs for magnetic field $H$ less than $H_c$, and superconductivity is destroyed when $H > H_c$.

The coherence length of a type II superconductor is about equal to or less than its London penetration depth. Type II superconductors have two critical magnetic

fields, $H_{c1}$ and $H_{c2}$. When $H < H_{c1}$, type II superconductors will exhibit the Meissner effect. When $H_{c1} < H < H_{c2}$, a type II superconductor will be in the mixed state, where localized magnetic vortices can penetrate the superconductor without destroying its superconductivity. When $H > H_{c2}$, the superconducting state is destroyed.

### 1.2.2 Two-fluid model and surface resistance

Due to skin effect, the power dissipation of an rf current is larger than dc current. Surface resistance is used for calculating power dissipation at microwave frequency. Surface resistance is the real part of surface impedance, which is defined as the ratio of the tangential electric and magnetic fields ($E_t / H_t$) at the surface of the conductor. Surface impedance can be written as $Z_s = R_s + jX_s$, where $R_s$ is the surface resistance and $X_s$ is the surface reactance.

The surface impedance of normal conductors can be calculated from their conductivity ($\sigma$) using

$$Z_s = \sqrt{\frac{j\mu\omega}{\sigma}} = (1+j)\sqrt{\frac{\mu\omega}{2\sigma}}, \tag{1.9}$$

where $\omega = 2\pi f$ is the angular frequency. For normal conductors, $\sigma$ is a real number so

$$R_s = X_s = \sqrt{\frac{\mu\omega}{2\sigma}}. \tag{1.10}$$

For superconductor at microwave frequency, the conductivity can be derived from the two-fluid theory [5]. The two-fluid model is based on the concept that there are two types of conducting current in the superconducting state. They are the

superconductive current with carrier density $n_s$ and the normal current with carrier density $n_n$. The total carrier density is $n = n_s + n_n$. The conductivity is given by

$$\sigma = \sigma_1 - j\sigma_2 = \frac{n_n q_n^2 \tau}{m_n} - j\frac{1}{\omega\mu\lambda_L{}^2}, \tag{1.11}$$

where $\tau$ is the relaxation time for electron scattering.

At temperatures below $T_c$, the variation of $n_n$, $n_s$ and $\lambda_L$ with temperature ($T$) are given by

$$\frac{n_n}{n} = \left(\frac{T}{T_c}\right)^4, \tag{1.12}$$

$$\frac{n_s}{n} = 1 - \left(\frac{T}{T_c}\right)^4, \tag{1.13}$$

and

$$\lambda_L(T) = \lambda_L(0)\left[1 - \left(\frac{T}{T_c}\right)^4\right]^{-\frac{1}{2}}, \tag{1.14}$$

where $\lambda_L(0) = \sqrt{\frac{m_s}{\mu n_s q_s{}^2}}$.

In the limit of local electrodynamics ($\xi << \lambda_L$), which holds true for almost all the HTS materials, the surface impedance can be calculated from the complex electrical conductivity using

$$Z_s(\omega) = \sqrt{\frac{j\omega\mu_0}{\sigma_1 - j\sigma_2}}. \tag{1.15}$$

Assuming $\sigma_1 << \sigma_2$, which is a good approximation for temperature lower than and not too close to $T_c$, the surface resistance and surface reactance can be approximated using

$$R_s = \frac{1}{2}\sigma_1 \mu^2 \omega^2 \lambda_L{}^3, \tag{1.16}$$

and

$$X_s(\omega) = \mu\omega\lambda_L. \tag{1.17}$$

As the microwave power dissipated by a superconductor can be calculated from $R_s$ using [6]

$$P = \frac{1}{2} R_s \int_{surface} |\mathbf{H}_t|^2 ds, \tag{1.18}$$

it is essential that $R_s$ be small for microwave devices to have low loss.

### 1.3 Microwave applications of superconductor thin film

Superconducting microwave devices can be broadly divided into three categories based on the superconductive property it exploited: those based on the transition between the superconducting state and the normal state, those based on Josephson junction and those based on the extremely low surface resistance of the superconducting state.

The transition between the superconducting state and the normal state can be used for fabricating microwave devices such as switch [7-9], tunable attenuator [10] or limiter [11]. A superconducting switch is used to control the transmission of microwave signal and is usually integrated into part of a microwave circuit. The switch is activated by the application of a control signal in the form of temperature,

magnetic field or dc electrical current change, such that the switch ceases to be superconductive and stops the transmission of the microwave signal. A tunable attenuator works similarly except that control signal is only sufficient to attenuate the transmitted power. A limiter is also similar except the microwave signal is used as the control signal. A limiter can be used to protect power sensitive microwave component from overload.

In 1962, B. D. Josephson proposed that a junction formed by two weakly connected superconductors can allow the nonlinear superconducting quantum tunneling of Cooper pairs [12]. This phenomenon was confirmed experimentally by P. W. Anderson and J. M. Rowell in 1964 [13]. Such junction structures are now called Josephson junction. Josephson junction can be used in microwave devices such as rf detectors and mixers [14-20], rf generators and oscillators [21-24], amplifiers [25-28] and phase shifters [29,30]. Jospehson junction based microwave devices have the potentials of been extremely low noise, very low power consumption and the ability to perform up to very high frequency.

The third category of superconducting microwave devices exploit the very low surface resistance of superconductors. Passive microwave devices can benefit from the very low surface resistance of superconductors in two ways. One way is directly from the reduced microwave dissipation which means lower insertion loss or higher Q factor. The other way is from the miniaturization of microwave devices without significant performance degradation. While almost all passive microwave components can benefit from reduced microwave dissipation, the advantage of superconductor is most apparent in devices such as delay lines, resonators, and filters where low loss is critical.

The miniaturization of HTS microstrip resonators and filters are examined in this thesis. More details on the applications and advantages of HTS microwave resonators and filters are found in chapters 4 and 5.

## 1.4 Structure of HTS thin film microwave devices

HTS thin film can be used to fabricate planar-structure superconducting microwave circuits and the superconducting microwave devices mentioned in section 1.3. Modern microwave circuits are mostly implemented using planar structure instead of three-dimensional structure such as coaxial or hollow waveguide configurations, because of their light weight, compactness and ease of manufacture. The cross sectional views of commonly used planar structures such as coplanar, microstrip or stripline configuration transmission line are shown in figure 1.1.

Coplanar configuration HTS circuits are the easiest to fabricate among the three types of planar configurations, as only a single layer of HTS thin film is required. However packaging of coplanar circuit with good rf grounding is difficult to achieve and spurious transmission modes are easily excited in coplanar transmission line [6].

Microstrip configuration circuits with conventional metallic conductors are one of the most popular structures used by industry as they are easy to fabricated, easy to package and have fairly good microwave performance. Both coplanar and microstrip configurations allow easy attachment of discrete microwave components to the circuit to form hybrid microwave integrated circuit. However, to fabricate a fully HTS thin film microstrip circuit requires the deposition of HTS thin films on both sides of a substrate, which is more difficult than the fabrication of single layer HTS thin film required by coplanar circuit.

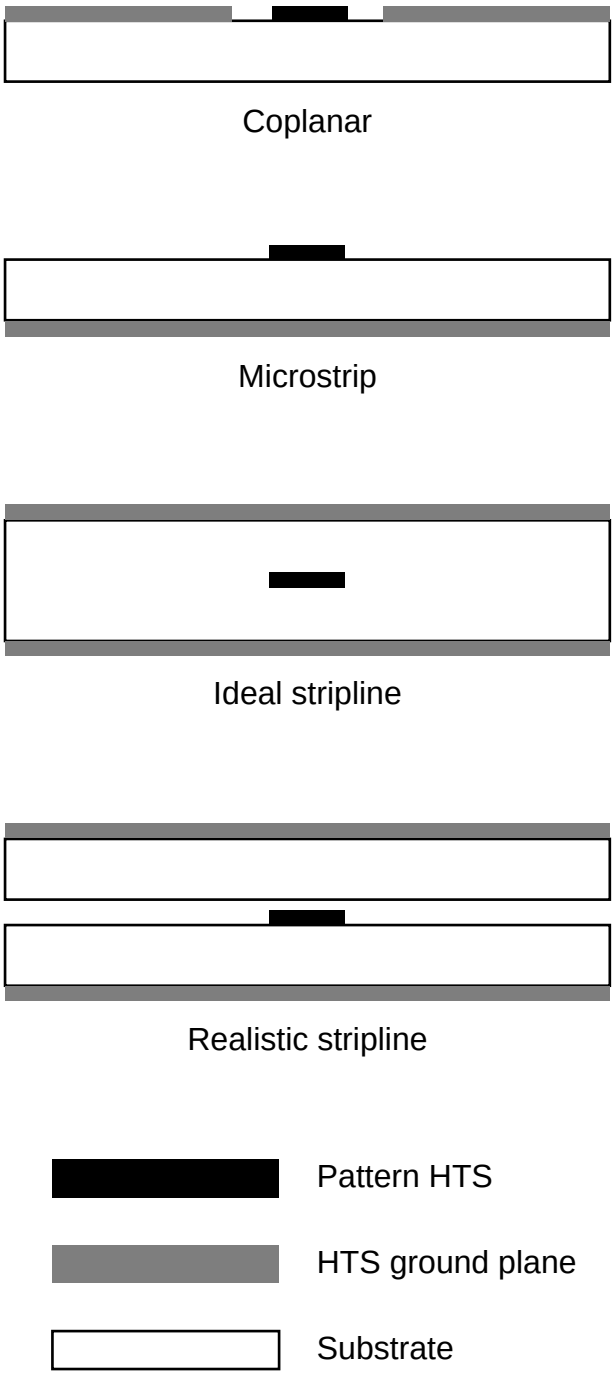


Figure 1.1 Cross sectional view of the coplanar, microstrip and stripline transmission lines.

Both the coplanar and microstrip configurations are open structures and have the problems of radiation leakage, coupling with cavity and dispersion. Radiation leakage and coupling with cavity can usually be avoided or minimized with appropriate circuit design and packaging. Dispersion occurs in partially open structure, such as coplanar and microstrip transmission lines, because part of the electromagnetic field is outside the dielectric substrate and travels at a different velocity from that of those inside the substrate. Dispersion caused a transmission line to have frequency dependent characteristic impedance and effective dielectric constant [31,32]. Fortunately, dispersion usually will not pose a serious problem as long as the operating frequency range of the microwave device is not very wide.

Stripline configuration, unlike coplanar and microstrip configuration, does not suffer from radiation leakage and frequency dispersion, and has excellent microwave performance. However stripline configurations do have its drawbacks. In practice, HTS stripline circuits are formed by sandwiching the patterned HTS thin film between two substrates with ground planes. The small air gap that will inevitably be formed between the substrates can cause perturbation of the effective dielectric constant and affects the performance of the device or circuit. Furthermore, integration of external devices and connection of the input/output lines are very difficult in stripline configuration.

All the HTS microwave devices mentioned in this dissertation are in the microstrip configuration. A specially designed pulsed laser deposition setup was used to fabrication high quality YBCO thin film on both faces of a substrate (see chapter 2).

## 1.5 YBCO thin film on $LaAlO_3$ substrate

As all the superconducting microwave devices developed in the course of this thesis were fabricated using YBCO thin films deposited on $LaAlO_3$ (LAO) substrates, the properties of YBCO thin film and LAO substrate are discussed in this section.

YBCO is the first superconductor discovered with $T_c$ above liquid nitrogen boiling point and remains the most widely studied and used of all HTS materials. While there are now many other HTS with $T_c$ higher than that of YBCO, the temperature difference is not sufficient to enable a significant change in the required cooling method. The toxic hazards associated with fabricating the newer mercury and thallium based HTS also contribute to the continuing popularity of YBCO.

YBCO is a member of the ceramic perovskite family. YBCO is usually fabricated with stoichiometry ranging from $YBa_2Cu_3O_6$ to $YBa_2Cu_3O_7$. For this reason, YBCO is often referred to as $YBa_2Cu_3O_{7-\delta}$, where $0 \le \delta \le 1$. For $\delta > 0.7$, the unit cell of YBCO is tetragonal and the material is anti-ferromagnetic and non-superconductive. For $\delta < 0.7$, the unit cell is orthorhombic and the material is no longer anti-ferromagnetic but superconductive, with the superconducting transition temperature increasing to slightly above 90 K as $\delta$ is reduced toward the optimum value of about 0.1. YBCO is a highly anisotropic material with fairly complex layered structure as can be seen in figure 1.2. The superconductive properties of YBCO are anisotropic with the $H_c$, $J_c$, $\xi$ and penetration depth along *ab*-plane differing significantly from those of the *c*-plane.

High quality epitaxial YBCO thin film with *c*-axis orientation and good crystallinity has properties very suitable for microwave applications. The surface resistance of good quality YBCO thin film is typically less than 1 mΩ at 10 GHz and

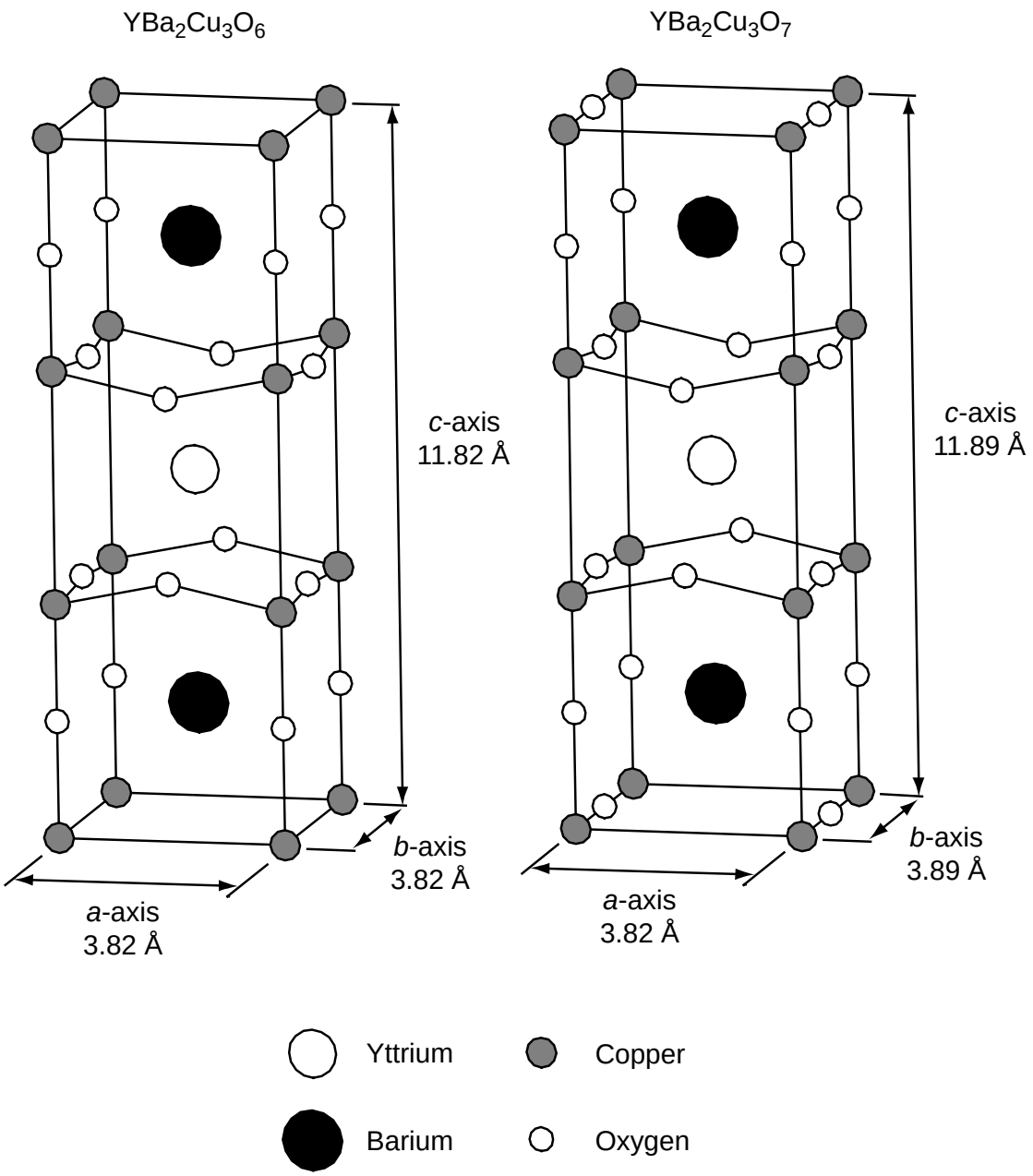


Figure 1.2 Unit cells of $YBa_2Cu_3O_6$ and $YBa_2Cu_3O_7$.

77 K, which is a few orders of magnitude lower than that of normal metal such as copper, silver or gold. Optimized YBCO thin films are typically 200 to 500 nm thick, have $T_c \approx 91\,\mathrm{K}$ (which is slightly lower than single-crystal YBCO) and $J_c > 10^{10}$ $\mathrm{Am}^{-2}$ at 77 K. Expitaxial YBCO thin film can be deposited on suitable substrate by a variety of deposition techniques such as pulsed laser ablation, molecular beam epitaxy, chemical vapor deposition or magnetron sputtering.

To fabricate high quality epitaxial YBCO thin film, the substrate material must satisfy the following conditions: has crystallinity lattice match and similar thermal expansivity between YBCO and substrate, has high temperature stability, has no chemical reaction at interface of YBCO and substrate, and has a reasonably stable and robust surface that can be highly polished. In some cases, lattice mismatch between the YBCO thin film and the substrate can be overcome by first depositing a suitable buffer layer such as $CeO_2$ or yttrium stabilized $ZrO_2$ (YSZ) thin film. The substrate must be inert at high temperature due to the high deposition temperature required during YBCO thin film fabrication.

For the fabrication of microwave devices with low microwave dissipation, an additional requirement for the substrate is that the loss tangent (see section 4.3.2) of the substrate has to be low.

The properties of some substrates commonly used for fabricating YBCO thin film are listed in Table 1.1. Substrates commonly used for fabrication of microwave devices include LAO, LSAT, $Al_2O_3$ (with buffer layer) and MgO. The data in Table 1.1 are compiled from various sources [33-39]. It should be noted that there is much variation in the literature on the data for the dielectric constant and loss tangent. This is partly due to the fact that the microwave properties are strongly influenced by the

growth method and purity of the substrate. The matter is further complicated by the fact that the properties of some substrates are anisotropic. Another cause for the variation is due to the measurement method and conditions. The microwave properties listed in Table 1.1 are for temperature and frequency at or near 77 K and 10 GHz.

**Table 1.1: Properties of materials used for YBCO thin film substrate**

| Material | Structure | Lattice parameter (Å) | Lattice mismatch (%) | Melting point (°C) | Thermal expansion ($10^{-6}$ °$C^{-1}$) | $\varepsilon_r$ | tan $\delta$ | Notes |
|---|---|---|---|---|---|---|---|---|
| *r* cut α-$Al_2O_3$ | Hexagonal<br>(Cubic) | 4.759<br>(5.41) | 6<br>(0.7) | 2049<br>(2600) | 8-9.4<br>(9.9) | 9.4-11.6<br>(21.2-26) | $10^{-8}$<br>- | (For $CeO_2$ buffer layer) |
| $LaAlO_3$ | Rhombohedral<br>Cubic (> 435 °C) | 5.357<br>3.821 | 2 | 2100 | 10-13 | 20.3-27 | $7.6\times10^{-6}$-$3\times10^{-4}$ | Twinning |
| LSAT | Cubic | 7.732 | 0.2 | 1840 | 10 | 22-23.7 | $10^{-5}$-$10^{-3}$ | $(LaAlO_3)_{0.3}$–$(Sr_2AlTaO_6)_{0.35}$ |
| MgO | Cubic | 4.21 | 9 | 2825 | 12.8-14 | 9.6-10 | $6.2\times10^{-6}$ | Hygroscopic, cleaves easily |
| $SrTiO_3$ | Cubic | 3.905 | 1.4 | 2080 | 9.4-10.4 | 300 | $3\times10^{-4}$-$2\times10^{-2}$ | - |
| YSZ | Cubic | 5.14 | 6 | 2500 | 10.3-11.4 | 25.4-33 | 6-$7\times10^{-4}$ | 9 mol % $Y_2O_3$ |
| YBCO | Orthorhombic<br>Tetragonal (> 600 °C) | *a*=3. 82, *b*=3.89<br>3.89 | 0 | - | 10-13 | - | - | - |

LAO substrates with <100> surface orientation are often used when fabricating YBCO thin films for passive microwave devices. LAO is chemically inert and has a melting point of 2100 °C. Good quality LAO substrate can have loss tangent in the order of $10^{-5}$ to $10^{-6}$ which makes the fabrication of low loss microwave devices possible. Furthermore, LAO has a relatively high dielectric constant of around 24 which is helpful for reducing device size.

LAO has lattice spacing which is favorable for the fabrication of high quality expitxial *c*-axis oriented YBCO thin film. At temperatures greater than around 500 °C, LAO has cubic structure with lattice parameter of 3.82 Å. At temperatures below

around 500 °C, LAO has a rhombohedral structure with lattice parameter of 5.36 Å, which is close to the diagonal of the YBCO *ab*-plane.

One major drawback of using LAO is that it exhibits twinning [5,40,41]. Twinning is a crystal growth disorder in which the specimen is composed of distinct domains whose unit cell orientation differs in a symmetrical way, resulting in irregularities in the structure of a thin film, due to the interface boundary between the domains [5]. Twinning can occur in crystals with non-cubic unit cell. LAO undergoes a cubic to rhombohedral structural phase transition whenever temperature is decreased pass 500 °C, resulting in randomly formed twinnings which can cause an increase in the structural defects and surface roughness of the thin film and substrate. These defects can result in dielectric constant inhomogeneity in the LAO substrate [42]. These defects can also cause YBCO thin films to have increased surface resistance, decreased power handling and irregular current distribution [43]. As a result of twinning, LAO substrate is not suitable for producing devices with very narrow line width or fine features.

References


[1] J. R. Gavaler, "Superconductivity in NbGe films above 22 K", *Applied Physics Letters*, vol. 23, no. 8, pp. 480-482, 1973.

[2] J. G. Bednorz and K. A. Müller, "Possible High $T_c$ Superconductivity in the Ba-La-Cu-O system", *Zeitschrift für Physik B: Condensed Matter*, vol. 64, pp. 189-193, 1986.

[3] M. K. Wu, J. R. Ashburn, C. J. Torng, P. H. Hor, R. L. Meng, L. Gao, Z. J. Huang, Y. Q. Wang, and C. W. Chu, "Superconductivity at 93 K in A New Mixed-Phase Y-Ba-Cu-O Compound System at Ambient Pressure", *Physical Review Letters*, vol. 58, no. 9, pp. 908-910, 1987.

[4] J. Bardeen, L. Cooper, and R. Schrieffer, "Theory of Superconductivity", *Physical Review*, vol. 108, no. 5, pp. 1175-1204, 1957.

[5] Z. Y. Shen, *High-Temperature Superconducting Microwave Circuits*, Artech House, Inc., 1994.

[6] M. J. Lancaster, *Passive Microwave Device Applications of High-Temperature Superconductors*, Cambridge University Press, 1996.

[7] B. S. Karasik, I. I. Milostnaya, M. A. Zorin, A. I. Elantev, G. N. Goltsman, and E. M. Gershenzon, "High-Speed Current Switching of Homogeneous YBaCuO Film Between Superconducting and Resistive States", *IEEE Transactions on Applied Superconductivity*, vol. 5, no. 2, pp. 3042-3045, 1995.

[8] A. C. Leuthold, R. T. Wakai, G. K. G. Hohenwarter, and J. E. Nordman, "Characterization of a Simple Thin-Film Superconducting Switch", *IEEE Transactions on Applied Superconductivity*, vol. 4, no. 3, pp. 181-183, 1994.

[9] A. Frenkel, T. Venkatesan, C. Lin, X. D. Wu, and A. Inam, "Dynamic Electrical Response of $Y_1Ba_2Cu_3O_{7-X}$", *Journal of Applied Physics*, vol. 67, no. 8, pp. 3767-3775, 1990.

[10] L. Jian, T. C. Yaw, C. K. Ong, and C. S. Teck, "RF tunable attenuator and modulator using high Tc superconducting filter", *Electronics Letters*, vol. 35, no. 1, pp. 55-56, 1999.

[11] V. N. Keis, A. B. Kozyrev, T. B. Samoilova, and O. G. Vendik, "High-Speed Microwave Filter-Limiter Based on High-$T_c$ Superconducting Films", *Electronics Letters*, vol. 29, no. 6, pp. 546-547, 1993.

[12] B. D. Josephson, "Possible new effects in superconductive tunnelling", *Physics Letters*, vol. 1, no. 7, pp. 251-253, July1962.

[13] P. W. Anderson and J. M. Rowell, "Probable Observation of the Josephson Superconducting Tunneling Effect", *Physical Review Letters*, vol. 10, no. 6, pp. 230-232, 1963.

[14] H. B. Wang, L. X. You, P. H. Wu, and T. Yamashita, "Microwave Responses of an Insular Intrinsic Josephson Junction Stack Fabricated From Bi-Sr-Ca-Cu-O Single Crystal", *IEEE Transactions on Applied Superconductivity*, vol. 11, no. 1, pp. 1199-1202, 2001.

[15] J. R. Tucker, "Predicted conversion gain in superconductor-insulator-superconductor quasiparticle mixers", *Applied Physics Letters*, vol. 36, no. 6, pp. 477-479, 1980.

[16] J. R. Tucker, "Quantum Limited Detection in Tunnel Junction Mixers", *IEEE Journal of Quantum Electronics*, vol. QE-15, no. 11, pp. 1234-1258, 1979.

[17] T.-M. Shen and P. L. Richards, "Conversion gain in mm-wave quasiparticle heterodyne mixers", *Applied Physics Letters*, vol. 36, no. 9, pp. 777-779, 1980.

[18] T. V. Duzer and C. W. Turner, *Principles of Superconductive Devices and Circuits*, 2nd Ed., Prentice Hall, Inc., 1999.

[19] D. P. Bulter, W. Yang, J. Wang, and Bhandari, "Conversion loss of a $YBa_2Cu_3O_7$ grain boundary mixer at 20 GHz", *Applied Physics Letters*, vol. 61, no. 2, pp. 333-335, 1992.

[20] T. Nozue, Y. Yasuoka, J. Chen, H. Suzuki, and T. Yamashita, "Microwave Mixing Characteristics of Thin Film YBCO Josephson Mixers at 77-K", *IEICE Transactions on Electronics*, vol. E75C, no. 8, pp. 929-934, 1992.

[21] T. Yamashita, "New devices based on an HTS intrinsic Josephson junction", *Physica C*, vol. 362, pp. 58-63, 2001.

[22] W. Reuter, M. Siegel, K. Herrmann, J. Schubert, W. Zander, A. I. Braginski, and P. Muller, "Fabrication and characterization of $YBa_2Cu_3O_7$ step-edge junction arrays", *Applied Physics Letters*, vol. 62, no. 18, pp. 2280-2282, 1993.

[23] V. K. Kaplunenko, J. Mygind, N. F. Pedersen, and A. V. Ustinov, "Radiation detection from phase-locked serial dc SQUID arrays", *Journal of Applied Physics*, vol. 73, no. 4, pp. 2019-2023, 1993.

[24] P. Barbara, A. B. Cawthorne, S. V. Shitov, and C. J. Lobb, "Stimulated Emission and Amplification in Josephson Junction Arrays", *Physical Review Letters*, vol. 82, no. 9, pp. 1963-1966, 1999.

[25] T. Yamashita and M. Tachiki, "Single-Crystal Switching Gates Fabricated Using Cuprate Superconductors", *Japanese Journal of Applied Physics Part 1-Regular Papers Short Notes & Review Papers*, vol. 35, no. 8, pp. 4314-4317, 1996.

[26] J. E. Nordman, "Superconductive amplifying devices using fluxon dynamics", *Superconductor Science & Technology*, vol. 8, no. 9, pp. 681-699, 1995.

[27] A. Z. Kain and H. R. Fetterman, "Parametric interactions in high-Tc superconducting step edge junctions at X-band", *Physica C*, vol. 209, no. 1-3, pp. 281-286, 1993.

[28] J. Delahaye, J. Hassel, R. Lindell, M. Sillanpaa, M. Paalanen, H. Seppa, and P. Hakonen, "Low-Noise Current Amplifier Based on Mesoscopic Josephson junction", *Science*, vol. 299, no. 5609, pp. 1045-1048, 2003.

[29] J. H. Takemoto-Kobayashi, C. M. Jackson, C. Pettiette-Hall, and J. F. Burch, "High-$T_c$ Superconducting Monolithic Phase Shifter", *IEEE Transactions on Applied Superconductivity*, vol. 2, no. 1, pp. 39-44, 1992.

[30] D. J. Durand, J. Carpenter, E. Ladizinsky, L. Lee, C. M. Jackson, A. Silver, and A. D. Smith, "The Distributed Josephson Inductance Phase Shifter", *IEEE Transactions on Applied Superconductivity*, vol. 2, no. 1, pp. 33-38, 1992.

[31] D. M. Pozar, *Microwave Engineering*, 2nd Ed., John Wiley & Sons, Inc., 1998.

[32] R. E. Collin, *Foundation for Microwave Engineering*, 2nd Ed., Mcgraw-Hill, 1992.

[33] R. Wordenweber, "Growth of high-$T_c$ thin films", *Superconductor Science & Technology*, vol. 12, no. 6, p. R86-R102, 1999.

[34] S. C. Tidrow, A. Tauber, W. D. Wilber, R. T. Lareau, C. D. Brandle, G. W. Berkstresser, A. J. VenGraitis, D. M. Potrepka, J. I. Budnick, and J. Z. Wu, "New substrates for HTSC microwave devices", *IEEE Transactions on Applied Superconductivity*, vol. 7, no. 2, pp. 1766-1768, 1997.

[35] D. J. Tao, H. Wu, X. D. Xu, R. S. Yan, F. Y. Liu, A. P. B. Sinha, X. P. Jiang, and H. L. Hu, "Czochralski growth of (La,Sr)(Al,Ta)$O_3$ single crystal", *Optical Materials*, vol. 23, no. 1-2, pp. 425-428, 2003.

[36] H. J. Scheel, M. Berkowski, and B. Chabot, "Substrates for High-Temperature Superconductors", *Physica C*, vol. 185, pp. 2095-2096, 1991.

[37] E. K. Hollmann, O. G. Vendik, A. G. Zaitsev, and B. T. Melekh, "Substrates for high-$T_c$ superconductor microwave integrated circuits", *Superconductor Science & Technology*, vol. 7, no. 9, pp. 609-622, 1994.

[38] B. C. Chakoumakos, D. G. Schlom, M. Urbanik, and J. Luine, "Thermal expansion of $LaAlO_3$ and (La,Sr)(Al,Ta)$O_3$, substrate materials for superconducting thin-film device applications", *Journal of Applied Physics*, vol. 83, no. 4, pp. 1979-1982, 1998.

[39] J. M. Phillips, "Substrate selection for high-temperature superconducting thin films", *Journal of Applied Physics*, vol. 79, no. 4, pp. 1829-1847, 1996.

[40] H. J. Scheel, M. Berkowski, and B. Chabot, "Problems in epitaxial growth of high-$T_c$ superconductors", *Journal of Crystal Growth*, vol. 115, no. 1-4, pp. 19-30, 1991.

[41] G. Koren and E. Polturak, "Is $LaAlO_3$ a viable substrate for the deposition of high quality thin films of $YBa_2Cu_3O_{7-\delta}$?", *Superconductor Science & Technology*, vol. 15, no. 9, pp. 1335-1339, 2002.

[42] D. Reagor and F. Garzon, "Dielectric and optical properties of substrates for high-temperature superconductor films", *Applied Physics Letters*, vol. 58, no. 24, pp. 2741-2743, 1991.

[43] A. P. Zhuravel, A. V. Ustinov, K. S. Harshavardhan, and S. M. Anlage, "Influence of $LaAlO_3$ surface topography on rf current distribution in superconducting microwave devices", *Applied Physics Letters,* vol. 81, no. 26, pp. 4979-4981, 2002.

# CHAPTER 2:
# FABRICATION OF YBCO THIN FILM BY PULSED LASER DEPOSITION

The experimental setup and procedure for the fabrication of the superconducting YBCO thin film samples are described in this chapter. All the superconducting YBCO thin film samples mentioned in this dissertation were prepared using the homemade Pulsed Laser Deposition (PLD) system at the Centre for Superconducting and Magnetic Materials (CSMM).

The PLD system used to prepare the YBCO thin film incorporated a laser beam scanning setup and a silicon radiation heater. The laser beam scanning setup enables the production of high-uniformity large-area thin film. The silicon radiation heater enables the production of YBCO thin film on both faces of a substrate, which is required for the production of superconducting microwave devices with microstrip geometry.

## 2.1 Pulsed Laser Deposition

PLD is a type of physical vapour deposition technique for thin film fabrication in which pulses of laser beam are used as the heat source to vapourize the target material. Although PLD technique was first reported in 1965 [1], PLD technique did not generate much interest until 1987, when the PLD technique was successfully applied to the fabrication of perovskite HTS thin film [2]. The fabrication of perovskite HTS demonstrated an important advantage PLD have over other thin film fabrication techniques, i.e. the ability and ease in the fabrication of thin film with complex multi-element composition, by simply using target with composition identical to that of the required thin film. Another advantage of the PLD technique is

that it requires relatively simple experimental setup, as can be seen in the following section.

PLD is not without its drawbacks. One drawback is that the region with stoichiometry suitable for thin film deposition within the “plume” formed by the laser ablated material has a narrow angular distribution. A photograph of the YBCO plume is shown in Figure 2.1. The narrow angular distribution of the region within the plume with suitable stoichiometry results in the difficulty of fabricating large area thin film with high uniformity. This problem can be solved by scanning the laser over a target with large surface area. Another drawback is the “splashing” from the target which can result in particulates on the deposited thin film. While the problem of splashing can be somewhat alleviated by methods such as the use of high density target with smooth surface, splashing remains a critical problem for the PLD technique.

Although these drawbacks have restricted the use of PLD technique from industrial applications which usually require high-uniformity large-area thin film, the PLD technique is highly suitable for research purpose, which usually requires thin films of multi-element composition in various stoichiometries.

In contrast to the relatively simple experimental setup for PLD, the theory of PLD mechanism is highly complex. Detailed explanations on the theory and mechanism of PLD can be found in references such as [3].

## 2.2 Experimental setup

The schematic diagram of the experimental setup and a photograph of the interior of the vacuum chamber used for the fabrication of the YBCO thin film samples are shown in figure 2.2 and figure 2.3 respectively.

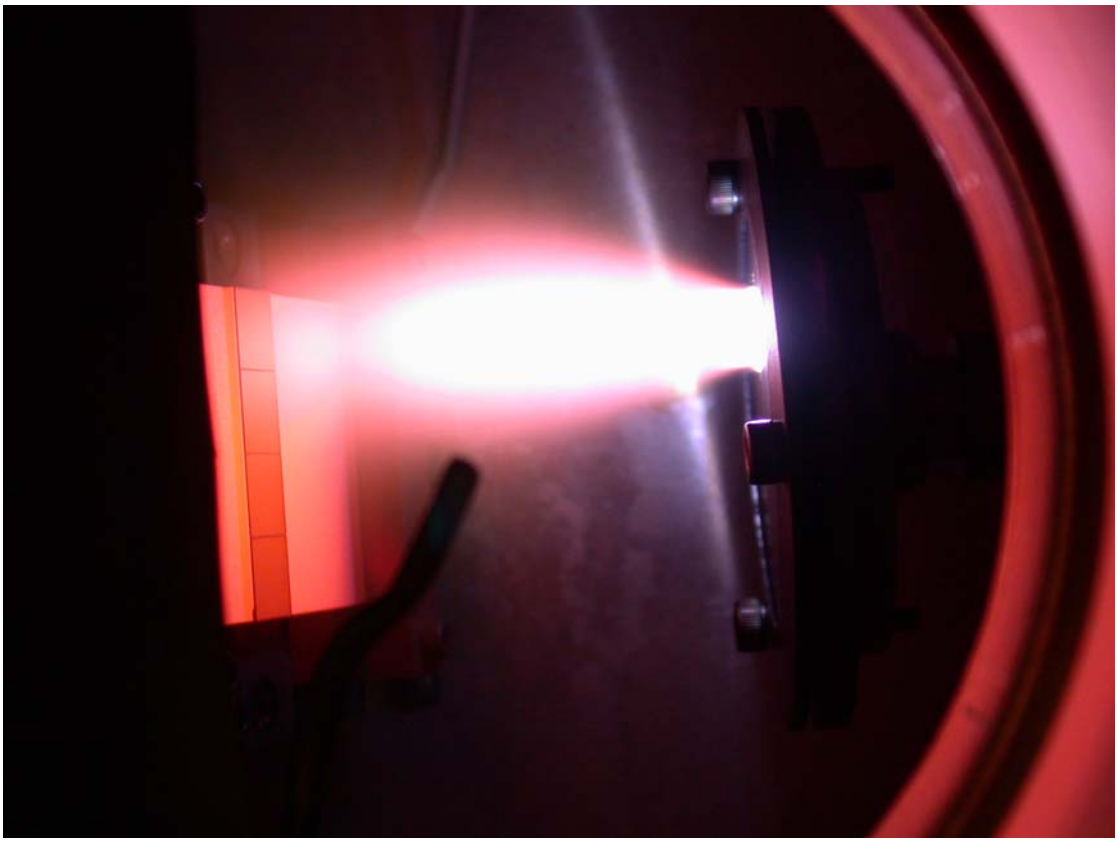

Figure 2.1 Photograph of the plume formed during pulsed laser deposition.

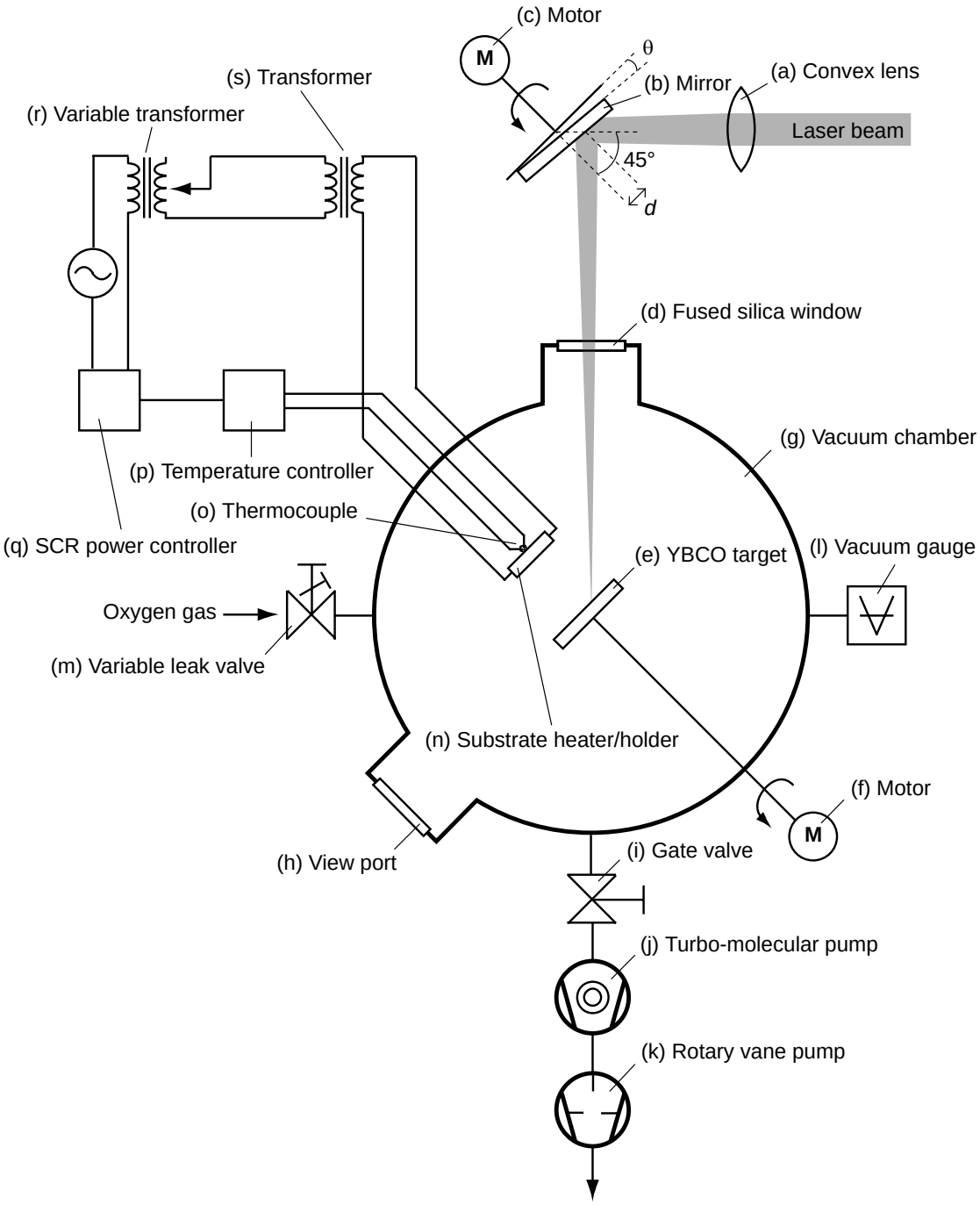


Figure 2.2 Schematic diagram of the PLD setup used for YBCO thin film fabrication.

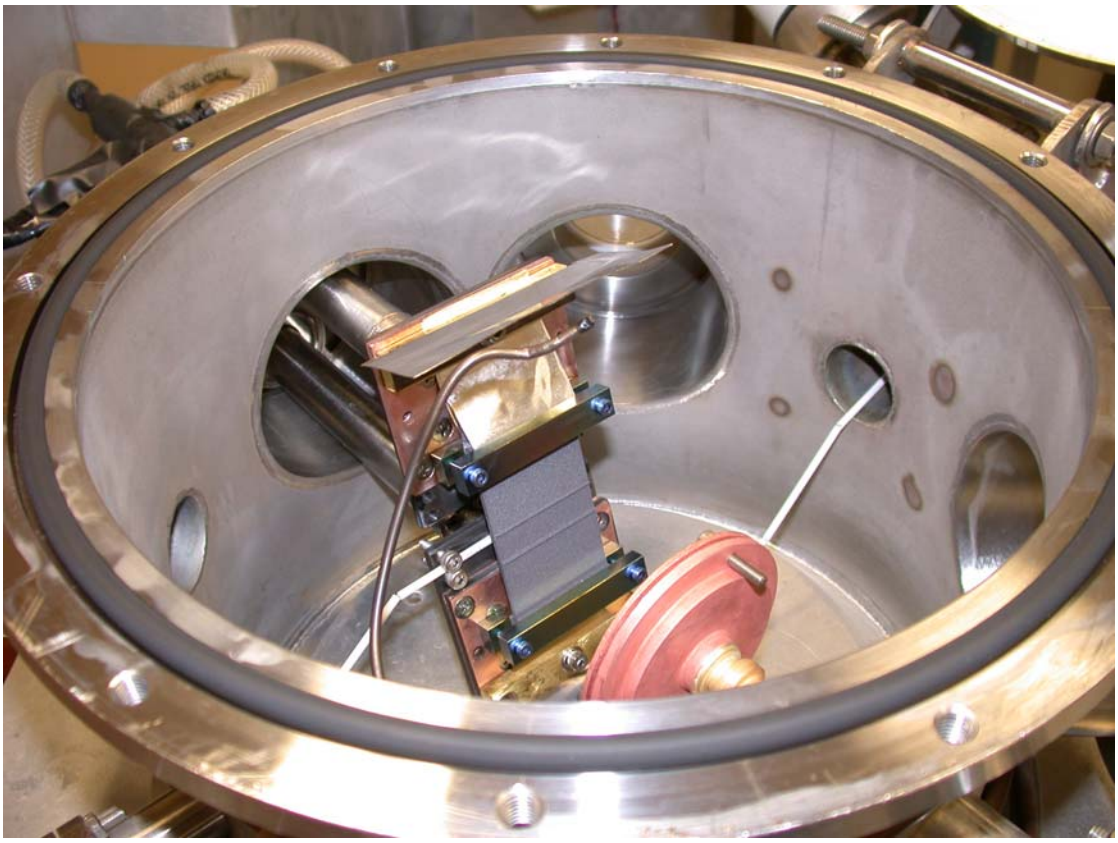

Figure 2.3 Photograph of the PLD vacuum chamber interior.

### 2.2.1 Excimer laser and optics

An excimer laser (Compex 201[1]) filled with 99.995 % purity KrF gas mixture[2] consisting of by pressure, 3.93 % krypton, 0.1 % fluorine, and 1.71 % helium with neon balance, was used to produce the ultra-violet (UV) laser pulse with wavelength of 248 nm. Laser operating in UV wavelength is preferred in PLD, as most materials exhibit good absorption in this spectral region. The excimer laser is capable of producing pulse with maximum energy of up to 650 mJ, with FWHM pulse duration of 25 ns, at pulse repetition rate of up to 10 Hz.

As the dimension of the laser beam spot directly output by the laser is 24 mm by 12 mm, the maximum energy density is only about 0.2 J/cm$^2$, which is below the energy density of about 2 J/cm$^2$ needed for the PLD of YBCO thin film. To increase the energy density of the laser beam, a convex lens, marked in figure 2.2 as (a), was used to focus the laser beam to a small, high energy density spot at the YBCO target. The lens is made from optical-quality UV-grade fused silica. Normal optical glass is not a suitable lens material, as UV transmission will be highly attenuated.

To deposit the thin film with high-uniformity over a large area, a 45° incidence angle UV dielectric mirror (Part no. 16MFQ025[3]), marked in figure 2.2 as (b), mounted on motor driven rotating holder, marked in figure 2.2 as (c), was used to scan the laser beam over the YBCO target. The rotation axis of the mirror holder and the incident laser beam was at an angle of 45°. The path of the focused laser beam spot on the YBCO target was elliptical in shape and could be adjusted by varying the parameters $\theta$ and $d$ shown in figure 2.2. $\theta$ is the tilt angle between the mirror and

[1] Lambda Physik, Göttingen, Germany
[2] Spectra Gases, Inc., New Jersey, USA
[3] Melles Griot, California, USA

the mirror holder, and $d$ is the distance between where the laser beam hits the mirror and the rotation axis of the mirror holder. Ideally, the mirror should be placed before the focusing lens to prevent the dielectric mirror from been damage by the focused high energy density laser beam. Although such an arrangement was not possible due to the space constraint in the experiment setup, the mirror was placed sufficiently close to the lens so that the energy density of the laser beam on the mirror is still low. The laser beam entered the vacuum chamber through an optical quality UV grade fused silica window, marked in figure 2.2 as (d).

### 2.2.2 YBCO target

The laser beam was aligned such that that focused laser spot would hit the YBCO target, marked in figure 2.2 as (e), in the vacuum chamber. Although superconducting bulk YBCO samples had been fabricated in CSMM, a commercially manufactured hot pressed YBCO target[4] was used for fabricating the YBCO thin film as it had a higher density (5.4 g/cm$^3$) than the homemade YBCO targets and also because the required target diameter was relatively large at 10 cm. During thin film deposition, the target was driven to rotate by a motor, marked in figure 2.2 as (f), connected to the target holder by a rotary vacuum feed-through. The rotation of the target maximizes the target surface area usage and prolongs the period before the target requires resurfacing. The rotation of the target also prevents the target from cracking due to uneven heating.

### 2.2.3 Vacuum chamber and vacuum pumping system

The homemade vacuum chamber, marked in figure 2.2 as (g), was made from 316 stainless steel. The vacuum chamber had a top access door which enables easy

[4] Physcience Opto-electronics Co., Ltd., Beijing, PRC

loading and unloading of the substrates onto the heater located in the chamber. Copper piping was wrapped around and welded to the vacuum chamber, to water-cool the chamber and prevent heat induce damage to the glass view ports, fused silica laser window and Viton o-ring vacuum seals of the chamber, during high temperature heating of the substrate.

The vacuum pumping system of the chamber consists of a turbo-molecular drag pump (TMH 064 with TCP 015 drive unit[5]), marked in figure 2.2 as (j), with a rotary vane backing pump (DUO 2.5[5]), marked in figure 2.2 as (k), and could pump down the chamber to a pressure of about $1 \times 10^{-6}$ mbar from atmospheric pressure in about 3 hours. The vacuum pressure measurement system (PKR 250 sensor gauge with TPG 251 controller[6]), marked in figure 2.2 as (l), consist of a Pirani guage for measurement from 1000 to 0.01 mbar and a cold cathode ionization gauge for pressure measurement from 0.01 to $5 \times 10^{-9}$ mbar.

As the oxygen pressure in the chamber had to be carefully controlled during the deposition of perovskite oxide such as YBCO, high purity oxygen was feed into the chamber by a variable leak valve (Part no. 215 010[7]), marked in figure 2.2 as (m).

### 2.2.4 Silicon radiation heater

A set of custom made single-crystal highly-doped silicon heating elements[4], marked in figure 2.2 as (n), was used as the substrate holder/heater. The dimension of the silicon heater for substrate with 10 mm height is shown in figure 2.4. The set of silicon heaters was designed to accommodate substrates with different dimensions, with width of up to 40 mm. For substrate with smaller width, several substrates could

[5] Pfeiffer Vacuum Technology AG, Asslar, Germany
[6] Balzers AG, Balzers, Fürstentum Liechtenstein
[7] Leybold Vakuum GmbH, Cologne, Germany

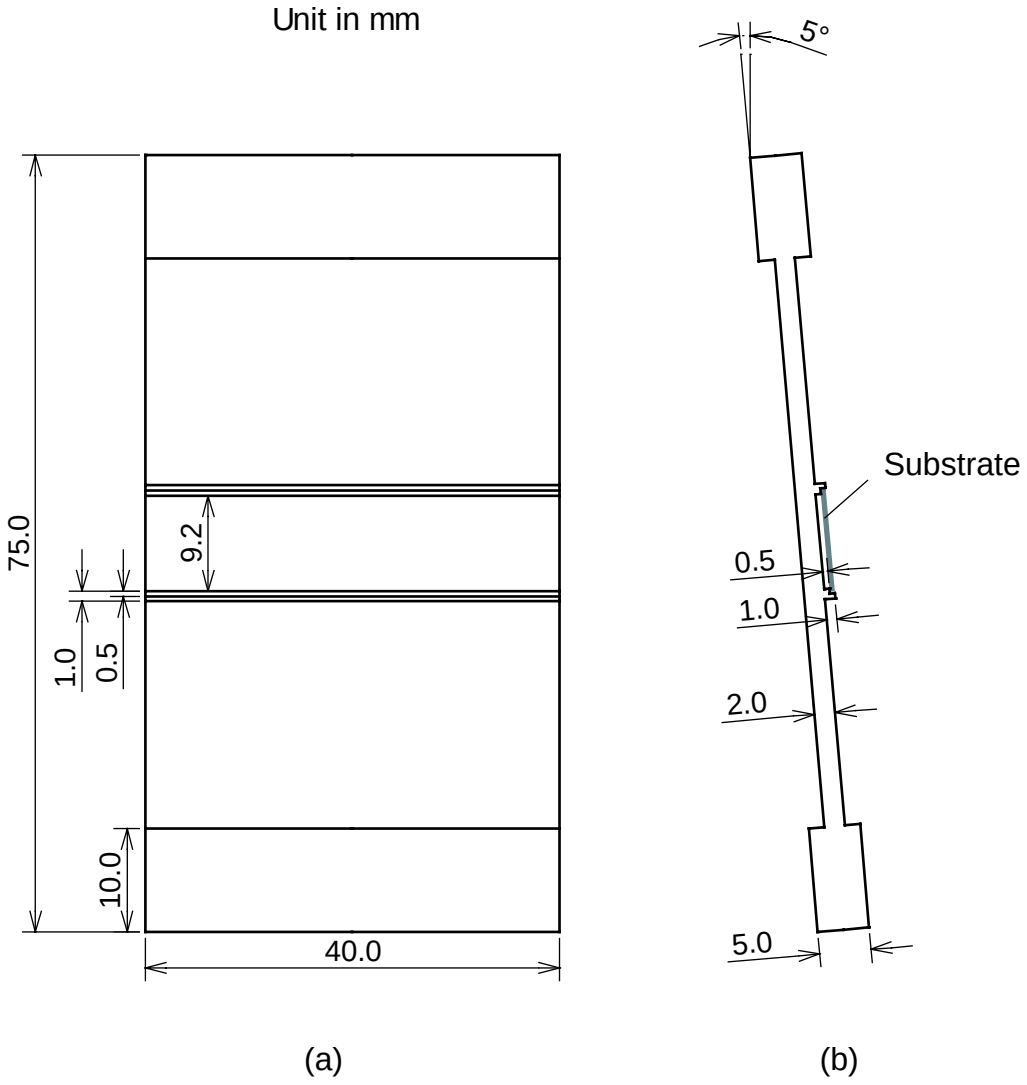


Figure 2.4 Dimension of the silicon heater for substrate with 10 mm height. (a) Front view. (b) Side view of the heater shown with 5° tilt and loaded with substrate.

be placed on the heater at the same time, as shown in figure 2.5. The silicon heater can operate at temperature of up to 960 °C with temperature uniformity of ± 2 °C over a $30 \times 30$ mm$^2$ area. The high operating temperature and temperature uniformity of the silicon heater allow the silicon heating element to function as a non-contact radiation heater. Unlike most conventional substrate heaters, it is not necessary to attach the substrate to the heater with silver paste or some other thermal conductive layer to ensure sufficiently high thermal conductivity and temperature uniformity. The use of silicon heater allows the deposition of thin film on both faces of a substrate, as it eliminated the problem of contamination on the side of the substrate facing the heater.

The silicon heater was mounted with 5° tilted from the vertical axis which allows the substrate to rest on the ledge of the heater without the need to secure the substrate with clamps, as shown in figure 2.4 (b). Only the top and bottom edges of the substrate are in contact with the heater. The substrate could be easily loaded or unloaded from the heater with a pair of tweezers. The heater was designed with 0.5 mm gap between the heater and substrate as shown in figure 2.6. The heater was clamped to water-cooled electrical feed-through. Silver foils with thickness of 0.1 mm were inserted between clamps of the electrical feed-through and the silicon heater, to improve electrical contact and more importantly, to prevent the brittle silicon heater from cracking due to thermal expansion mismatch.

### 2.2.5 Temperature control system

A homemade K-type thermocouple, marked in figure 2.2 as (o), was used for temperature measurement. The thermocouple was made by resistance welding together the tips of 0.2 mm diameter chromel and alumel wires. A photograph of the

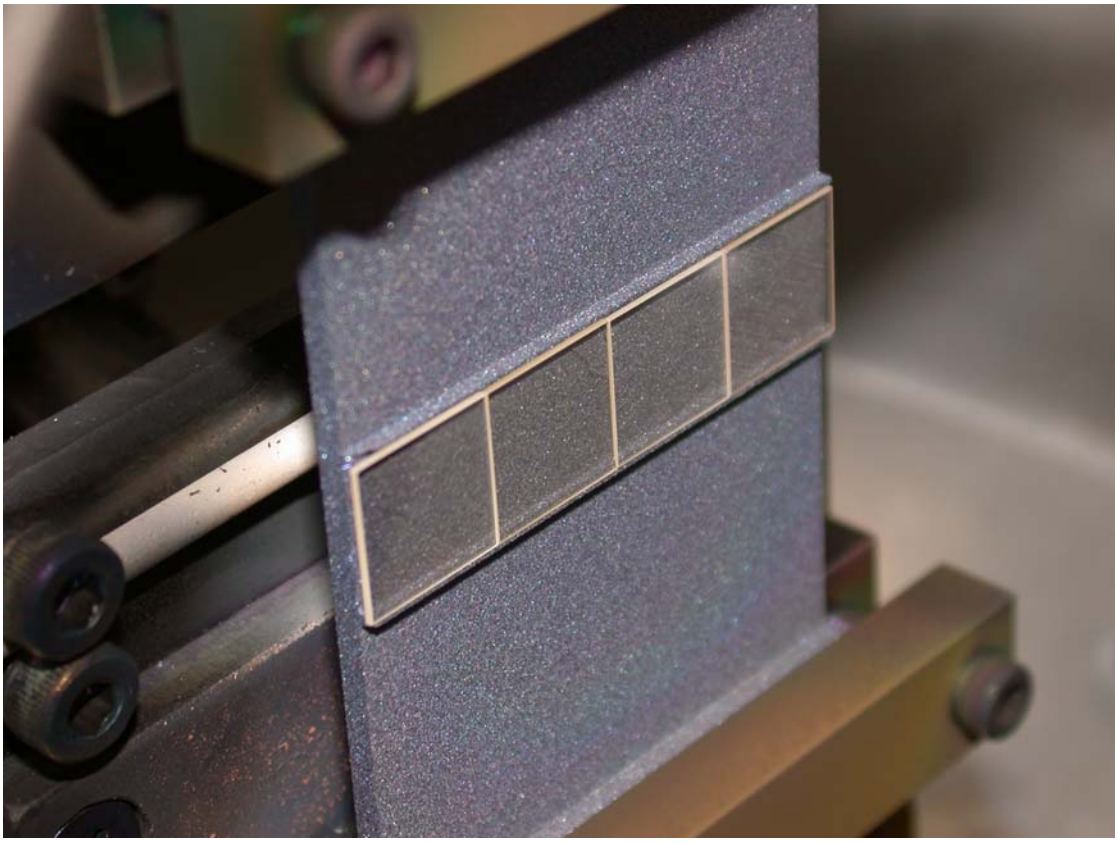

Figure 2.5 Photograph of the silicon heater loaded with four 10 mm × 10 mm × 0.5 mm substrates.

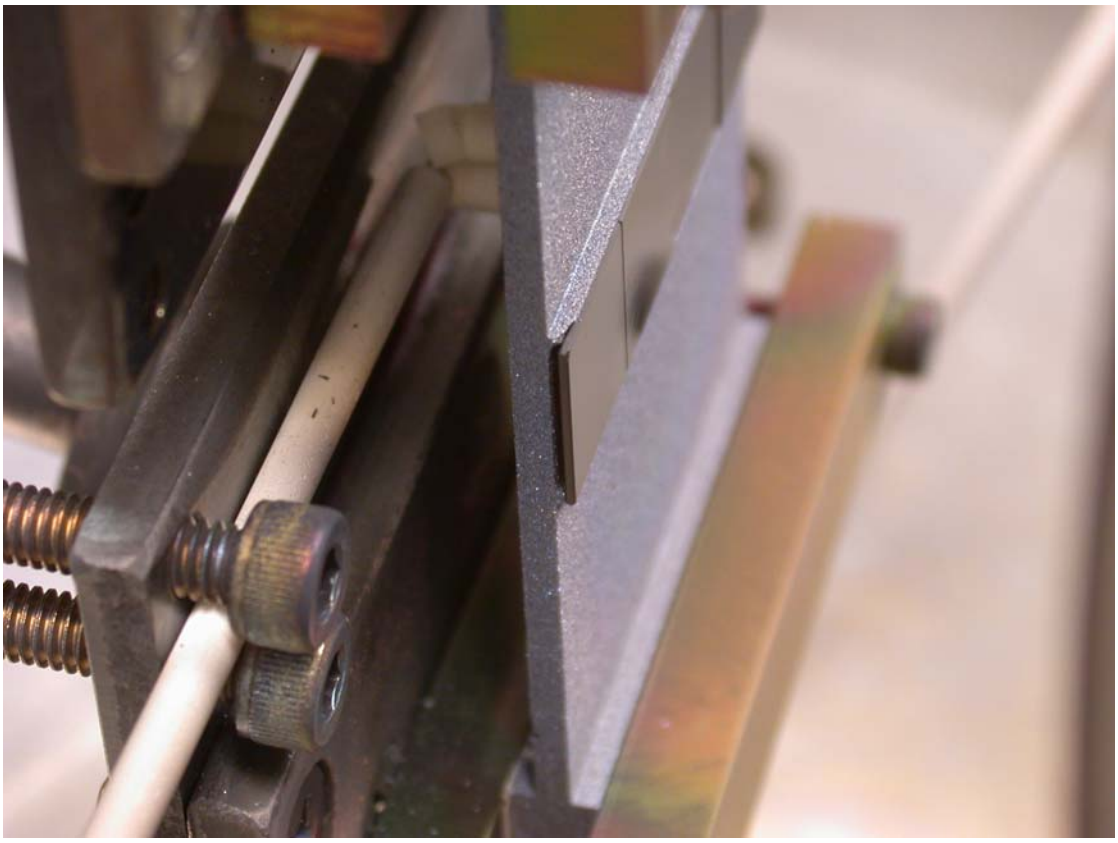

Figure 2.6 Photograph showing the gap between the substrate and the silicon heater.

thermocouple is shown in figure. 2.7. The chromel and alumel wires were insulated using high temperature resistant aluminum oxide ceramic tubes. The homemade thermocouple had a very low heat capacity, and thus had a very fast response time which allows better temperature control.

To measure the surface temperature of the substrate ($T_s$), it was necessary to place the tip of the thermocouple on the substrate surface. This will however result in a shadow on the deposited thin film. In the experiment setup used, the temperature reading during thin film deposition was based on the temperature of the heater ($T_h$), measured by a thermocouple placed directly in contact with the back of the silicon heater. As $T_s$ and $T_h$ were not equal, $T_s$ was obtained from prior temperature calibration measurement with two thermocouples; i.e. one thermocouple at the back of the heater and another thermocouple placed directly on the substrate. The two-thermocouple temperature calibration measurement had to be performed for substrate with different thickness or material.

The K-type thermocouple was connected to a programmable PID temperature controller (904[8]), marked in figure 2.2 as (p). The control signal from the programmable temperature controller was used to control a phase angle firing SCR power controller (TE10 A[8]), marked in figure 2.2 as (q). A variable transformer, marked in figure 2.2 as (r), and a high output current transformer, marked in figure 2.2 as (s), were used to step down the 230 V mains voltage to a suitable input voltage for the silicon heater, which required low voltage (of less than 20 V) but high current (of up to 90 A). Using the heating system setup described here, the temperature could be

[8] Eurotherm Control Ltd., Worthing, UK

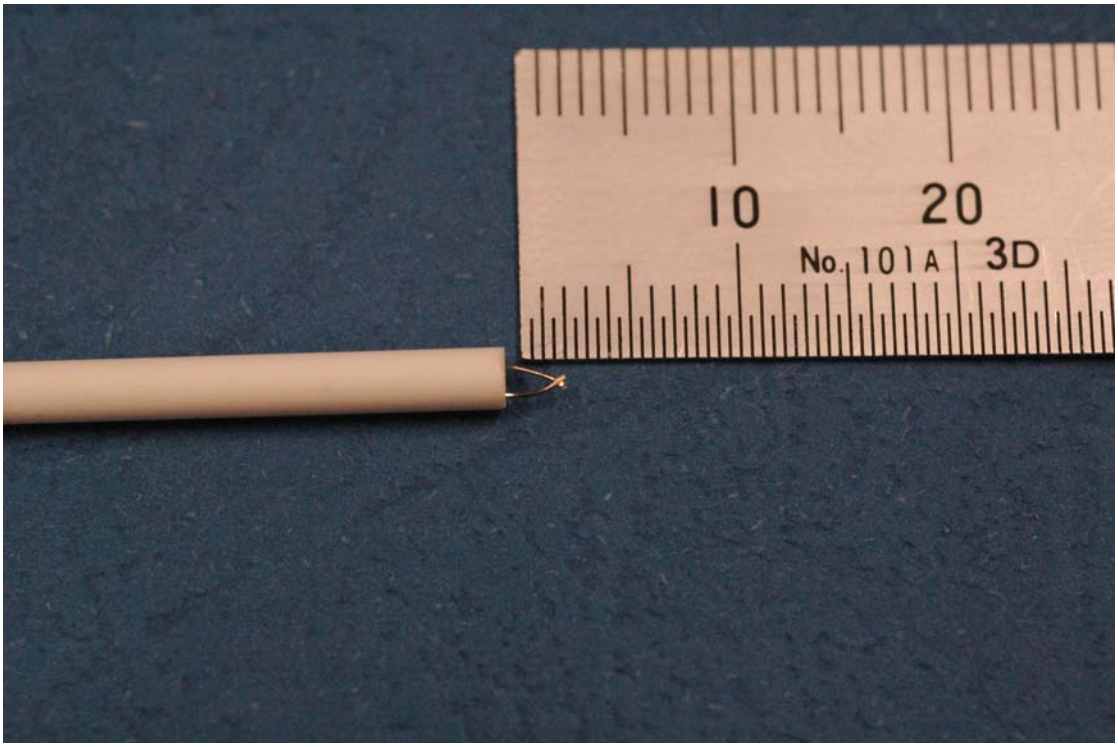


Figure 2.7 Photograph of the homemade K-type thermocouple.

controlled with error of less than ± 1 °C at thin film deposition temperature of around 850 °C.

## 2.3 YBCO thin film pre-deposition preparation

Prior to the actual YBCO thin film deposition, it is necessary to prepare the vacuum chamber and clean the substrate. The preparation of the vacuum chamber include cleaning of the fused silica laser window, “resurfacing” of the YBCO target, and adjusting the position and alignment of the rotating mirror and focusing lens. The rotating mirror and focusing lens was adjusted to focus the laser beam on the target and to obtain optimum scanning of the laser beam spot across the target.

### 2.3.1 Fused silica laser window cleaning

The fused silica laser window had to be cleaned regularly to remove the coating of target material ablated during PLD and deposited on the fused silica window. Over time, the build up of the coating on the window could significantly reduce the energy density of the laser beam on the target, affecting both the growth rate and quality of the thin film.

To clean the fused silica window, the window was removed from the vacuum chamber and dipped in 10 % (by volume) nitric acid to dissolve the YBCO coating. The window was then thoroughly rinsed with distill water. After rinsing with distill water, the window was rinsed with ethanol (99.9 % purity) and blown dry using compressed nitrogen gas.

### 2.3.2 Resurfacing the YBCO target

The surface of the YBCO target will requires resurfacing as it becomes rougher after a period of laser ablation [4]. Rough surface on a target is a contributing cause of

particulates on the thin film and would also cause deviation of the thin film stoichiometry [5,6]. The surface composition of a multi-elemental target may also change after prolong laser ablation, due to the differences in the ablation rate of elements. For best results, the YBCO target should be resurfaced before every PLD run.

To resurface the target, the target was first sanded with a medium roughness silicon carbide sandpaper (320 grit) until its surface was flat, then polished to a smooth surface using fine sandpapers (800 grit follow by 1200 grit). The target was then blown clean with compressed nitrogen gas to get rid of residue particles from the sanding and polishing process. After the target was mounted in the chamber, the target surface was further conditioned by laser ablation for five minutes. The heater was covered with aluminum foil to prevent deposition of YBCO on the heater surface during the laser ablation conditioning of the target surface and when adjusting the alignment and position of the mirror and focusing lens.

### 2.3.3 Substrate cleaning

All the YBCO thin film samples mentioned in this dissertation were deposited on commercially available 0.5 mm thick, single-single or double-side polished LAO substrate with <100> surface orientation[9].

It is necessary for the substrate surface to be very clean prior to the deposition process to ensure fabrication of good quality thin film. The substrate was cleaned by first immersing it in an acetone (purity > 99.8 %) ultrasonic bath for 10 minutes to remove organic contaminants. Then it was flushed thoroughly with running distill water, and immersed in a 10 % (by volume) nitric acid ultrasonic bath for 10 minutes

[9] Hefei Kejing Materials Technology Co. Ltd., Anhui, PRC

to remove inorganic contaminants. The substrate was then again flushed thoroughly with running distill water, and immersed in acetone ultrasonic bath for 10 minutes. The substrate was then transferred to and stored in high purity ethanol (> 99.9 %) until it is ready to be loaded into the vacuum chamber. Before loading into the chamber, the substrate was blown dry using compressed nitrogen gas.

## 2.4 Deposition parameters for YBCO thin film

As the YBCO thin films fabricated in this thesis were for the fabrication of microwave devices, the deposition parameters were optimized for the lowest surface resistance, measured using the characterization method described in chapter 3. The YBCO thin films were deposited with the following optimized parameters: energy density of 2.5 J/cm$^2$, target to substrate distance of 5.5 cm, $T_h$ at 860 °C ($T_s$ at 755 °C) and oxygen pressure at 0.2 mbar.

To deposit the YBCO thin film to a thickness of at least 2.5 times the penetration depth, i.e. 500 nm thick, required 30 minutes of deposition time with the laser pulse repetition rate at 5 Hz.

After deposition, the YBCO thin film was annealed at $T_h$ = 580 °C for 30 minutes at oxygen pressure of 1 bar. The detailed procedure of the thin film deposition process is listed in appendix 1. $T_h$ was lowered by 10 °C to 850 °C when depositing YBCO thin film on the second side of the substrate. This was necessary as the radiation absorption of a substrate already deposited with YBCO thin film on one side was higher than a bare substrate [7].

References

[1] H. M. Smith and A. F. Turner, "Vacuum Deposited Thin Films Using a Ruby Laser", *Applied Optics*, vol. 4, no. 1, pp. 147-148, 1965.

[2] D. Dijkkamp, T. Venkatesan, X. D. Wu, S. A. Shaheen, N. Jisrawi, Y. H. Minlee, W. L. Mclean, and M. Croft, "Preparation of Y-Ba-Cu oxide superconductor thin films using pulsed laser evaporation from high $T_c$ bulk material", *Applied Physics Letters*, vol. 51, no. 8, pp. 619-621, 1987.

[3] D. B. Chrisey and G. K. Hubler, *Pulsed Laser Deposition of Thin Films*, John Wiley & Sons, 1994.

[4] T. P. Obrien, J. F. Lawler, J. G. Lunney, and W. J. Blau, "The effect of laser fluence on the ablation and deposition of $YBa_2Cu_3O_7$", *Materials Science and Engineering B-Solid State Materials for Advanced Technology*, vol. 13, no. 1, pp. 9-13, 1992.

[5] D. S. Misra and S. B. Palmer, "Laser ablated thin films of $Y_1Ba_2Cu_3O_{7-\delta}$: the nature and origin of the particulates", *Physica C*, vol. 176, no. 1-3, pp. 43-48, 1991.

[6] C. C. Chang, X. D. Wu, R. Ramesh, X. X. Xi, T. S. Ravi, T. Venkatesan, D. M. Hwang, R. E. Muenchausen, S. Foltyn, and N. S. Nogar, "Origin of surface roughness for *c*-axis oriented Y-Ba-Cu-O superconducting films", *Applied Physics Letters*, vol. 57, no. 17, pp. 1814-1816, 1990.

[7] A. C. Westerheim, B. I. Choi, M. I. Flik, M. J. Cima, R. L. Slattery, and A. C. Anderson, "Radiative substrate heating for high-$T_c$ superconducting thin-film deposition: Film-growth-induced temperature-variation", *Journal of Vacuum Science & Technology A-Vacuum Surfaces and Films*, vol. 10, no. 6, pp. 3407-3410, 1992.

# CHAPTER 3:
# CHARACTERIZATION OF YBCO THIN FILM

In this chapter, the methods used to characterize the YBCO thin film samples mentioned in this dissertation are reviewed and the typical characterization results are presented. In addition to the dc and rf electrical properties, the structural properties of the YBCO thin film were also characterized. As the properties of YBCO thin films are extremely sensitive to structural imperfection, impurities and strain, structural analysis plays an important role in the optimization of the PLD parameters used to fabricate the YBCO thin films. The crystallinity of the YBCO thin films was examined using X-ray diffraction. The surface morphology of the YBCO thin films was examined using atomic force microscopy and scanning electron microscopy. The dc electrical transport properties of the YBCO thin films were examined using four-wire measurement of resistance versus temperature. The surface resistance of the YBCO thin films at microwave frequency was characterized using a resonant method developed at CSMM.

## 3.1 X-Ray Diffraction

X-ray diffraction (XRD) is widely used in the study of crystalline structure [1]. Two types of XRD techniques were used to characterize the YBCO thin films; Bragg-Brentano geometry scan and rocking curve measurement. Bragg-Brentano scan can detect the presence of impurities or unwanted phases in the YBCO thin film sample, since their crystalline structure or orientation are different and will give rise to a different set of Bragg's diffraction peaks. Bragg-Brentano scan was also used to determine the orientation and lattice parameter of the fabricated YBCO thin film.

Rocking curve measurement was used as an indicator of the in-plane crystalline quality of the YBCO thin film.

### 3.1.1 Bragg-Brentano geometry scan

Bragg-Brentano geometry scan is also commonly called the $\theta$-$2\theta$ scan. In $\theta$-$2\theta$ scan, the sample is irradiated by a collimated monochromatic (in an ideal setup) X-ray beam at an angle of $\theta$ with respect to the surface of the sample. The intensity of the diffracted beam at an angle of $2\theta$ with respect to the incident beam is measured, to obtain the intensity versus $\theta$ or $2\theta$ diffraction spectrum. Peaks can occur in the diffraction spectrum at values of $\theta$ where the Bragg's equation is satisfied, i.e.:

$$n\lambda = 2d\sin\theta\,, \tag{3.1}$$

where $n$ is an integer, $\lambda$ is the X-ray wavelength and $d$ is the distance between adjacent crystal planes with the same Miller index.

As YBCO has orthorhombic symmetry, $d$ is given by:

$$\frac{1}{d^2} = \frac{h^2}{a^2} + \frac{k^2}{b^2} + \frac{l^2}{c^2}, \tag{3.2}$$

where $h$, $k$, $l$ are the Miller index and $a$, $b$, $c$ are the lattice parameters.

Although the *c*-axis can be calculated using equations (3.1) and (3.2), the surface displacement of the YBCO thin film sample from the diffractor axis usually cause a significant error in the result. The error in $d$ due to the displacement from the diffractor axis has the relation:

$$\frac{\Delta d}{d} \propto \frac{\cos^2\theta}{\sin\theta}. \tag{3.3}$$

A more accurate value of the *c*-axis lattice parameter can be obtained from the y-axis intercept of the least square fitting of the calculated $d(\theta)$ versus $\cos^2\theta/\sin\theta$ graph [1].

### 3.1.2 Rocking curve measurement

In rocking curve measurement, the relative geometry of the X-ray source and detector is kept fixed at that of a designated Bragg's diffraction peak while the angle between the incident X-ray and sample surface is varied. Rocking curve measurement is also called $\omega$ scan, as the angle between the incident X-ray and sample surface is commonly denoted by $\omega$. The FWHM (full width at half maximum) value of the peak in the intensity versus $\omega$ rocking curve is an indication of the in-plane crystalline orientation quality, as regions of differing crystal orientation will successively come into the diffraction position as the sample is rotated. YBCO thin film with good in-plane crystalline quality will have a small FWHM.

### 3.1.3 XRD measurement setup

The XRD measurements presented in this dissertation were carried out using the Philips PW1710 based diffractometer controller[1] at Department of Physics, National University of Singapore. The diffractometer used a PW2273/00 X-ray source[1] with PW1729/40 high tension generator[1] set at 30 kV and 20 mA to produced mainly copper $K_{\alpha1}$ radiation ($\lambda$ = 1.54056 Å) with a small amount of $K_{\alpha2}$ radiation ($\lambda$ = 1.54439 Å). The diffractometer used the PW1820 goniometer[1] with PW1768 specimen holder[1]. A PW1397/60 theta drive[1] was mounted on the goniometer for the purpose of rocking curve measurement. A PW1711/10 xenon filled proportional

[1] Philips Analytical X-ray, B. V., Almelo, Netherlands

counter[1] with a PW1752 graphite monochromator[1] was used to detect the diffracted X-ray. Control of the diffractometer and data collection/analysis was done using a personal computer running the PC-APD (PW1877) (Version 3.6B) XRD peak analysis software[1]. Functions of the software include peak search, curve smoothing, $K_{\alpha 2}$ stripping and background subtraction. The $\theta$-$2\theta$ scans were usually done using the following parameters: continuous scan mode, sampling time of 2 second per step and step size of 0.02°.

### 3.1.4 XRD measurement results

A $\theta$-$2\theta$ scan for a YBCO thin film sample fabricated on a LAO substrate using the optimized PLD parameters and procedure described in chapter 2 is shown in figure 3.1. The $\theta$-$2\theta$ scan shown in figure 3.1 is representative of the typical $\theta$-$2\theta$ scans for both the first and second sides of a double-sided YBCO thin films fabricated using the optimized PLD parameters and procedure. Only the *c*-axis peaks were observed, indicating the presence of impurity or unwanted phase is negligible.

The graph of the calculated $d(\theta)$ versus $\cos^2\theta/\sin\theta$ is shown in figure 3.2. From the extrapolated y-axis intercept, the *c*-axis lattice parameter for the YBCO thin film was 11.681 Å.

A rocking curve of a YBCO thin film sample is shown in figure 3.3. The rocking curve shown in figure 3.3 is representative of the typical measured rocking curves for the first and second sides of a double-sided YBCO thin films fabricated using the optimized PLD parameters and procedure. The FWHM for the (005) peak was typically about 0.45°, indicating that the thin films had well ordered in-plane crystallinity.

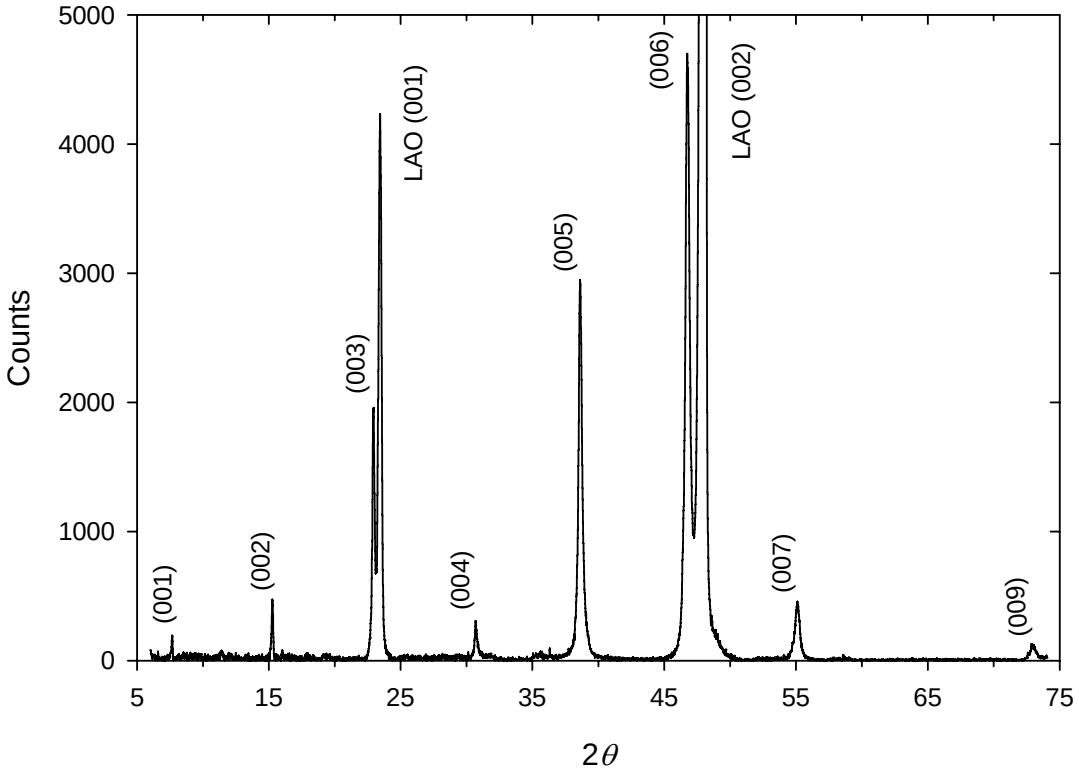


Figure 3.1 The $\theta - 2\theta$ XRD scan of a typical YBCO thin film sample.

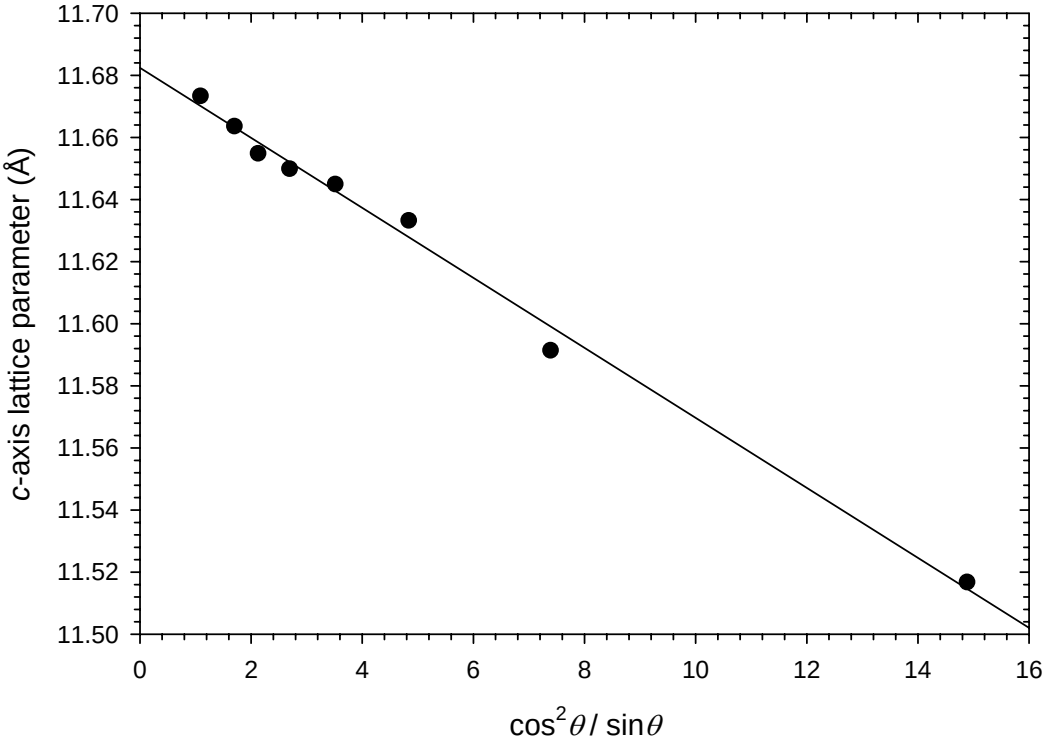


Figure 3.2 Graph of the calculated *c*-axis lattice parameter against $\cos^2\theta/\sin\theta$ for a typical YBCO thin film sample.

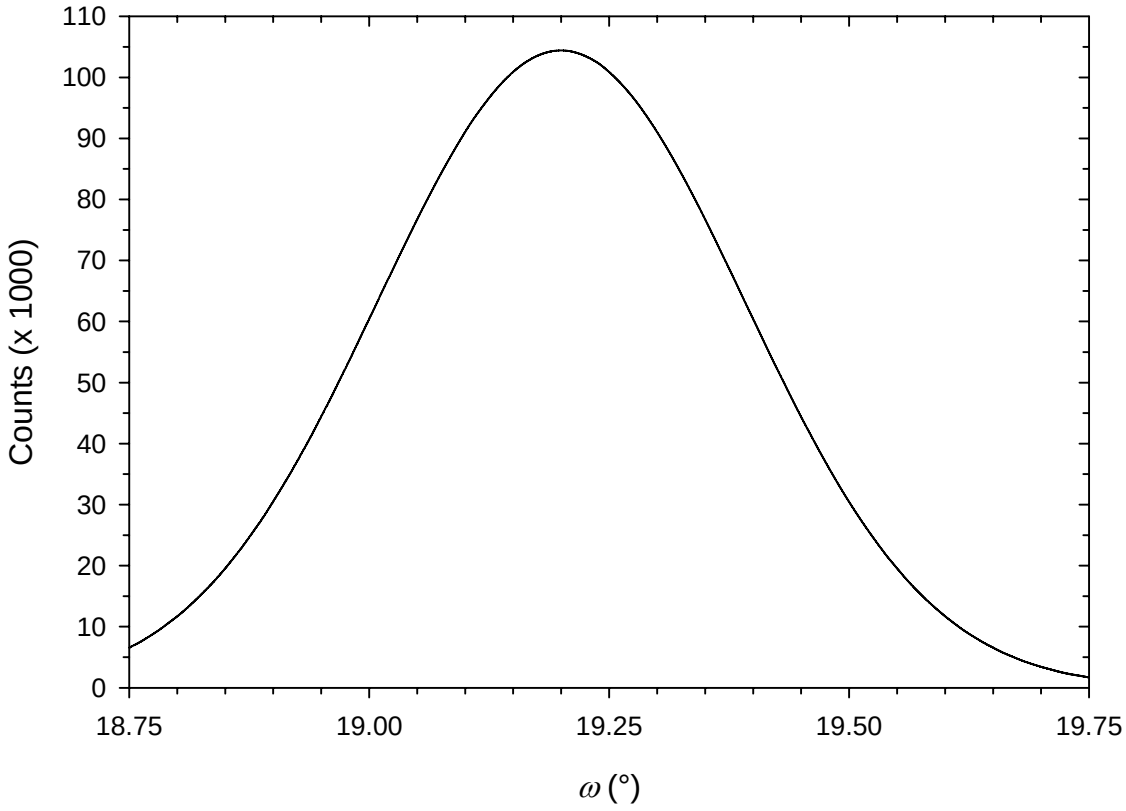


Figure 3.3 The rocking curve of the (005) peak for a typical YBCO thin film sample.

## 3.2 Scanning electron microscopy and atomic force microscopy

Scanning Electron Microscopy (SEM) [2] and Atomic Force Microscopy (AFM) [3] were used to examine the surface morphology of the YBCO thin films. Both SEM and AFM provide a convenient way to visualize the surface topography of YBCO thin film, with no prior sample preparation required. Sample charging is not a problem for SEM of YBCO thin film as YBCO is sufficiently conductive even at room temperature. While both SEM and AFM can be used to observe features such as defects, particulates and grain structure, SEM provides a rapid means of imaging both large and small surface area. Imaging with AFM is comparatively much slower and only a small section of the surface can be scanned at a time (maximum area of 90 × 90 $\mu m^2$ for the instrument used here). The main advantage of AFM lies on its ability to provide quantitative height analysis such as surface roughness.

The SEM and AFM images of the YBCO thin films presented in this dissertation were taken using the JSM-6700F field emission scanning electron microscope[2] and the Digital Instruments Dimension 3000 atomic force microscope[3] at Department of Physics, National University of Singapore.

A SEM image of a YBCO thin film sample is shown in figure 3.4. The image is representative of the typical SEM images for both sides of a double-sided YBCO thin films fabricated using the optimized PLD parameters and procedure. Many large irregularly-shaped outgrowths could be found randomly dispersed on the surface of the YBCO thin films. However unlike the SEM image of a YBCO thin film deposited

[2] Jeol, Tokyo, Japan
[3] Veeco Instruments Inc., New York, USA

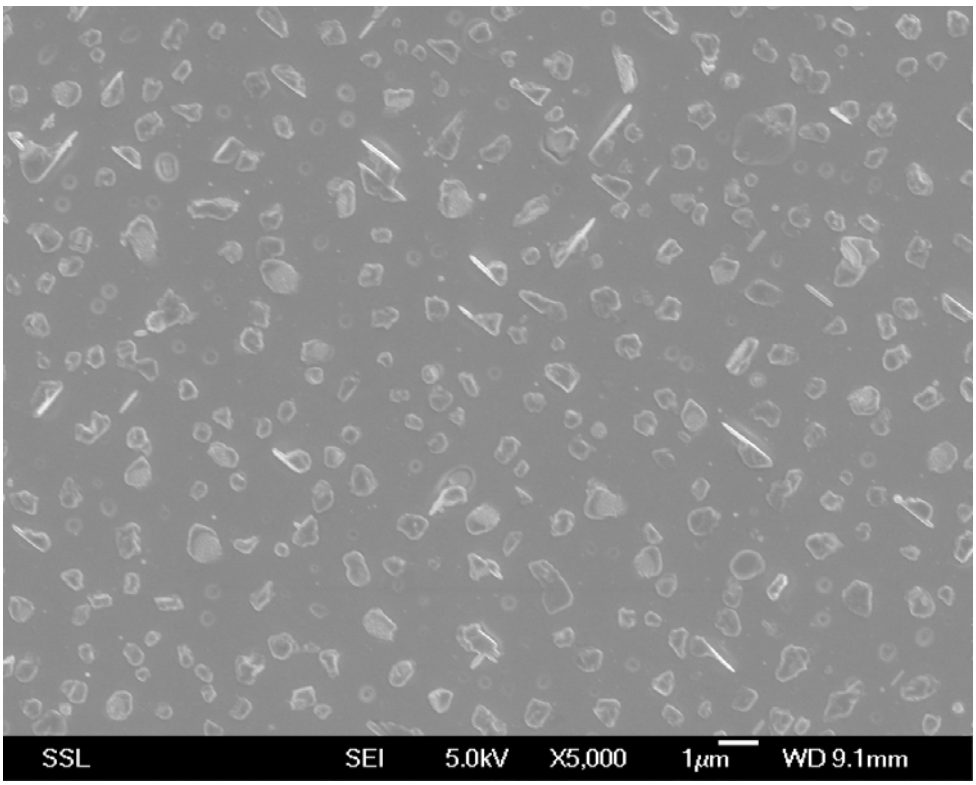


Figure 3.4 The SEM image of a typical YBCO thin film sample deposited with the optimized deposition parameters.

on a substrate with temperature below 700 °C during the PLD process (shown in figure 3.5), only very few bar-shaped *a*/*b*-axis grains were found.

An AFM image of an YBCO thin film sample is shown in figure 3.6. The image is representative of the typical AFM images for both sides of a double-sided YBCO thin films fabricated using the optimized PLD parameters and procedure. The large plateau-shaped outgrowths randomly dispersed on the surface of the YBCO thin films typically had height of up to 500 nm and average diameter of about 480 nm. These outgrowths caused the YBCO thin films to have a very rough surface, with rms (root mean square) roughness of 80 nm. The underlying area below the outgrowths had an rms surface roughness of about 10 nm.

In addition to AFM and SEM, optical microscopy was also used as a quick and easy means of examining the surface of the YBCO thin film samples. While optical microscopy lacks the sensitivity of SEM and AFM, surface features on YBCO thin films such as cracks, particulates, voids, hillocks and twinning can usually be observed using an optical microscope.

## 3.3 Four-wire measurement of dc resistance variation with temperature

Four-wire measurements of dc resistance variation with temperature were used to obtain the $T_c$, $T_c$ transition width and critical current density of the YBCO thin film samples.

### 3.3.1 Principle of four-wire dc resistance measurement

Conventional two-wire measurement method is not suitable for measuring the resistance of a superconducting sample because the voltage drop across the test leads and sample due to contact resistance is much larger than the voltage drop across the

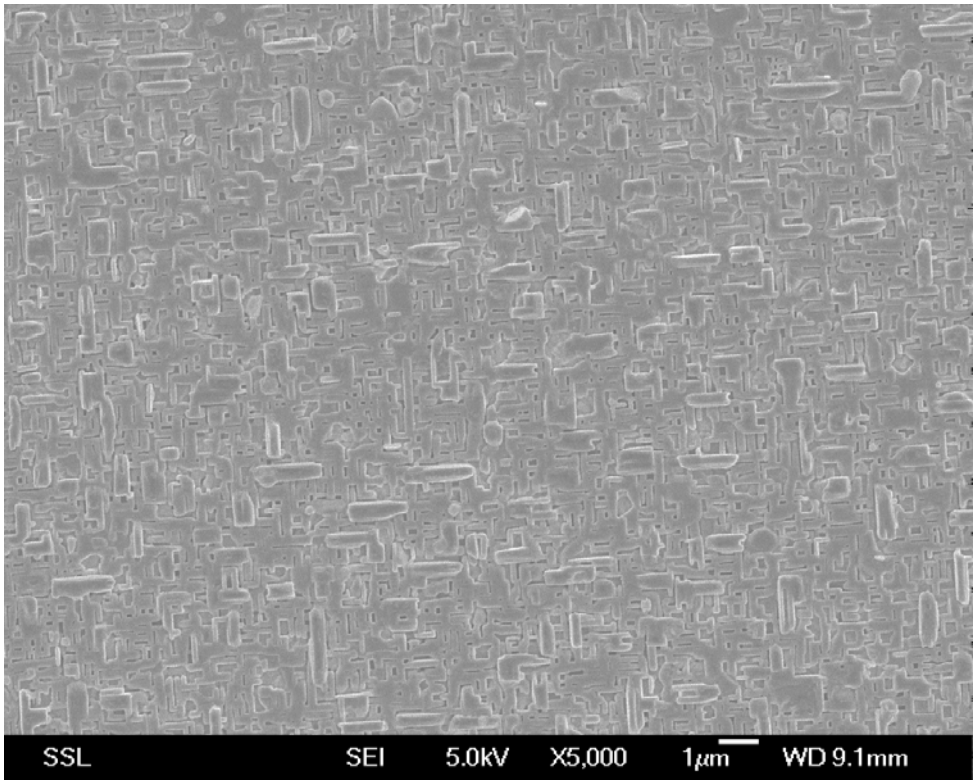


Figure 3.5 The SEM image of an YBCO thin film sample deposited with substrate temperature below 700 °C during PLD.

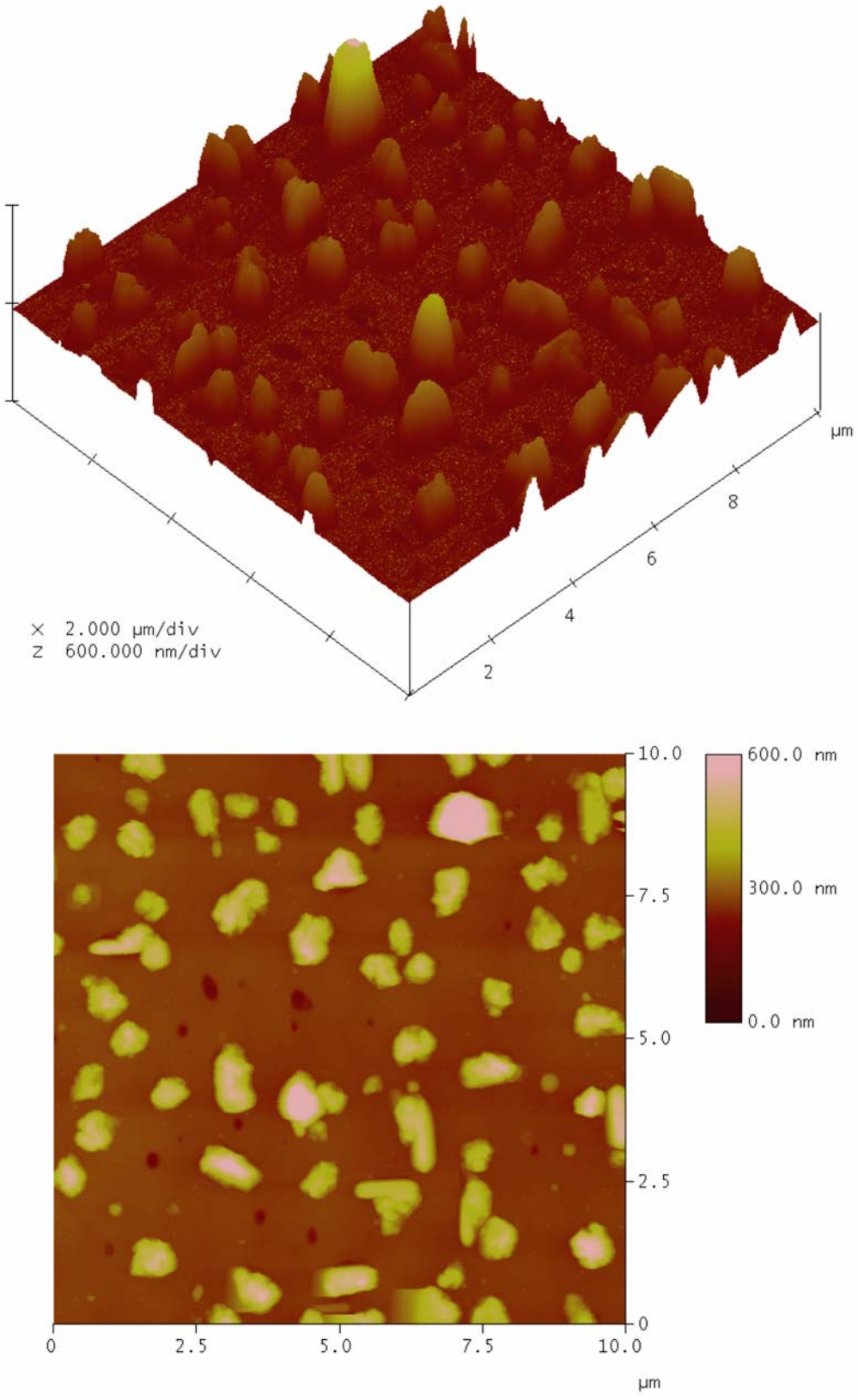


Figure 3.6 An AFM image of a typical YBCO thin film sample.

sample. Four-wire measurement is used to eliminate the measurement error due to contact resistance.

A circuit diagram illustrating the four-wire measurement setup is shown in figure 3.7. In the four-wire measurement method, a current source is used to drive a constant current across the sample. A high-input-resistance nano-voltmeter, which draws negligible current, is used to measure the voltage across the sample. As only a very small current flow through the voltage sensing leads, the voltage drop across the sense leads due to contact resistance is negligible and the measured voltage will be essentially the same as the voltage across the sample. The resistance of the sample can be calculated using:

$$R_{\text{sample}} = \frac{V_{\text{measured}}}{I}. \tag{3.4}$$

While the quantity measured by the four-wire measurement method is resistance, resistivity can be calculated using the van der Pauw method [4,5] or by patterning the YBCO thin film sample into a micro-bridge. In the micro-bridge method, the YBCO thin film is patterned into a narrow strip, with the strip width in micrometer range.

The resistivity ($\rho$) of the micro-bridge can be calculated from the measured resistance using

$$\rho = R_{\text{sample}} \frac{w \times t}{l}, \tag{3.5}$$

where $w$ and $l$ are the width and length of the microbridge, and $t$ is the thickness of the thin film.

The micro-bridge method can also be used to measure the critical current density; by increasing the current output from the current source until the sample

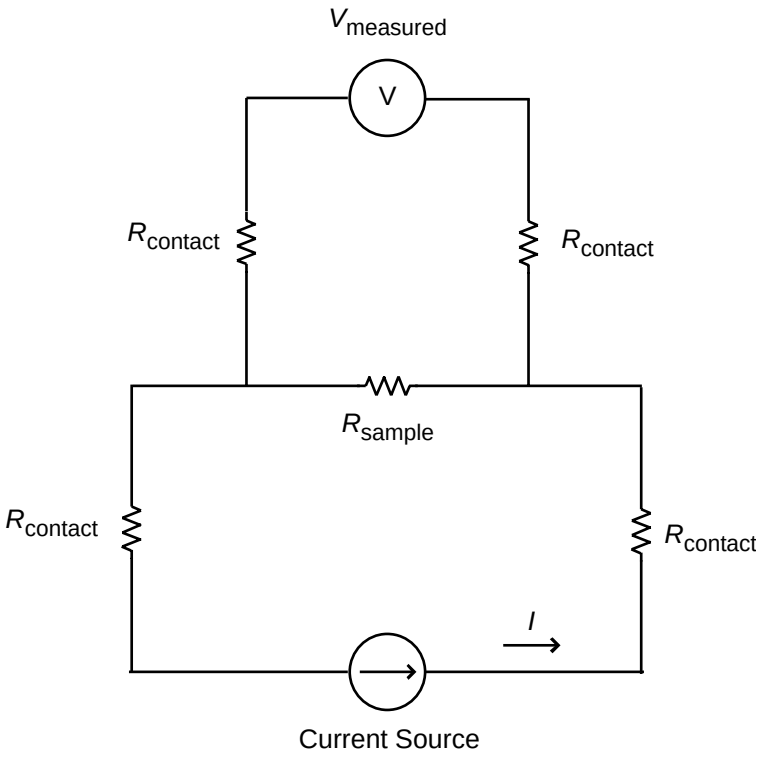


Figure 3.7 A circuit diagram illustrating the four-wire measurement setup.

ceased to be superconducting. The electric field criterion of 0.1 μV/mm is typically used; i.e. the sample is considered to be no longer superconductivity if the voltage detected across a 1 mm long micro-bridge is 0.1 μV or more.

### 3.3.2 Experimental setup of four-wire resistance measurement

The layout of a typical micro-bridge pattern is shown in figure 3.8. The YBCO thin films were patterned using UV photolithography and wet etching (see appendix 3) into a 50 μm wide by 500 μm long micro-bridge. The voltage sensing line was designed to be as narrow as possible so that it could approximate a point contact. Gold contact pads were deposited onto the YBCO thin film (see appendix 2) for the purpose of resistance welding the test lead wires (see appendix 5). The test lead wires could also be directly cold pressed onto the YBCO thin film using small lumps of suitably treated indium (see appendix 4), although connections made this way were less reliable.

A schematic diagram of the measurement setup used for the four-wire measurement of dc resistance versus temperature is shown in figure 3.9. In addition to a current source (Model 220[4]) and nano-voltmeter (Model 182[4]), a temperature controller (Model 340[5]) was used to vary the temperature. Temperature was measured by a silicon diode temperature sensor (DT-471-SD[5]). A nichrome wire with polyimide insulation (NI055880[6]) was used as the heating element. A personal computer with a GPIB to PCI interface card[7] was connected to the current source, voltmeter and temperature controller for the purpose of instrument control and data collection. The

[4] Keithley Instruments Inc., Ohio, USA
[5] Lake Shore Cryotronics Inc., Ohio, USA
[6] Goodfellow Cambridge Ltd., Huntingdon, UK
[7] National Instruments Corp., Texas, US

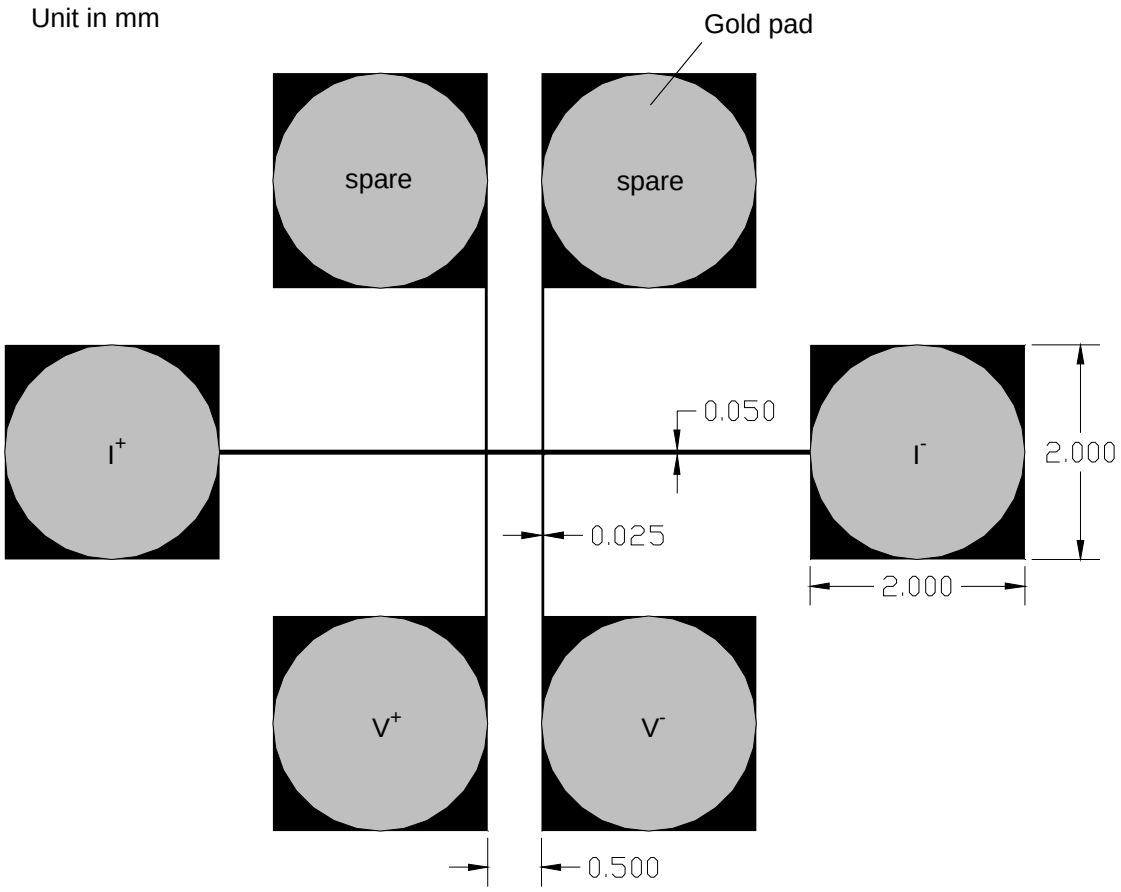


Figure 3.8 The layout of a typical micro-bridge pattern used in four-wire resistance measurement.

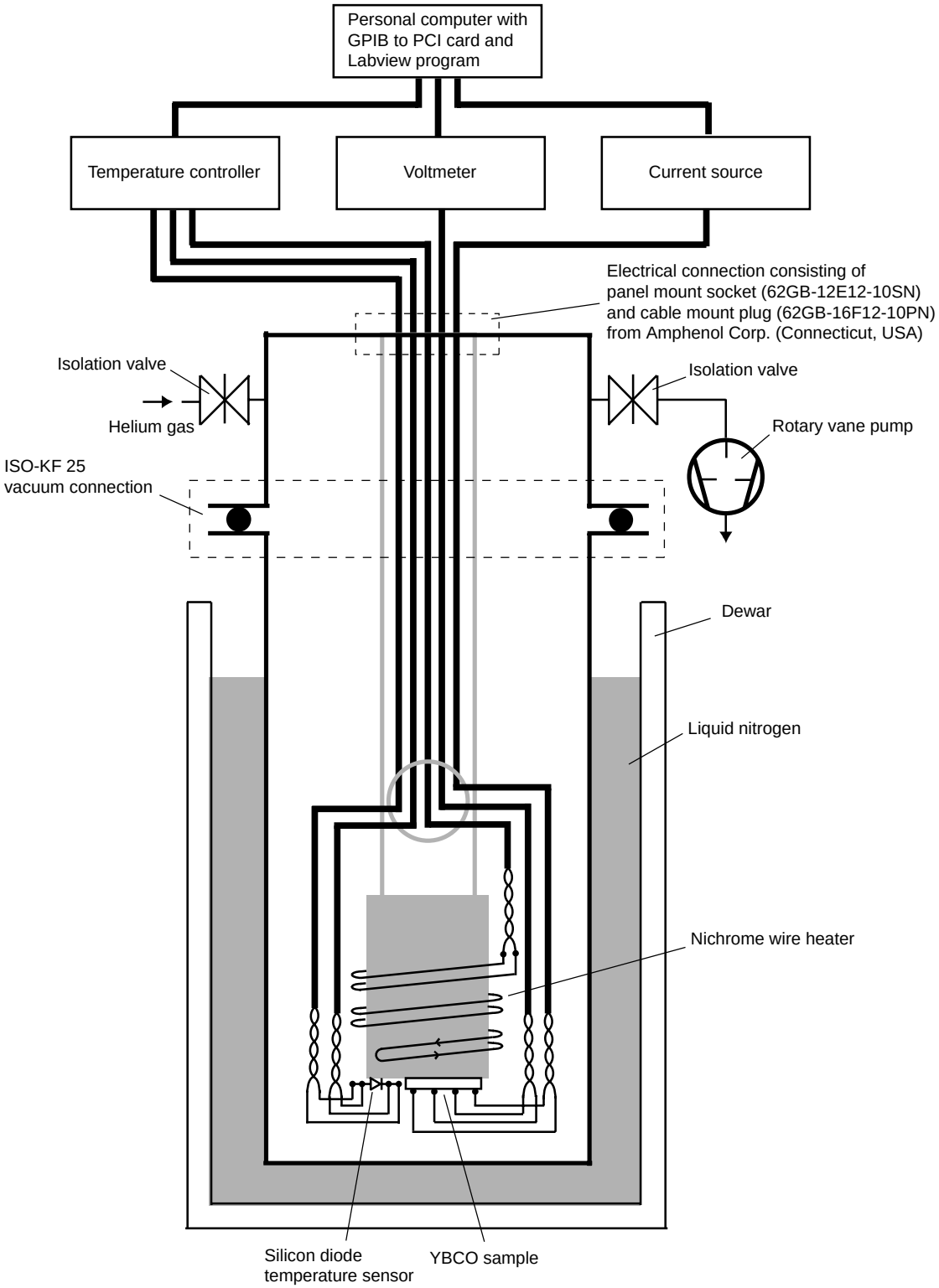


Figure 3.9 Schematic diagram of the four-wire resistance measurement setup with temperature variation.

instrument control and data collection software program was written in Labview[7] (Version 7.1).

All the electrical wire pairs were twisted whenever possible and were trimmed to the shortest possible length to minimize noise from stray electromagnetic fields. This was especially important for the voltage sensing wire pair of the sample and the silicon diode temperature sensor (which also uses 4-wire measurement). The nichrome heating wire was folded back at the middle of its length before been coiled around the sample holder (see figure 3.9) to reduce magnetic field emission.

During measurement, the YBCO thin film sample was placed in a homemade air-tight brass dip-stick which was partially immersed in liquid nitrogen. Before immersing the dip-stick, air in the dipstick was purged using a rotary vacuum pump and refilled with helium gas. The air was removed from the dip-stick to prevent moisture from condensing on the sample when at low temperature. The evacuated dip-stick was refilled with helium gas to aid sample cooling.

### 3.3.3 Results from the four-wire resistance measurement

The typical resistivity versus temperature graph of the YBCO thin films is shown in figure 3.10. The resistivity in the non-superconducting state was relatively low, had linear temperature dependence, and could be extrapolated to about zero resistivity at 0 K. These are characteristics commonly found in YBCO samples with high critical current density and low surface resistance [6]. The measured $T_c$ was typically about 91 K, with a critical temperature transition width of less than 1 K, and critical current density of more than $2 \times 10^6$ A/cm$^2$ at zero magnetic field and 77 K.

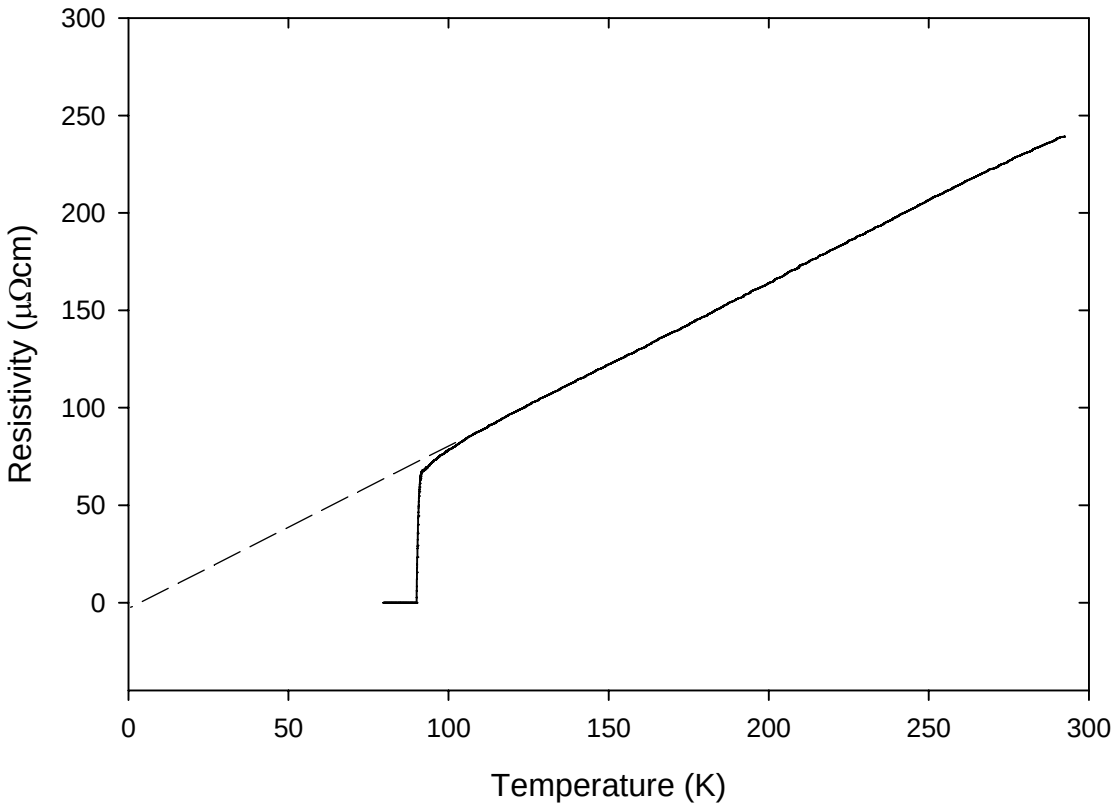


Figure 3.10 The resistivity versus temperature graph of a typical YBCO thin film sample.

## 3.4 Surface resistance measurement

Surface resistance is the most critical parameter for determining the performance of a superconducting material in low loss microwave device application. Thus accurate measurement of surface resistance is required to monitor and control the quality the YBCO thin films fabricated for microwave devices. In this thesis, the surface resistance of the fabricated YBCO thin films mentioned was measured using a dielectric resonator wall-loss perturbation technique previously developed by other researchers in CSMM [7]. One important advantage of this measurement technique is that it is non-destructive and the YBCO thin film can be used for fabricating microwave device after the surface resistance measurement.

### 3.4.1 Principle of the surface resistance measurement method

The derivation of the surface resistance from Q factor measurement in the dielectric resonator wall-loss perturbation technique is briefly described here. A more detail explanation on the principle of the surface resistance measurement and on Q factor can be found in [7] and chapter 4 respectively.

The unloaded Q factor of the dielectric resonator can be written as

$$\frac{1}{Q_u} = \frac{1}{Q_{\text{sample}}} + \frac{1}{Q_{\text{others}}}, \tag{3.6}$$

where $Q_u$ is the unloaded Q factor of the dielectric resonator, $Q_{\text{sample}}$ is the loss contribution from the YBCO thin film sample and $Q_{\text{others}}$ is the loss contribution from the rest of the resonator. Note that only $Q_l$, that is the loaded Q factor of the dielectric

resonator taken as a whole, can be experimentally measured. $Q_u$ can be calculated from $Q_l$ using the equations found in section 4.1.2.

As the loss from an YBCO thin film sample is due to ohmic dissipation, $Q_{\text{sample}}$ can be expressed as

$$Q_{\text{sample}} = \frac{2\pi\mu_0 f_0}{R_s} G, \tag{3.7}$$

where $G$ is a geometrical factor dependant on the structure of the resonator, $f_0$ is the resonant frequency and $R_s$ is the surface resistance of the resonator. Equation (3.6) can then be written as

$$\frac{1}{Q_u} = A + BR_s, \tag{3.8}$$

where $A$ and $B$ are constants that are independent of the surface resistance of the sample.

The surface resistance of a sample can be calculated from the measured loaded Q factor once the constants $A$ and $B$ are known. While $A$ and $B$ can in theory be obtained by simply using two calibration samples of known surface resistance, such as gold and silver, the resulting calculation for surface resistance will have a large error as YBCO thin film typically has $R_s$ of less than 1 mΩ while even the best metallic conductor has $R_s$ of greater than 10 mΩ at 77 K and 10 GHz.

If a dielectric pill resonator operating in the $TE_{011+\delta}$ resonance mode is used as the basis of the measurement probe, a calibrator that acts as a sample with zero surface resistance can be constructed, by making the calibrator as having the same geometry as the dielectric pill resonator. During zero surface resistance calibration, the dielectric

pill resonator and the mirror-image calibrator are mounted face to face, such that the structure will operate as a $TE_{012+\delta}$ mode resonator. The unloaded Q factor measured from this structure will be the same as that obtained from a thin film sample with zero surface resistance. The constant *A* can then be obtained from the Q factor measurement with the mirror-image calibrator and the constant *B* from another measurement with a calibration sample of known surface resistance, such as gold or silver.

### 3.4.2 Structure of the surface resistance measurement probe

The schematic diagram of the surface resistance measurement probe is shown in figure 3.11. It consists of a cylindrical LAO dielectric pill with diameter of 6 mm and height of 5.5 mm, which acts as the resonating element, resting on top of the measurement sample. The position of the LAO dielectric resonating element was secured using a holder made from Telfon. A silver-coated brass enclosure was used to reduce the radiation loss. After mounting the YBCO thin film sample on the surface resistance measurement probe, the enclosure was sealed in helium gas environment with indium wire seal to prevent the formation of water condensation and the ingress of liquid nitrogen during cooling by immersion in liquid nitrogen. Q factor measurement of the resonator was made at the frequency of about 10.65 GHz, which is the $TE_{011+\delta}$ mode resonant frequency.

### 3.4.3 Results of surface resistance measurement

The surface resistance measurements were carried out at 77 K, with frequency at about 10.65 GHz. The unloaded Q factor obtained with the mirror-image calibrator was 31095. A silver disc was used as the second calibration sample. The unloaded Q

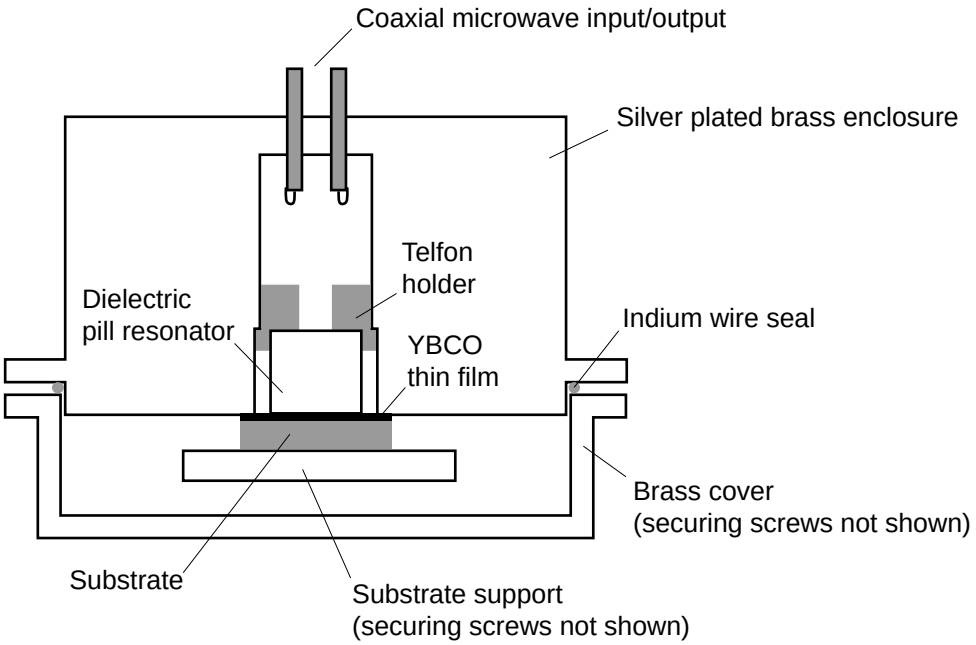


Figure 3.11 The schematic diagram of the surface resistance measurement setup.

factor obtained with the silver disc was 15126. The surface resistance of silver was taken as 11.5 mΩ.

The surface resistance uncertainty due to calibration and measure uncertainty was about 150 μΩ and 10 μΩ respectively, so the absolute uncertainty of the surface resistance measurement is about 160 μΩ.

Figure 3.12 shows the transmission S-parameter of the surface resistance measurement setup loaded with a typical YBCO thin film sample, which gave a loaded Q factor of 29610. The unload Q factor obtained with YBCO thin films prepared using the optimized PLD parameters and procedure were typically greater than 28500, with the best samples at 30500, which corresponds to surface resistance of between 1 mΩ to 0.2 mΩ.

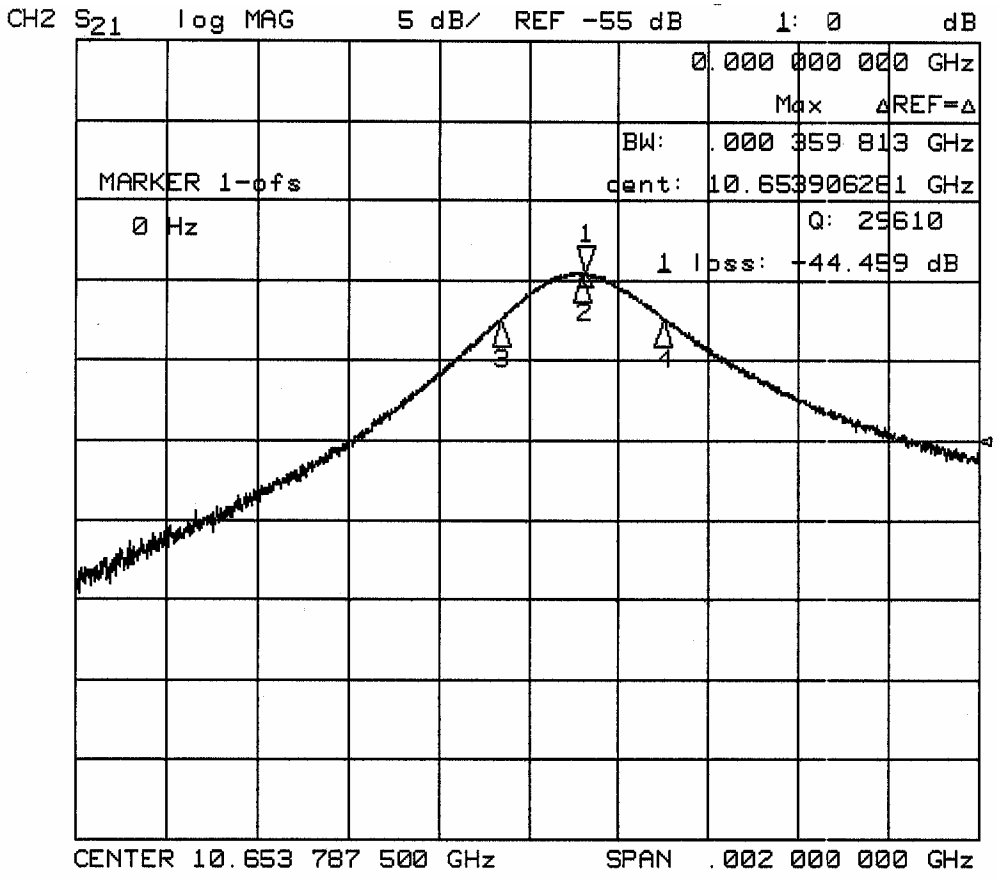


Figure 3.12 The transmission S-parameter of the surface resistance measurement setup loaded with a typical YBCO thin film sample.

References

[1] B. D. Cullity and S. R. Stock, *Elements of X-Ray Diffraction*, 3rd Ed., Prentice Hall, 2001.

[2] P. J. Goodhew, J. Humphreys, and R. Beanland, *Electron microscopy and analysis*, 3rd Ed., Taylor & Francis, 2001.

[3] G. Binnig, C. F. Quate, and Ch. Gerber, "Atomic Force Microscope", *Physical Review Letters*, vol. 56, no. 9, pp. 930-933, 1986.

[4] L. J. van der Pauw, "A Method of Measuring the resistivity and Hall Coefficient of Lamellae of Arbitrary Shape", *Philips Technical Review*, vol. 20, no. 8, pp. 220-224, 1958.

[5] L. J. van der Pauw, "A method of measuring specific resistivity and Hall effect of discs of arbitrary shape", *Philips Research Reports*, vol. 13, no. 1, pp. 1-9, 1958.

[6] D. M. Ginsberg, *Physical Properties of High Temperature Superconductor III*, World Scientific Publishing Co. Pte. Ltd., 1992.

[7] C. K. Ong, L. Chen, J. Lu, S. Y. Xu, X. Rao, and B. T. G. Tan, "Mirror-image calibrator for resonant perturbation method in surface resistance measurements of high $T_c$ superconducting thin films", *Review of Scientific Instruments*, vol. 70, no. 7, pp. 3092-3096, 1999.

# CHAPTER 4:
# MICROWAVE RESONATOR AND Q FACTOR

A microwave resonator is a structure which supports electromagnetic field oscillation of microwave frequency range within its structure. Microwave resonators are the basic components of a bandpass filter, and they also serve as the resonant elements in other microwave devices, such as oscillator and are found in nearly all microwave systems.

A microwave resonator has a set of resonant frequencies which are dependent on the physical structure of the resonator. In addition to resonant frequency, the quality factor, also called Q factor, is another important characteristic parameter of a resonator. In a filter, the Q factor of the resonators determines the limit of the achievable selectivity and insertion loss. The use of HTS thin films allow the fabrication of miniaturized planar resonators with high Q factor.

In this chapter, an introduction to the fundamental definitions and relations used to calculate the Q factors of a microwave resonator is given in section 4.1. The detailed derivation of the equations used to calculated Q factors is not given, but can be found in references such as [1,2]. The importance of high Q factor resonator in bandpass filter is discussed in section 4.2. The factors affecting the Q factor of microstrip resonator are examined in section 4.3. The microstrip half-wavelength transmission line resonator, which is one of the simplest forms of microstrip resonator, is briefly described in section 4.4. In section 4.5, a novel type of miniaturized microstrip resonator based on the dual-spiral geometry is introduced.

## 4.1 Q factors of a microwave resonator

The unloaded Q factor for a resonator is defined as

$$\begin{aligned} Q_u &= 2\pi \frac{\text{Energy stored in resonator}}{\text{Energy dissipated by resonator in one oscillation}} \\ &= \omega \frac{\text{Energy stored in resonator}}{\text{Average power dissipated by resonator}} \end{aligned}, \tag{4.1}$$

where $\omega$ is the angular frequency.

During the Q factor measurement of a microwave resonator, some energy will be lost in the connections used to couple energy in and out of the resonator, so the measured Q factor is actually the loaded Q factor ($Q_l$) which can be express as

$$\frac{1}{Q_l} = \frac{1}{Q_u} + \frac{1}{Q_e}, \tag{4.2}$$

where $Q_e$ is called the external Q factor and characterized the loss due to the input/output coupling connection.

The coupling coefficient ($\beta$) is defined as

$$\beta = \frac{Q_u}{Q_e}, \tag{4.3}$$

so the unloaded Q factor can be written as

$$Q_u = (1+\beta)Q_l. \tag{4.4}$$

$Q_u$ is used to characterize a resonator, as $Q_u$ depends on the intrinsic properties of the resonator, unlike $Q_l$ which varies with the couplings of the resonator.

### 4.1.1 One-port measurement of Q factor

The Q factor of a microwave resonator can be obtained experimentally from S-parameters measurement of the resonator using a vector network analyzer. For one-port measurement, only the $S_{11}$ reflection data is available. Resonance occurs when $|S_{11}|$ is at a minimum, with the frequency at the minimum corresponding to the resonant frequency ( $f_0$ ).

The loaded Q factor can be calculated from the measured $S_{11}$ using

$$Q_l = \frac{f_0}{f_2 - f_1}, \tag{4.5}$$

where $f_1$ and $f_2$ are the frequencies about the resonant frequency where the magnitude of $S_{11}$ is

$$|S_{11}(f_1, f_2)|^2 = \frac{1+|S_{11}(f_0)|^2}{2}. \tag{4.6}$$

To calculate $Q_u$, it is necessary to first determine if the resonator is under-coupled, critically-coupled or over-coupled, i.e. $\beta < 1$, $\beta = 1$ or $\beta > 1$ respectively. One method of identifying the coupling type is by visual inspection of the $S_{11}$ data in Smith chart format [3,4]. A resonator is under-coupled when the $S_{11}$ data points about the resonant frequency does not enclose the characteristic impedance ( $Z_0$ ) centre point of the Smith chart. A resonator is critically-coupled if the circle passes exactly through the centre point. If the circle encloses the centre point, the resonant circuit is over-coupled. Examples of $S_{11}$ data in Smith chart format for the three types of coupling are shown in figure 4.1.

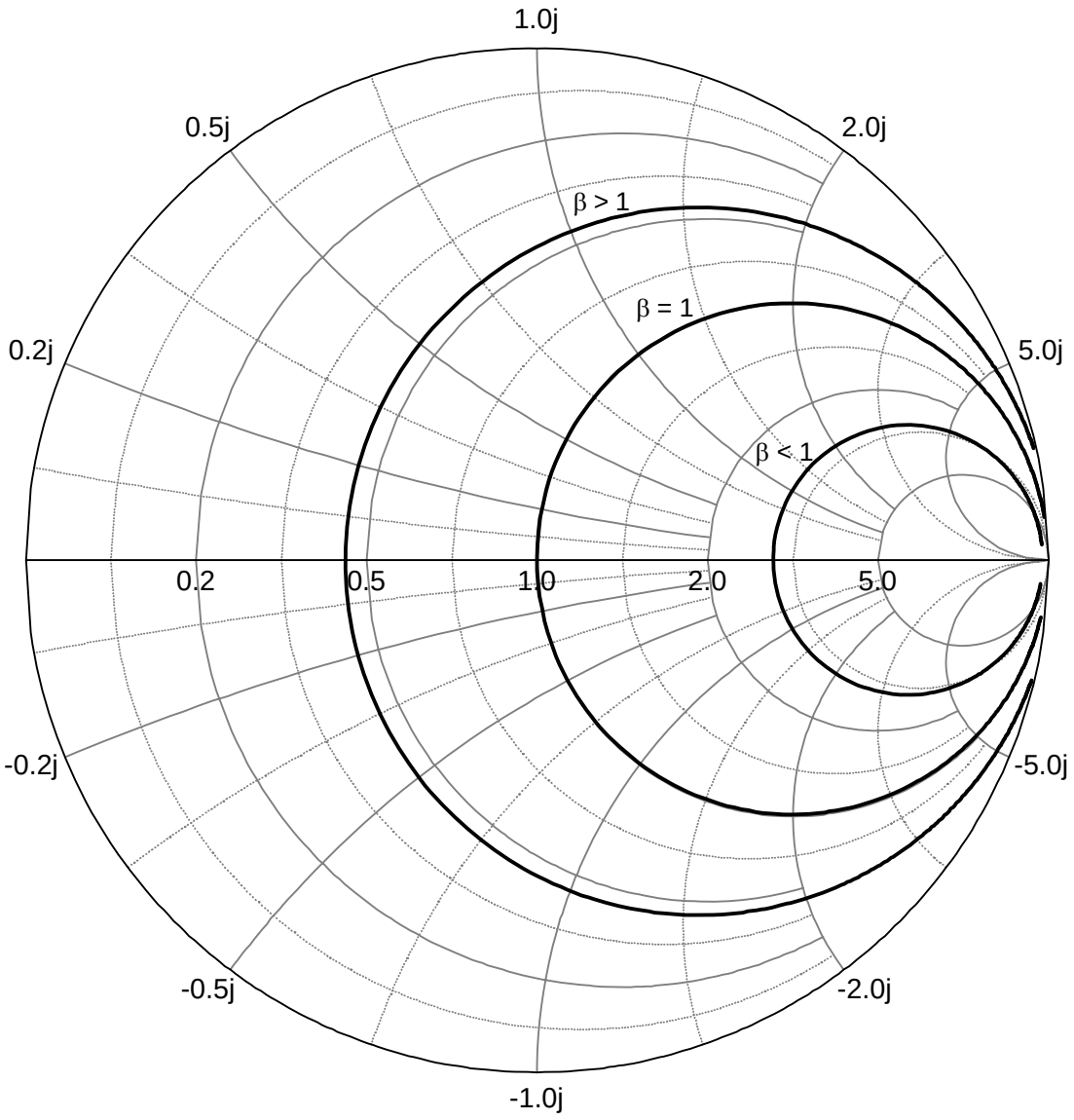


Figure 4.1. The $S_{11}$ responses, in Smith chart format, of an under-coupled resonator, critically-coupled resonator and over-coupled resonator.

Another method of determining the coupling type is by examining the gradient of the $S_{11}$ phase at $f_0$. A resonator is under-coupled if the gradient of the $S_{11}$ phase at $f_0$ is positive, whereas a resonator is over-coupled if the gradient of the $S_{11}$ phase at $f_0$ is negative. Examples of the $S_{11}$ magnitudes and phases for the under-coupled and over-coupled resonators are shown in figures 4.2 and 4.3 respectively.

For an under-coupled resonator, $\beta$ and $Q_u$ can be calculated using

$$\beta = \frac{1-|S_{11}(f_0)|}{1+|S_{11}(f_0)|} \tag{4.7}$$

and

$$Q_u = \frac{2Q_l}{1+|S_{11}(f_0)|}. \tag{4.8}$$

For an over-coupled resonator, $\beta$ and $Q_u$ can be calculated using

$$\beta = \frac{1+|S_{11}(f_0)|}{1-|S_{11}(f_0)|} \tag{4.9}$$

and

$$Q_u = \frac{2Q_l}{1-|S_{11}(f_0)|}. \tag{4.10}$$

For a critically-coupled resonator, $Q_u = 2Q_l$.

### 4.1.2 Two-port measurement of Q factor

In two-port measurement of Q factor, resonance occurs when $|S_{21}|$ is at a maximum value and the frequency at the maximum corresponds to the resonant frequency. The loaded Q factor is also calculated using equation (4.5), however $f_1$

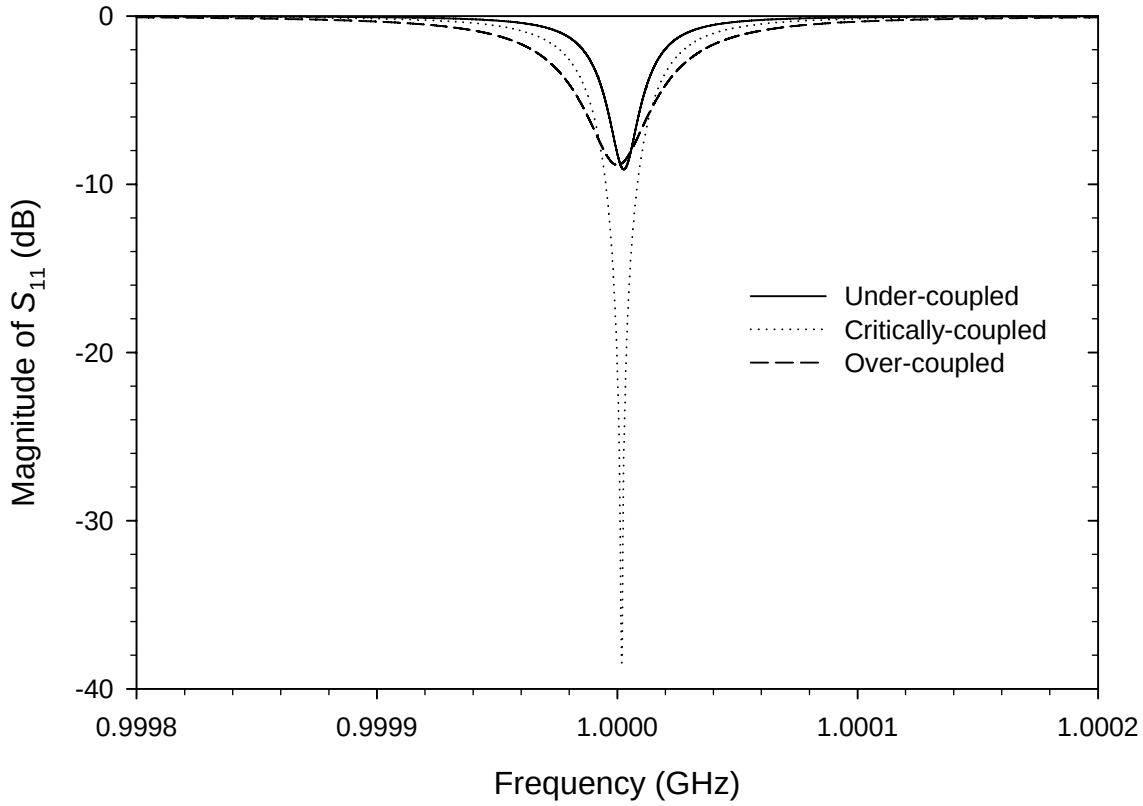


Figure 4.2. The $S_{11}$ magnitude response of an under-coupled resonator, critically-coupled resonator and over-coupled resonator.

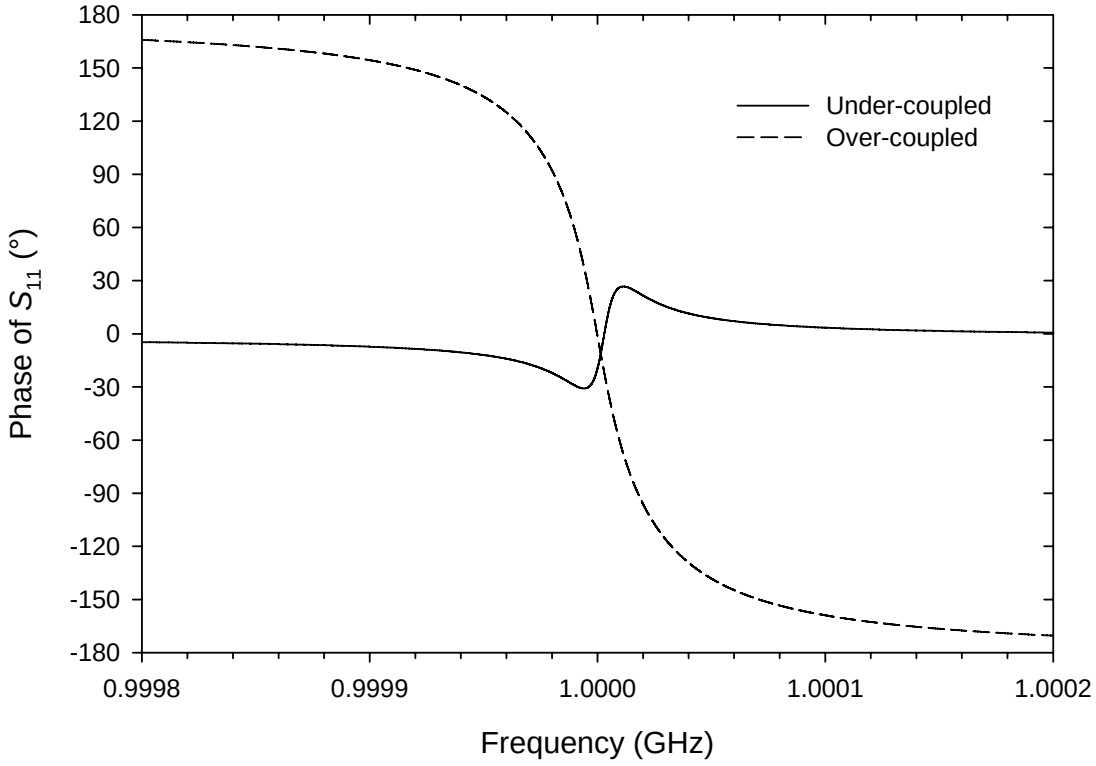


Figure 4.3. The $S_{11}$ phase response of an under-coupled resonator and over-coupled resonator.

and $f_2$ are the frequencies about the resonant frequency where the magnitude of $S_{21}$ is

$$\left|S_{21}(f_1, f_2)\right|^2 = \frac{\left|S_{21}(f_0)\right|^2}{2}. \tag{4.11}$$

As the coupling loss due to the two ports may be different, the loaded Q factor can be written as

$$\frac{1}{Q_l} = \frac{1}{Q_u} + \frac{1}{Q_{e1}} + \frac{1}{Q_{e2}}, \tag{4.12}$$

where $Q_{e1}$ and $Q_{e2}$ are the external Q factor for the 2 ports. The coupling coefficients, $\beta_1$ and $\beta_2$ are defined as

$$\beta_1 = \frac{Q_u}{Q_{e1}}, \tag{4.13}$$

and

$$\beta_2 = \frac{Q_u}{Q_{e2}}. \tag{4.14}$$

$\beta_1$ can be calculated from S-parameter using

$$\beta_1 = \frac{1 - S_{11}(f_0)}{S_{11}(f_0) + S_{22}(f_0)}, \tag{4.15}$$

$$\beta_1 = \frac{\left(S_{11}(f_0) - 1\right)^2}{1 - S_{11}^2(f_0) - S_{21}^2(f_0)}, \tag{4.16}$$

or

$$\beta_1 = \frac{S_{21}^2(f_0)}{1 - S_{22}^2(f_0) - S_{21}^2(f_0)}. \tag{4.17}$$

$\beta_2$ can be calculated using

$$\beta_2 = \frac{1 - S_{22}(f_0)}{S_{11}(f_0) + S_{22}(f_0)}, \tag{4.18}$$

$$\beta_2 = \frac{\left(S_{22}(f_0) - 1\right)^2}{1 - S_{22}^2(f_0) - S_{21}^2(f_0)}, \tag{4.19}$$

or

$$\beta_2 = \frac{S_{21}^2(f_0)}{1 - S_{11}^2(f_0) - S_{21}^2(f_0)}. \tag{4.20}$$

The unloaded Q factor can then be calculated using

$$Q_u = (1 + \beta_1 + \beta_2) Q_l. \tag{4.21}$$

When both couplings to the resonator are identical, i.e. $\beta_1 = \beta_2 = \beta$, only $S_{21}$ needs to be measured. $\beta$ and $Q_u$ can be calculated using

$$\beta = \frac{S_{21}(f_0)}{2\left[1 - S_{21}(f_0)\right]}, \tag{4.22}$$

and

$$Q_u = \frac{Q_l}{1 - S_{21}(f_0)}. \tag{4.23}$$

Note that for reciprocal passive devices such as resonator, $S_{21}$ can be replaced by $S_{12}$ since they are equal. Furthermore, the S-parameters in the above equations are in ratio/magnitude format. The following equation can be used to convert S-parameters from dB to ratio format

$$S(\text{ratio}) = 10^{\frac{S(\text{dB})}{20}}. \tag{4.24}$$

## 4.2 The importance of high Q factor resonators in microwave bandpass filter

The insertion loss of a microwave filter is determined by the unloaded Q factor of the resonators that make up the filter. For a bandpass filter designed from a lowpass prototype filter, the insertion loss can be estimated from the unloaded Q factor using

$$L = 4.343 \sum_{i}^{n} \frac{\Omega_c}{FBW.Q_{ui}} g_i, \tag{4.25}$$

where $L$ is the insertion loss in dB, $Q_{ui}$ and $g_i$ are the unloaded Q factor and lowpass prototype element value of the $i^{\text{th}}$ resonator respectively, $\Omega_c$ is the lowpass cutoff frequency and $FBW$ is the fractional bandwidth of the bandpass filter [5,6].

From equation (4.25), it can be seen that a bandpass filter built from resonators with low unloaded Q factor will have high insertion loss. Furthermore, a bandpass filter with a narrow bandwidth, i.e. small $FBW$, will also have a higher insertion loss unless it is built from resonators with high Q factor.

## 4.3 Factors affecting the Q factor of HTS microstrip resonator

The power loss in a microstrip resonator is due to the dissipations in the conductor and dielectric substrate as well as radiation leakage. Therefore the average power lost is

$$\text{Power dissipated by resonator} = P_c + P_d + P_r, \tag{4.26}$$

where $P_c$, $P_d$ and $P_r$ are power dissipated due to conductor loss, dielectric loss and radiation loss respectively. Thus $Q_u$ can be written as

$$\frac{1}{Q_u} = \frac{1}{Q_c} + \frac{1}{Q_d} + \frac{1}{Q_r}, \tag{4.27}$$

where $Q_c$, $Q_d$ and $Q_r$ are the conductor, dielectric and radiation Q factor respectively.

### 4.3.1 Conductor Q factor

The conductor Q factor is defined as

$$Q_c = \omega \frac{\text{Energy stored in resonator}}{\text{Average power lost due to ohmic dissipation}}. \tag{4.28}$$

The energy stored in a resonator can be expressed as

$$\text{Energy stored in resonator} = \frac{1}{2}\mu_0 \int_{\text{resonator}} |\mathbf{H}|^2 dV, \tag{4.29}$$

where the integration is over the whole volume of the resonator. The average power lost due to conductor ohmic dissipation can be expressed as

$$P_c = \frac{1}{2} R_s \int_{\text{conductor}} |H_t|^2 dS, \tag{4.30}$$

where $R_s$ is the surface resistance of the conductor and $H_t$ is the magnetic field component normal to the conductive surface, with the integration over the conductive surface area of the resonator. Thus $Q_c$ can be expressed as

$$\begin{aligned} Q_c &= \frac{\mu_0 \omega}{R_s} \frac{\int_V |H|^2 dV}{\int_S |H_t|^2 dS}, \\ &= \frac{\mu_0 \omega}{R_s} G_c \end{aligned} \tag{4.31}$$

where $G_c$ is the conductive geometric factor determined by the design of the resonator. For a resonator with a number of different conductive parts, each conductive part is

integrated accordingly and then summed together to obtain the total power loss due to ohmic dissipation.

It should be note that the equation (4.30) is exact only for an infinite plane conductor. In the case of superconducting thin film with finite thickness, the effective surface resistance ($R_{s,\text{eff}}$) should be used. The effective surface resistance increases with decreasing conductive layer thickness and can be approximated using

$$R_{s,\text{eff}} = R_s \left[ \coth\left(\frac{t}{\lambda}\right) + \frac{t}{\lambda} \frac{1}{\sinh^2\left(\frac{t}{\lambda}\right)} \right], \tag{4.32}$$

where $t$ and $\lambda$ are the thickness and penetration depth of the superconducting thin film respectively [2].

From equation (4.32), it can be seen that the thickness of a superconducting thin film should be at least 2.5 times that of the penetration depth for $R_{s,\text{eff}} \approx R_s$. Therefore based on the relatively conservative estimated that the fabricated YBCO thin film had a penetration depth of 200 nm, the YBCO thin film samples used for fabricating microwave devices mentioned in this dissertation were grown to a thickness of about 500 nm.

The line width of the microstrip resonator also plays an important factor in the determination of the conductive Q factor. As the line width of a microstrip line decreases, the current density becomes very high within the microstrip line. Thus a narrower microstrip line has a decreased power handling ability. Furthermore, a sufficiently high current density will drive the HTS into a non-linear power dependence range, which has increased effective surface resistance, thus reducing the conductive Q factor.

### 4.3.2 Dielectric Q factor

In a microstrip resonator, energy is dissipated by dielectric medium such as the substrate. The power dissipation in a dielectric medium can be calculated using

$$\begin{aligned} P_d &= \frac{1}{2}\sigma_d \int_{\text{dielectric}} |\mathbf{E}|^2 \, dV \\ &= \frac{1}{2}\omega\varepsilon \tan\delta \int_{\text{dielectric}} |\mathbf{E}|^2 \, dV \end{aligned} . \tag{4.33}$$

The loss tangent ( $\tan\delta$ ) of a dielectric material, is defined as

$$\tan\delta = \frac{\sigma_d}{\omega\varepsilon}, \tag{4.34}$$

where

$$\sigma_d = \omega\varepsilon'' + \sigma . \tag{4.35}$$

$\varepsilon''$ and $\sigma$ are the dielectric material losses due to its dielectric damping and conductivity dissipation respectively.

The dielectric Q factor can be written as

$$\begin{aligned} Q_d &= \frac{\int_{resonator} \mu |\mathbf{H}|^2 dV}{\tan\delta \int_{dielectric} \varepsilon |\mathbf{E}|^2 dV} , \\ &= \frac{1}{G_d \tan\delta} \end{aligned} \tag{4.36}$$

where $G_d$ is the dielectric structure parameter. For a resonator with a number of different dielectric parts, $Q_d$ can be calculated using

$$\frac{1}{Q_d} = \sum_i G_{d,i} \tan(\delta)_i , \tag{4.37}$$

as each dielectric part has its own value for the dielectric structure parameter and loss tangent. Other than the shape of the resonator, $G_d$ also depends on dielectric constant and thickness of the substrate.

For the case when a resonator is completely filled with a dielectric medium, the two integrals in equation (4.36) cancel out each other and $Q_d$ is simply

$$Q_d = \frac{1}{\tan \delta}. \tag{4.38}$$

$G_d$ is always less than one for a microstrip resonator and equation (4.38) can be taken as the lower limit for $Q_d$.

From equation (4.38), it can be seen that the dielectric loss due to the substrate is not a significant contribution to the $Q_u$ of a HTS microstrip resonator with unloaded Q factor in the range of $10^5$ if a low loss material such as LAO is used.

### 4.3.3 Radiation and housing Q factor

In a partially open structure such as a microstrip resonator, electromagnetic radiation from a microstrip resonator will constitute a source of energy loss. Radiation can be reduced by designing a resonator such that the electromagnetic field tends to be confined within the substrate.

The use of thin substrate with high dielectric constant will also reduce radiation [7], however this will also lead to an increase in the loss by the conductors, and will not necessary improve the overall unloaded Q factor.

As HTS microstrip devices are usually enclosed in a metallic enclosure, the radiation leakage will be dissipated as currents induce on the surface of the metallic

enclosure. Thus the term housing Q factor is also used when the microstrip resonator is shielded by an enclosure.

The power dissipated by the induced current on the housing can be calculated using

$$P_{\text{housing}} = \frac{1}{2} R_s \int_{\text{housing}} \left|\mathbf{H}_t\right|^2 dS \,, \tag{4.39}$$

where the integration is over the interior surface of the housing and $R_s$ is the surface resistance of the housing material. Thus the power loss can be reduced by plating the housing with a highly conductive metal such as gold.

In general, the loss due to the induced current is reduced with a housing of larger dimension. A larger housing will reduce the parasitic coupling between the resonator and the surfaces of the enclosure, thus reducing the induced current and loss due to housing. However an increase in the housing dimension will decrease the resonant frequency of the housing (see section 9.5). To prevent the occurrence of modal coupling between the housing resonance and resonator, the housing resonance must be kept well away from that of the resonator, and so the housing cannot be too large.

## 4.4 Half-wavelength microstrip resonator

One of the simplest forms of microstrip resonator is the half-wavelength microstrip resonator consisting of a section of straight microstrip line. For a section of straight microstrip line with length $l$, the fundamental resonant frequency is

$$f_0 = \frac{c}{2l\sqrt{\varepsilon_{eff}}} \,, \tag{4.40}$$

where $c$ is the velocity of light in free space and $\varepsilon_{eff}$ is the effective dielectric constant. $\varepsilon_{eff}$ can be thought of as the dielectric constant of a homogeneous medium that replaces the air and dielectric regions of the microstrip transmission line. $\varepsilon_{eff}$ can be approximated using

$$\varepsilon_{eff} = \frac{\varepsilon_r + 1}{2} + \frac{\varepsilon_r - 1}{2} \frac{1}{\sqrt{1 + 12h/w}}, \tag{4.41}$$

where $\varepsilon_r$ and $h$ are the dielectric constant and thickness of the substrate, and $w$ is the width of the microstrip line [4].

It should be noted that equations (4.40) and (4.41) only provide an approximation as the fringe fields at the edges of the microstrip line are not very precisely taken into account, especially when $w < h$, and also because the fringe fields at the ends of the microstrip line are ignored.

The unloaded Q factor of a superconducting microstrip half-wavelength resonator can be estimated using [8]

$$Q_u = \mu_0 f_0 \frac{\pi^2}{2} \frac{\ln(8h/w)}{\ln(w/\lambda)} \frac{w}{R_s}. \tag{4.42}$$

Note that equation (4.42) does not consider dielectric dissipation.

## 4.5 Miniaturized dual-spiral microstrip resonators

The miniaturization of a microwave resonator can be accomplished by changing the geometry of the resonator, for example from a three-dimensional structure such as waveguide or cavity based resonator, to a two-dimensional planar structure such as coplanar or microstrip resonator. The planar resonators can be further miniaturized based on methods which can be broadly divided into five categories [9]: by use of

substrate with high dielectric constant, by exploiting the internal inductance of superconducting transmission line, by folding of the transmission line, by use of slow wave transmission line and by use of lumped element components.

The folding of a planar transmission line resonator can make the utilization of a substrate surface area more efficient, by reducing the surface area required by the overall circuit. The folding of a transmission line in a planar resonator can also change the inductance of the resonator structure, which can benefit the Q factor and further reduce the size of the resonator.

Dual-spiral resonators are a type of miniaturized planar resonator based on the folding of a transmission line. The dual-spiral resonator consists of two spiral arms connected together with the two spirals wound in the same or opposite direction as shown in figure 4.4. In this dissertation, the dual-spiral with spirals wound in the same direction is termed s-type dual-spiral, whereas the dual-spiral with spirals wound in the opposite directions is termed the u-type dual-spiral.

The spirals in a dual-spiral resonator can be circular or rectangular in shape. Circular spirals are expected to give better performance at high power as the electrical current crowding effect at the right angle bends is eliminated. However rectangular spiral usually utilizes surface area more efficiently, and is easier to study with full-wave electromagnetic simulation as it conforms to the rectangular meshing scheme usually used in electromagnetic simulation software, and thus can be simulated faster. In this thesis, only the square type dual-spirals are examined.

### 4.5.1 Geometry analysis of square dual-spiral resonators

For a dual-spiral resonator with a square spiral arm as shown in figure 4.5, the geometry of the spiral arm pattern can be defined by: the width of the track $w$, the

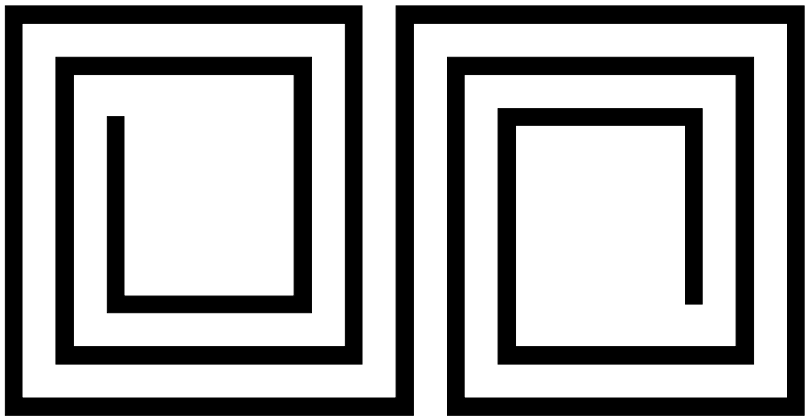

(a)

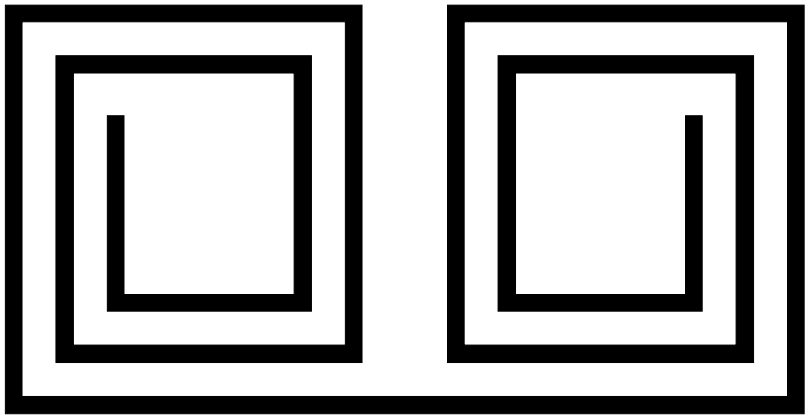

(b)

Figure 4.4 (a) A s-type dual-spiral with the two arms wound in the same direction. (b) A u-type dual-spiral with the two arms wound in the opposite directions.

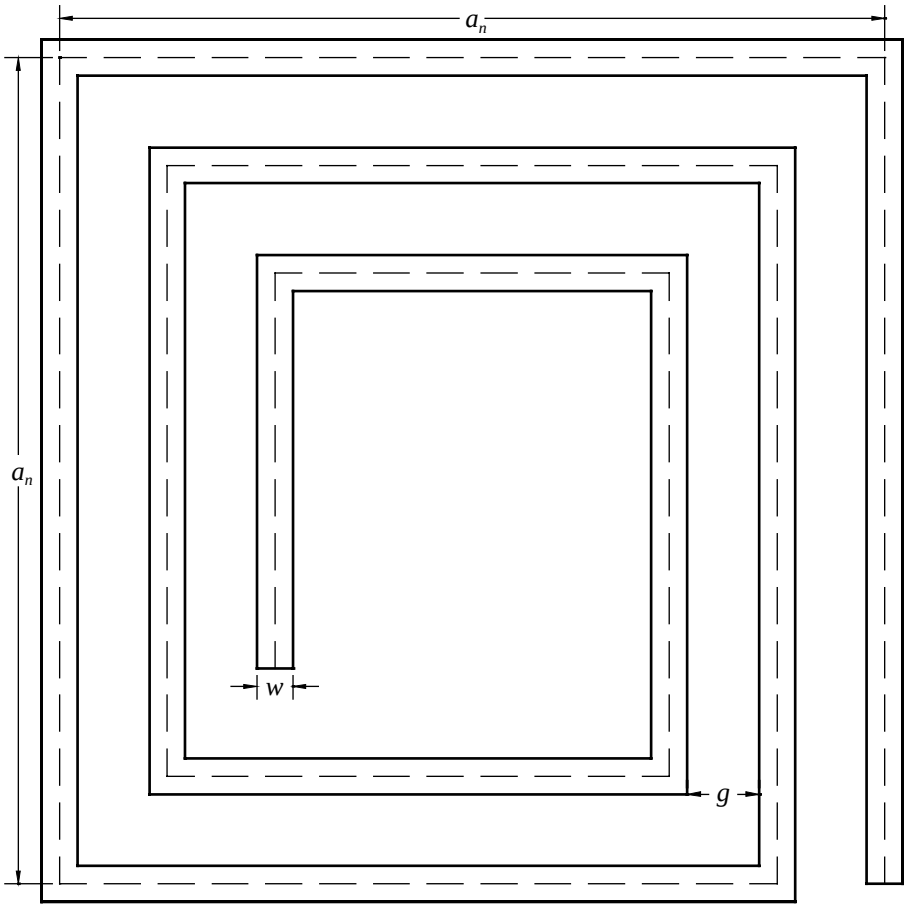


Figure 4.5 The variables used to define a square spiral arm.

separation between two tracks $g$, the side length of the outermost spiral $a_n$, and the length of the path about centre of the dual-spiral track $l$ (represented by the dash line in figure 4.5). The spiral is formed by a set of $n$ squares with increasing side length given by

$$a_i = a_1 + 2(i-1)(w+g), \tag{4.43}$$

where the $i$ index indicates the $i^{\text{th}}$ square, starting from the innermost square.

For a microstrip dual-spiral resonator of a given width, the length $l$ is usually close to the length of a straight half-wavelength microstrip resonator of the same width and resonant frequency. From a geometrical viewpoint, for a given $a_n$, $l$ can be defined arbitrarily such that the desired resonant frequency is obtained, provided that $l < l_{\max}$, where $l_{\max}$ is given by

$$l_{\max} = 8a_1 + 8a_2 + \ldots + 8a_{n-1} + 7a_n. \tag{4.44}$$

The advantage for using such a form of definition for the dual-spiral is that the exterior perimeter of the resonator is fixed. However, using such a geometry definition usually yields a spiral pattern that is somewhat irregular, as there might be one, two, three or four line segments in the innermost square. Furthermore, the last line segment usually has a length that is less than $a_1$, as the winding of the two symmetrical spirals is terminated at the point when the length $l$ is reached.

The dual-spiral geometry can be defined to have a more regular geometry such that the number of segment and length of the segments in the innermost square are all equal by using $n$, the number of coils/squares in an arm of the dual-spiral, instead of $a_n$ as a definition parameter of the dual-spiral. In this case, $a_n$ is not an arbitrary value but is dependent on $n$.

### 4.5.2 Optimal compact geometry for s-type dual-spiral

For the s-type spiral filter with a given $n$, and with geometry as shown in figure 4.4, i.e. with 6 line segments of length $a_1$, the total length of the dual-spiral is

$$l = 6a_1 + 8a_2 + 8a_3 + \cdots + 8a_{n-2} + 8a_{n-1} + 7a_n . \tag{4.45}$$

The length of the side for the $i^{\text{th}}$ square is defined as

$$\begin{aligned} a_i &= a_0 + 2(i-1)(w+g) + (w+g) \\ &= a_0 + (2i-1)(w+g) \end{aligned} . \tag{4.46}$$

The third term in the first line of equation (4.46), i.e. $w+g$, is to prevent a spiral with $a_1$ so small, such that the lines are touching. Therefore $l$ is

$$\begin{aligned} l &= 6a_1 + 8a_2 + 8a_3 + \cdots + 8a_{n-2} + 8a_{n-1} + 7a_n \\ &= \left( \sum_{i=1}^{n} 8a_i \right) - 2a_1 - a_n \\ &= \left\{ \sum_{i=1}^{n} 8\left[ a_0 + (2i-1)(w+g) \right] \right\} - 2[a_0 + (w+g)] - [a_0 + (2n-1)(w+g)] \\ &= (8n-3)a_0 - g - w - 2gn - 2nw + 8gn^2 + 8wn^2 \end{aligned} , \tag{4.47}$$

which gives

$$a_0 = \frac{l + g + w + 2gn + 2nw - 8gn^2 - 8wn^2}{8n-3} . \tag{4.48}$$

Since it is necessary for $a_1 \geq w+g$, it follows from equation (4.46) that $a_0 \geq 0$. The dual-spiral is most compact when $a_0$ is smallest, i.e. $a_0 = 0$, which gives

$$\frac{l + g + w + 2gn_{\max} + 2n_{\max}w - 8gn_{\max}^2 - 8wn_{\max}^2}{8n_{\max} - 3} = 0 , \tag{4.49}$$

where $n_{\max}$, when round down to the nearest integer, is the largest number of coils in a spiral arm possible for a given $l$. Solving for $n_{\max}$ gives

$$n_{\max} = \frac{1}{8(g+w)}\left(g + w + \sqrt{8gl + 8lw + 18wg + 9g^2 + 9w^2}\right). \tag{4.50}$$

### 4.5.3 Optimal compact geometry for u-type dual-spiral

For the u-type dual-spiral resonator shown in figure 4.4 with $n$ coils, the total length is

$$\begin{aligned} l &= 6a_1 + 8a_2 + 8a_3 + \cdots + 8a_{n-2} + 8a_{n-1} + 6a_n \\ &= \left(\sum_{i=1}^{n} 8a_i\right) - 2a_1 - 2a_n \\ &= \sum_{i=1}^{n} 8\left[a_0 + (2i-1)(w+g)\right] - 2[a_0 + (w+g)] - 2[a_0 + (2n-1)(w+g)] \\ &= (8n-4)a_0 - 4gn - 4wn + 8gn^2 + 8wn^2 \end{aligned} \quad . \tag{4.51}$$

Substituting the value of $a_i$ with the definition given in equation (4.46) into equation (4.51) gives

$$a_0 = \frac{1}{8n-4}\left(l + 4gn + 4wn - 8gn^2 - 8wn^2\right). \tag{4.52}$$

The dual-spiral is most compact when $a_0 = 0$, which gives

$$\frac{1}{8n_{\max} - 4}\left(l + 4gn_{\max} + 4wn_{\max} - 8gn_{\max}^2 - 8wn_{\max}^2\right) = 0, \tag{4.53}$$

where $n_{\max}$, when round down to the nearest integer, is the largest number of coils in a spiral arm possible for a given $l$. Solving for $n_{\max}$ gives

$$n_{\max} = \frac{1}{4(w+g)}\left(w + g + \sqrt{w^2 + 2wg + g^2 + 2wl + 2gl}\right). \tag{4.54}$$

## 4.6 Comparison of dual-spiral resonators with half-wavelength resonator

The Q factors of the dual-spiral resonators were studied using a full wave electromagnetic simulation software, IE3D[1] (Version 10). In the simulations, the substrate was defined as 0.5 mm thick, with $\varepsilon_r = 23.8$ and $\tan\delta = 1\times10^{-5}$, corresponding to LAO substrate. The conductive layers were defined as 500 nm thick HTS thin film with penetration depth of 200 nm. The resonators have a resonant frequency of 1 GHz and track width of 0.2 mm. The gap between the tracks of the dual-spiral resonators was set at 0.2 mm. The dual-spiral resonators were simulated with under-coupled one-port input/output and the unloaded Q factor was calculated using the method presented in section 4.1.1.

The unloaded Q factors of the s- and u-type dual-spiral resonators are about the same at 101540 and 101460 respectively, but are more than twice of the half-wavelength resonator which is only 49880. The higher Q factor of the dual-spiral resonators is due to lesser current crowding at the edges of the microstrip lines and more even current distribution, as can be seen from figure 4.6. The dual-spiral resonators are also much more compact than the straight half-wavelength resonator as can be seen from the scaled layout of the resonators in figure 4.7.

[1] Zeland Software Inc., California, USA

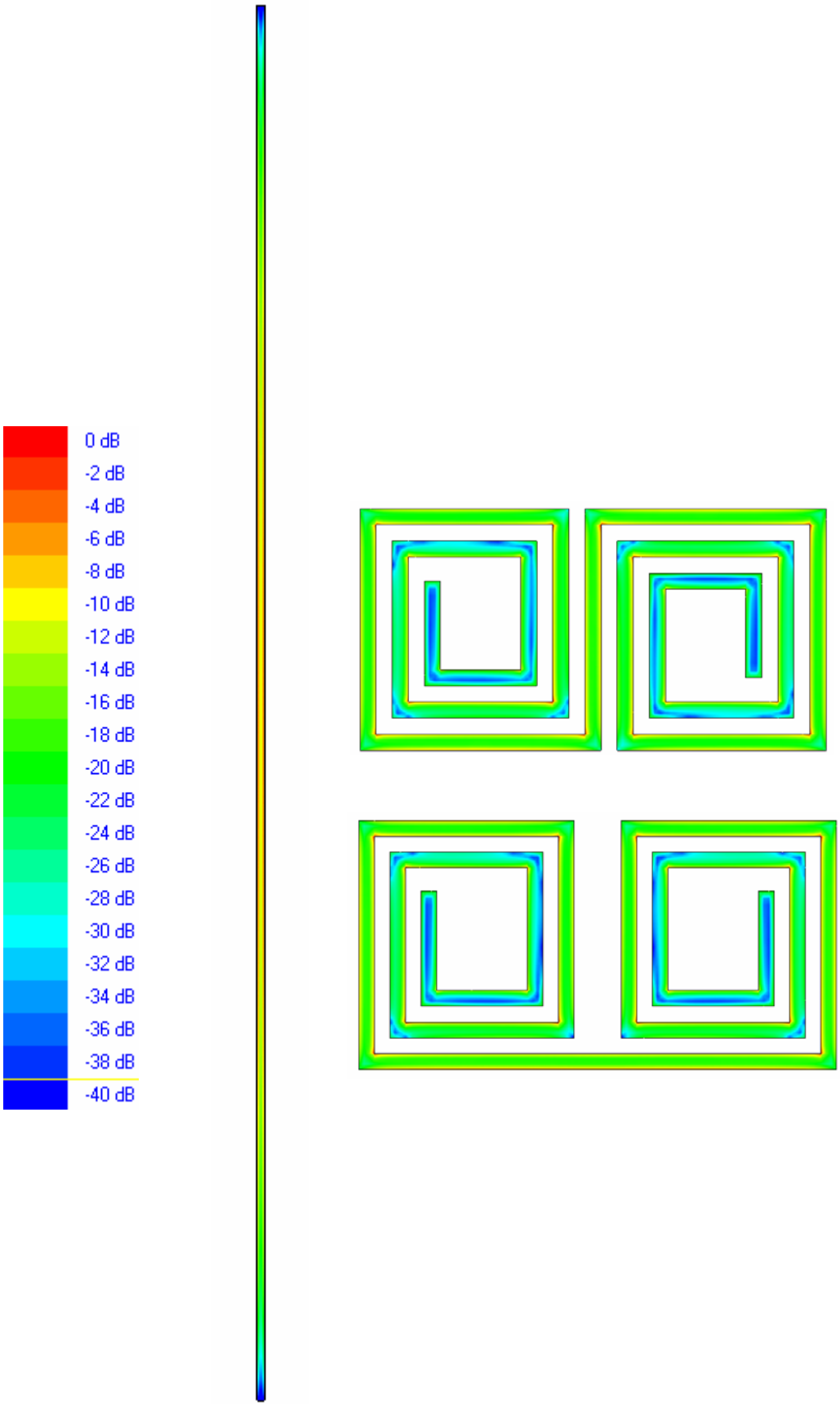


Figure 4.6 The electric current density within the half-wavelength, s-type dual-spiral and u-type dual-spiral resonators at resonance. All resonators have 0.2 mm track width.

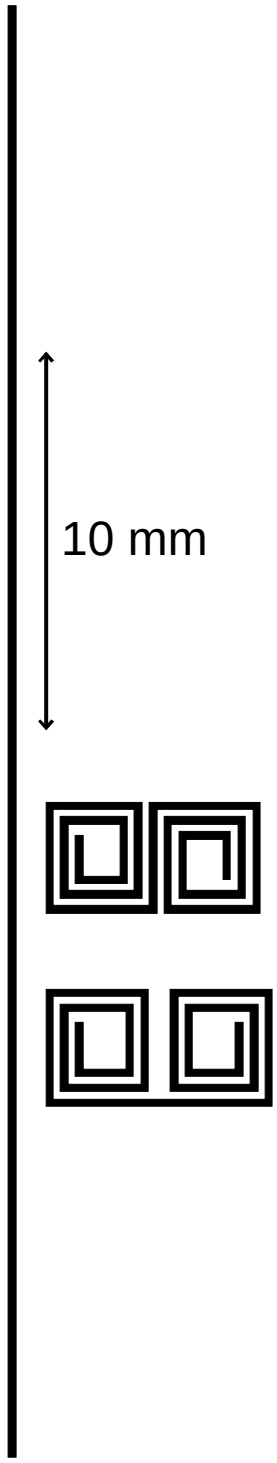


Figure 4.7 The scaled layout of 1 GHz s-type dual-spiral, u-type dual-spiral and half-wavelength resonators.

References

[1] M. Sucher and J. Fox, *Handbook of Microwave Measurements Vol. II*, 3rd Ed., John Wiley & Sons Inc., 1963.

[2] M. J. Lancaster, *Passive Microwave Device Applications of High-Temperature Superconductors*, Cambridge University Press, 1997.

[3] P. H. Smith , *Electronic applications of the Smith Chart : in waveguide, circuit, and component analysis* , McGraw-Hill, 1969.

[4] D. M. Pozar, *Microwave Engineering*, 2nd Ed., John Wiley & Sons Inc., 1998.

[5] G. L. Matthaei, L. Young, and E. M. T. Jones, *Microwave filters, impedance-matching networks, and coupling structures,* Artech House, 1980.

[6] S. B. Cohn, "Dissipation Loss in Multiple-Coupled-Resonator Filters", *The Proceedings of the IRE*, vol. 47, pp. 1342-1348, Aug.1959.

[7] E. J. Denlinger, "Radiation from Microstrip Resonators", *IEEE Transactions on Microwave Theory and Techniques*, vol. 17, no. 4, pp. 235-236, 1969.

[8] R. B. Hammond, E. R. Soares, B. A. Willemsen, T. Dahm, D. J. Scalapino, and J. R. Schrieffer, "Intrinsic limits on the *Q* and intermodulation of low power high temperature superconducting microstrip resonator", *Journal of Applied Physics*, vol. 84, no. 10, pp. 5662-5667, 1998.

[9] M. J. Lancaster, F. Huang, A. Porch, B. Avenhaus, J.-S. Hong, and D. Hung, "Miniature Superconducting Filters", *IEEE Transactions on Microwave Theory and Techniques*, vol. 44, no. 7, pp. 1339-1346, 1996.

# CHAPTER 5:
# HTS MICROSTRIP CROSS-COUPLED DUAL-SPIRAL BANDPASS FILTER

This chapter presents the use of the microstrip dual-spiral resonators for the miniaturization of HTS microwave bandpass filter. The use of microstrip dual-spiral resonator for bandpass filter was first demonstrated by researchers from CSMM in [1,2], and subsequently by other researchers in [3,4]. The use of dual-spiral resonators for cross-coupled filter was first demonstrated in [5], and this work is presented in this chapter.

Dual-spiral resonators are highly suitable for the miniaturization of HTS filter as it has a very compact geometry and high Q factor. In addition, the dual-spiral resonators also allow easy implementation of both positive and negative inter-resonator couplings. Such opposite phase couplings can be used to design cross-coupled filters, such as the cross-coupled cascaded quadruplet filter, which uses a pair of finite frequency transmission zero to enhance filter selectivity.

## 5.1 Microwave bandpass filter

A microwave bandpass filter is a two-port frequency selection device that is designed to block the transmission of microwave signals except those in a specific frequency range. Figure 5.1 shows the transmission S-parameter response of a bandpass filter and the typical terms used to characterize a bandpass filter. The sensitivity of a filter is defined by the insertion loss while the selectivity of a filter, i.e. how rapidly the transmission outside the passband falls off, is usually defined by the 3 dB bandwidth and the rejection bandwidth (usually in the 30 to 60 dB range).

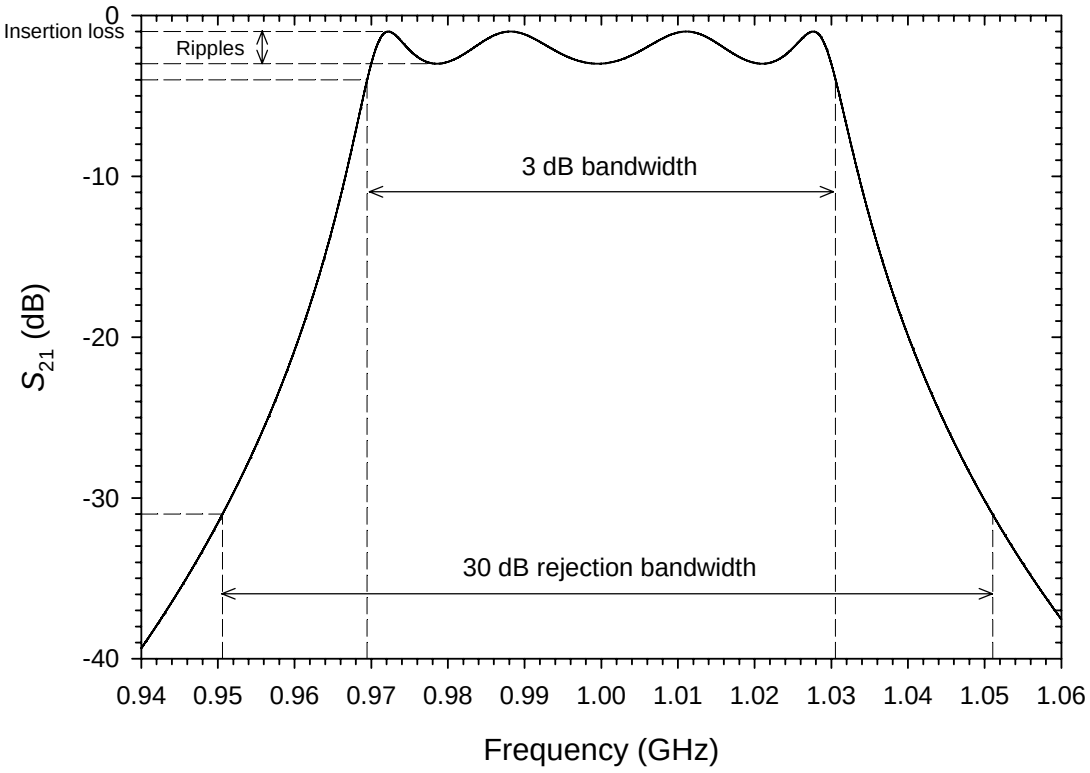


Figure 5.1 A graph illustrating the typical parameters used to specify a bandpass filter. The graph shows the transmission S-parameter response of a bandpass filter with 1 GHz central frequency, 1 dB insertion loss, 2 dB ripples, 6 % 3 dB bandwidth and 10 % 30 dB rejection bandwidth.

### 5.1.1 Applications of bandpass filter with high sensitivity and high selectivity

Microwave bandpass filter is an important component in many microwave systems. Many modern applications require bandpass filter with ever more stringent specifications such as higher sensitivity, higher selectivity, smaller size and lighter weight.

Both high selectivity and high sensitivity are often desired in many filter applications. For example in the base station of the mobile phone system or radar, higher sensitivity will result in longer coverage range. Other advantages for mobile phone system include better reception, less drop calls and the reduction of transmission power for the mobile handset which increases the operating time for the battery operated handset and possibly provides improvement to health and environment safety.

High selectivity is required to reduce interference from adjacent frequency band. With the recent explosive growth of wireless microwave applications such as mobile telecommunication and wireless networking, the microwave frequency spectrum is becoming increasingly congested resulting in collocation interferences. With higher selectivity, it is possible to reduce inference without resorting to wider frequency separation which wastes frequency bandwidth.

### 5.1.2 Advantages of HTS microwave bandpass filter

The design of narrow bandpass filter with both high sensitivity and high selectivity can be very challenging. The basic building block of a microwave filter is the microwave resonator. Generally, to have a bandpass filter with higher selectivity, the filter needs more resonators. The increase in the number of resonators will lead to

an increase in energy dissipation and lower the sensitivity of a filter. Thus the requirement of high sensitivity with high selectivity is contradictory in filter design. The increase in the number of resonators will also increase the size and weight of a filter.

The advantage of using HTS thin films to fabricate planar filters is that these HTS filters can be made to be highly selective while retaining high sensitivity. This is because very high Q factor resonator can be fabricated using HTS thin film, resulting in negligible insertion loss even when many resonators are used in a filter.

Another important advantage of using HTS thin film in filter application is the miniaturization of filter. HTS resonator can be designed to be very small while retaining high Q factor. Reducing the size of the conventional resonators used in a filter generally results in increase insertion loss. HTS allow a much greater degree of reduction in size than normal metals without reduction in performances.

Both commercial and defense microwave systems can benefit from the application of miniaturized HTS filters. One example of commercial application is in the receiver front-end of the mobile phone base station. The optimum placement of the receiver front-end is right behind the antenna. Thus the receiver front-end is required to be sufficiently small and light-weight enough to be mast mountable. Size and weight are also important considerations in avionic and satellite applications such as radar and relay systems. The miniaturization of HTS filter is also advantageous to practical implementation as it simplifies both the filter cooling requirement and HTS thin film fabrication process.

## 5.2 Cross-coupled filter

When designing filters, an important requirement is the correct implementation of the couplings between the resonators. Energy passing through the coupling between two resonators will be phase-shifted and amplitude adjusted. The coupling must provide for the correct vector addition of energy between the resonators, as required by the filter design. Frequently, such couplings are described as “positive” or “negative”, a nomenclature referring to the phase shift of the coupling.

Filters that have a single path for the energy transit from the input to output are usually derived from “ladder networks” based circuits, so called because the alternating series and shunt elements have the form of a ladder. These filters can approximate various transfer functions (e.g. Butterworth, Chebychev, Bessel, Gaussian, etc.) with monotonic attenuation characteristics [6]. Such filters typically have either purely positive or negative coupling between the adjacent resonators. Sometimes, a better approximation of these monotonic functions is possible if some of the inter-resonator couplings are negative while some are positive. If both forms of coupling are used, the attenuation characteristics can be made more symmetrical. Providing both types of coupling in a filter can be difficult, because the most physical structure of most filters force the inter-resonator couplings to be either positive or negative, but not both within the same structure.

Filters that have more than one path for energy to move between the input and output offer certain potential advantages compared to purely ladder-derived networks and are commonly called cross-coupled filter [7-11]. Depending on the filter requirement, the required couplings within the filter might be positive, negative or both types.

Cross-coupled filters are traditionally realized using three-dimensional structure such as waveguide cavities or dielectric resonators [12], which are bulkier than planar structures. However, with the development of HTS technology, there is an increasing interest in developing HTS thin film filters with two-dimensional structure such as the microstrip structure. The difficulty with using planar structures to implement cross-coupled filter is finding resonator structures that allow suitable inter-resonator couplings. Previously proposed microstrip cross-coupled filters are mostly based on open-loop resonators and its variations [13].

### 5.2.1 Response of cross-coupled bandpass filter

Cross coupling of resonators can be used to introduce finite frequency transmission-zeros near the passband so that higher selectivity can be obtained without using more resonators. The transfer function of such filters is

$$\left|S_{21}\left(\Omega\right)\right|^2 = \frac{1}{1+\varepsilon^2 F_n^2\left(\Omega\right)}, \tag{5.1}$$

where

$$\varepsilon = \frac{1}{\sqrt{10^{-\frac{L_R}{10}}-1}}, \tag{5.2}$$

and

$$F_n(n) = \cosh\left[(n-2)\cosh^{-1}\left(\Omega\right) + \cosh^{-1}\left(\frac{\Omega_a\Omega-1}{\Omega_a-\Omega}\right) + \cosh^{-1}\left(\frac{\Omega_a\Omega+1}{\Omega_a+\Omega}\right)\right]. \tag{5.3}$$

$n$ is the number of resonators and $L_R$ is the passband return loss in dB. $\Omega$ is the normalized low-pass prototype frequency calculated using

$$\Omega = \frac{1}{FBW}\left(\frac{f}{f_c} - \frac{f_c}{f}\right), \tag{5.4}$$

where $FBW$ is the 3 dB fractional bandwidth, $\Omega_a$ is the normalized low-pass prototype transmission zero frequency, $f$ is the frequency and $f_c$ is the central frequency.

From the frequency response for Butterworth, Chebyshev and cross-coupled response filters shown in figure 5.2, it can be seen that the cross-coupled filter shows obvious advantage in selectivity. As shown in figure 5.3, a Chebyshev response filter needs up to 7 resonators to have selectivity comparable with that of a cross-coupled filter with 4 resonators. The higher selectivity of cross-coupled filters comes at a price of poorer isolation in the rejection bandwidth as can be seen in figure 5.3. However, the isolation in the rejection bandwidth can be improved by using more resonators and setting the transmission zero frequency further from the central frequency as seen in figures 5.3 and 5.4. Furthermore, in many applications, higher selectivity is more important and cross-coupled response filters provided sufficient rejection bandwidth isolation.

## 5.3 Cascaded quadruplet filter

At least 4 resonators are needed to realize a cross-coupled filter with a pair of attenuation poles at finite frequency. This type of cross-coupled filter is also called the cascaded quadruplet filter. The general coupling structure for this class of filters is depicted in figure 5.5, where each node represents a resonator and $M_{1,2}$, $M_{2,3}$, $M_{3,4}$ and $M_{1,4}$ represent the coupling between resonators 1 and 2, 2 and 3, 3 and 4 as well as 1 and 4 respectively. The full lines indicate the main path couplings, and the

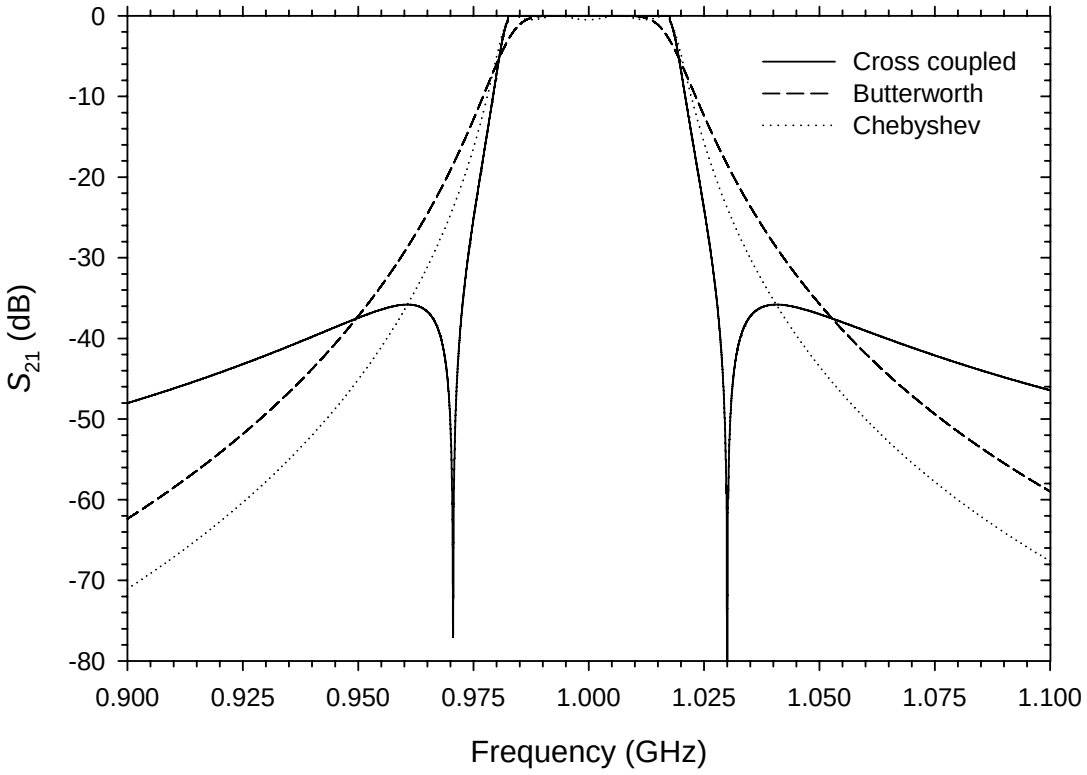


Figure 5.2 The transmission S-parameter of four-resonator bandpass filter with cross-coupled, Butterworth and Chebyshev responses.

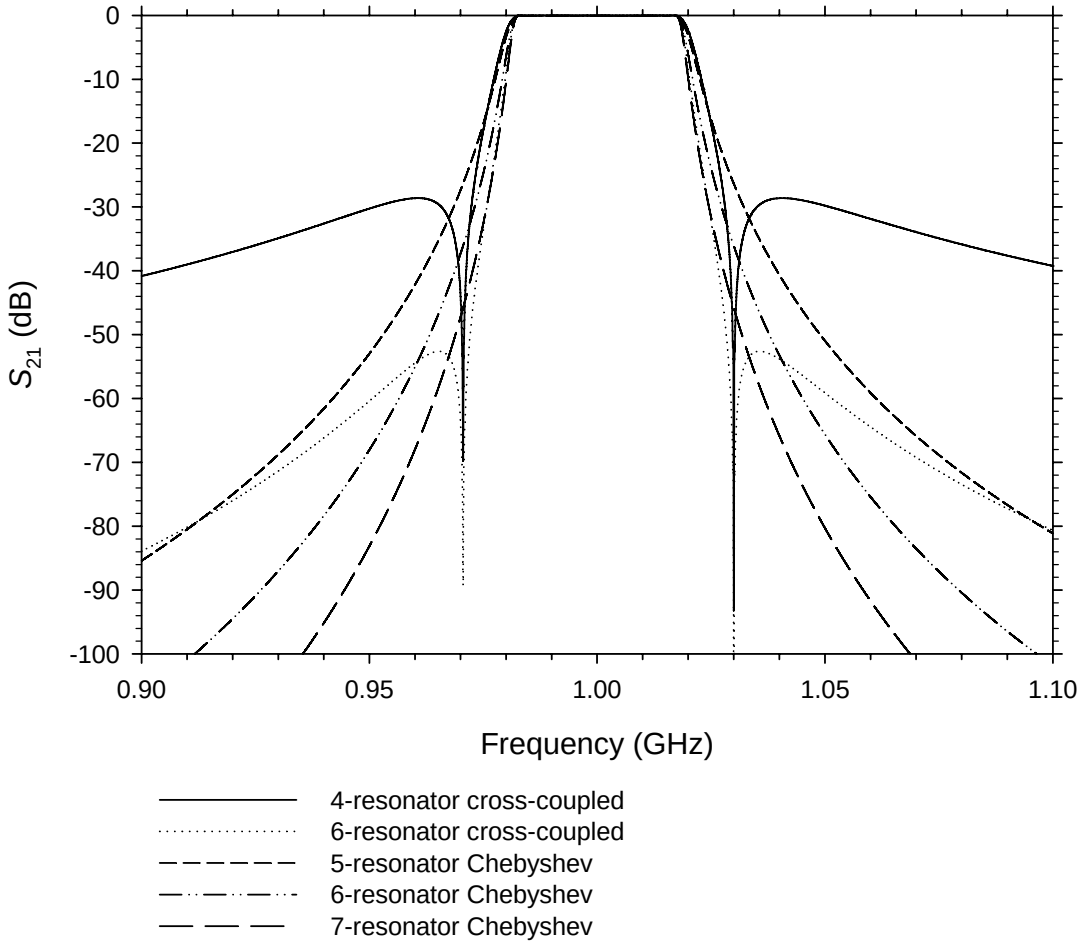


Figure 5.3 Comparison of Chebyshev and cross-coupled responses filters with different numbers of resonators.

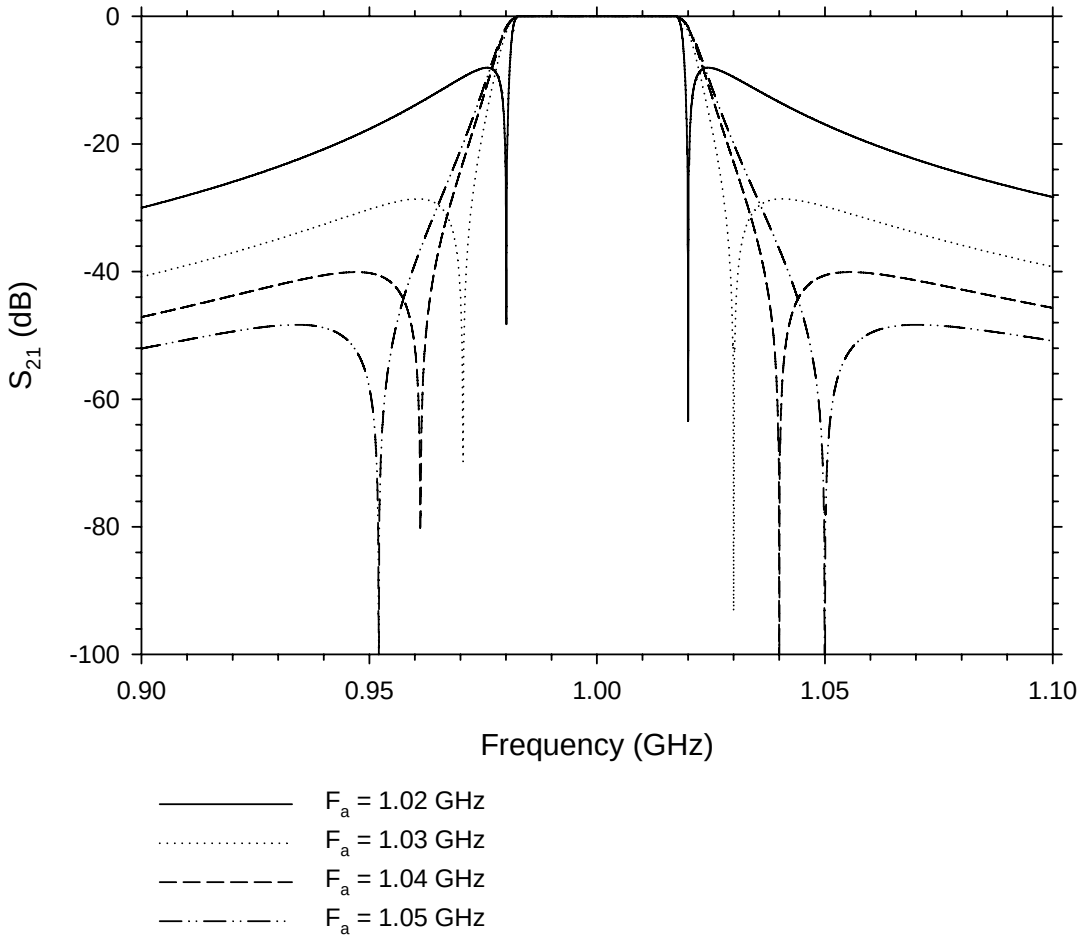


Figure 5.4 Comparison of 4-resonator cross-coupled responses filters with the transmission zeros at different frequencies.

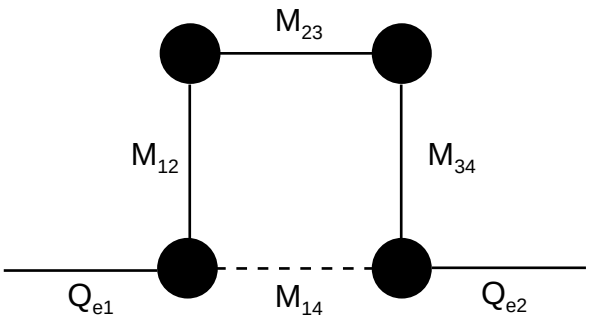


Figure 5.5 Coupling structure of a cascaded quadruplet cross-coupled filter. The nodes represent the four resonators and the lines represent the couplings.

broken line denotes the cross coupling. It is essential that the sign of cross coupling be opposite to that of the other couplings in order to realize a pair of transmission zeros at finite frequencies. This means that $M_{1,2}$, $M_{2,3}$, $M_{3,4}$ are of opposite phase to $M_{1,4}$.

The coupling coefficients and external quality factor of a cascaded quadruplet filter can be determined in terms of circuit elements of a low-pass prototype filter, which consist of capacitors and ideal admittance inverters. The relationships between the bandpass design parameters and low-pass elements are:

$$Q_{ei} = Q_{eo} = \frac{C_1}{FBW}, \tag{5.5}$$

$$M_{1,2} = M_{3,4} = \frac{FBW}{\sqrt{C_1 \times C_2}}, \tag{5.6}$$

$$M_{2,3} = \frac{FBW \times J_2}{C_2}, \tag{5.7}$$

and

$$M_{1,4} = \frac{FBW \times J_1}{C_1}, \tag{5.8}$$

where $C_n$ is the capacitance of the $n^{\text{th}}$ lumped capacitor and $J_n$ is the characteristic admittance of the $n^{\text{th}}$ inverter.

An approximation synthesis may be carried out using the following formulas for $1.8 \le \Omega_a \le 2.4$ [13]:

$$\begin{aligned} C_1(\Omega_a) = {} & 1.22147 - 0.35543 \times \Omega_a + 0.18337 \times \Omega_a{}^2 \\ & -0.0447 \times \Omega_a{}^3 + 0.00425 \times \Omega_a{}^4 \end{aligned}, \tag{5.9}$$

$$\begin{aligned} C_2(\Omega_a) = {} & 7.22106 - 9.48678 \times \Omega_a + 5.89032 \times \Omega_a{}^2 \\ & -1.65776 \times \Omega_a{}^3 + 0.17723 \times \Omega_a{}^4 \end{aligned}, \tag{5.10}$$

$$J_1(\Omega_a) = -4.30192 + 6.26745 \times \Omega_a - 3.67345 \times \Omega_a{}^2 + 0.9936 \times \Omega_a{}^3 - 0.10317 \times \Omega_a{}^4 , \quad (5.11)$$

and

$$J_2(\Omega_a) = 8.17573 - 11.36315 \times \Omega_a + 6.96223 \times \Omega_a{}^2 - 1.94244 \times \Omega_a{}^3 + 0.20636 \times \Omega_a{}^4 . \quad (5.12)$$

The frequency response can be calculated by:

$$S_{21}(\Omega) = \frac{Y_o(\Omega) - Y_e(\Omega)}{[1 + Y_o(\Omega)][1 + Y_e(\Omega)]}, \quad (5.13)$$

and

$$S_{11}(\Omega) = \frac{1 - Y_o(\Omega) \times Y_e(\Omega)}{[1 + Y_o(\Omega)][1 + Y_e(\Omega)]}, \quad (5.14)$$

where $Y_e$ and $Y_o$ are the even and odd mode input admittance of the filter, which can be expressed in terms of the elements in a ladder structure as:

$$Y_e = j(\Omega C_1 - J_1) + \frac{1}{j(\Omega C_2 - J_2)}, \quad (5.15)$$

and

$$Y_o = j(\Omega C_1 + J_1) + \frac{1}{j(\Omega C_2 + J_2)}. \quad (5.16)$$

As an example, a filter with the following specification was designed: central frequency at 1 GHz, *FBW* of 3.5 %, 45 dB rejection bandwidth of 6 % and 20 dB passband return loss. This specification can be satisfied for $\Omega_a = 1.69$. Using the equations (5.9) to (5.12), the required lumped capacitor capacitance and inverter characteristic admittance are $C_1 = 0.96345$, $C_2 = 1.45602$, $J_1 = -0.2476$, $J_2 = 1.16472$, and from equations (5.5) to (5.8), the inter-resonator couplings and

external quality factor are $M_{1,2} = M_{3,4} = 0.03$ , $M_{2,3} = 0.028$ , $M_{1,4} = -0.009$ , $Q_{ei} = Q_{eo} = 27.5$ . The theoretical response of the filter is shown in figure 5.6.

## 5.4 Inter-resonator couplings of dual-spiral resonators

The next step of the filter design is to characterize the inter-resonator couplings and external quality factors of the dual-spiral resonators in term of their physical structures so that a filter with physical dimension and structure satisfying the required design parameters can be determined.

When two resonators with the same resonant frequency are coupled together, the resultant structure will have a pair of resonant peaks, with one resonant frequency lower $(f_{r1})$ and the other higher $(f_{r2})$ than the original resonant frequency of the single resonator. The coupling coefficient, which characterized the magnitude of the inter-resonator coupling, can be calculated using [14]

$$M = \frac{f_{r2}^2 - f_{r1}^2}{f_{r2}^2 + f_{r1}^2}. \tag{5.17}$$

When designing cross-coupled filters, both the magnitude and phase of the inter-resonator couplings must be correct. An inter-resonator coupling is positive (also called inductive or magnetic) when a positive phase shift is observed at the split resonance frequencies whereas a negative phase shift indicates a negative (also called capacitive or electric) coupling. Example of the transmission S-parameter responses of positive and negative couplings is shown in figure 5.7 (a) and (b) respectively.

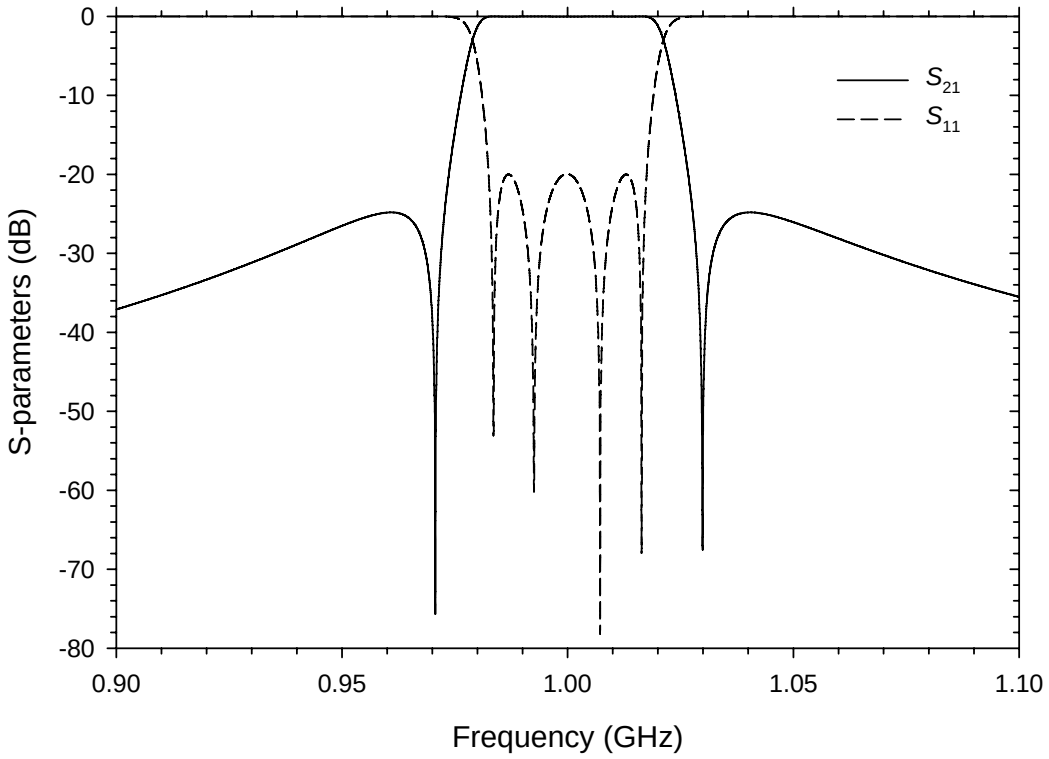


Figure 5.6 Theoretical S-parameter responses of a cascaded quadruplet cross-coupled filter with central frequency at 1 GHz, $FBW = 3.5\%$ and 45 dB bandwidth = 6 %.

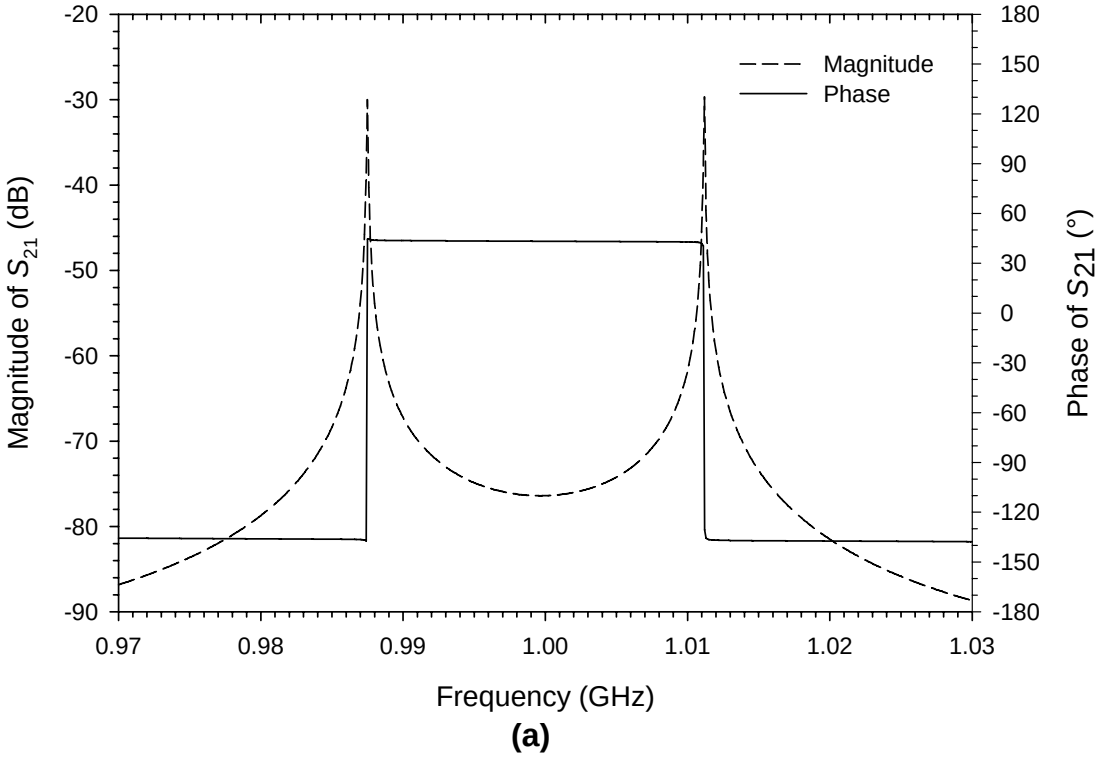


**(a)**

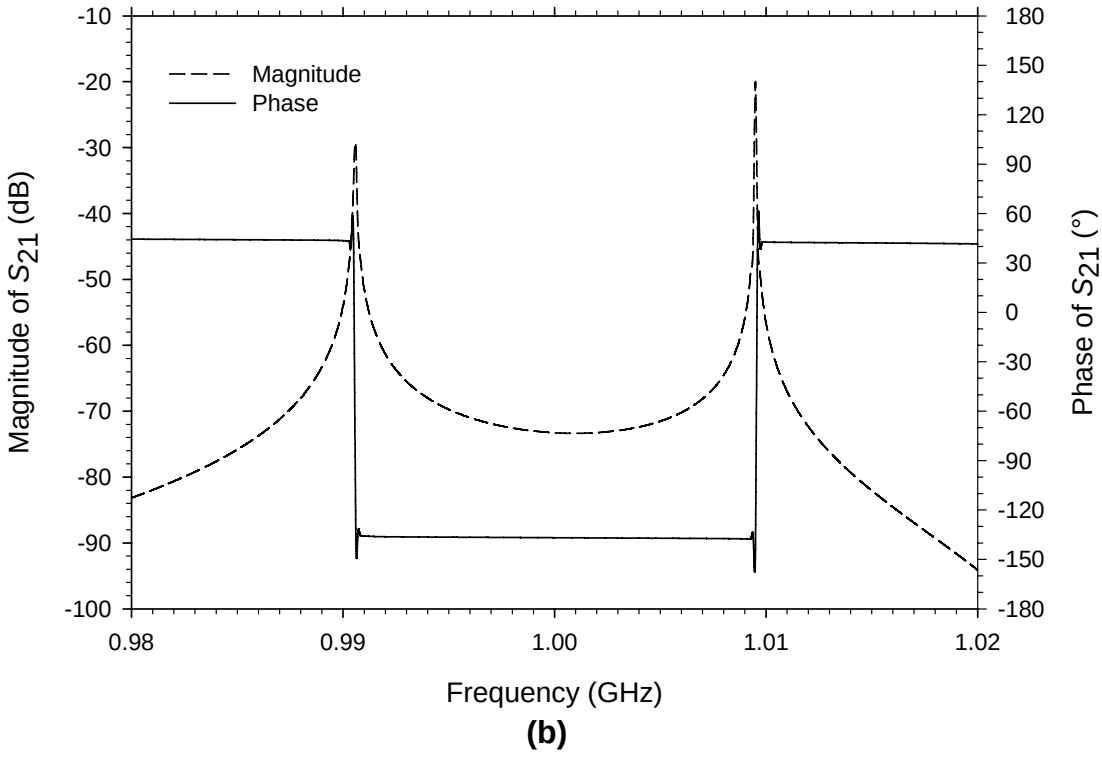


**(b)**

Figure 5.7 Example of the transmission S-parameter for (a) positive and (b) negative inter-resonator couplings.

As it is difficult to obtain accurate explicit equations for resonance and coupling of dual-spiral resonators, a full-wave electromagnetic simulation software, IE3D[1] (Version 10), was used to examine the characteristics of the dual-spiral inter-resonator coupling. Both the coupling coefficient and external quality factors can be accurately modeled using full-wave simulation.

In the simulations, the substrate was defined as 0.5 mm thick, with $\varepsilon_r = 23.8$ and $\tan\delta = 1\times10^{-5}$, corresponding to the LAO substrate used in the fabrication of the YBCO thin films. The conductive layers were defined as 500 nm thick HTS layer with penetration depth of 200 nm.

Figures 5.8 and 5.9 show some of the various dual-spiral resonator pair configurations examined. From the examination of the dual-spiral resonators, it was found that when only one spiral from each resonator is adjacent to the other resonator, the inter-resonator coupling sign is determined by the relative winding direction of these two adjacent spirals, i.e. when the two spirals are wound in the opposite direction as in figure 5.8, the coupling is positive whereas when the spirals are wound in the same direction as in figure 5.9, the coupling is negative. Furthermore, the relative position of the two spirals does not affect the coupling type, as the resonator pairs shown in figure 5.10 remain positively coupled even when their relative position was changed.

In cases where all four spirals are in close proximity as in figure 5.11, the inter-resonator coupling is dependant on the resultant interaction of all four spirals. In some cases, the coupling sign will change when separation between the resonators is varied.

[1] Zeland Software Inc., California, USA

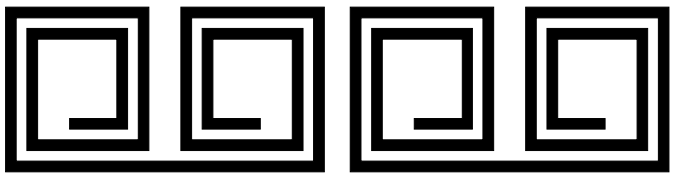

(a)

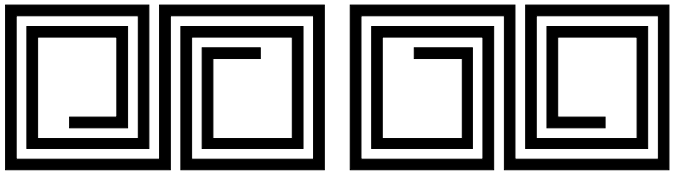

(b)

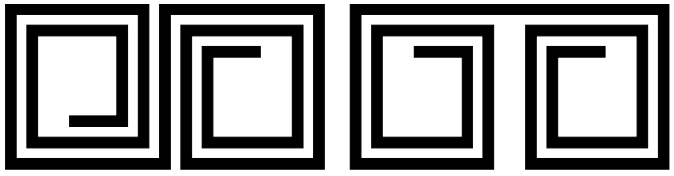

(c)

Figure 5.8 Examples of dual-spiral resonator pair with positive coupling.

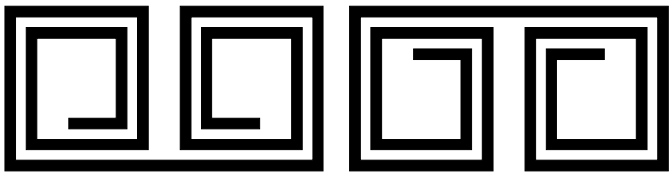

(a)

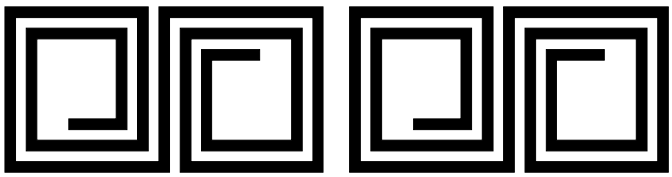

(b)

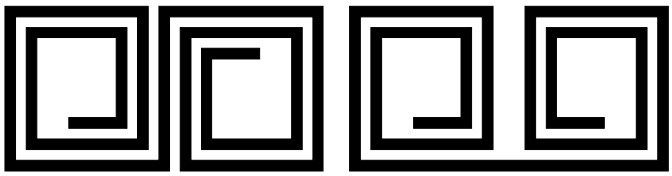

(c)

Figure 5.9 Examples of dual-spiral resonator pair with negative coupling.

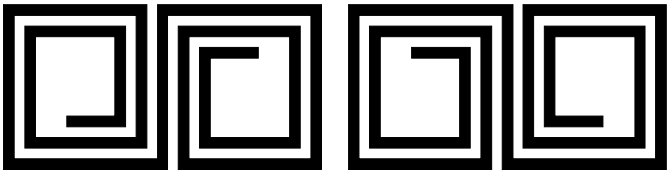

(a)

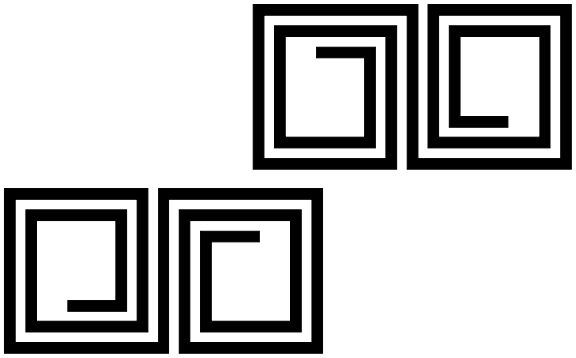

(b)

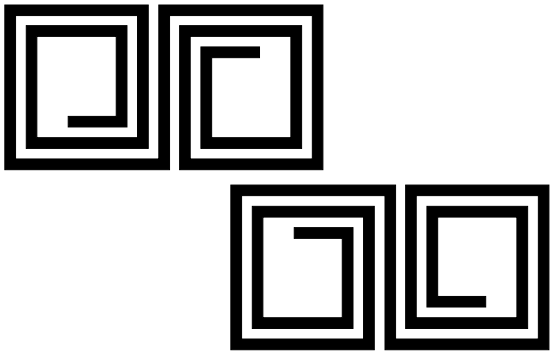

(c)

Figure 5.10 The resonator pair in (a), (b) and (c) are positive even when the relative position of the two adjacent spirals is different.

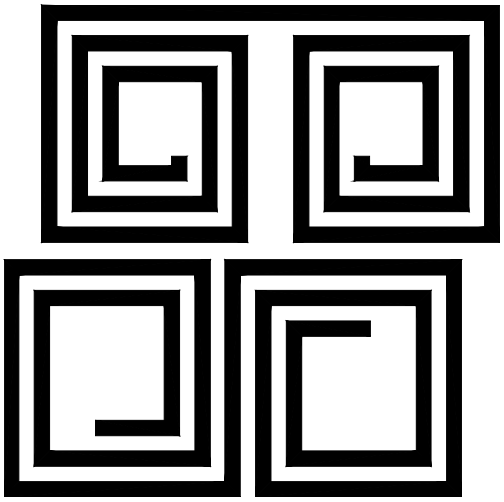

Figure 5.11 An example of the case when all four spirals are in close proximity.

The variation of coupling coefficient with resonators separation, obtained from simulation for selected resonator pairs are shown in figure 5.12.

## 5.5 Dual-spiral cross-coupled bandpass filter

Although there are a few dual-spiral pair configurations giving positive or negative coupling, the resonator pair shown in figure 5.12 (b) is used for $M_{1,4}$ coupling and resonator pair shown in figure 5.12 (a) is used for $M_{2,3}$ coupling. The resulting geometry will result in identical, although horizontally reflected resonator pairs for $M_{1,2}$ and $M_{3,4}$. The inter-resonator distance between resonator 1 and resonator 2, and the inter-resonator distance between resonator 3 and resonator 4, will then be the same, as $M_{1,2}$ and $M_{3,4}$ are required to be equal by the filter synthesis equations. The required separations between the resonators can be obtained from the graphs in figure 5.12.

$Q_{ei}$ and $Q_{eo}$, the input and output external quality factors were also obtained from full-wave EM simulations. $Q_{ei}$ and $Q_{eo}$ were determined by the distances between the input/output feed-line and the centre of the resonator, with further distance giving stronger coupling.

The finalized filter design is shown in figure 5.13. The inter-resonator distances in the finalized design had been slightly adjusted based on full-wave electromagnetic simulation to give optimized result. The S-parameters of the optimized design based on simulation and measurement at 77 K are shown in figure 5.14. The filter was fabricated using the expitaxial YBCO thin film deposited on both sides of a 15 mm × 20 mm × 0.5 mm LAO substrate with <100> surface orientation using the PLD

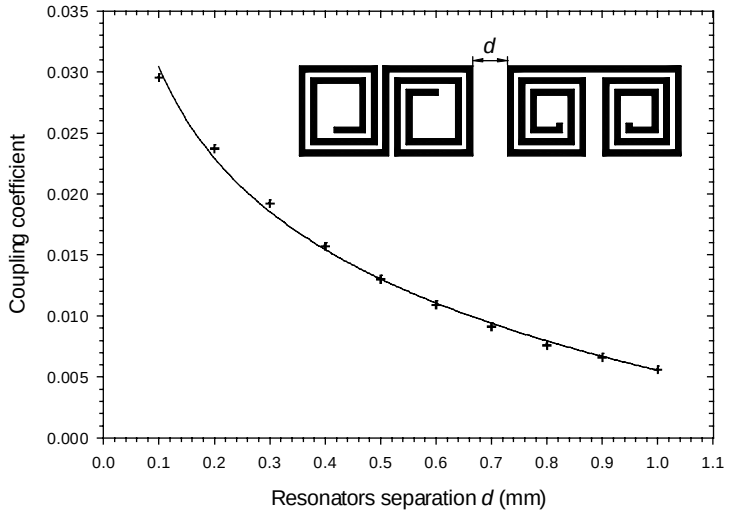


(a)

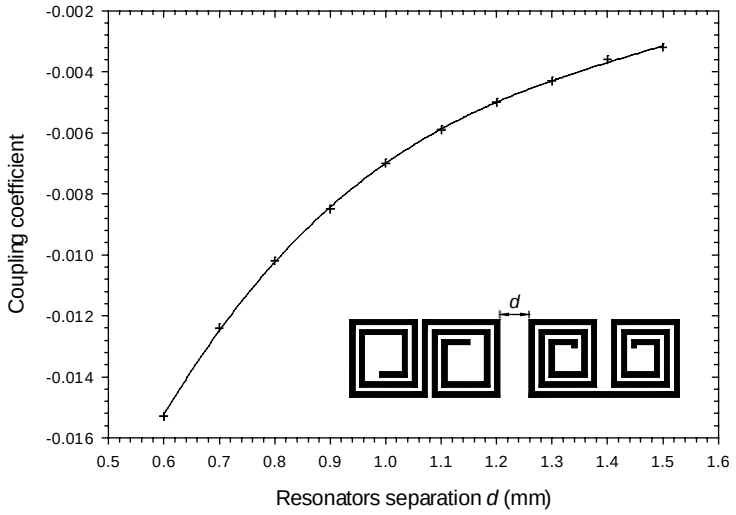


(b)

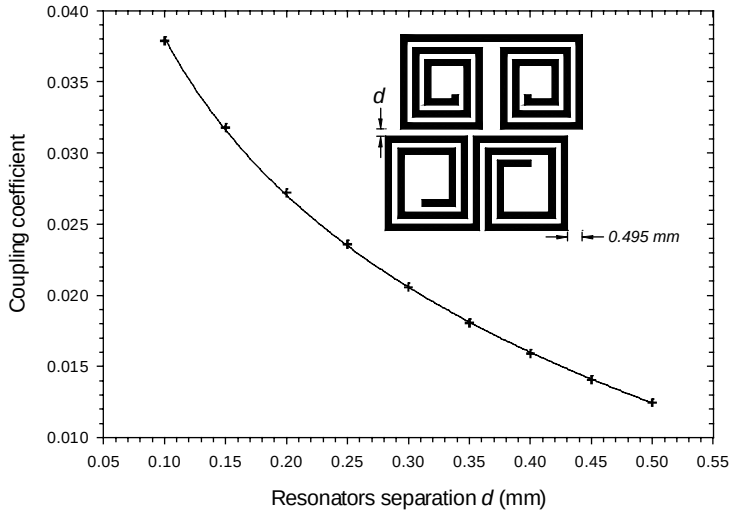


(c)

Figure 5.12 Variation of coupling coefficient, obtained from simulation, with resonators separation for selected resonator pairs.

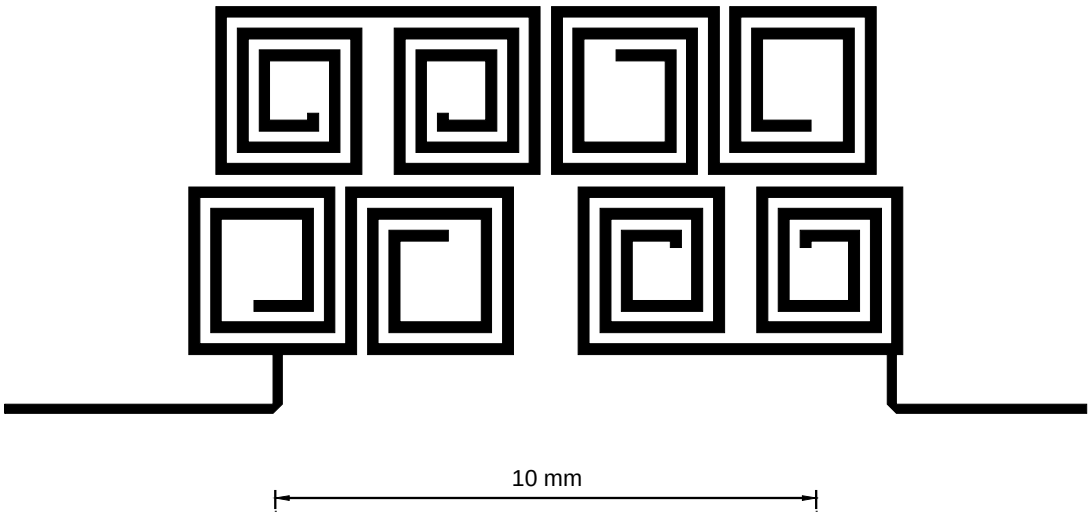


Figure 5.13 Layout of the cross-coupled dual-spiral filter.

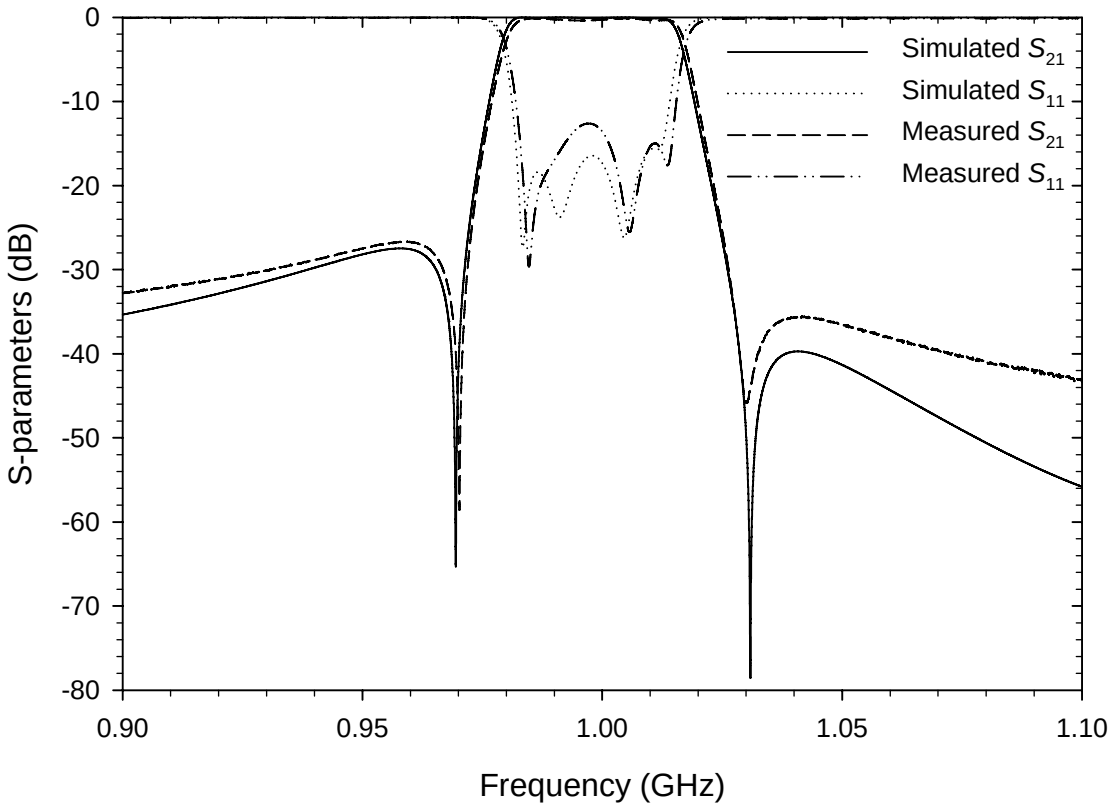


Figure 5.14 Simulated and measured S-parameters responses of the cross-coupled dual-spiral filter.

procedure described in chapter 2, with the patterning and packaging done using the procedures described in chapter 9. The dimension of the brass casing used for the packaging is shown in figure 5.15. The measured responses closely matched the simulated results, with passband insertion loss and ripple both at less than 0.2 dB.

## 5.6 Conclusion

In this chapter, the inter-resonator coupling of dual-spiral pair in various configurations was examined. It was found that the dual-spiral resonators allow easy implementation of both positive and negative inter-resonator couplings thus providing a viable way of synthesizing planar cross-coupled filter which has enhanced selectivity. A cascaded quadruplet cross-coupled filter was designed, using a combination of synthesis equations and full-wave EM simulations which enables the rapid and accurate design of the filter. The fabricated filter had a filter response that closely matched the simulated results and successfully demonstrated the application of dual-spiral resonators in filter miniaturization.

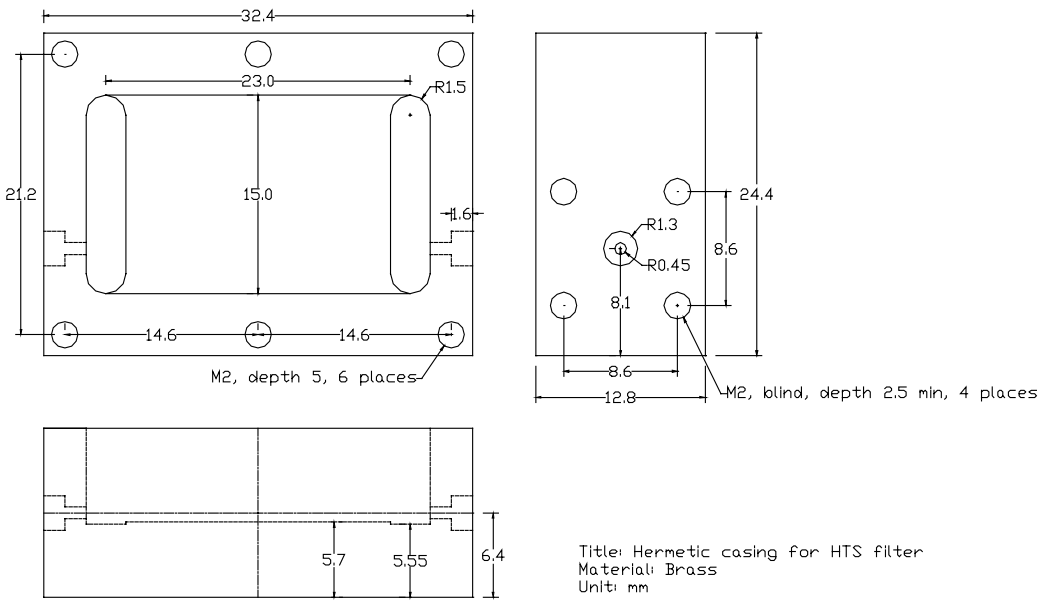


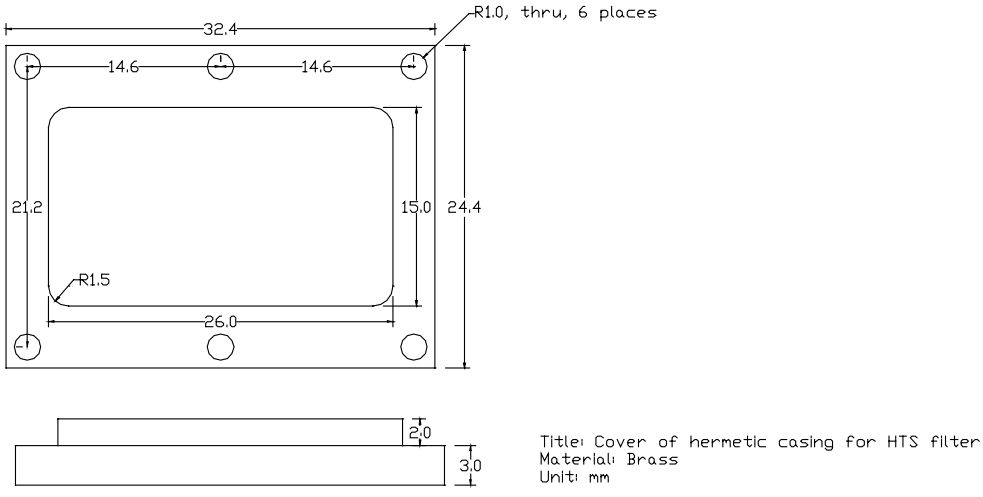


Figure 5.15 Design of the casing for the cross-coupled dual-spiral filter.

References


[1] C. K. Ong, L. F. Chen, J. Lu, C. Y. Tan, and B. T. G. Tan, "High-temperature superconducting bandpass spiral filter", *IEEE Microwave and Guided Wave Letters*, vol. 9, no. 10, pp. 407-409, 1999.

[2] L. F. Chen, C. Y. Tan, J. Lu, C. K. Ong, and B. T. G. Tan, "High-temperature superconducting dual-spiral resonators and their application in filter miniaturization", *Superconductor Science & Technology*, vol. 13, no. 4, pp. 368-372, 2000.

[3] F. Huang, "Ultra-Compact Superconducting Narrow-Band Filters Using Single- and Twin-Spiral Resonators", *IEEE Transactions on Microwave Theory and Techniques*, vol. 51, no. 2, pp. 487-491, 2003.

[4] F. Huang, "Superconducting microwave bandpass filter using spiral resonators with no air bridges", *Electonics Letters*, vol. 37, no. 6, pp. 361-362, 2001.

[5] C. Y. Tan, L. F. Chen, J. Lu, X. S. Rao, and C. K. Ong, "Cross-coupled dual-spiral high-temperature superconducting filter", *IEEE Microwave and Wireless Components Letters*, vol. 13, no. 6, pp. 247-249, 2003.

[6] G. L. Matthaei, L. Young, and E. M. T. Jones, *Microwave filters, impedance-matching networks, and coupling structures*, Artech House, 1980.

[7] R. Levy and P. Petre, "Design of CT and CQ Filters Using Approximation and Optimization", *IEEE Transactions on Microwave Theory and Techniques*, vol. 49, no. 12, pp. 2350-2356, 2001.

[8] R. Levy, "Filters with Single Transmission Zeros at Real or Imaginary Frequencies", *IEEE Transactions on Microwave Theory and Techniques*, vol. 24, no. 4, pp. 172-181, 1976.

[9] R. M. Kurzrok, "General Four-Resonator Filters at Microwave Frequencies", *IEEE Transactions on Microwave Theory and Techniques*, vol. 14, no. 6, pp. 295-296, 1966.

[10] R. M. Kurzrok, "Correction to "General Four-Resonator Filters at Microwave Frequencies"", *IEEE Transactions on Microwave Theory and Techniques*, vol. 14, no. 10, p. 498, 1966.

[11] R. J. Cameron, "General Coupling Matrix Synthesis Methods for Chebyshev Filtering Functions", *IEEE Transactions on Microwave Theory and Techniques*, vol. 47, no. 4, pp. 433-442, 1999.

[12] R. Levy and S. B. Cohn, "A History of Microwave Filter Research, Design, and Development", *IEEE Transactions on Microwave Theory and Techniques*, vol. 32, no. 9, pp. 1055-1067, 1984.

[13] J.-S. Hong and M. J. Lancaster, "Design of Highly Selective Microstrip Bandpass Filters with a Single Pair of Attenuation Poles at Finite Frequencies",

*IEEE Transactions on Microwave Theory and Techniques*, vol. 48, no. 7, pp. 1098-1107, 2000.

[14] J.-S. Hong and M. J. Lancaster, "Coupling of Microstrip Square Open-Loop Resonators for Cross-coupled Planar Microwave Filters", *IEEE Transactions on Microwave Theory and Techniques*, vol. 44, no. 12, pp. 2099-2109, 1996.

# CHAPTER 6:
# FERROELECTRIC THIN FILMS AND MULTILAYERS

Ferroelectricity was discovered by Joseph Valasek in 1921 during studies on the dielectric properties of Rochelle salt [1]. Since the early 1960s, ferroelectric materials have been studied for applications in microwave devices [2,3]. These earlier studies were based on bulk samples. The interest in using ferroelectric materials for microwave applications arises from the substantial non-linear change in the dielectric constant of a ferroelectric material with the application of an electric field, which could be exploited to fabricate tunable microwave devices whose characteristic could be changed by applying an electric field.

Recently, there are renewed interests in ferroelectric materials [4-6], mainly due to interests in the thin film form of ferroelectric materials, the emergent of applications, and the compatibility of ferroelectric thin film with HTS thin film in terms of structural properties, fabrication methods and applications.

In this chapter, the fabrication and characterization of $Ba_{0.1}Sr_{0.9}TiO_3$ ferroelectric thin films and $Ba_{0.1}Sr_{0.9}TiO_3$/YBCO ferroelectric/HTS multilayer thin films are described.

## 6.1 Barium strontium titanate ferroelectric thin films

Ferroelectric materials usually do not contain iron; the term ferroelectricity originated because ferroelectric materials have electric field response that is similar to the magnetic field response of a ferromagnetic material. Ferroelectric materials are defined by the exhibition of spontaneous electrical polarization, which can be reversed or reoriented upon the application of a sufficiently large electric field. The

spontaneous electrical polarization of ferroelectric materials is due to the asymmetric arrangement of ions within the unit cell, such that the centres of the positive and negative charges do not coincide, resulting in a permanent electric dipole moment. Group of adjacent unit cells tends to polarize in the same direction, forming a ferroelectric domain.

In typical perovskite ferroelectric materials such as $BaTiO_3$, which has the perovskite $ABO_3$ unit cell structure shown in figure 6.1, the barium, titanium and oxygen atoms occupy the corner, body-centered and face-centered sites respectively. When in the ferroelectric state, the Ti atom can be in either of the two thermodynamically stable positions inside the oxygen octahedral. The Ti atom can be displaced upward or downward relative to the oxygen atoms, depending on the polarity of the applied electric field. This displacement generates a dipole moment inside the oxygen octahedral. The Ti atom remains in one of the displaced position and generates a residual polarization even in the absence of an applied electric field.

The complex permittivity of ferroelectric materials is a function of temperature and applied electric field. Ferroelectric materials show ferroelectric effect, i.e. spontaneous polarization, only when they are below a certain temperature, referred to as the Curie temperature, at which point they undergo a phase transition. Above the Curie temperature, ferroelectric materials are in a paraelectric phase, i.e. no spontaneous polarization, however they retained a non-linear dielectric constant variation with applied electric field. The dielectric constant, loss tangent and variation of dielectric constant with applied electric field for ferroelectric materials are greatest at the Curie temperature. Ferroelectric materials for microwave applications are usually operated at temperature slightly above the Curie temperature, i.e. in paraelectric phase, as losses due to microwave dissipation in ferroelectric phase are

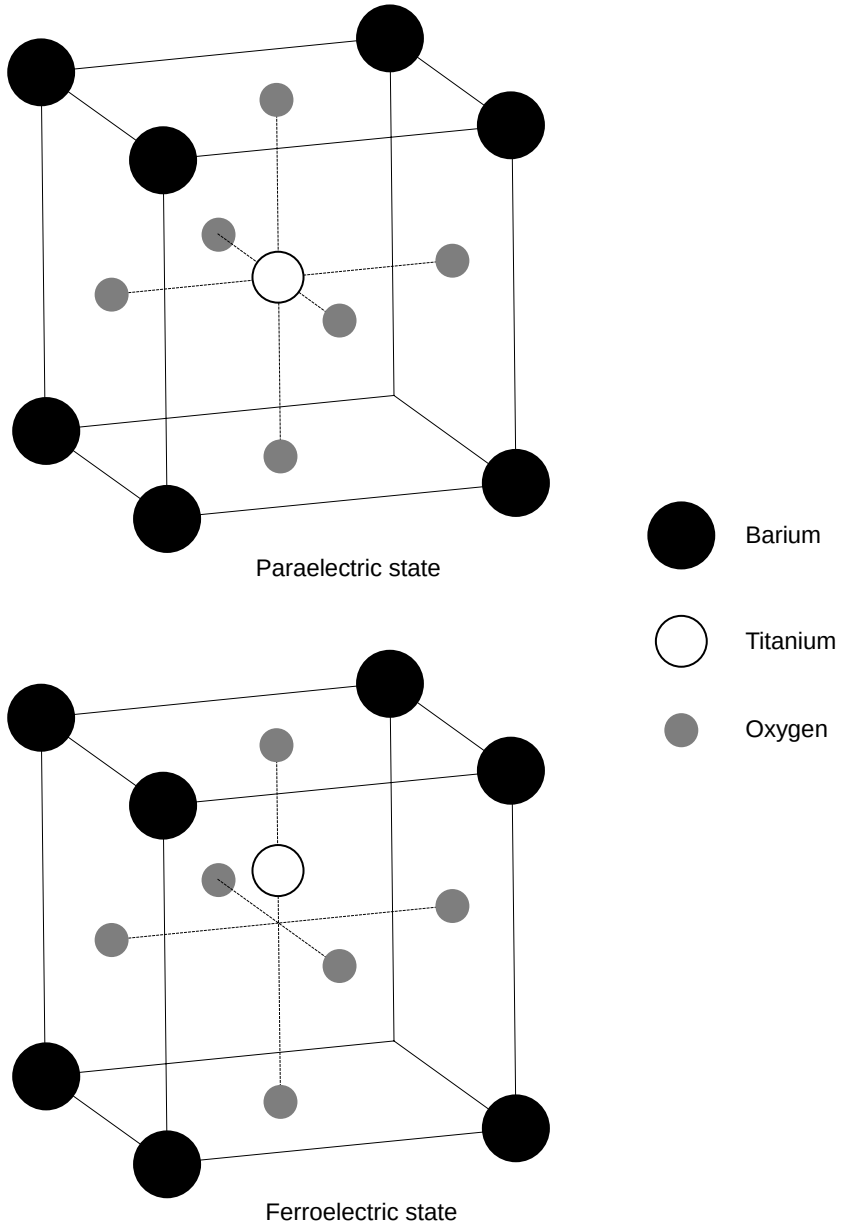


Figure 6.1 A diagram illustrating the simplified crystal structure of the $BaTiO_3$ unit cell in paraelectric and ferroelectric states.

larger, although the loss difference at higher frequency had been reported to be not so significant [7].

Since the discovery of ferroelectricity in Rochelle salt, many other ferroelectric materials have been discovered, including $BaTiO_3$, $SrTiO_3$, $PbTiO_3$, $PbZrO_3$, $LiNbO_3$, $LiTaO_3$ and $KTaO_3$. $SrTiO_3$ is of particular interest because of its structure compatibility with HTS and its relatively low loss tangent. While pure crystalline $SrTiO_3$ is paraelectric at all temperature, ferroelectricity has been observed in ceramic, thin film, and doped $SrTiO_3$ samples. Barium doped $SrTiO_3$, i.e. $Ba_xSr_{1-x}TiO_3$ (BST) where x ranges from 0 to 1, is the most studied ferroelectric material for microwave applications. For BST, as x is increased from 0 to 1, the Curie temperature increases up to about 400 K, which is the Curie temperature for pure $BaTiO_3$. Thus the Curie temperature of BST can be tailored to suit the application temperature.

The complex permittivity of ferroelectric thin film, in addition to being very sensitive to composition variation, as in the case of doping, is also very sensitive to the variation in the structure quality of thin film. Ferroelectric thin film with identical composition but deposited under different deposition condition can have very different complex permittivity due to structural effects such as defects, mechanical stress, and interface and surface behaviors.

## 6.2 $Ba_{0.1}Sr_{0.9}TiO_3$ thin films

All the BST thin films presented in this dissertation were fabricated using the PLD technique. The BST thin films for HTS/ferroelectric tunable microwave devices were prepared using BST target with composition of x at 0.1, i.e. $Ba_{0.1}Sr_{0.9}TiO_3$ as the Curie temperature for this composition is about 77 K [6].

### 6.2.1 Preparation of $Ba_{0.1}Sr_{0.9}TiO_3$ target

The targets used in PLD are usually prepared using the solid-state reaction method. While a single-crystal target is better, as a high-density target reduces the particulates in the resulting thin film, single-crystal form of multi-components targets such as $Ba_{0.1}Sr_{0.9}TiO_3$ are usually not readily available or easily prepared. As such, solid-state reaction is the most commonly used synthesis method for preparing multi-components targets. The advantages of the solid-state reaction include the ready availability of oxide precursors, low cost and the precise weighting of the reaction components.

Solid-state target preparation of oxide target involves the repeated grinding, compaction, and sintering of the component oxides until a single-phase material is achieved. A common variation of this technique is the use of carbonates or oxalates as precursors for the oxides. Upon the first calcining, the precursors decompose into ultra fine grain oxide powders. The high reactivity of these powders helps the solid-state reaction process in the following sintering.

As the solid-state reaction method depends on the inter-diffusion between the oxide powders, it is necessary to use fine, well-compacted powders and to sinter them at a temperature high enough for the diffusion length to exceed the particle size.

The $Ba_{0.1}Sr_{0.9}TiO_3$ targets were prepared using solid-state reaction of $BaTiO_3$ and $SrTiO_3$ powders with particle size of less than 2 micron and purity greater than 99.99 %. The $BaTiO_3$ and $SrTiO_3$ powders with the composition molar ratio of 1:9 were mixed evenly together by ball milling. The mixed powder was then heated at 1250 °C for 24 hours. The fired sample was ball milled again and the resulting powder

is cold pressed into a disc shape target with a pressure of about 3000 kg/cm$^2$ using a hydraulic press.

The disc was then sintered in atmospheric environment with the following heating profile:

- Heat from room temperature to 650 °C at 100 °C/hour, then maintain at 650 °C for 6 hours.
- Heat from 650 °C to 1425 °C at 100 °C/hour, then maintain at 1425 °C for 24 hours.
- Cool from 1425 °C to 650 °C at 100 °C/hour, then maintain at 650 °C for 6 hours.
- Cool from 650 °C to room temperature at 100 °C/hour.

### 6.2.2 Preparation of $Ba_{0.1}Sr_{0.9}TiO_3$ thin films

The PLD deposition parameters used for the preparation of the $Ba_{0.1}Sr_{0.9}TiO_3$ thin films were: laser energy of 250 mJ with energy density at 2 J/cm$^2$, distance between the target and substrate at 3.5 cm, and ambient oxygen partial pressure of 0.2 mbar during the deposition. The $Ba_{0.1}Sr_{0.9}TiO_3$ thin films were deposited on <100> surface-oriented single-crystal LAO substrates attached to resistive heater with silver paste. Single side polished LAO substrates were used for preparing samples used solely for characterization purpose. When preparing samples for making microstrip devices, double side polished LAO substrates were used.

To obtain the optimal growth conditions, the samples were prepared with substrate temperature at 720 °C, 770 °C and 790 °C during deposition. The films were grown using laser pulse repetition rate of 3 or 4 Hz for about 45 minutes, to obtained thin film with thickness of about 350 to 400 nm. After deposition, the ferroelectric films were annealed *in-situ* with oxygen partial pressure of 0.2 mbar and

1 bar, and at substrate temperature of 700 °C for 30 to 60 minutes, and allowed to cool down to room temperature over a period of 40 minutes.

### 6.2.3 Crystallinity of the $Ba_{0.1}Sr_{0.9}TiO_3$ thin films

XRD studies of the $Ba_{0.1}Sr_{0.9}TiO_3$ thin films revealed that all the films obtained were *c*-axis oriented without significant impurity phase or disorientation, however the films grown under different conditions have different lattice constant and degree of crystallinity. As can seen from figure 6.2, the film grown at 770 ºC had the lowest FWHM for the (002) peak, implying the highest crystallinity, while those grown at a higher or lower temperature showed wider peaks. The films annealed at oxygen pressure of 1 bar exhibited higher FWHM as compared with those annealed at 0.2 mbar. Furthermore the FWHM for the films annealed at 0.2 mbar had less variation with the substrate temperature during deposition. Therefore it was apparent that *in-situ* annealing the films with 1 bar oxygen partial pressure disrupted the formation of good lattice structure.

There was a high possibility that oxygen vacancies existed in the as-deposited $Ba_{0.1}Sr_{0.9}TiO_3$ films, and annealing was necessary. For undoped STO crystal, the lattice parameter is 3.90 Å, which was indicated in figure 6.2 by a dashed line. For $Ba_{0.1}Sr_{0.9}TiO_3$, the lattice parameter should be slightly higher. XRD of the prepared samples showed that the lattice parameters for films annealed in 1 bar oxygen are all below this value, which indicates there were A-site or B-site vacancies in the lattice.

Based on the above results, the $Ba_{0.1}Sr_{0.9}TiO_3$ films were prepared at deposition temperature of 780 ºC. After deposition, the films were annealed *in-situ* with oxygen partial pressure of 25 mbar for 1, 2, 3 and 4 hours. The lattice parameters for the four

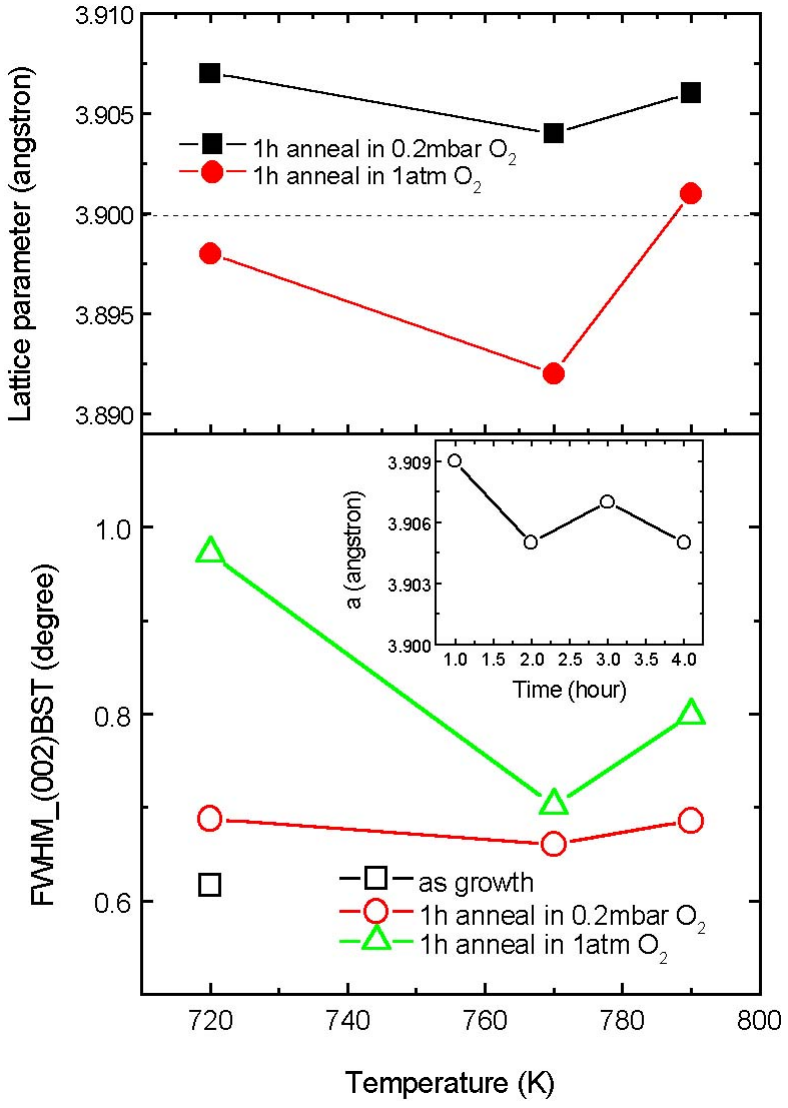


Figure 6.2 Top panel: Lattice parameter of $Ba_{0.1}Sr_{0.9}TiO_3$ films grown at different substrate temperatures. Bottom panel: The FHWM of the (002) XRD peak for $Ba_{0.1}Sr_{0.9}TiO_3$ grown at three different temperatures, with and without annealing at different oxygen pressures. Inset is the lattice parameters for films grown at 780 °C and annealed in an oxygen pressure of 25 mbar for 1 to 4 hours.

samples are shown in the inset of figure 6.2. It was observed that with the increase in annealing time, the lattice parameter tends to 3.904 Å. At the same time, the FWHM of its (002) peak increased with annealing time, reaching 1.1° after 3 hours annealing. This experiment suggested that the *in-situ* annealing at a temperature around 780 ºC can compensate the oxygen deficiency in the films, but did not improve the crystallinity of the thin films.

### 6.2.4 Surface morphology of the $Ba_{0.1}Sr_{0.9}TiO_3$ thin films

To grow high quality YBCO thin films on the BST films, the surface of the BST film should be smooth on nanometer scale. Therefore the BST films were also characterized using AFM and the images are shown in figure 6.3. All the films were relatively free of droplets, with very smooth and homogeneous surface, especially at higher deposition and annealing temperatures. The rms surface roughness was within 5 nm. For samples annealed at oxygen partial pressure of 1 bar, the grain size and shape were clear. The films grown at 720 ºC showed sphere-like grains, while the films grown at 770 ºC consist of short rods aligned along a and b directions of the substrate, which suggested the films had good in-plane orientation. The films grown at 790 ºC also showed very clear in-plane alignment. It was obvious that with increase of the substrate temperature during the deposition, the grain size was increased. No clear grains could be observed when the annealing oxygen partial pressure was reduced to 0.2 mbar.

### 6.2.5 Microwave permittivity characterization of $Ba_{0.1}Sr_{0.9}TiO_3$ thin films

The measurement method used to characterize the complex permittivity of the ferroelectric thin film samples is described in chapter 7. The variation of dielectric

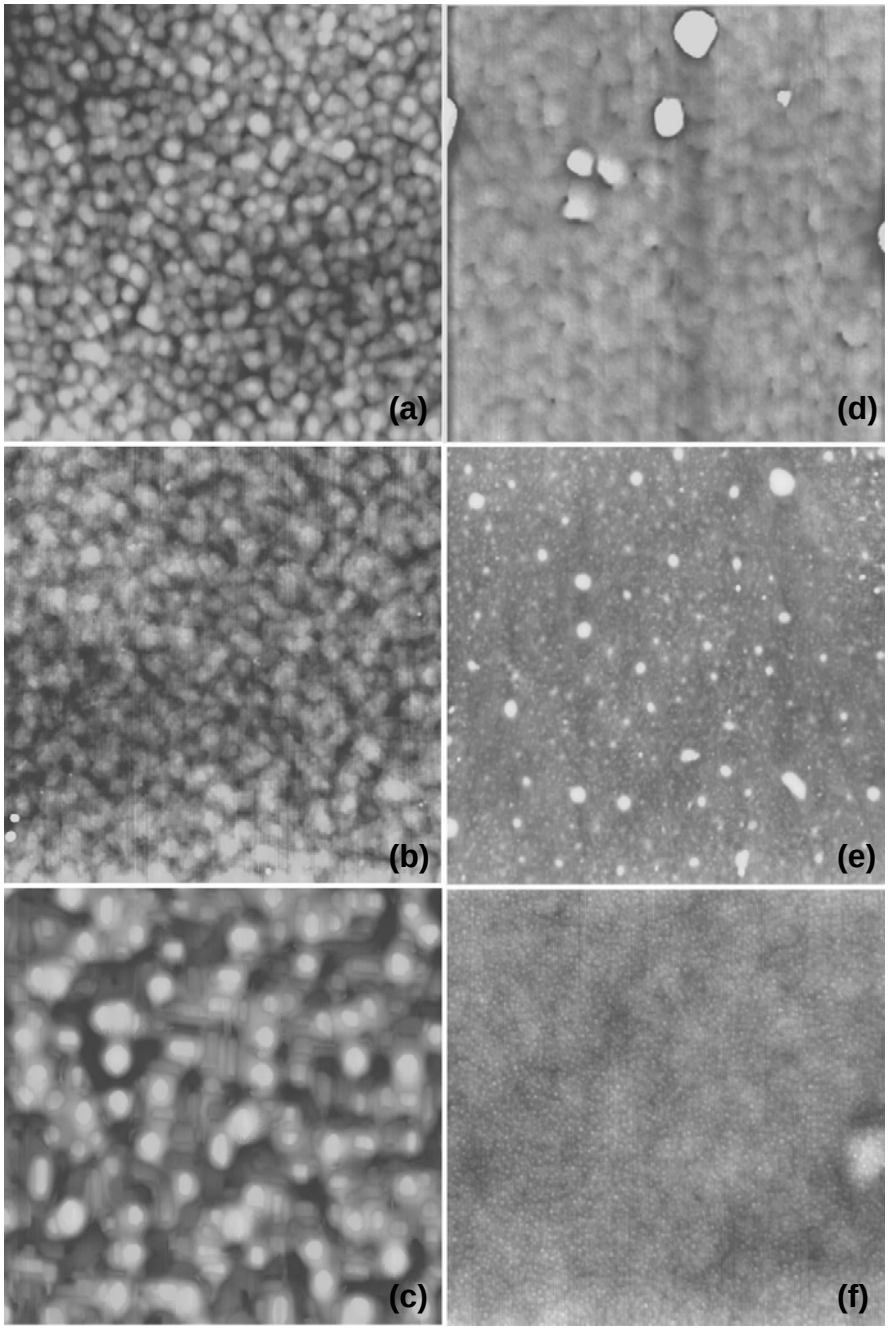


Figure 6.3 AFM images of the BST films with scan area of 2 μm × 2 μm. (a), (b) and (c) are images of films grown at 720, 770 and 790 °C respectively and annealed *in-situ* for 1 hour in 1 bar $O_2$. (d), (e) and (f) are images of films grown at 720, 770 and 790 °C respectively and annealed in-situ for 1 hour in 0.2 mbar $O_2$.

constant with temperature for the $Ba_{0.1}Sr_{0.9}TiO_3$ thin film grown with substrate temperature at 770 ºC is shown in figure 6.4. Figure 6.5 showed the variation of the dielectric constant with the applied electric field at measurement temperature of 75 K. The dielectric constant tunability was about 12 % for an applied electric field of 800 V/mm.

## 6.3 Epitaxial YBCO/BST/LAO/YBCO thin film multilayer

To prepare the YBCO/BST/LAO/YBCO thin film multilayer, YBCO thin films were deposited by PLD on both sides of the LAO substrate: the side with the $Ba_{0.1}Sr_{0.9}TiO_3$ ferroelectric film and the plain LAO side, using a silicon radiation heater. Prior to deposition, the silver residue on the substrate from the ferroelectric thin film deposition was removed by immersing the substrate in 20 % nitric acid ultrasonic bath for 30 minutes. The deposition conditions for YBCO thin films were: oxygen partial pressure of 0.2 mbar, laser pulse frequency of 5 Hz, per pulse laser energy of 250 mJ with energy density of 2.5 mJ, substrate temperature of 760 °C and deposition duration of 30 minutes.

After deposition, the films are cooled to 580 °C and annealed *in-situ* for 30 minutes with oxygen partial pressure of 1 bar. The prepared YBCO films had a thickness of around 500 nm. Figure 6.6 showed the $\theta - 2\theta$ XRD scan of the YBCO/BST/LAO trilayer. The $\theta - 2\theta$ scan indicated no significant presence of impurities or unwanted phases and that the thin films were well oriented.

Initial samples were prepared with the YBCO first deposited on the ferroelectric side, before flipping the substrate over to deposit the second YBCO layer. However, measurement of surface resistance indicated that the surface resistance of the YBCO deposited on the ferroelectric side grown this way was unsatisfactory ( $R_s$ > 1 mΩ).

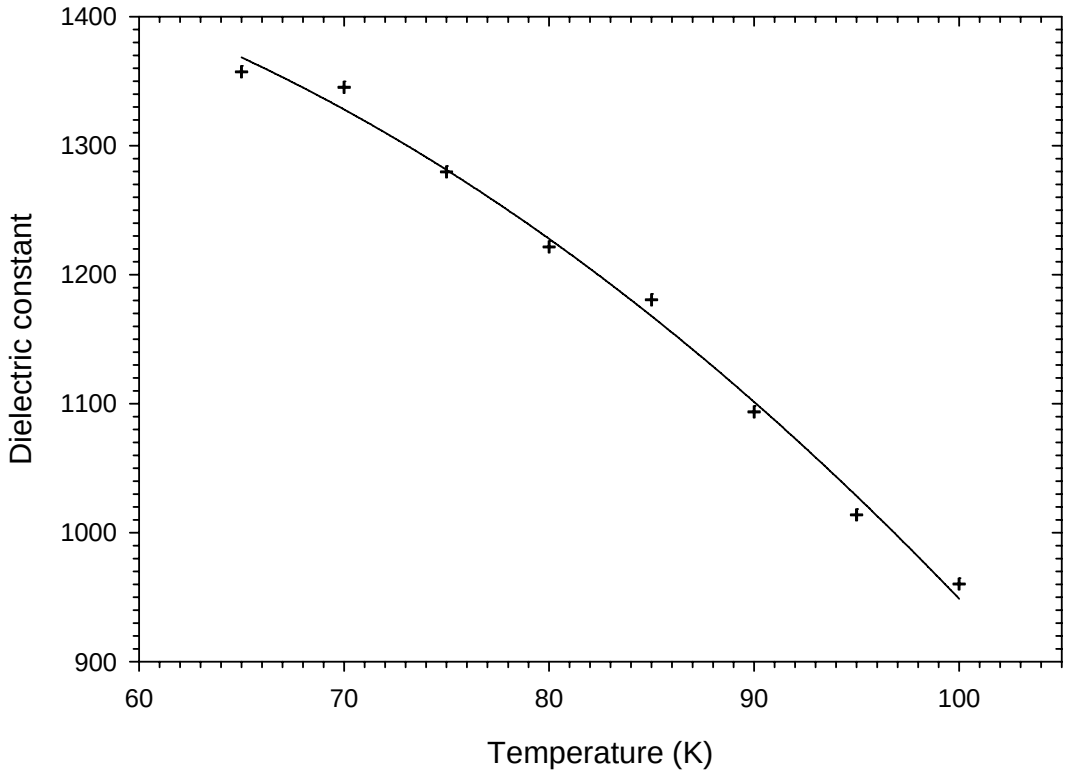


Figure 6.4 The variation of dielectric constant with temperature for $Ba_{0.1}Sr_{0.9}TiO_3$ thin film grown with substrate temperature at 770 ºC.

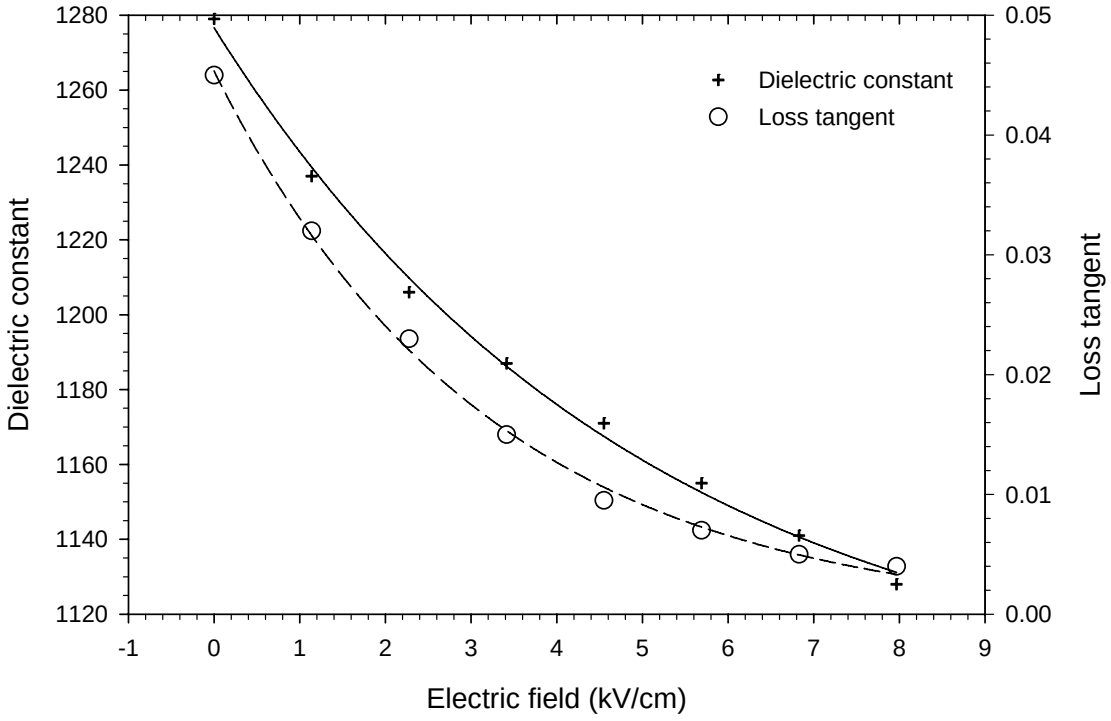


Figure 6.5 The variation of dielectric constant and loss tangent with electric field for $Ba_{0.1}Sr_{0.9}TiO_3$ thin film grown with substrate temperature at 770 ºC.

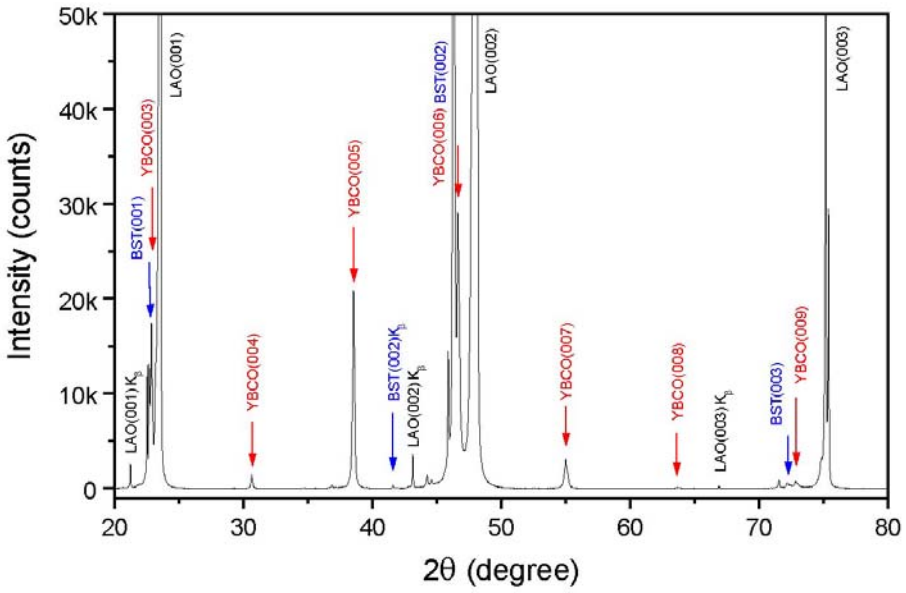


Figure 6.6 The $\theta - 2\theta$ XRD scan of the YBCO/BST/LAO multilayer thin films.

This was probably due to the diffusion/reaction between the $Ba_{0.1}Sr_{0.9}TiO_3$ and YBCO thin films when the second side YBCO was deposited. This diffusion/reaction occurred as the silicon heater had a very high temperature gradient, which made the side closer to the heater at a much higher temperature than the side where YBCO was being deposited.

A way to overcome this problem was to deposit YBCO thin film on the side without the ferroelectric thin film layer first. By depositing the YBCO in this manner, the substrate side with the YBCO/BST thin film multilayer would not be exposure to excessively high temperature. Surface resistance of YBCO thin films deposited in this manner was measured to be between 0.3 mΩ to 0.7 mΩ for the ferroelectric side and 0.4 mΩ to 0.7 mΩ for YBCO thin films grown on the LAO side.

References

[1] J. Valasek, "Piezo-Electric and Allied Phenomena in Rochelle Salt", *Physical Review*, vol. 17, no. 4, pp. 475-481, 1921.

[2] G. Rupprecht and R. O. Bell, "Microwave Losses in Strontium Titanate above the Phase Transition", *Physical Review*, vol. 125, no. 6, pp. 1915-1920, 1962.

[3] S. N. Das, "Quality of a Ferroelectric Material", *IEEE Transactions on Microwave Theory and Techniques*, vol. 12, no. 4, pp. 440-445, 1964.

[4] A. K. Tagantsev, V. O. Sherman, K. F. Astafiev, J. Venkatesh, and N. Setter, "Ferroelectric materials for microwave tunable applications", *Journal of Electroceramics*, vol. 11, no. 1-2, pp. 5-66, 2003.

[5] F. A. Miranda, G. Subramanyam, F. W. Van Keuls, R. R. Romanofsky, J. D. Warner, and C. H. Mueller, "Design and development of ferroelectric tunable microwave components for Ku- and K-band satellite communication systems", *IEEE Transactions on Microwave Theory and Techniques*, vol. 48, no. 7, pp. 1181-1189, 2000.

[6] M. J. Lancaster, J. Powell, and A. Porch, "Thin-film ferroelectric microwave devices", *Superconductor Science & Technology*, vol. 11, no. 11, pp. 1323-1334, 1998.

[7] S. S. Gevorgian and E. L. Kollberg, "Do We Really Need Ferroelectrics in Paraelectric Phase Only in Electrically Controlled Microwave Devices", *IEEE Transactions on Microwave Theory and Techniques*, vol. 49, no. 11, pp. 2117-2124, 2001.

# CHAPTER 7:
# NONDESTRUCTIVE COMPLEX PERMITTIVITY CHARACTERIZATION OF FERROELECTRIC THIN FILMS AT MICROWAVE FREQUENCY

The development of planar ferroelectric microwave devices requires accurate knowledge of the dielectric properties, i.e. dielectric constant ($\varepsilon_r$) and loss tangent ($\tan\delta$) of the ferroelectric thin films, which are electric field, temperature and frequency dependent. This chapter presents a non-destructive method developed for the dielectric properties measurement of ferroelectric thin film at microwave frequency using a planar circuit method consisting of microstrip dual-resonator [1].

## 7.1 Planar circuit characterization methods for complex permittivity of ferroelectric thin films at microwave frequencies

Many efforts have been made in the characterization of the dielectric properties of ferroelectric thin films at microwave frequencies, and the methods developed generally fall into planar-circuit methods such as in [2-4] and near-field scanning microwave microscope methods such as in [5-7].

In the planar circuit method, the ferroelectric thin film under test is usually fabricated into a planar device, and the dielectric properties of the thin film are derived from the device properties. The planar circuit methods can be generally classified into transmission line methods, resonator methods, and capacitor methods. In a transmission line method, the thin film sample is usually fabricated into a coplanar waveguide. The $\varepsilon_r$ and $\tan\delta$ of the thin film are derived from the phase and amplitude of the transmission coefficient of the coplanar waveguide. Two approaches are often used to apply the dc bias voltages. One approach is to apply the bias voltage

across the two ground planes of the coplanar circuit [8]. In this approach, the two ground planes are dc isolated from each other. The disadvantage of this approach is that it is difficult to achieve good grounding for the transmission line. Another approach is to apply the bias voltage to the signal trace of the coplanar waveguide. In this case, bias tees are often used to isolate the microwave instruments and the dc bias voltage source. The advantages of coplanar waveguide method are that it only requires one layer of metallization and its wide measurement frequency range; however its accuracy and sensitivity are usually not very high.

In the resonator method, the ferroelectric thin film under study is usually fabricated into a coplanar resonator. The $\varepsilon_r$ and $\tan\delta$ of the ferroelectric film are deduced from the resonant frequency and Q factor of the coplanar resonator. The bias voltage can be directly applied to the resonator through the electric field node of the resonator or/and an rf choke. Resonator methods usually have higher accuracy and sensitivity, but measurements can only be conducted for a single or several discrete frequencies, i.e. at the fundamental and harmonic resonant frequencies.

In the capacitor method, the ferroelectric thin film is fabricated into a planar capacitor, and the $\varepsilon_r$ and $\tan\delta$ of the thin film are derived from the capacitance and Q factor of the capacitor. The capacitance and Q factor of a capacitor at rf and microwave frequencies are often measured by integrating the capacitor into a transmission line or a resonant structure. If the capacitor is integrated into a transmission line, the capacitance and Q factor of the capacitor can be derived from the phase and amplitude of the transmission coefficient through the transmission line. If the capacitor is integrated into a resonant structure, the capacitance and Q factor of the capacitor can be deduced from the resonant frequency and Q factor of the resonant

structure. The dc bias voltage is often applied between the two electrodes of the capacitor.

The planar circuit methods are usually destructive in the sense that metallization has to be coated on the ferroelectric thin film. Having a non-destructive testing method is desirable for device fabrication as it allows the confirmation of the thin film properties before committing the resources to fabricate it into a device.

## 7.2 Principle of measurement

The microstrip dual-resonator fixture presented here consists mainly of two identical half-wavelength resonators with the same fundamental resonant frequency as shown in figure 7.1. The resonant frequency of each of the planar half-wavelength resonator can be calculated using equation (4.40).

When two resonators with the same fundamental resonant frequency are coupled together, the resonance will degenerate into two resonant frequencies, $f_1$ and $f_2$. The difference between $f_1$ and $f_2$ is related to the coupling between the two resonators. In the setup presented here, a gap separating the two resonators was used to provide the capacitive inter-resonator coupling, and change in the capacitance of the gap will cause a corresponding change in $f_1$ and $f_2$.

Figure 7.2 shows the current distribution of the microstrip dual-resonator structure. Here $f_1$ is assigned to the lower resonant frequency. At the resonant frequency $f_1$, the current in the two resonators flows in the same direction, whereas at frequency $f_2$, the current in the two resonators flows in the opposite direction. As the current density is higher near the gap at frequency $f_1$, $f_1$ has a longer wavelength and is more sensitive to change in the capacitance of the gap. The ferroelectric thin film

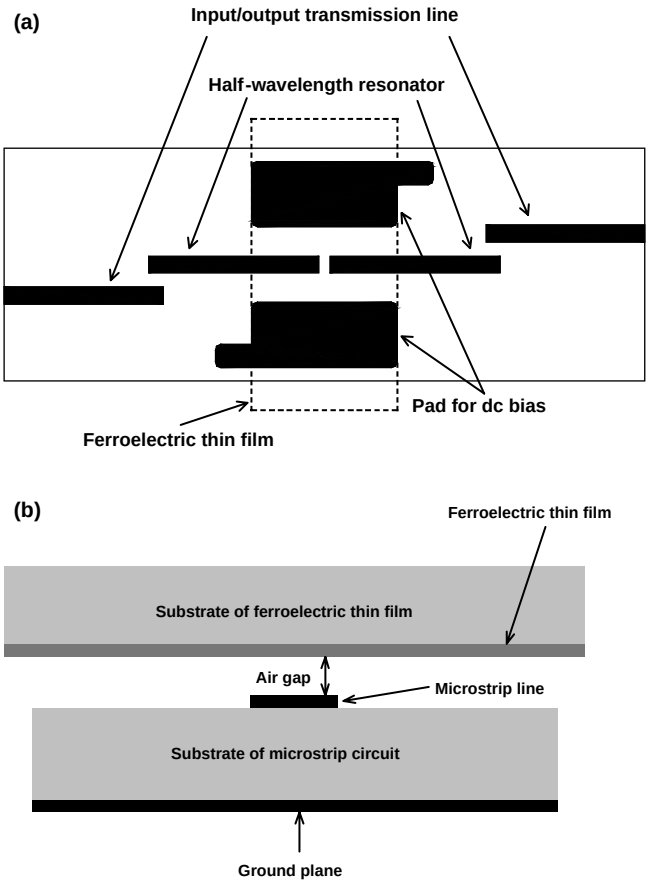


Figure 7.1 Schematic diagram of the microstrip dual-resonator measurement fixture. (a) Top view. (b) Cross sectional view.

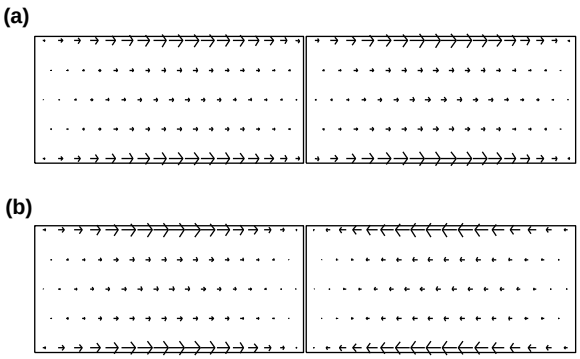


Figure 7.2 Current distribution of the microstrip dual-resonator at (a) the lower resonant frequency $f_1$ and (b) the higher resonant frequency $f_2$.

sample was placed over the gap between the two resonators, thus changing the capacitance of the gap and the inter-resonator coupling. The capacitance of the gap can be calculated from $f_1$ and $f_2$ using

$$C = -\frac{\tan(\pi f_1 / f_2)}{4\pi f_1 Z_0}, \tag{7.1}$$

where $Z_0$ is the characteristic impedance of the microstrip line [2,3].

The Q factor due to the loss in the capacitor ($Q_c$) is given by

$$\frac{1}{Q_c} = \frac{1}{Q_1} - \frac{1}{Q_2}, \tag{7.2}$$

where $Q_1$ and $Q_2$ are the quality factors corresponding to $f_1$ and $f_2$ respectively. For a planar ferroelectric capacitor, the $\tan\delta$ of the ferroelectric thin film can be calculated using [2]

$$\tan\delta = \frac{1}{\xi}\left(\frac{1}{Q_1} - \frac{1}{Q_2}\right), \tag{7.3}$$

where

$$\xi = \frac{2}{1 - 2\varphi / \sin 2\varphi}, \tag{7.4}$$

and

$$\varphi = \pi \frac{f_1}{f_2}. \tag{7.5}$$

The above equations are based on the assumption that the dielectric properties of the ferroelectric thin film under test remain constant over the frequency range of $f_1$ and $f_2$.

Using equations (7.1) to (7.5), the capacitance of the gap and $\tan\delta$ of the ferroelectric thin film can be derived from the experimentally measured resonant frequencies $f_1$ and $f_2$, and their quality factors $Q_1$ and $Q_2$. The conclusion obtained above could be extended to higher-order harmonic resonant frequencies, but it is generally more difficult to distinguish the higher-order degenerate frequencies. To accurately characterize samples over a wide frequency range, fixtures with different fundamental frequency are usually required.

Although it is possible to find the $\varepsilon_r$ of ferroelectric thin film from the capacitance of the gap, a more direct and accurate approach of using full-wave electromagnetic simulation, which takes into account the distributive nature of the capacitive gap at microwave frequency, was used here to determine the relationship between $f_1$ and $\varepsilon_r$ of the ferroelectric thin film.

### 7.3 Determination of dielectric constant

Other than the structure and dimension of the microstrip dual-resonator circuit, the resonant frequency $f_1$ is also affected by the $\varepsilon_r$ and dimension (especially the thickness) of the ferroelectric thin film, as well as the air gap, arising from the unevenness of the microstrip circuit surface, between the microstrip circuit and ferroelectric thin film.

To ensure the measurement repeatability and reliability, it is necessary to ensure that the height of this air gap does not change significantly with different sample loading. It was found that by using a piece of suitable elastic spacer placed between the sample and the lid of the casing to press the sample towards the microstrip dual-resonator circuit, good measurement repeatability can be achieved.

The thickness of the air gap between the sample and the microstrip circuit was determined using a LAO substrate without ferroelectric film as a calibration sample. As $\varepsilon_r$ of LAO is known, the thickness of the air gap can be found by comparing the resonant frequency of the measured results with simulation results, in which the air gaps were varied. This method is based on the following two assumptions which are usually satisfied. First, for different samples, the air gaps between the microstrip circuit and the thin films are the same. Second, the air gaps for the substrates with and without the film are the same.

The loading of a LAO substrate into the measurement fixture was repeated for ten times, to estimate the uncertainty and repeatability of the air gap thickness. It was found that the uncertainty of the measured resonant frequencies was within 2 MHz.

The full-wave electromagnetic simulation software, IE3D[1] (Version 10) was used for the design and simulation of the dual-resonator circuit. From the simulations, it was found that the maximum thickness of the air gap, corresponding to the minimum resonant frequency, was 1.05 μm, and the minimum thickness of the air gap, corresponding to the maximum resonant frequency was 1.00 μm.

After obtaining the value and uncertainty of the air gap between the ferroelectric thin film and the microstrip circuit, a series of simulations was carried out to obtain the relationship between $f_1$ and $\varepsilon_r$ of the ferroelectric thin film. Figure 7.3 shows the simulated $f_1$ and $\varepsilon_r$ curve for 500 nm thick ferroelectric thin film with air gaps of 1.000 μm, 1.025 μm, and 1.050 μm. $f_1$ is also dependent on the thickness of the ferroelectric thin film, as can be observed in the simulated $f_1$ and $\varepsilon_r$ curve for 300 nm, 500 nm, and 1000 nm thick ferroelectric thin films with air gap of 1.025 μm shown in

[1] Zeland Software Inc., Califonia, USA

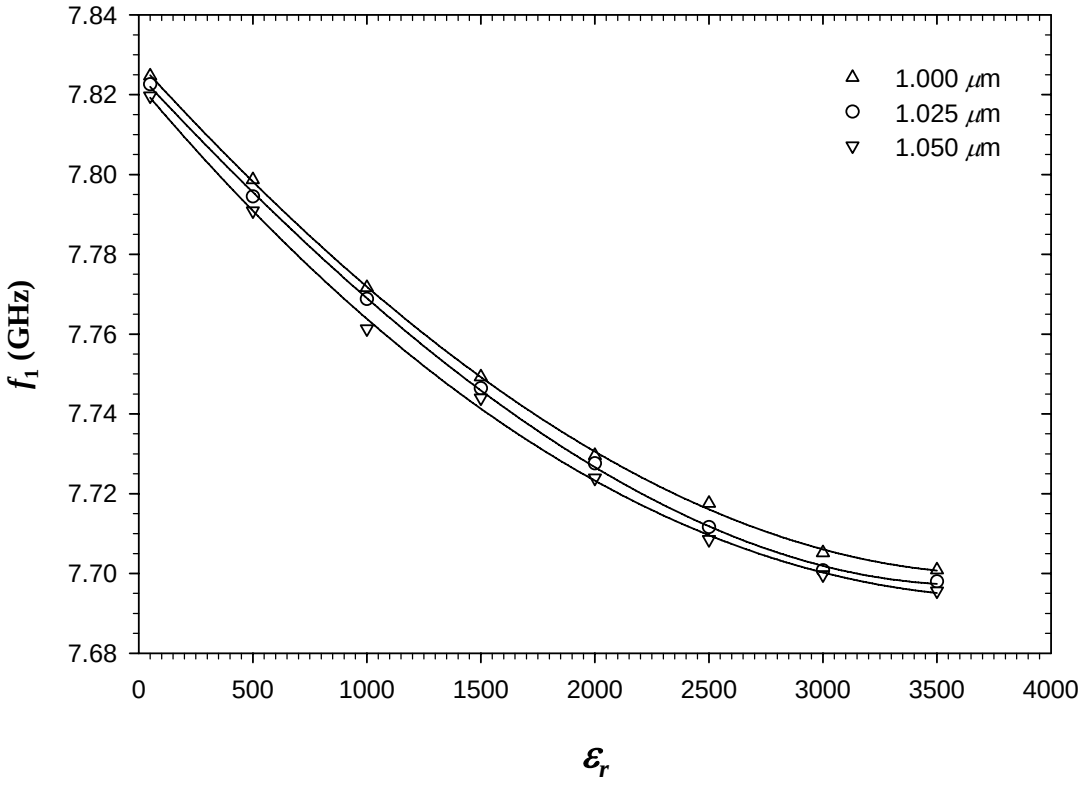


Figure 7.3 The simulated $f_1$ and $\varepsilon_r$ curve for 500 nm thick ferroelectric thin film with air gap of 1.000 μm, 1.025 μm, and 1.050 μm.

figure 7.4.

The $\varepsilon_r$ and dimension of the substrate on which the ferroelectric thin film is deposited can also affect $f_1$, and it is important that the correct values of these parameters were used in the simulations. For the simulations, the $\varepsilon_r$ of the substrate was set as 23.8 and had dimension of 5 mm × 10 mm × 0.5 mm, corresponding to the LAO substrates used for depositing the ferroelectric thin films.

## 7.4 Design and fabrication of the measurement fixture

In addition to the two half-wavelength resonators, the microstrip dual-resonator measurement fixture also have two sections of microstrip transmission lines used to provide the parallel non-contact input/output coupling to the microstrip resonators, and two electrode pads for applying dc bias voltage across the ferroelectric thin film.

The substrate used for the microstrip circuit is TMM10i[2]. The TMM10i substrate has a thickness of 0.635 mm, $\varepsilon_r$ of 9.8 and $\tan\delta$ of 0.0016 at 10 GHz. The substrate is coated on both sides with 17.5 μm thick electrodeposited copper, with conductivity of $5.5 \times 10^7$ S/m.

The resonators and input/output microstrip lines are 0.58 mm wide to obtain 50 Ω characteristic impedance. Each resonator has a length of about 5 mm, with 36 μm gap separating the two resonators.

The two electrode pads used for applying dc bias voltage across the ferroelectric thin film were placed far apart from the two resonators to minimize their effects on the resonance of the dual-resonator. An advantage of placing the pads far apart was that the electric field was more uniform across the area near the gap of the dual- resonator;

[2] Rogers Corporation, Connecticut, USA

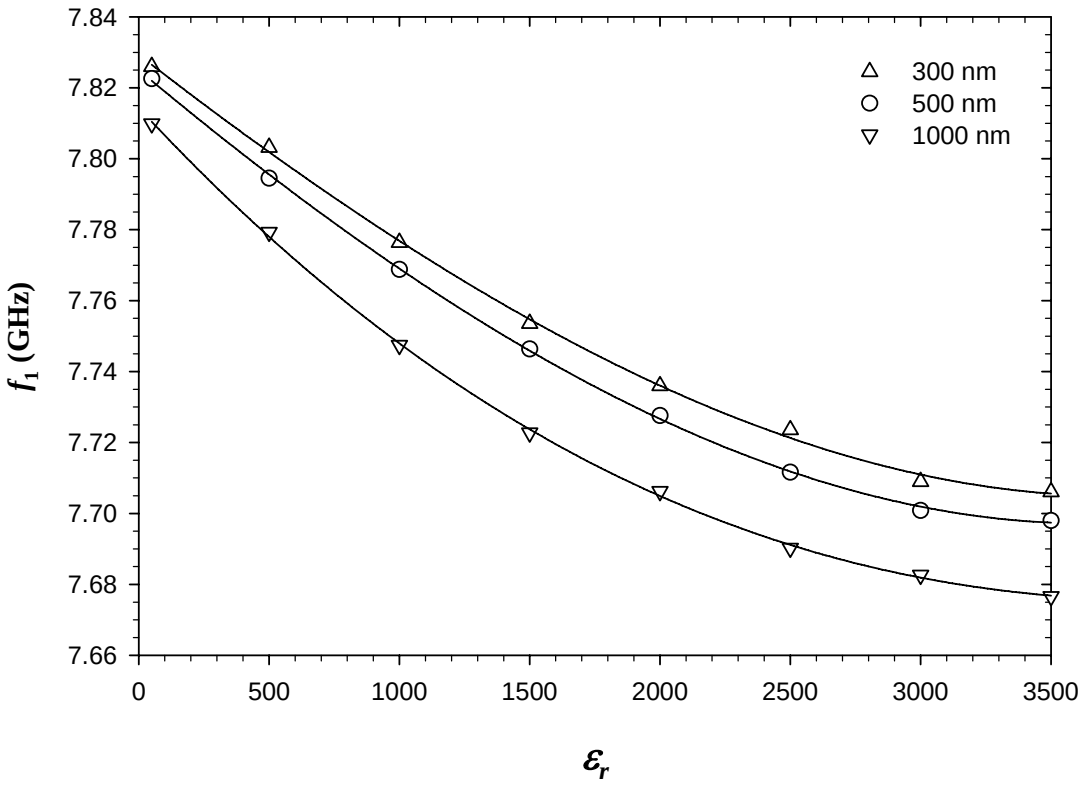


Figure 7.4 The simulated $f_1$ and $\varepsilon_r$ curve for 300 nm, 500 nm, and 1000 nm thick ferroelectric thin film with air gap of 1.025 μm.

however a higher voltage was required to obtain the required electric field. Simulations indicated that the distance of 2.6 mm between the two electrode pads used in the present design ensured the two electrode pads had negligible effects on the resonance of the dual-resonator.

The microstrip dual-resonator circuit was patterned using conventional photolithography and wet chemical etching. The circuit was packaged in a brass casing with the ground plane of the circuit directly soldered to the casing. SMA launchers with hermetic drop-in glass seal were used for the rf and dc input/output. A photograph of the fixture is shown in figure 7.5. For measurement at low temperature, after loading the ferroelectric thin film, the brass casing was hermetically sealed in a helium environment with relative humidity at less than 1 % to prevent water condensation from affecting measurement.

## 7.5 Results and discussions

The measurement method was applied on a piece of $Ba_{0.5}Sr_{0.5}TiO_3$ thin film deposited by pulsed laser deposition on a polished LAO substrate with <100> surface orientation and dimension of 5 mm × 10 mm × 0.5 mm. XRD measurement indicated that the $Ba_{0.5}Sr_{0.5}TiO_3$ thin film is *c*-axis orientated with lattice constant of about 3.950 Å. AFM measurement indicated the rms surface roughness of the film is about 1.4 nm with grain size of about 30 nm. The resonant frequencies and quality factors of the dual-resonator measurement were measured using a HP 8719C vector network analyzer[3].

The temperature dependence of the dielectric constant of the $Ba_{0.5}Sr_{0.5}TiO_3$ thin film is shown in figure 7.6 which indicates that the Curie temperature of the thin film

[3] Agilent Technologies, California, USA

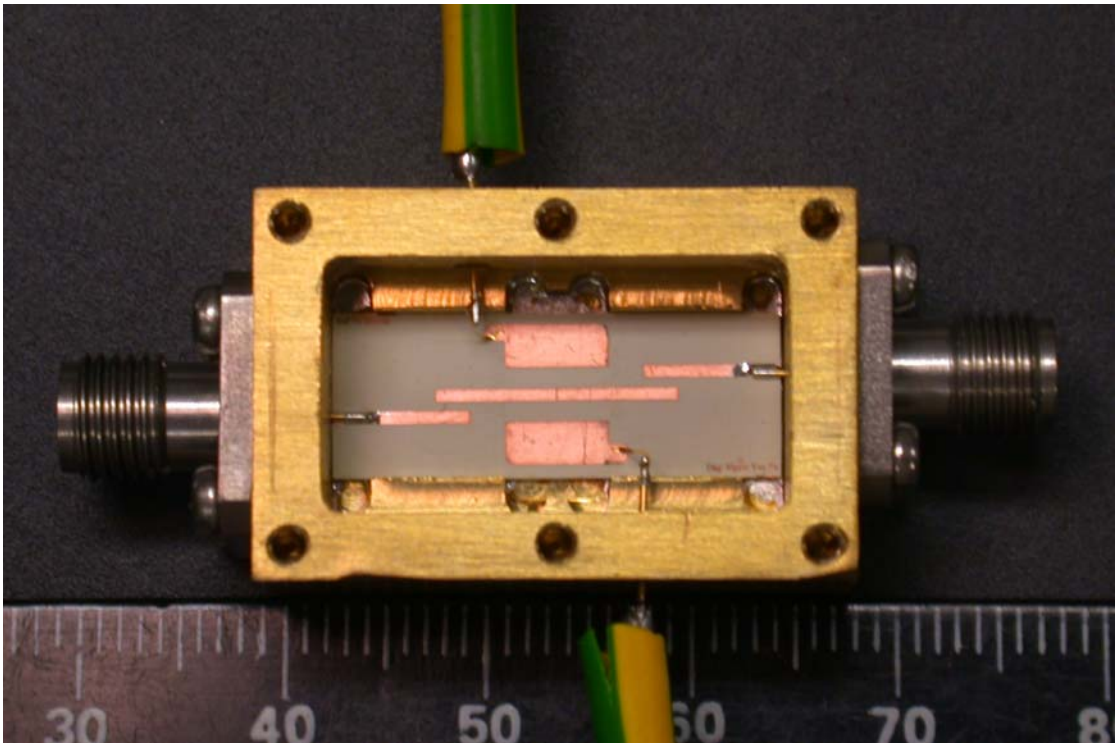


Figure 7.5 Photograph of the microstrip dual-resonator measurement fixture for complex permittivity of ferreoelectric thin film.

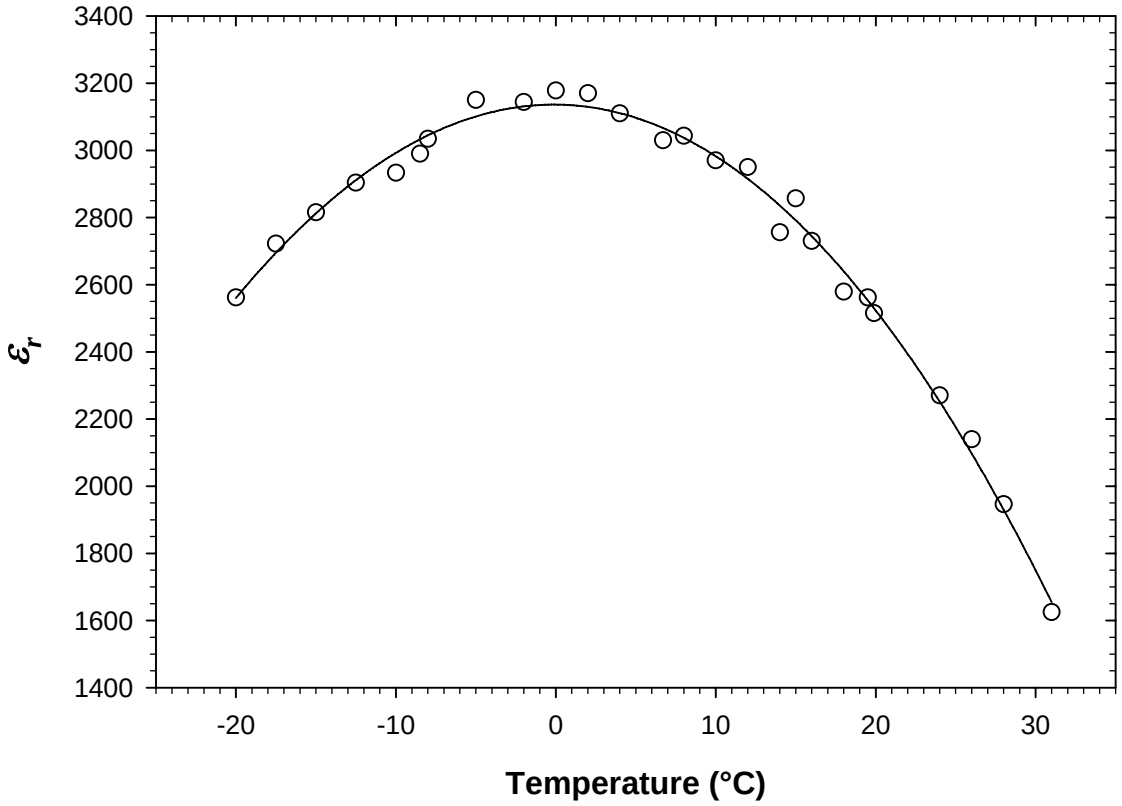


Figure 7.6 The measured variation of dielectric constant with temperature for $Ba_{0.5}Sr_{0.5}TiO_3$ thin film.

is about 0 °C. A Peltier-effect thermo-electric cooler (596-504[4]) was used to cool the fixture and a K-type thermocouple probe (707-6150[4]) was used to measure the temperature. Figure 7.7 shows the electric field dependence of the thin film measured at 30 °C. When 8 kV/cm electric field was applied, the $\varepsilon_r$ tunability of the thin film is about 20 %, with $\tan\delta$ decreasing from about 0.030 to 0.027. This method was also used to characterize $Ba_{0.5}Sr_{0.5}TiO_3$–$Bi_{1.5}Zn_{1.0}Nb_{1.5}O_7$ composite thin films [9] and $Al_2O_3$ doped $Ba_{0.5}Sr_{0.5}TiO_3$ thin films [10].

This method can be extended to the measurement of ferroelectric thin film with very low Curie temperature, which is used in the development of superconductor and ferroelectric hybrid microwave devices. At very low temperatures, for example liquid nitrogen temperature, most of the elastic spacer materials will lose their elasticity and shrink, which may results in an uncontrolled and large air gap between the ferroelectric thin film and the microstrip circuit. This problem could be solved by pressing the sample with a spring-loaded plunger [8]. A spring-loaded plunger fixture was used successfully to measure low-temperature-application $BaTi_4O_9$ doped $Ba_{0.1}Sr_{0.9}TiO_3$ thin films [11].

It should be noted that the air gap also affects the electric field applied to the sample. The total capacitance $C$ of the structure shown in figure 7.8 is given by:

$$\frac{1}{C}=\frac{1}{C_s}+\frac{1}{C_{g1}}+\frac{1}{C_{g2}}, \tag{7.6}$$

where $C_s$ is the capacitance due to the ferroelectric thin film, $C_{g1}$ and $C_{g2}$ are the equivalent capacitances due to the air gaps at the two electrodes. If the bias voltage

[4] Farnell Components Pte Ltd, Tai Seng Drive, Singapore

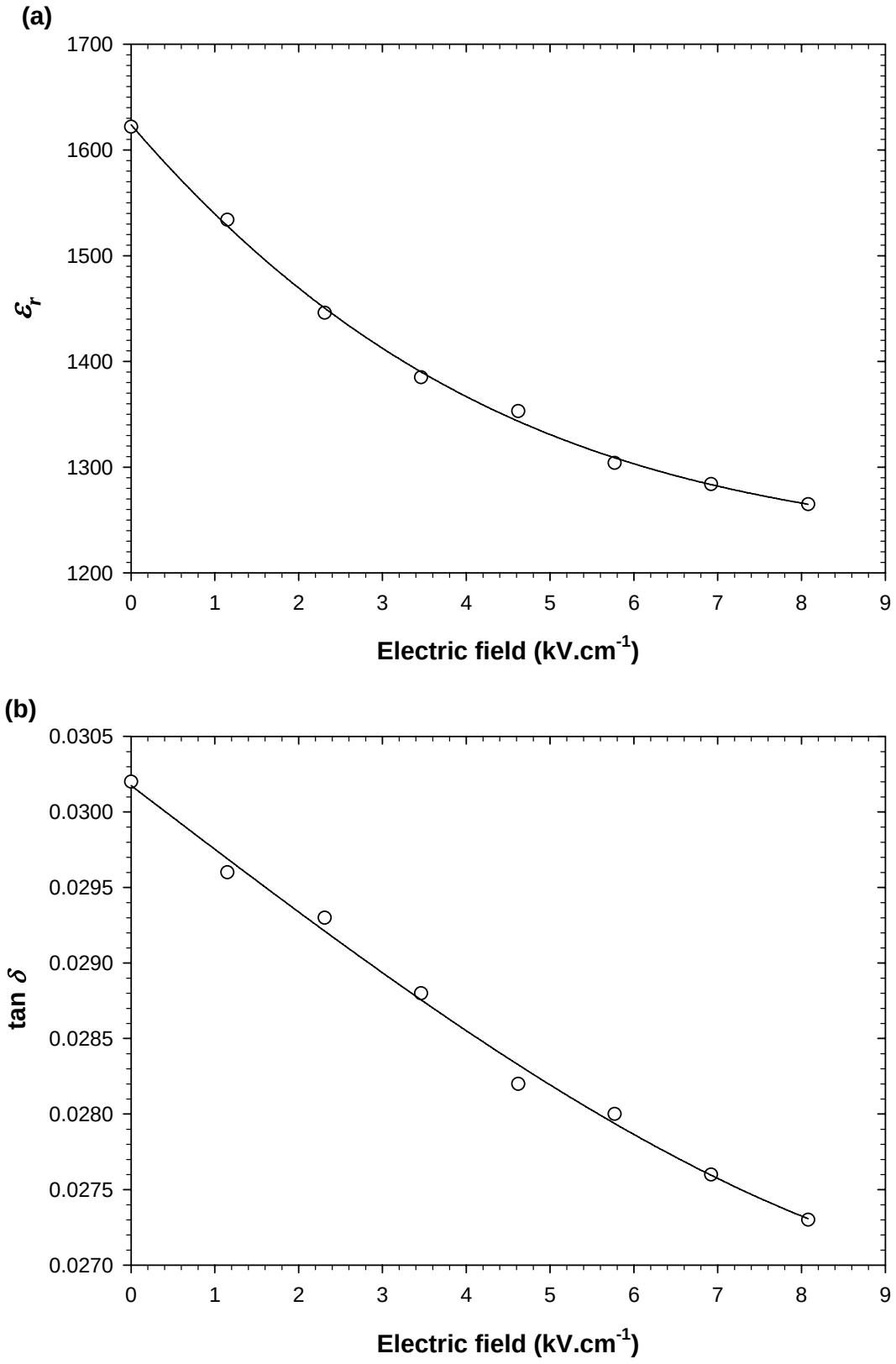


Figure 7.7 The measured electric field dependence of (a) dielectric constant and (b) loss tangent of $Ba_{0.5}Sr_{0.5}TiO_3$ thin film at 30 °C.

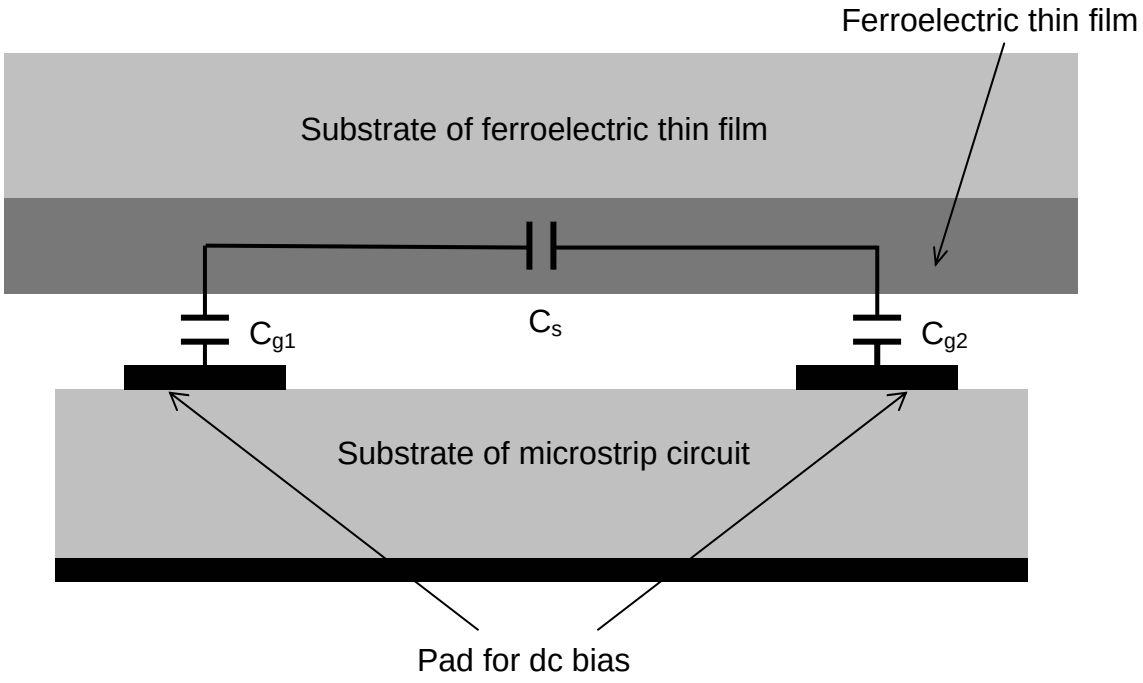


Figure 7.8 Equivalent circuit model of the capacitance between the two pads for dc bias.

applied to the two electrodes is $V$ , the actual voltage applied to the sample $V_s$ is given by:

$$V_s = \frac{V}{C_s}\left(\frac{1}{C_s}+\frac{1}{C_{g1}}+\frac{1}{C_{g2}}\right)^{-1}. \tag{7.7}$$

If there is no air gap, $C_{g1}$ and $C_{g2}$ become infinity, and from equation (7.7), we get $V_s = V$ . However, as the air gap is inevitable, $V_s$ is always less that $V$ . Therefore it is important to decrease the air gap, and that the tunability obtained from this method can be taken as a lower limit.

References


[1] C. Y. Tan, L. F. Chen, K. B. Chong, and C. K. Ong, "Nondestructive microwave permittivity characterization of ferroelectric thin film using microstrip dual resonator", *Review of Scientific Instruments*, vol. 75, no. 1, pp. 136-140, 2004.

[2] A. B. Kozyrev, O. I. Soldatenkov, T. B. Samoilova, A. V. Ivanov, C. H. Mueller, T. V. Rivkin, and G. A. Koepf, "Response time and power handling capability of tunable microwave devices using ferroelectric films", *Integrated Ferroelectrics*, vol. 22, no. 1-4, pp. 849-860, 1998.

[3] D. Galt, J. C. Price, J. A. Beall, and T. E. Harvey, "Ferroelectric Thin-Film Characterization Using Superconducting Microstrip Resonators", *IEEE Transactions on Applied Superconductivity*, vol. 5, no. 2, pp. 2575-2578, 1995.

[4] R. A. Chakalov, Z. G. Ivanov, Y. A. Boikov, P. Larsson, E. Carlsson, S. Gevorgian, and T. Claeson, "Fabrication and investigation of $YBa_2Cu_3O_{7-\delta}/Ba_{0.05}Sr_{0.95}TiO_3$ thin film structures for voltage tunable devices", *Physica C*, vol. 308, no. 3-4, pp. 279-288, 1998.

[5] D. E. Steinhauer, C. P. Vlahacos, F. C. Wellstood, S. M. Anlage, C. Canedy, R. Ramesh, A. Stanishevsky, and J. Melngailis, "Quantitative imaging of dielectric permittivity and tunability with a near-field scanning microwave microscope", *Review of Scientific Instruments*, vol. 71, no. 7, pp. 2751-2758, 2000.

[6] J. H. Lee, S. Hyun, and K. Char, "Quantitative analysis of scanning microwave microscopy on dielectric thin film by finite element calculation", *Review of Scientific Instruments*, vol. 72, no. 2, pp. 1425-1434, 2001.

[7] Y. Lu, T. Wei, F. Duewer, Y. Lu, N.-B. Ming, P. G. Schultz, and X.-D. Xiang, "Nondestructive Imaging of a Dielectric-Constant Profiles and Ferroelectric Domains with a Scanning-Tip Microwave Near-Field Microscope", *Science*, vol. 276, pp. 2004-2006, 1997.

[8] M. J. Lancaster, J. Powell, and A. Porch, "Thin-film ferroelectric microwave devices", *Superconductor Science & Technology*, vol. 11, no. 11, pp. 1323-1334, 1998.

[9] L. Yan, L. B. Kong, L. F. Chen, K. B. Chong, C. Y. Tan, and C. K. Ong, "$Ba_{0.5}Sr_{0.5}TiO_3$-$Bi_{1.5}Zn_{1.0}Nb_{1.5}O_7$ composite thin films with promising microwave dielectric properties for microwave device applications", *Applied Physics Letters*, vol. 85, no. 16, pp. 3522-3524, 2004.

[10] K. B. Chong, L. B. Kong, L. F. Chen, L. Yan, C. Y. Tan, T. Yang, C. K. Ong, and T. Osipowicz, "Improvement of dielectric loss tangent of $Al_2O_3$ doped $Ba_{0.5}Sr_{0.5}TiO_3$ thin films for tunable microwave devices", *Journal of Applied Physics*, vol. 95, no. 3, pp. 1416-1419, 2004.

[11] L. Yan, L. F. Chen, C. Y. Tan, C. K. Ong, M. A. Rahman, and T. Osipowicz, "$Ba_{0.1}Sr_{0.9}TiO3$-$BaTi_4O_9$ composite thin films with improved microwave dielectric properties", *European Physical Journal B*, vol. 41, no. 2, pp. 201-205, 2004.

# CHAPTER 8:
# TUNABLE HTS/FERROELECTRIC MICROWAVE RESONATORS AND FILTER

## 8.1 Introduction

This chapter presents the work done on tunable microwave resonators and filter fabricated using the HTS and ferroelectric thin films. In addition to using the conventional approach of having the HTS thin film circuit on a layer of ferroelectric thin film deposited on an entire face of a substrate, a fabrication process was developed to enable the fabrication of patterned ferroelectric thin film. The patterned ferroelectric thin film process was used to fabricate tunable resonator and bandpass filter with improved performance.

### 8.1.1 Tunable microwave devices

Tunable microwave devices can be used to reconfigure the operating performance or characteristic of a system by means of an electric control signal. Examples of tunable microwave devices include varactors, tunable resonators, phase shifters, frequency tunable filters, variable-power dividers and variable-frequency oscillators [1].

Tunable microwave devices can cut the cost and complexity of a system by reducing the number of circuits required for separate operating conditions, i.e. one tunable circuit can take the place of several static circuits thus reducing costs and space. Microwave circuits also often require a final trimming procedure at the end of the manufacturing processes for optimum response. Tunable microwave devices can eliminate the need for the complex and costly mechanical or laser trimming.

Furthermore, tunable circuits can be used to compensate the effects, aging or temperature has on a device, thus enhancing its lifetime and performance stability.

### 8.1.2 Ferroelectric tunable microwave devices

Current options for implementing tunable microwave devices include mechanical (servo/stepping motor), semiconductor, ferrite, MEMS and ferroelectric based methods. Ferroelectric based tunable microwave devices are very promising because they provide a combination of advantages such as small-size, light-weight, high-speed, good reliability, good tunability, very low power consumption and low cost.

The main drawback of using ferroelectric materials for tunable microwave devices is the relatively high dielectric loss tangent of ferroelectric materials, which leads to high microwave dissipation. However recent researches indicate that the loss tangent can be reduced with improved thin film fabrication methods and material enhancement such as by doping [2-4] or multilayering the ferroelectric thin film. Furthermore with proper device design, it is usually possible to reduce insertion loss if tunability is also reduced such that a compromise can be made for satisfactory performance. Until now, despite the relatively high loss associated with the use of ferroelectric materials, it is still among the best candidates for practical tunable microwave devices when considering the overall performances.

### 8.1.3 Miniaturized tunable HTS/ferroelectric microwave devices

Microwave systems of various kinds, especially the wireless mobile communication and networking systems in commercial sector, as well as communication and radar in defense sector, have been the driving force behind

substantial research efforts on miniaturized tunable devices. The purpose of miniaturization of the tunable devices is to reduce the space and weight requirement, and is desired in applications where portability or high device density are required.

There is much interests in developing miniaturized tunable microwave devices using HTS/ferroelectric thin films because of the possibility of implementing tunable microwave devices with superior performances, and the chemical, physical and production method compatibilities of HTS and ferroelectric thin films which makes the fabrication of such devices possible.

## 8.2 Design issues of planar ferroelectric microwave devices

The tunable microwave devices presented in this dissertation were based on the microstrip structure as the microstrip structure allows easy packaging and integration with other microwave components. Two types of microstrip tunable devices were developed: one type with the HTS thin film circuit on a layer of ferroelectric thin film deposited on the entire face of a substrate, and the other type which had patterned ferroelectric thin film.

For the tunable microstrip devices with the HTS thin film circuit on a layer of ferroelectric thin film deposited on the entire face of a substrate, the thin film multilayer, from bottom to up, consisted of HTS YBCO thin film ground plane, 0.5 mm thick LAO substrate with dielectric constant of 23.8 and loss tangent of $1 \times 10^{-5}$, the ferroelectric $Ba_{0.1}Sr_{0.9}TiO_3$ thin film layer, the patterned HTS YBCO thin film layer and a patterned gold layer for contact bonding (see figure 8.1).

Tunable ferroelectric microwave devices require some forms of electrodes to provide the dc tuning bias voltage. To enable a large tuning range with a low biasing

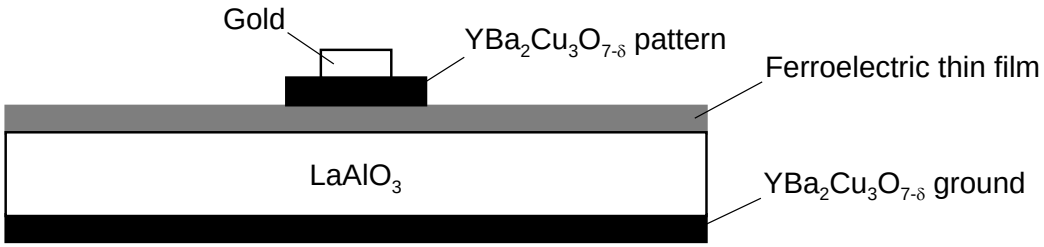


Figure 8.1 Cross sectional view of tunable microstrip device with the HTS thin film circuit on a layer of ferroelectric thin film deposited on the entire face of a substrate.

voltage, the ferroelectric thin film tuning area between the two biasing electrodes has to be large although the separation distance between the electrodes should be small. Furthermore, the ferroelectric tuning region should be located at a location where the microwave electric field of the device is most concentrated to achieve optimal tuning efficiency.

Figure 8.2 shows the possible configurations for providing the dc bias voltage in microstrip structure circuits. In figure 8.2 (a), the bias voltage is applied between the top circuit layer and the bottom ground plane. While this configuration provides the simplest method of applying voltage, it is also very inefficient in term of the required bias voltage. This is because the ferroelectric thin films are usually less than 1 μm thick whereas the substrates usually had thickness that are greater than 0.1 mm, resulting in requiring a very large voltage to achieve a sufficient electric field for tuning the ferroelectric thin film.

In figure 8.2 (b), the bias structure is highly efficient as the substrate between the biasing electrodes is removed. However it is very difficult to fabricate this type of structure using the PLD technique. This is because the YBCO thin films fabricated using PLD have very rough surface (see chapter 3), making it very hard to fabricate high quality ferroelectric thin film on top of the ground YBCO thin film deposited by PLD.

Figure 8.2 (c) shows the bias structure used for the tunable devices mentioned in this dissertation. This structure does not suffer from the inefficiency found in the structure shown in figure 8.2 (a) as the bias electric fields are mostly parallel to the ferroelectric thin film.

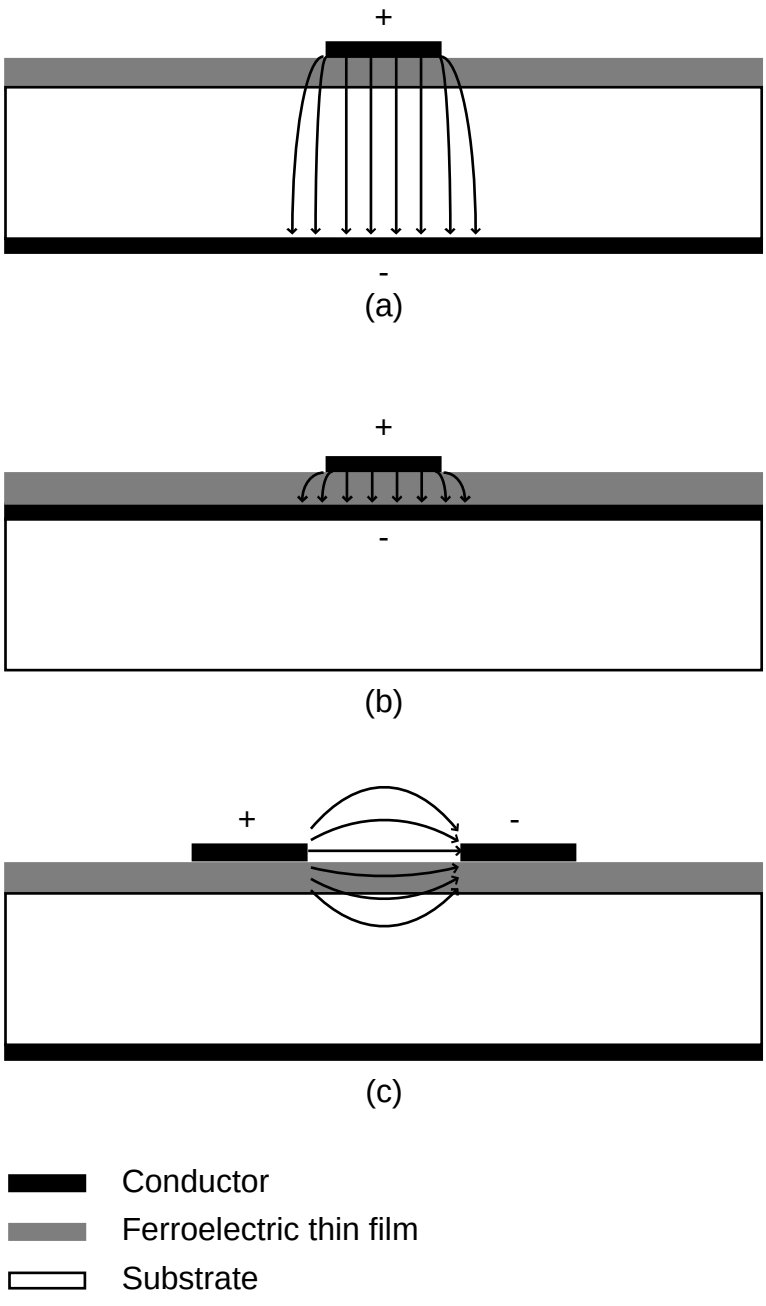


Figure 8.2 Possible configurations for providing the dc bias voltage in planar HTS/ferroelectric tunable microstrip circuits.

In the devices mentioned in this dissertation, the separation between the biasing electrodes was limited by the 25 μm line gap resolution of the soft mask use for lithography (see section 9.2). Other issues in designing tunable planar HTS/ferroelectric devices include the requirement for de-coupling the dc biasing voltage from the rf signal input/output and vice versa, which are discussed in the following sections.

This design of the tunable microwave devices mentioned in this chapter was done using the Sonnet Professional Suite [1] (Version 9.5), which is a full wave electromagnetic simulation program which allows simulation of planar microwave circuit with dielectric blocks.

## 8.3 Tunable resonator

An inter-digital type microstrip resonator was chosen to realize the tunable resonator with the thin film multilayer structure shown in figure 8.1. The inter-digital structure offers an attractive geometry for tunable planar devices as the effective tuning area of the ferroelectric thin film can be increased by increasing the number of inter-digital fingers, without increasing the exterior dimension of the resonator. It should be noted that more fingers will also reduce the resonant frequency of the resonator. Application of an electric field across the two halves of the resonator will induce a corresponding increase in the resonant frequency. Analysis of the capacitance of the inter-digital structure can be found in [5].

Each half of the inter-digital resonator was connected from its rf node to the dc contact pad by a narrow high-impedance line, to minimize the influence of the input dc voltage source on microwave performance. The input/output rf couplings were

[1] Sonnet Software Inc, New York, USA

achieved using non-contact parallel transmission line which also prevented the leakage of the dc biasing voltage into the rf input/output ports.

The layout and dimension of the inter-digital tunable resonator are shown in figure 8.3. The resonator was designed to have an unbiased resonant frequency of 13 GHz for ferroelectric thin film layer with thickness of 350 nm and dielectric constant of 1250. The simulated variation of the resonant frequency and unloaded Q factor with the dielectric constant, loss tangent and thickness of the ferroelectric thin film are shown in figures 8.4, 8.5 and 8.6.

The variations of the measured resonant frequency and unloaded Q factor with the applied electric field of the inter-digital tunable resonator are shown in figure 8.7. The tunable resonator had an unbiased resonant frequency of 13.035 GHz and unloaded Q factor of 78. With the application of a 350 V dc biasing voltage, i.e. electric field of 7 kV/mm, the resonant frequency was tuned to 13.715 GHz giving a frequency tuning of 5 %, with the unloaded Q factor increasing to 187.

It was observed that when the dc bias electric field was above 7 kV/mm, electric arcing across the gap of resonator was likely to occur. The occurrence of the electric discharge will permanently damage the resonator and “burnt” mark could be seen on the YBCO thin film as shown in figure 8.8.

## 8.4 Fabrication of patterned ferroelectric thin film

The high loss tangent of the ferroelectric thin film is a major obstacle in the development of high performance planar HTS/ferroelectric tunable microwave devices. The high loss tangent leads to devices with high insertion loss or low Q factor, an example of which can be seen in the previous section where the high loss tangent

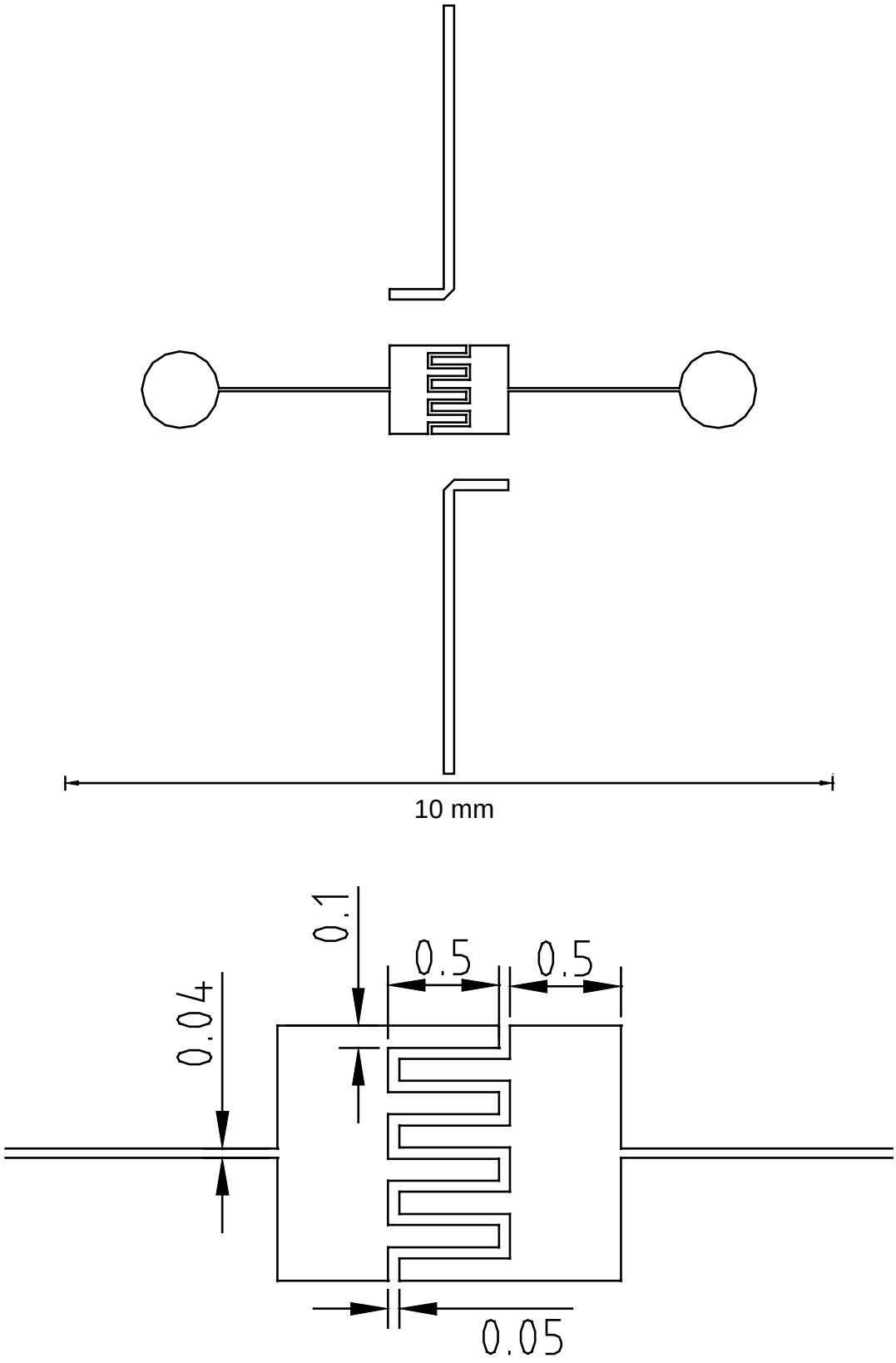


Figure 8.3 Layout and dimension of the tunable resonator. Unit in mm.

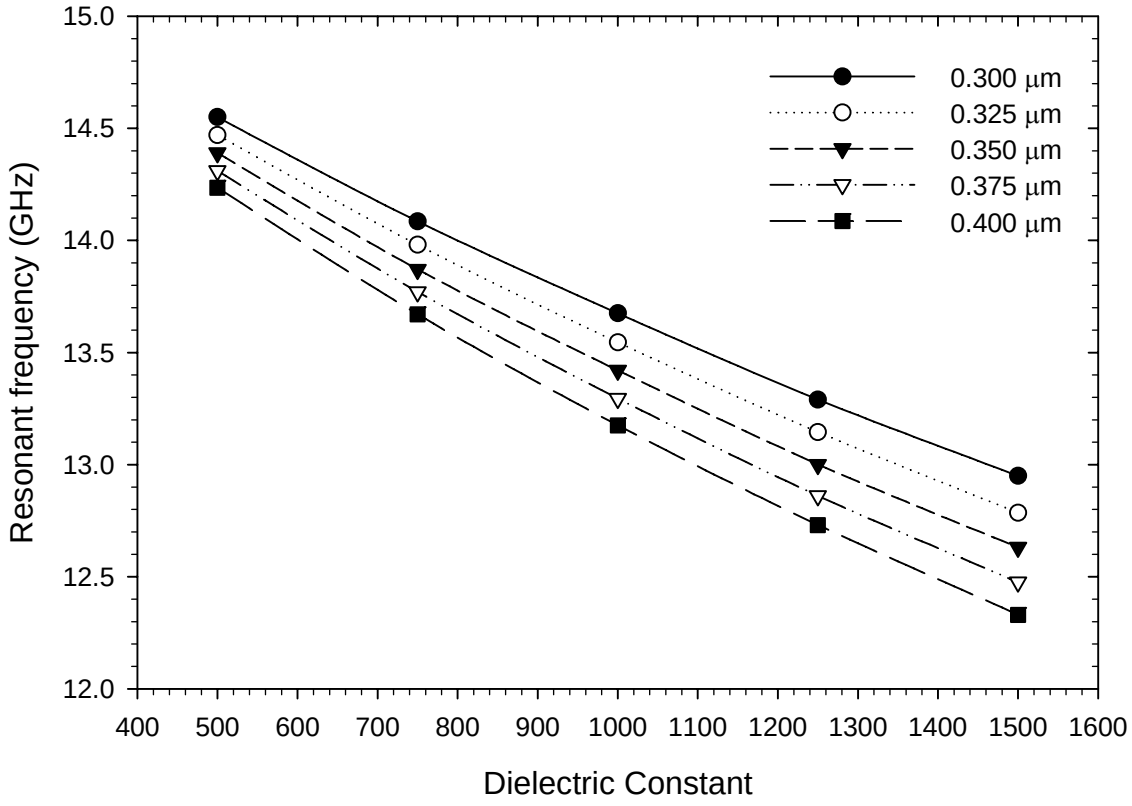


Figure 8.4 The simulated variation of the resonant frequency of the tunable resonator with dielectric constant for ferroelectric layer with different thickness.

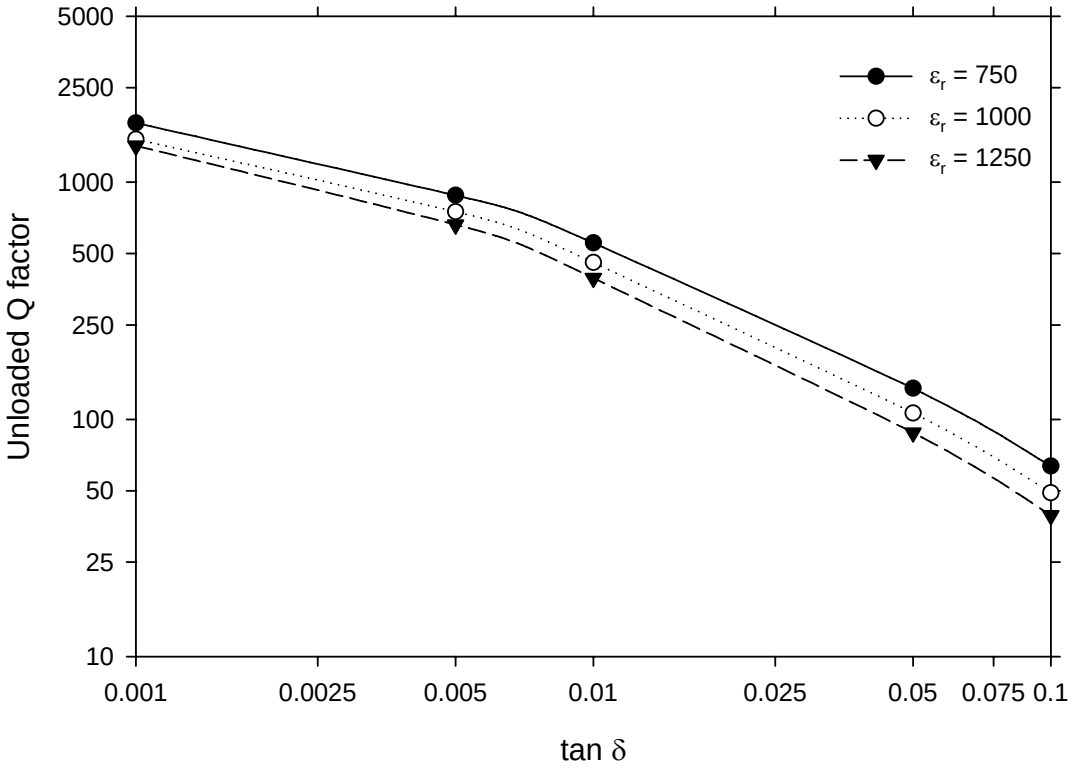


Figure 8.5 The simulated variation of the unloaded Q factor of the tunable resonator with loss tangent for 350 nm thick ferroelectric layer with different dielectric constant.

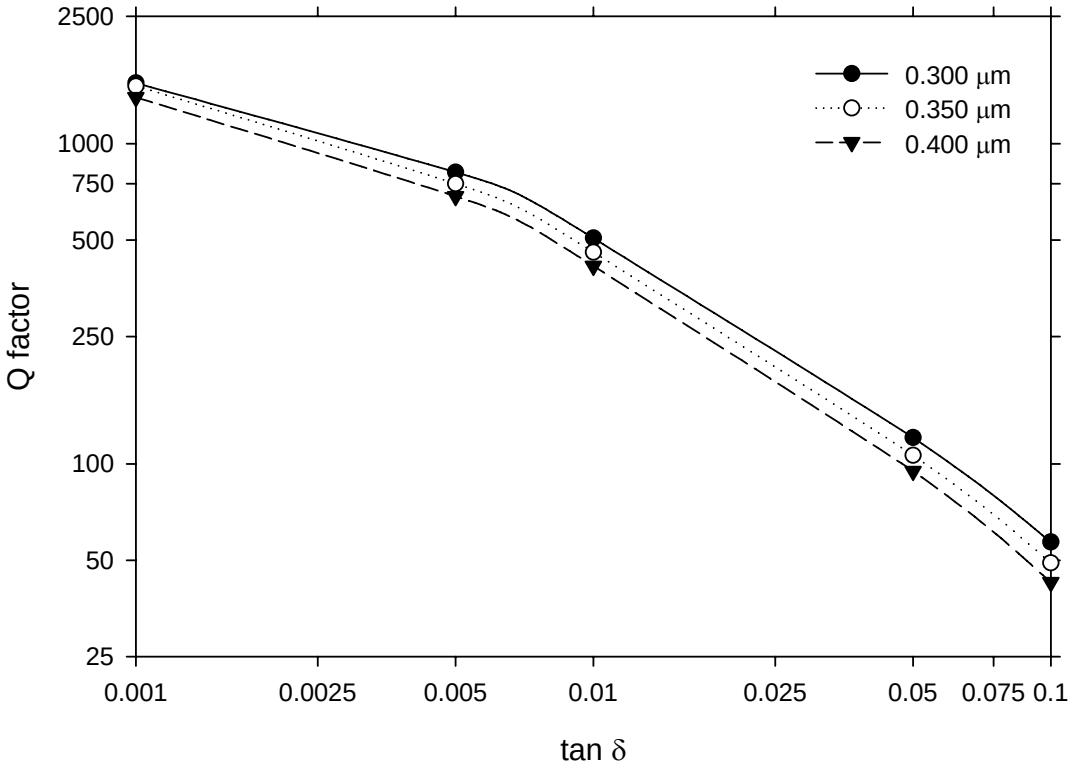


Figure 8.6 The simulated variation of the unloaded Q factor of the tunable resonator with loss tangent for ferroelectric layer with dielectric constant of 1250 and different thickness.

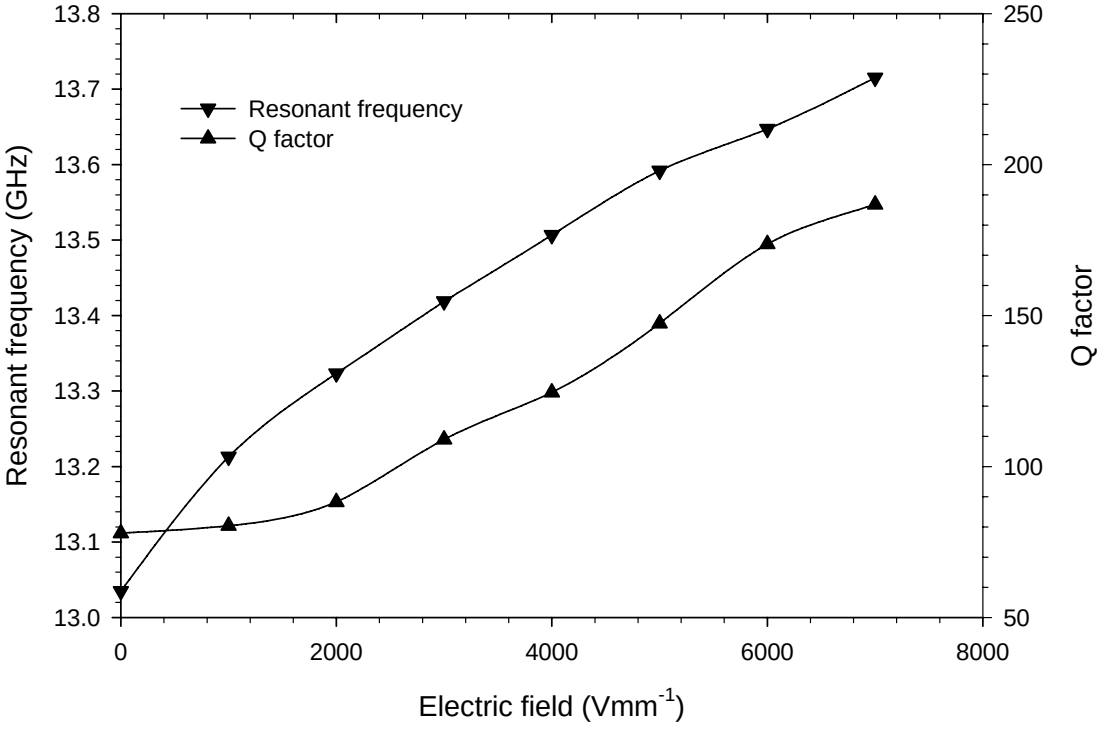


Figure 8.7 The measured variation of resonant frequency and unloaded Q factor with applied electric field for the inter-digital tunable resonator.

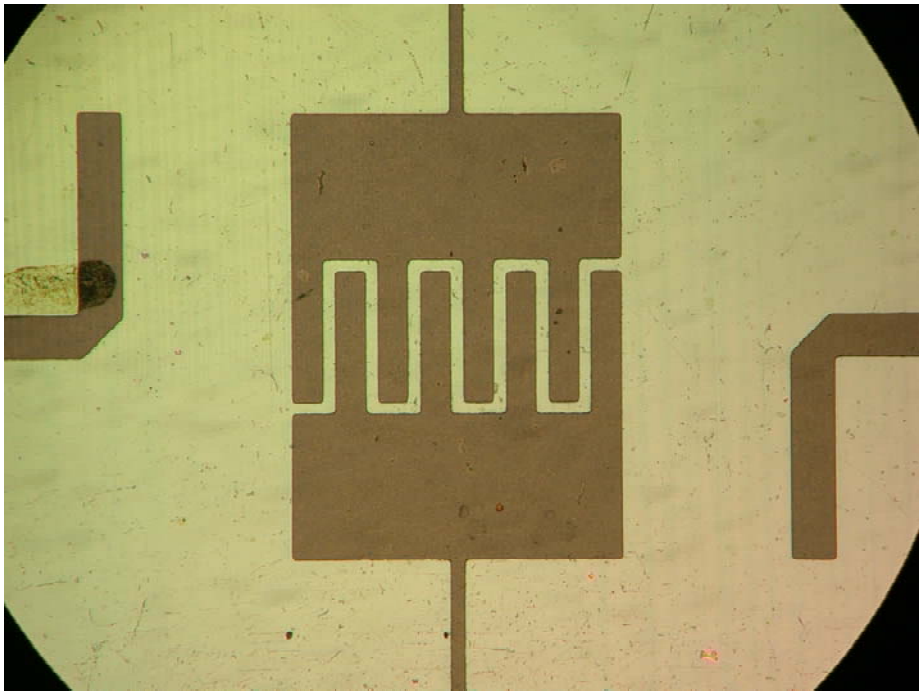

(a)

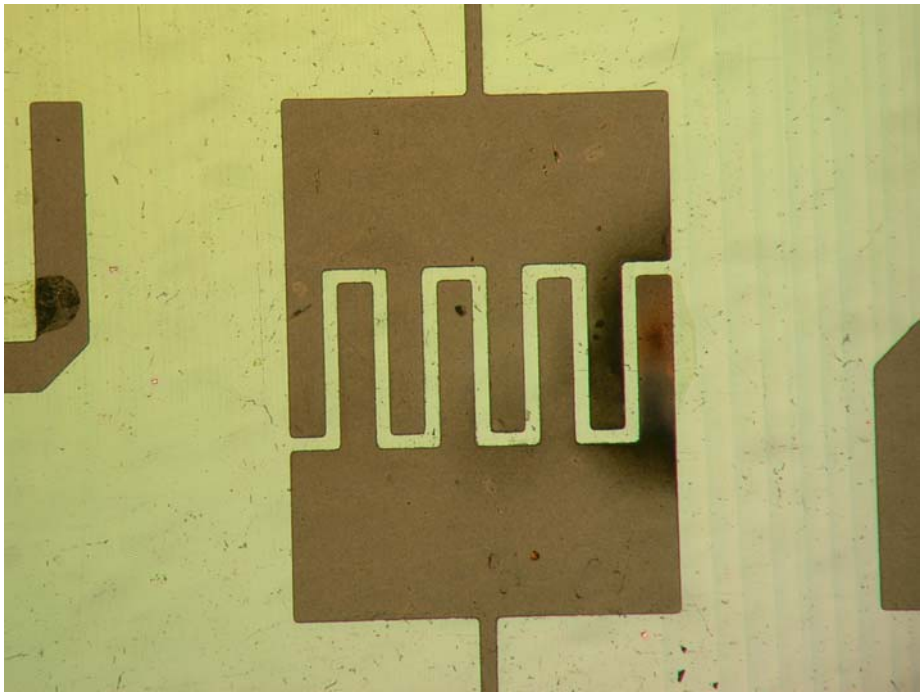

(b)

Figure 8.8 Photographs of an (a) undamaged and
(b) electrical discharge damaged tunable resonator.

of the $Ba_{0.1}Sr_{0.9}TiO_3$ thin film negated the advantage of using HTS thin film for high Q factor resonator.

Other than using ferroelectric material with lower loss tangent, the loss in tunable microwave devices can also be reduced by using improved device design. One method of device design improvement for planar tunable microwave device is by using ferroelectric thin films that are patterned such that the ferroelectric thin film is present only on selected areas of the substrate as shown in figure 8.9 (a), rather than on an entire surface of a substrate as shown in figure 8.9 (b).

In addition to reducing the microwave dissipation due to the ferroelectric thin film, the patterned ferroelectric thin film will also reduce or eliminate unintentional tuning from regions of ferroelectric thin film where tuning is unwanted. For the case where the ferroelectric thin film is on an entire face of a substrate, the problem of unintentional tuning is not easily solved even with the use of full wave electromagnetic simulation software. This is because the dielectric constant across the ferroelectric thin film is highly non-uniform due to its non-linear dependence on the dc electric field which varies with the circuit geometry. The highly non-uniform dielectric constant will make the creation of an accurate model for full wave electromagnetic simulation very difficult.

One approach for achieving ferroelectric thin film on only selected region is to use “drop-in” pieces of ferroelectric thin film grown on a separate substrate and subsequently attaching them to the substrate with the patterned conductive layer circuit [6,7]. However this approach is usually very difficult to implement in practice as it required the device design to have a very large displacement error tolerance for the placement position of the substrates or that the device to be assembled with very high precision.

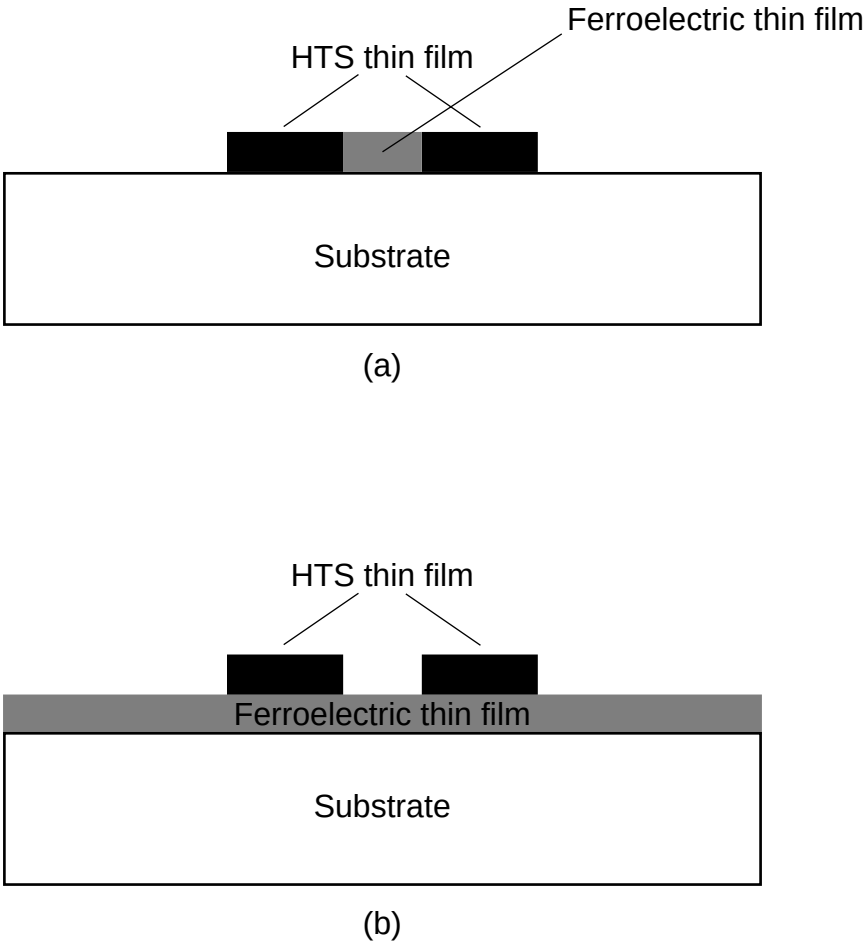


Figure 8.9 (a) Patterned ferroelectric thin film. (b) Ferroelectric thin film on the entire side of a substrate.

Conventionally, the means to achieve patterned ferroelectric thin film on the substrate is by chemical etching [8,9] or ion beam milling [10] of the ferroelectric thin film. Patterning of the ferroelectric thin film by chemical etching is not trivial as the ferroelectric thin film materials are very inert and chemicals capable of etching of the ferroelectric materials will also etch the substrate or/and conductive layers. The ion beam milling process is very slow and can result in damages to the substrate surface if not carefully controlled and monitored.

Conventional processes of chemical etching or ion beam milling will usually cause damage to either the substrate surface or/and conductive layer, and result in a fabricated device with poor performance. This problem of damaging the substrate surface or/and conductive layer is especially severe when HTS thin film, whose surface resistance is highly sensitive to damage, is used as the conductive layer [11,12]. Conventional lift-off process using an organic photoresist masking layer for patterning the ferroelectric thin film is also unsuitable due to the high temperature required for the deposition of high quality ferroelectric thin film.

### 8.4.1 Fabrication of patterned ferroelectric thin film

A method was developed to fabricate the patterned ferroelectric thin film without damaging the substrate surface [13]. This fabrication process for the patterned ferroelectric thin film is based on a lift-off method with YBCO thin film as a refractory masking layer. This fabrication process also has the advantage of allowing the $Ba_{0.1}Sr_{0.9}TiO_3$ ferroelectric thin film to be deposited at the high temperature required for good quality. Furthermore, the YBCO thin film used for the conductive circuit layer will not be degraded by exposure to wet etching or ion beam milling [14,15] during the patterning of the $Ba_{0.1}Sr_{0.9}TiO_3$ ferroelectric thin film.

The flowchart for the fabrication procedure is shown in figure 8.10. In this fabrication process, a layer of refractory masking YBCO film was first deposited on the LAO substrate. The advantages of using YBCO as the masking material are that it is thermally stable, can be easily etched with weak acids, and will not react with substrate material such as LAO. The thickness of the masking YBCO layer should be thicker than the required thickness of the ferroelectric thin film for better edge definition. The YBCO layer was fabricated using the PLD technique described in chapter 2.

The YBCO film was then patterned using conventional photolithographic technique with etching by diluted phosphoric acid described in chapter 9. The pattern of the etched masking YBCO layer was a negative image of the required ferroelectric thin film pattern.

The $Ba_{0.1}Sr_{0.9}TiO_3$ ferroelectric thin film was then deposited on the side of the substrate with the patterned masking layer. After the deposition of the ferroelectric thin film, the remaining masking YBCO layer was removed by etching with diluted nitric acid in ultrasonic bath. Consequently, unwanted regions of the ferroelectric thin film on top of the masking YBCO layer would also be removed, thus producing the required ferroelectric thin film pattern.

The SEM images of ferroelectric thin film with hill and pit formations on LAO substrate patterned using the above procedure is shown in figure 8.11. The edges of the formations in this instance were quite rough as the height of the masking YBCO thin film was only 400 nm compared to the height of the $Ba_{0.1}Sr_{0.9}TiO_3$ thin film which was about 350 nm.

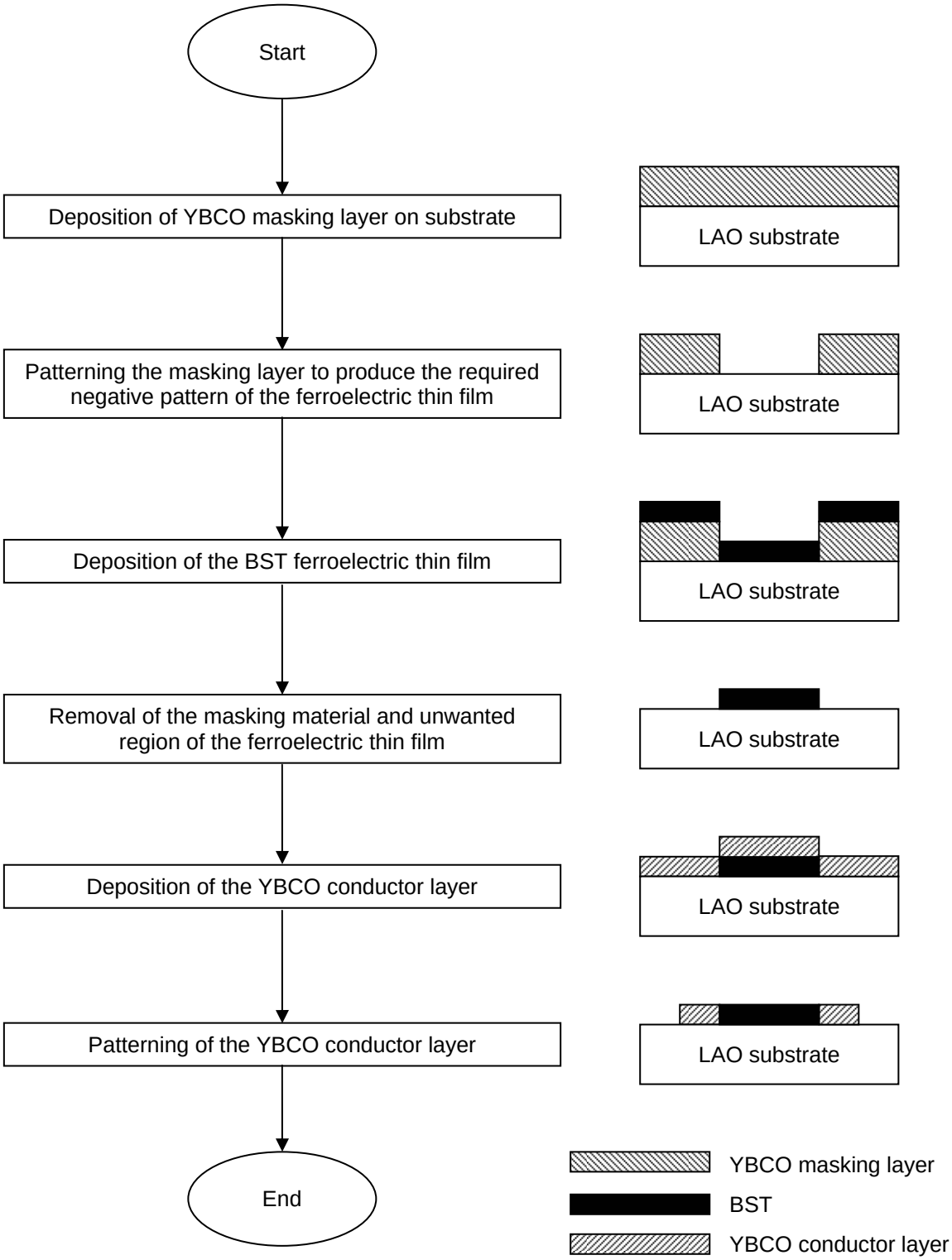


Figure 8.10 The flowchart of the fabrication process for patterned ferroelectric thin film.

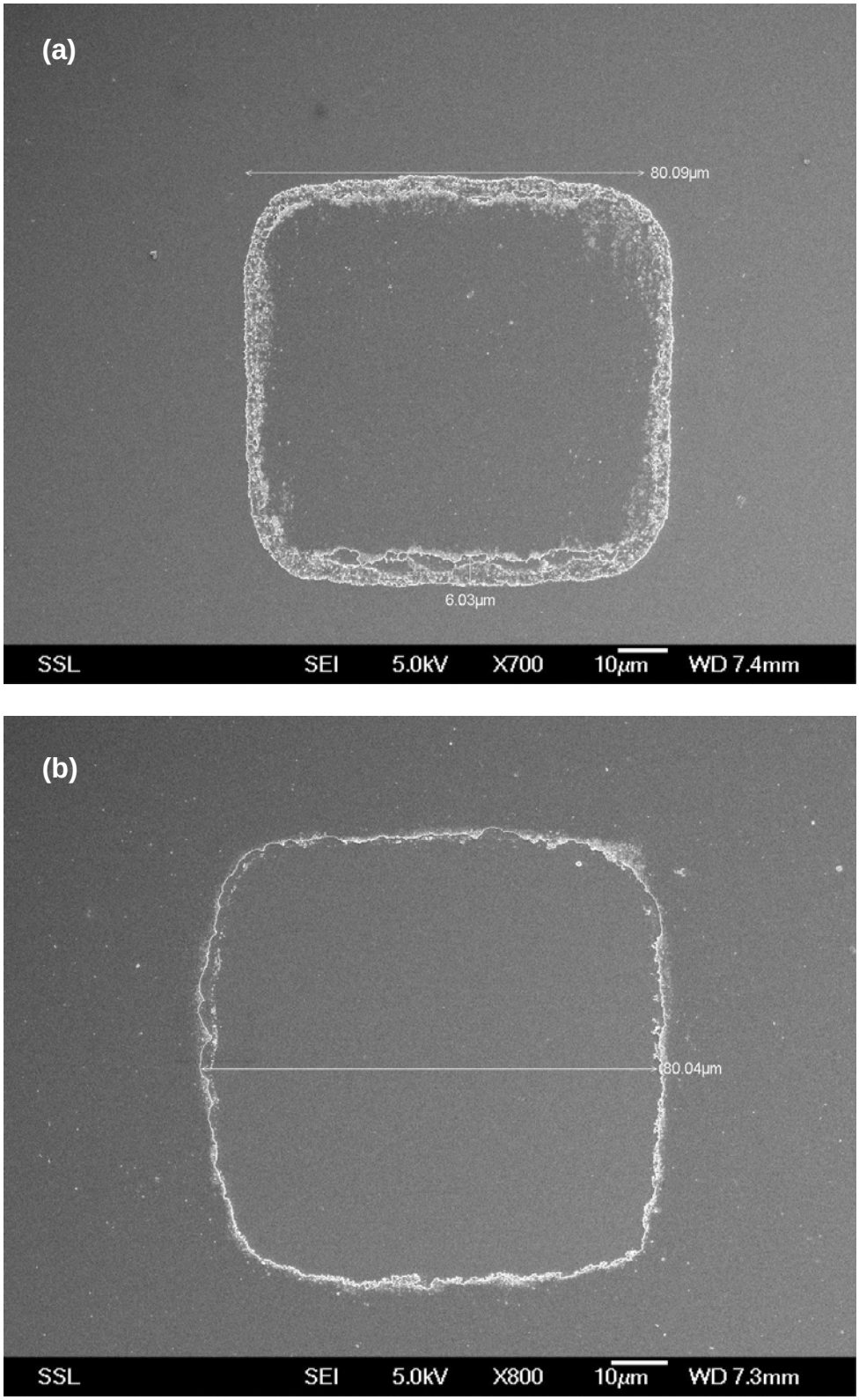


Figure 8.11 The SEM images of ferroelectric thin film (a) hill and (b) pit formations on LAO substrate.

## 8.5 Tunable resonator with patterned ferroelectric thin film

A tunable resonator with patterned ferroelectric thin film was designed using the open-loop geometry. The strong electric self coupling across the two ends of an open-loop resonator with a small gap is advantageous in the design of the tunable filter because the resonant frequency will be highly sensitive to changes in the dielectric constant across the gap. The layout and photograph of the resonator are shown figures 8.12 and 8.13. A small patch was added on the gap across the open-loop resonator to allow the application of the dc biasing electric field, thus two patches of ferroelectric thin film were required for each resonator.

The voltage node of the open-loop resonator was connected by a narrow high-impedance quarter-wavelength line to a radial line stub which acts as a open circuit, to minimize the leakage of microwave signal through the dc biasing inputs [16,17]. The input/output RF couplings were achieved using non-contact capacitive couplings which also prevented the leakage of the dc voltage biasing into the rf input/output ports.

The resonator was designed to have an unbiased resonant frequency of 12 GHz for ferroelectric thin film layer with thickness of 350 nm and dielectric constant of 1250. When an electric field is applied across the patches of ferroelectric thin film, the dielectric constant of the ferroelectric thin film is lowered. Thus the effective capacitance of the resonator is lowered and results in an increase in the resonant frequency of the resonator.

The variation of measured resonant frequency and unloaded Q factor with the applied electric field of the tunable resonator with patterned ferroelectric thin film is shown in figure 8.14. The tunable resonator had an unbiased resonant frequency of

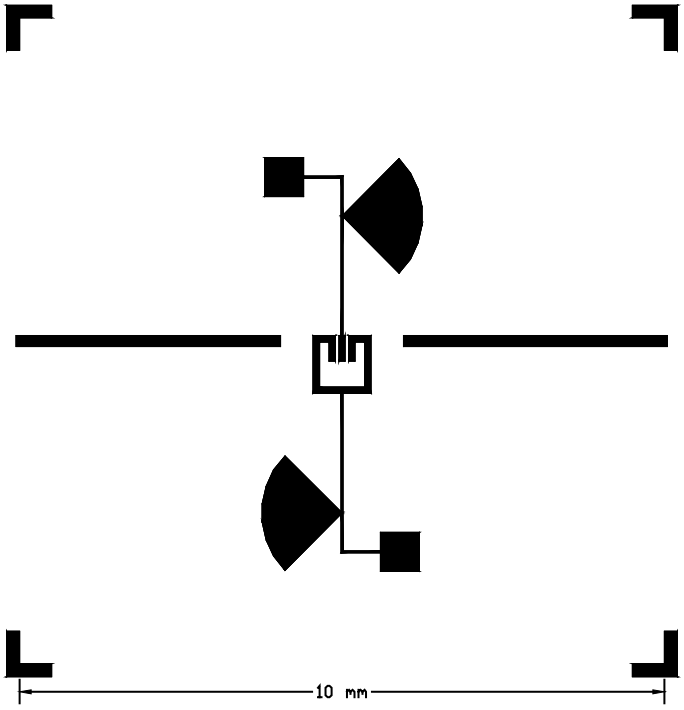


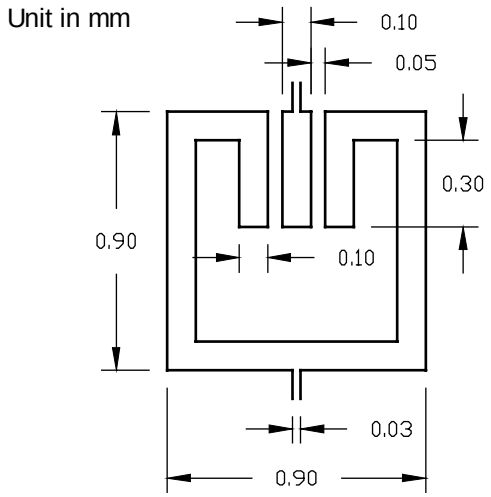


Figure 8.12 The layout and dimension of the YBCO layer for the tunable resonator with patterned ferroelectric thin film.

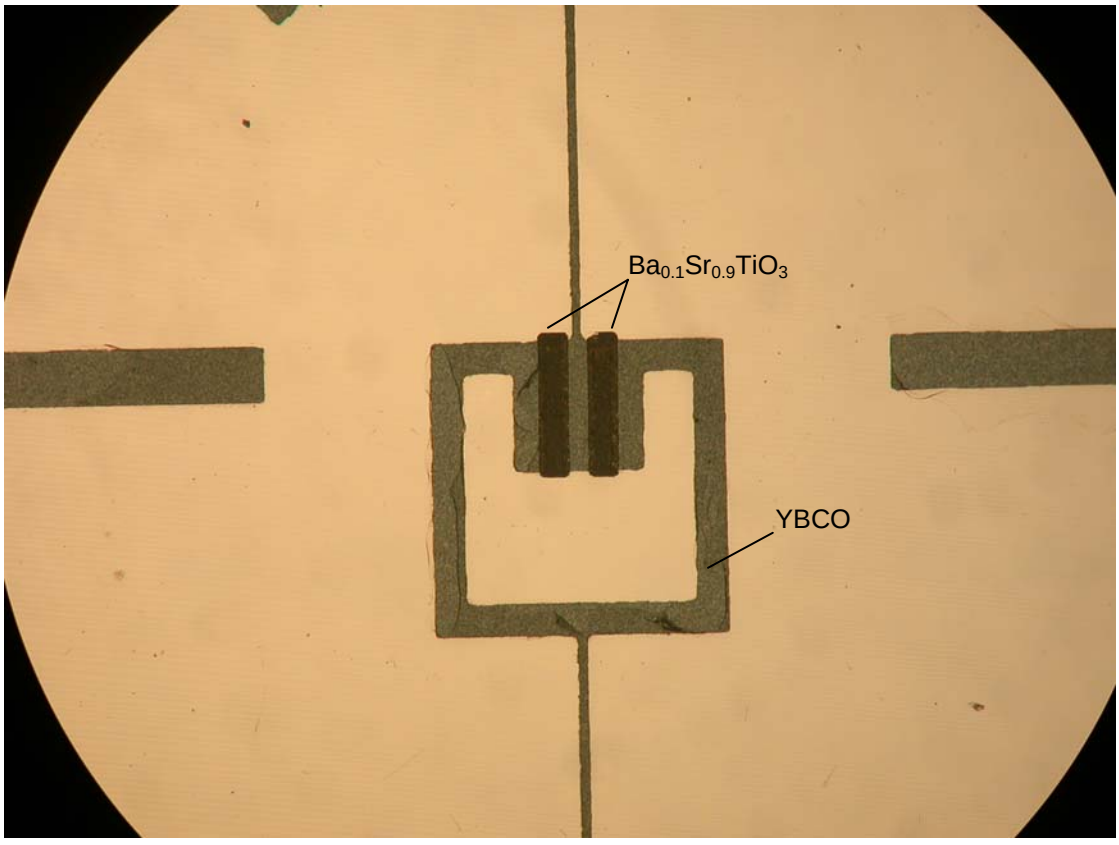


Figure 8.13 The photograph of the tunable resonator with patterned ferroelectric thin film.

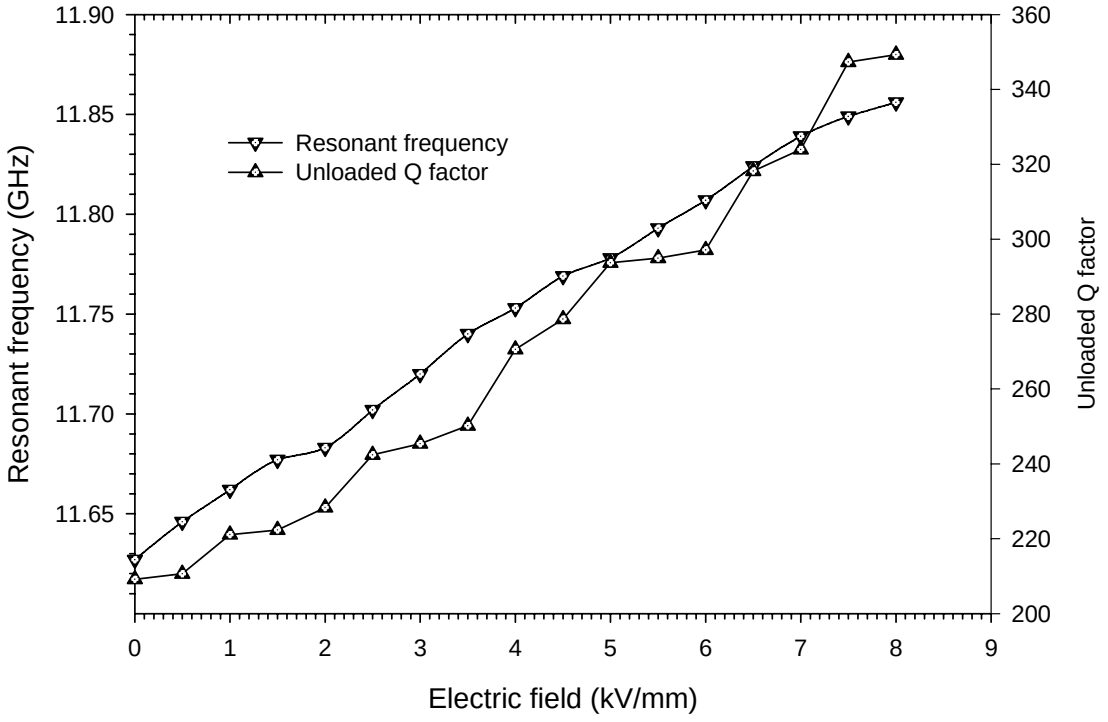


Figure 8.14 The measured variation of resonant frequency and unloaded Q factor with applied electric field for the tunable resonator with patterned ferroelectric thin film.

11.627 GHz and unloaded Q factor of 209. The lower than expected resonant frequency was due to the $Ba_{0.1}Sr_{0.9}TiO_3$ thin film been slightly thicker than the 350 nm used in the simulation. With the application of a biasing voltage of 400 V, i.e. electric field of 8 kV/mm, the resonant frequency was tuned to 11.856 GHz giving a frequency tuning of 2 % with the unload Q factor increasing to 349.

### 8.6 Tunable filter

A frequency tunable bandpass filter based on the abovementioned tunable open-loop microstrip resonator with patterned ferroelectric thin film was designed and fabricated [18]. The tunable filter was designed using Chebyshev prototype values with central frequency of 12 GHz, ripples of 0.1 dB, fractional bandwidth of 4 % and 35 dB bandwidth of 20 %. Based on these requirements, a three-stage filter is required [19].

Full wave electromagnetic simulations were used to find the required layout of the resonators and the external input/output couplings. The input/output rf couplings were achieved using non-contact parallel transmission line couplings which also act as the dc blocks. The rf choke for the dc biasing inputs were achieved by connecting the voltage node of the open-loop resonator with a narrow high-impedance quarter-wavelength line to a radial line stub.

Sections of the rf input/output on the HTS thin film circuit layer were coated with gold, so that the rf input/output can be bridged by gold ribbons to the K-connector using resistance welding (see chapter 9). The radial stubs on the HTS thin film circuit layer were similarly attached to the dc input/output K-connectors using gold wires.

The layout and photograph of the tunable filter circuit are shown in figures 8.15 and 8.16. The transmission and reflection S-parameters variation of the tunable filter with applied voltage is shown in figure 8.17. The tunable filter had a central frequency of 11.74 GHz in the electrically unbiased state. When the applied voltage was at 200 V, the central frequency increased to 11.93 GHz with the filter achieving a frequency tunability of 1.6 %. The measured central frequency of the tunable filter was lower than design value due to the fabricated ferroelectric thin film been thicker (about 400 nm) and having a higher dielectric constant (of about 1350) than the values used in the initial simulations which were set to a thickness of 350 nm and dielectric constant of 1250.

The insertion loss of the filter in the unbiased state is 1.6 dB and decreased to 0.35 dB when a voltage of 200 V was applied. The decrease in the insertion loss was due to the loss tangent of the ferroelectric thin film decreasing with increasing electric field. The low insertion loss of this tunable filter demonstrated the potential of using patterned ferroelectric thin film to achieve low loss tunable planar microwave devices.

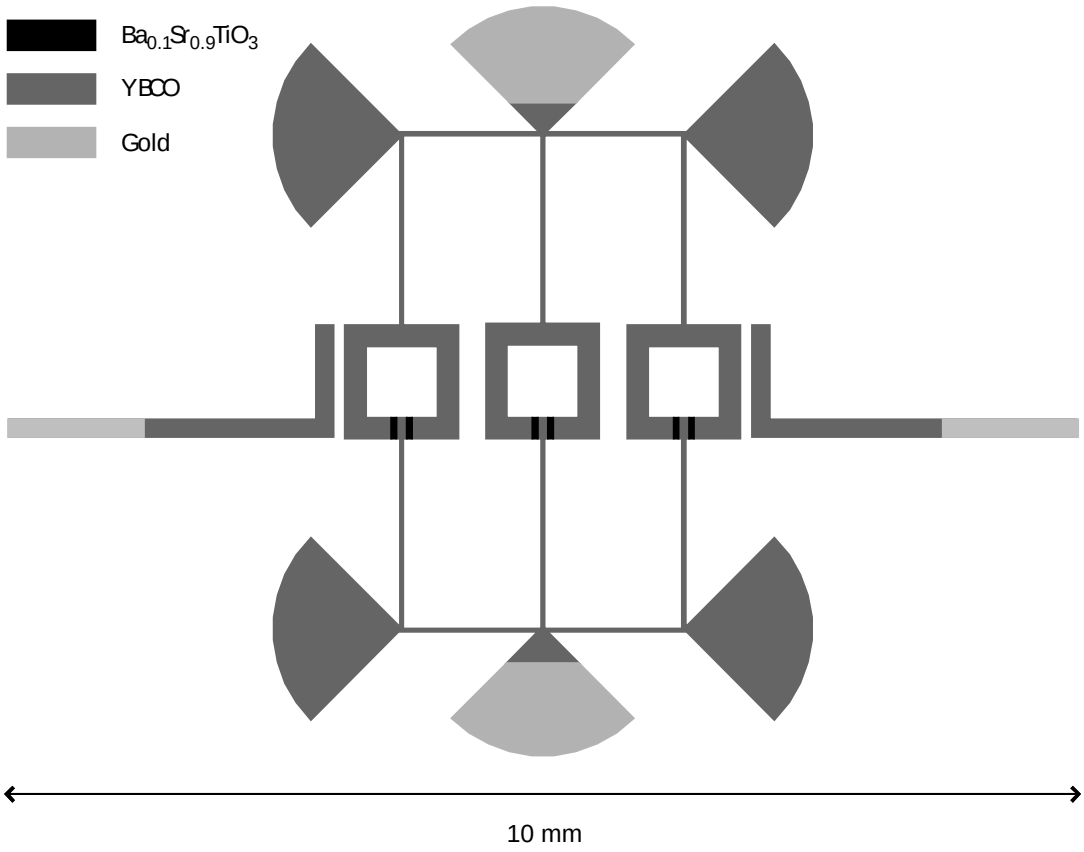


Figure 8.15 Layout of the three-stage HTS tunable filter with patterned ferroelectric thin film.

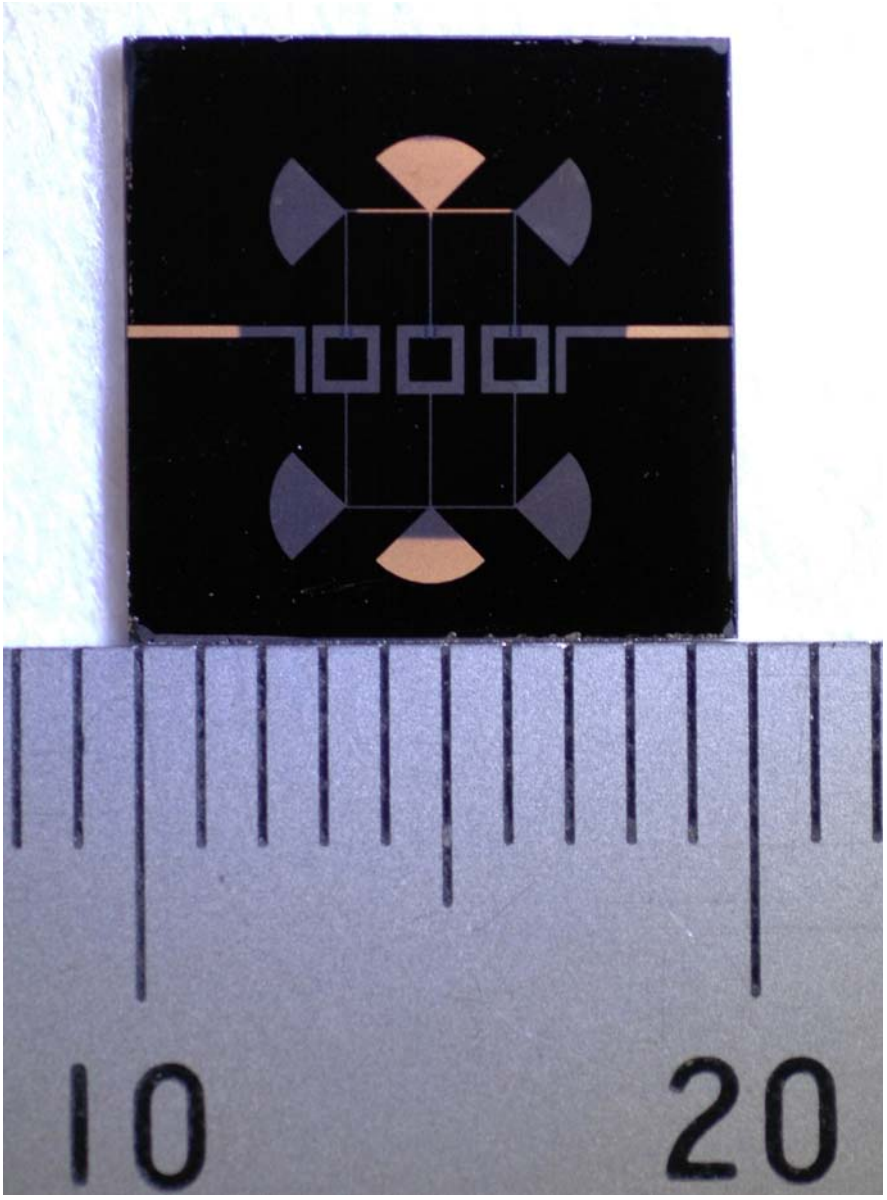


Figure 8.16 The photograph of the tunable HTS filter with patterned ferroelectric thin film.

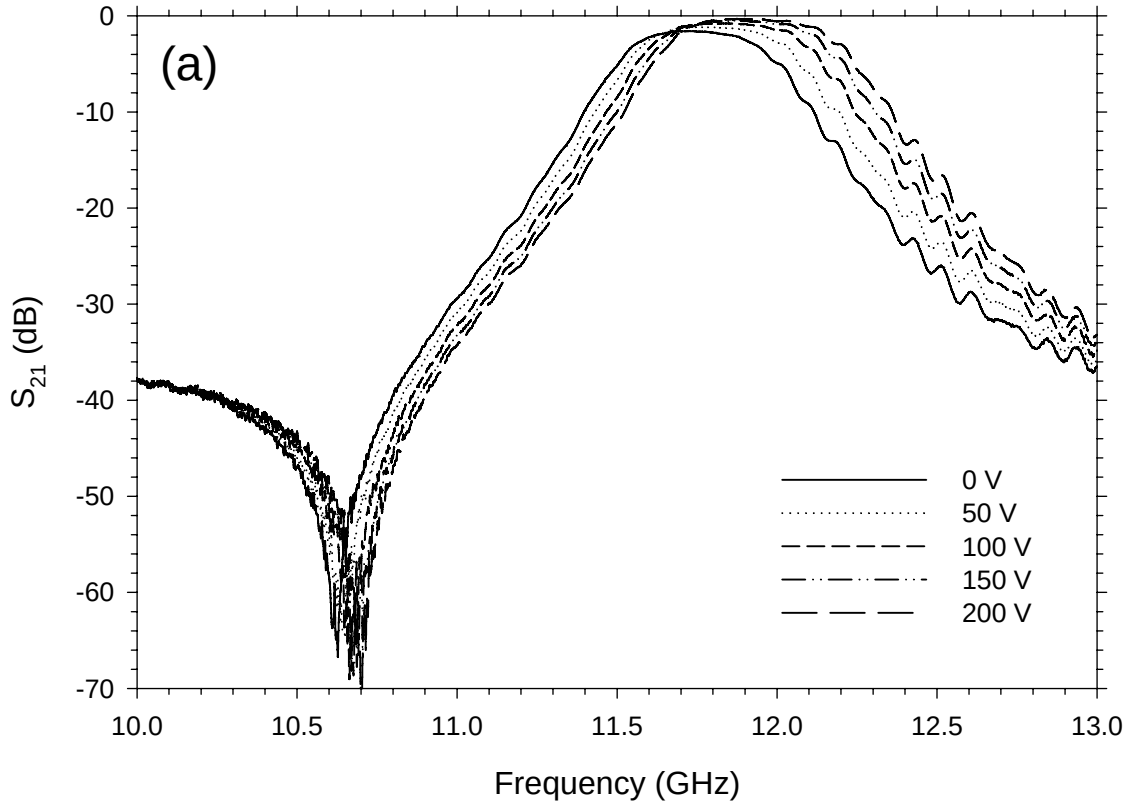


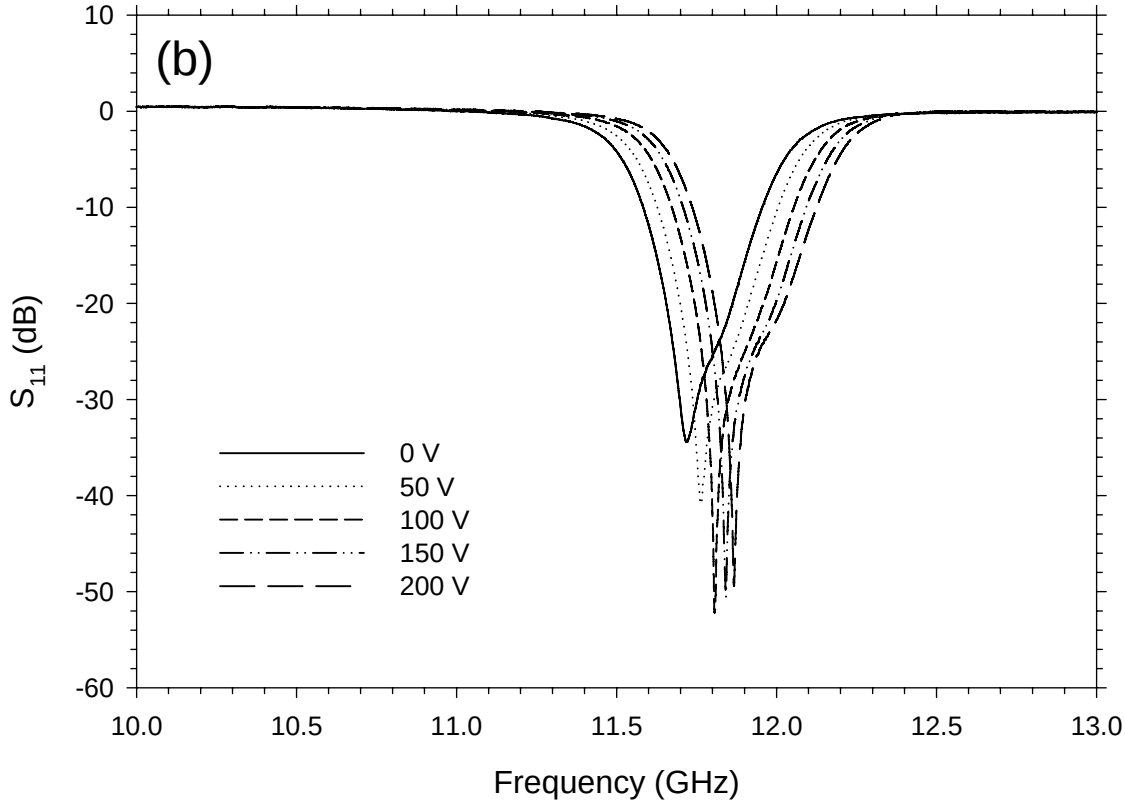


Figure 8.17 The measured (a) transmission and (b) reflection S-parameters of the tunable filter for different applied voltage.

References


[1] M. J. Lancaster, J. Powell, and A. Porch, "Thin-film ferroelectric microwave devices", *Superconductor Science & Technology*, vol. 11, no. 11, pp. 1323-1334, 1998.

[2] L. Yan, L. F. Chen, C. Y. Tan, C. K. Ong, M. A. Rahman, and T. Osipowicz, "$Ba_{0.1}Sr_{0.9}TiO_3$-$BaTi_4O_9$ composite thin films with improved microwave dielectric properties", *European Physical Journal B*, vol. 41, no. 2, pp. 201-205, 2004.

[3] L. Yan, L. B. Kong, L. F. Chen, K. B. Chong, C. Y. Tan, and C. K. Ong, "$Ba_{0.5}Sr_{0.5}TiO_3$-$Bi_{1.5}Zn_{1.0}Nb_{1.5}O_7$ composite thin films with promising microwave dielectric properties for microwave device applications", *Applied Physics Letters*, vol. 85, no. 16, pp. 3522-3524, 2004.

[4] K. B. Chong, L. B. Kong, L. F. Chen, L. Yan, C. Y. Tan, T. Yang, C. K. Ong, and T. Osipowicz, "Improvement of dielectric loss tangent of $Al_2O_3$ doped $Ba_{0.5}Sr_{0.5}TiO_3$ thin films for tunable microwave devices", *Journal of Applied Physics*, vol. 95, no. 3, pp. 1416-1419, 2004.

[5] S. Gevorgian, E. Carlsson, S. Rudner, L. D. Wernlund, X. Wang, and U. Helmersson, "Modelling of thin-film HTS/ferroelectric interdigital capacitors", *IEE Proceedings-Microwaves Antennas and Propagation*, vol. 143, no. 5, pp. 397-401, 1996.

[6] M. Misra, N. D. Kataria, H. Murakami, and M. Tonouchi, "Analysis of a flip-chip bonded tunable high-temperature superconducting coplanar waveguide resonator using the conformal mapping technique", *Superconductor Science & Technology*, vol. 16, no. 4, pp. 492-497, 2003.

[7] B. H. Moeckly, L. S. J. Peng, and G. M. Fischer, "Tunable HTS microwave filters using strontium titanate thin films", *IEEE Transactions on Applied Superconductivity*, vol. 13, no. 2, pp. 712-715, 2003.

[8] G. L. Larkins, R. Socorregut, and Y. A. Vlasov, "Superconducting microstrip hairpin filter with $BaTiO_3$ patches", *IEEE Transactions on Applied Superconductivity*, vol. 13, no. 2, pp. 724-726, 2003.

[9] F. A. Miranda, C. H. Mueller, F. W. Van Keuls, G. Subramanyam, and S. Vignesparamoorthy, "Performance enhancement of tunable bandpass filters using selective etched ferroelectric thin films", *Integrated Ferroelectrics*, vol. 50, pp. 121-131, 2002.

[10] S. F. Karmanenko, A. I. Dedyk, V. T. Barchenko, R. A. Chakalov, A. V. Lunev, A. A. Semenov, and L. T. Ter-Martirosyan, "Patterning of tunable planar ferroelectric capacitors based on the YBCO/BSTO film structure", *Superconductor Science & Technology*, vol. 11, no. 3, pp. 284-287, 1998.

[11] R. Wordenweber, "Growth of high-$T_c$ thin films", *Superconductor Science & Technology*, vol. 12, no. 6, p. R86-R102, 1999.

[12] J. M. Phillips, "Substrate selection for high-temperature superconducting thin films", *Journal of Applied Physics*, vol. 79, no. 4, pp. 1829-1848, 1996.

[13] C. K. Ong and C. Y. Tan, "Electrically Tunable Microwave Devices with Patterned Ferroelectric Thin Film", US Patent Application 11/074,417, Mar.8, 2005.

[14] M. Tonouchi, H. Shimakage, Z. Wang, S. Tomozawa, M. Hangyo, and Y. Murakami, "Atomic scale flattening and characterization of a YBCO film surface", *Superconductor Science & Technology*, vol. 9, no. 4A, p. A161-A165, 1996.

[15] T. Matsui, D. Yamaguchi, and H. Kamijo, "Damage to $YBa_2Cu_3Oy$ surface caused by Ar ion beam etching", *Japanese Journal of Applied Physics Part 2-Letters*, vol. 35, no. 1B, p. L97-L99, 1996.

[16] H. A. Atwater, "The Design of the Radial Line Stub: A Useful Microstrip Circuit Element", *Microwave Journal*, vol. 28, p. 149, Nov.1985.

[17] B. A. Syrett, "A Broad-Band Element for Microstrip Bias or Tuning Circuit", *IEEE Transactions on Microwave Theory and Techniques*, vol. 28, no. 8, pp. 925-927, 1980.

[18] C. Y. Tan and C. K. Ong, "Planar tunable HTS microwave filter with patterned ferroelectric thin film", *Superconductor Science & Technology*, vol. 19, no. 2, pp. 212-216, 2006.

[19] G. L. Matthaei, L. Young, and E. M. T. Jones, *Microwave filters, impedance-matching networks, and coupling structures*, Artech House, 1980.

# CHAPTER 9:
# THE FABRICATION AND PACKAGING OF HTS MICROWAVE DEVICES

The fabrication procedures and packaging for the HTS microwave devices developed in the course of this thesis are presented in this chapter. HTS thin films are very fragile materials; their surface resistance can easily be degraded by improper handlings such as exposure to moisture or heating in normal atmosphere [1]. As such, the fabrication procedures and packaging of the HTS YBCO thin film microwave devices have to be carefully designed to avoid causing such degradations.

## 9.1 Fabrication of HTS microstrip devices

The HTS YBCO thin film microstrip devices discussed in this thesis were fabricated using conventional UV photolithography and wet etching. The fabrication procedure for YBCO thin film microstrip devices can be divided into the 5 steps described below:

**Step 1**: The fabrication of the double-sided YBCO thin film by the PLD technique described in chapter 2.

**Step 2**: The measurement of the surface resistance on both sides of the fabricated double-sided YBCO thin film using the dielectric resonator wall-loss perturbation technique described in chapter 3. Only YBCO thin film samples with surface resistance less than 1 mΩ at 77 K and 10.65 GHz on both sides were used for microwave device fabrication.

**Step 3**: The deposition of the gold film by sputtering, for the gold pads required by gold wire/ribbon bonding of the dc/rf inter-connections. As gold adhered very well

to the YBCO thin film deposited by PLD, no surface treatment of the YBCO thin film or buffer layer was required.

The gold sputtering procedure is described in appendix 2. The gold film was selectively deposited on only certain areas of the YBCO thin film, by using an aperture mask made from 25 μm thick light-tight copper foil with half-hard temper (CU000500[1]). The alignment of the aperture mask and substrate need not be very accurate as the gold film would be further patterned in step 4. The selective deposition of the gold film was required to keep the area of the gold/YBCO multilayer to the minimum required for bonding, as the gold/YBCO multilayer had a higher effective surface resistance than the single layer YBCO thin film [2,3], and to prevent exposure of the YBCO thin film to moisture.

The fabrication of the copper aperture mask is similar to the photolithography and etching process for YBCO thin film, described in appendix 3, although $FeCl_3$ solution (0.5 kg/l concentration) was used as the etchant.

**Step 4**: The patterning of the gold film and YBCO thin film, which consist of applying, exposing and developing the photoresist, followed by the etching of the gold and YBCO thin film [4]. The detail description of the process is given in appendix 3.

**Step 5**: The packaging of the HTS thin film devices in hermetic casing with rf and dc connectors. The issues concerning the design of the packaging are discussed in sections 9.3 to 9.7 and the procedures for assembling the packaging are given in appendices 5 and 6.

[1] Goodfellow Cambridge Ltd., Huntingdon, UK

## 9.2 Mask design of HTS microstrip devices

Commercially produced soft masks[2] were used for the photolithography process. The minimum feature size of the microwave devices was limited by the mask resolution, which required the minimum size for both the line and gap features to be no less than 25 μm. The fabricated masks had dimension error of less than 5 μm.

The design of the masks can be in DXF or DWG formats[3] and were usually generated directly from the full wave electromagnetic simulation software. Usually four alignment marks corresponding to the four corners of a substrate were added to the mask design (see figure 8.12 for an example) to aid the mask and substrate alignment process during the exposure step described in step 9 of appendix 3. The masks were designed with the opaque patterns corresponding to the devices patterns as positive photoresist was used.

Since the wet etching of YBCO thin film is an isotropic process, some undercutting (i.e. etching of YBCO beyond the boundary of the photoresist) is inevitable. The undercutting caused the YBCO pattern to be smaller than the pattern on the mask. To compensate for undercutting, the dimension of the device layout on the mask is uniformly enlarged by 1 μm offset.

## 9.3 Packaging of HTS microstrip devices

The purposes of the housing for HTS microstrip devices are to provide a platform for the secure support of the substrate and the rf/dc connections, and to provide protection from the environment. While the packaging of microwave devices has always been demanding due to stringent requirement for the rf connection, the

[2] Innovative Laser Systems, Bukit Batok, Singapore
[3] Autodesk Inc., California, USA

packaging for HTS microwave devices is more demanding as the devices are subjected to temperature cycling between 77 K to 300 K, and requires hermetic sealing.

Microwave devices are often housed in a conductive metallic housing as it can provides rf shielding and reduce energy lost due to electromagnetic radiation leakage. Conductive housing can also provide the ground path for the microwave signal.

The main factors that were taken into consideration when designing the housing for HTS microstrip devices were: microwave performance, hermetic sealing and mechanical properties such as thermal expansion/contraction and thermal conductivity. The secondary considerations were the ease of fabricating the housing, the ease of installing the HTS microstrip devices and the possibility of reusing the housing.

The thermal conductivity of the housing material should be high so that the HTS device within the housing can be cooled down efficiently. This is especially important when using a cryocooler, which usually has limited cooling power.

The factors affecting the microwave performance of the housing include the type of microwave connector, the implementation of the transition from the connector to the microstrip circuit, the dimension of the housing cavity and the rf ground path provided by the housing.

The housings developed in this thesis were fabricated using CNC milling, mostly at the machining workshop of Department of Physics, National University of Singapore. For housings with gold plating, the fabrication was done by a commercial workshop[4].

[4] SQ Engineering & Trading Pte. Ltd., Hougang, Singapore

The housings were made from brass or aluminum. The choice of brass and aluminum was based mainly on the facts that they are readily available, can be easily machined and have fairly good electrical and thermal properties. While copper has excellent electrical and thermal properties, it is very difficult to fabricate the high precision housing required as copper is very soft and ductile. For aluminum housing, gold plating is essential as conventional soldering is not possible on aluminum.

### 9.4 Hermetic sealing

The housing for HTS microstrip circuits needs to be hermetically sealed. This is to prevent the condensation of atmospheric moisture on the HTS circuit when it is cooled down. The moisture can damage the HTS thin film and adversely affects the microwave performance as it acts as a high loss dielectric medium. In the case of tunable HTS/ferroelectric microwave devices, the moisture can act as a short-circuit path which reduces the maximum voltage that can be applied for tuning the devices.

The difficulty in designing hermetical seal for HTS packaging is the low temperature requirement. Conventional sealing material such as rubber or elastomer o-ring materials cannot be used as they lose their elasticity at low temperature.

A low temperature hermetic seal can be made by using indium. Indium is an ideal material for cryogenic compression hermetic seal as it remains soft and malleable even at low temperature. Furthermore, indium can bond with the contact surfaces. Indium had been reported to provide effective and reliable helium tight hermetic seals between metals or non-metallic materials like glass and ceramics at down to liquid helium temperature [5-7].

Correct flange geometry has to be used for reliable indium seals. The types of flange geometry can be divided into un-trapped seal, partially trapped seal and fully

trapped o-ring seal [8]. Indium seal with un-trapped seal flange geometry often leaks after a few temperature cycles. This is mainly due to the indium creping and flattening. The housings designed in this thesis were based on the partially trapped seal geometry which is more reliable.

An important requirement for the successful implementation of hermetic indium seal is that the surface indium oxide must be removed. Indium when exposed to air will form a self-passivating indium oxide layer that is about 8 to 10 nm thick. The oxide layer reduces the ability of indium to bond with other materials and may be a source for leakage if it gets compressed into the hermetic seal. The procedure for preparing indium wire seal is described in appendix 4. As the housings for the devices were fabricated by milling, the surfaces of the housing and cover in contact with the indium were not further polished [9].

The HTS microwave devices developed in this thesis were sealed in a homemade packaging chamber filled with helium gas and with relative humidity at less than 1 %. Helium was chosen as the packaging gas as it is a very inert gas with boiling point of about 4 K.

## 9.5 Effect of cavity dimension

A metallic housing will exhibit cavity resonances, as the electromagnetic waves are reflected by the conductive walls. The microwave response of a microwave circuit is usually adversely affected when the cavity resonant frequency of the housing falls within the circuit operating frequency, e.g. a loss dip within the passband of a bandpass filter or reduced Q factor in a resonator.

The $TE_{mnk}$ or $TM_{mnk}$ mode resonant frequency of a rectangular cavity can be calculated using:

$$f_{mnk} = \frac{c}{2\sqrt{\mu_r \varepsilon_r}} \sqrt{\left(\frac{m}{w}\right)^2 + \left(\frac{n}{h}\right)^2 + \left(\frac{k}{l}\right)^2}\,, \tag{9.1}$$

where $w$, $h$ and $l$ are the cavity width, height and length respectively [10].

When $h < w < l$, the lowest resonant frequency mode will be $TE_{101}$. Thus the lowest resonant frequency of an air-filled cavity can be estimated using:

$$f_{101} = 15\sqrt{\frac{1}{w^2} + \frac{1}{l^2}}\,, \tag{9.2}$$

where $f_{101}$ is in GHz and $w$ and $l$ are in cm.

As can be seen from equation (9.2), decreasing the dimension of the cavity will increase the frequency at which the lowest cavity resonance appears and it is an effective method of suppressing cavity resonance. However the cavity cannot be too small as it will need to accommodate the microstrip circuit, and to prevent coupling between the circuit and the cavity surfaces. A general guide is that the distance between a microstrip line and the cavity surfaces including both the side walls and top cover, should be at least 5 times the thickness of the substrate [11].

The presence of a dielectric substrate will decrease the cavity resonant frequency, with a greater decrease if a higher dielectric constant or thicker substrate is used. Accurate modeling of the cavity resonant frequencies of a cavity loaded with substrate by analytic formula is difficult especially if the effects of the circuit are included. However, the cavity resonant frequencies in such cases can usually be simulated quite accurately using 3D electromagnetic simulation software such as HFSS[5].

[5] Ansoft Corp., Pennsylvania, USA

## 9.6 Microwave connections

Two types of microwave connector standard were used for the housings developed in this thesis: the SMA[6] (Sub-Miniature A) connector and the K connector[7]. Both the SMA connector and K connector are threaded, coaxial connectors with 50 Ω characteristic impedance. Although SMA connector and K-connector can be physically connected with each other, they have different rf characteristics, for example the maximum operating frequency of SMA connector is 18 GHz while that of K connector is 40 GHz.

Both the SMA connector and K connector standards have commercially available hermetic feedthrough for microstrip transition. The hermetic feedthrough for microstrip transition consists of a connector socket and a glass bead embedded with a launcher pin. Hermetic seal is formed by soldering the glass bead to the housing.

### 9.6.1 Conventional hermetic microwave connection with microstrip transition

In a conventional microstrip circuit, the launcher pin from the glass bead is soldered directly to the metallic rf input/output microstrip line on the circuit. Before the glass bead is soldered to the casing, the microstrip circuit had to be first attached onto the housing. Figure 9.1 illustrates the design of a hermetic microwave connection for conventional metallic microstrip circuit.

Unfortunately such hermetic microwave connection cannot be directly used for HTS circuit. As the substrate with the HTS thin film microstrip circuit has to be attached to the casing before soldering the glass bead to the housing, the HTS thin film will be damaged by heat when soldering the glass bead. Furthermore, the

[6] Originally designed by the Bendix Scintilla Corp., now commonly available from many companies
[7] K connector is a registered trademark of the Anritsu Corp., Tokyo, Japan

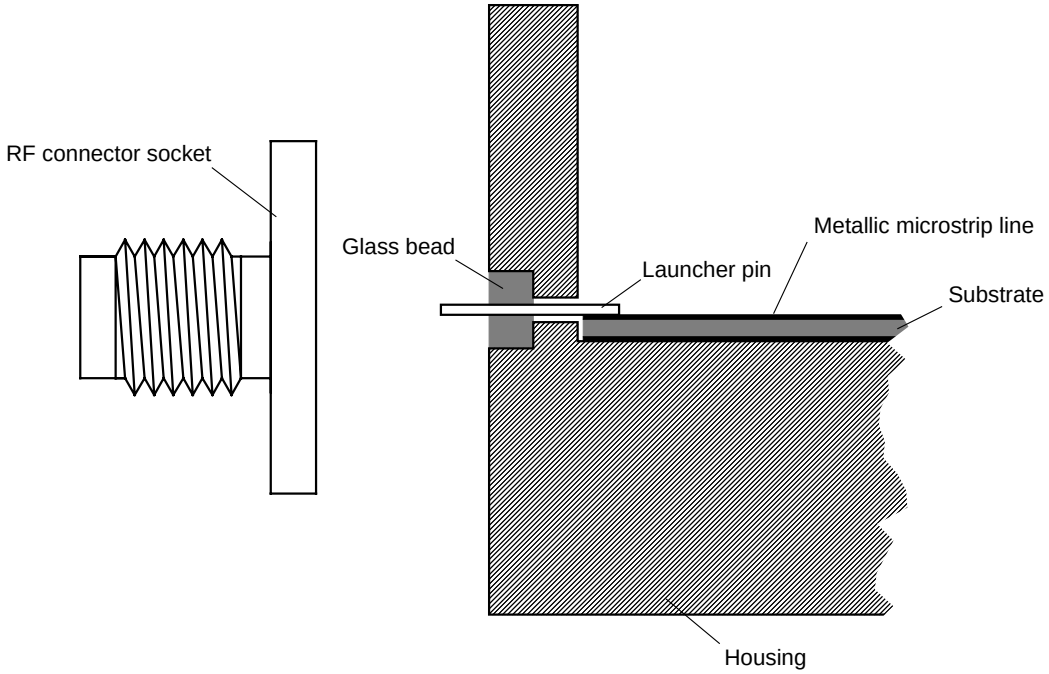


Figure 9.1 A hermetic microwave connection for conventional metallic microstrip circuit. The rf connector socket is secured by screws (not shown in diagram) to the housing.

launcher pin of the glass bead cannot be directly soldered to the HTS microstrip circuit without damaging the HTS thin film.

### 9.6.2 Unsuccessful hermetic microwave connection designs

The earliest microwave connection developed for the HTS microstrip devices mentioned in this thesis was based on the use of housing with a removable bottom cover as shown in figure 9.2. The HTS circuit was attached to the removable bottom which was secured to the housing only after the glass bead had been soldered. Unfortunately in this design, the gap between the bottom cover and the wall of the housing resulted in a ground path with parasitic inductance which had a significant adverse effect on the microwave propagation.

Another alternative design was to have the openings of the housing on the sides instead of on the top and/or bottom. The HTS microstrip substrate can then be slide into the housing from the side after the glass bead was soldered. However it was difficult to ensure that the rf input/output of the microstrip circuit and launcher pin was well aligned in this design.

Furthermore, the above two designs did not solved the problem of the poor electrical contact between the launcher pin and the microstrip circuit. The electrical contact can be somewhat improved by inserting a small piece of indium between the pin and substrate but proper electrical contact with this method cannot be reliably reproduce.

### 9.6.3 Successful hermetic microwave connection designs

A hermetic microwave connection design that was found to have satisfactory microwave performance and reliability is illustrated in figure 9.3. In this design, a conventional copper microstrip transmission line with 50 Ω characteristic impedance

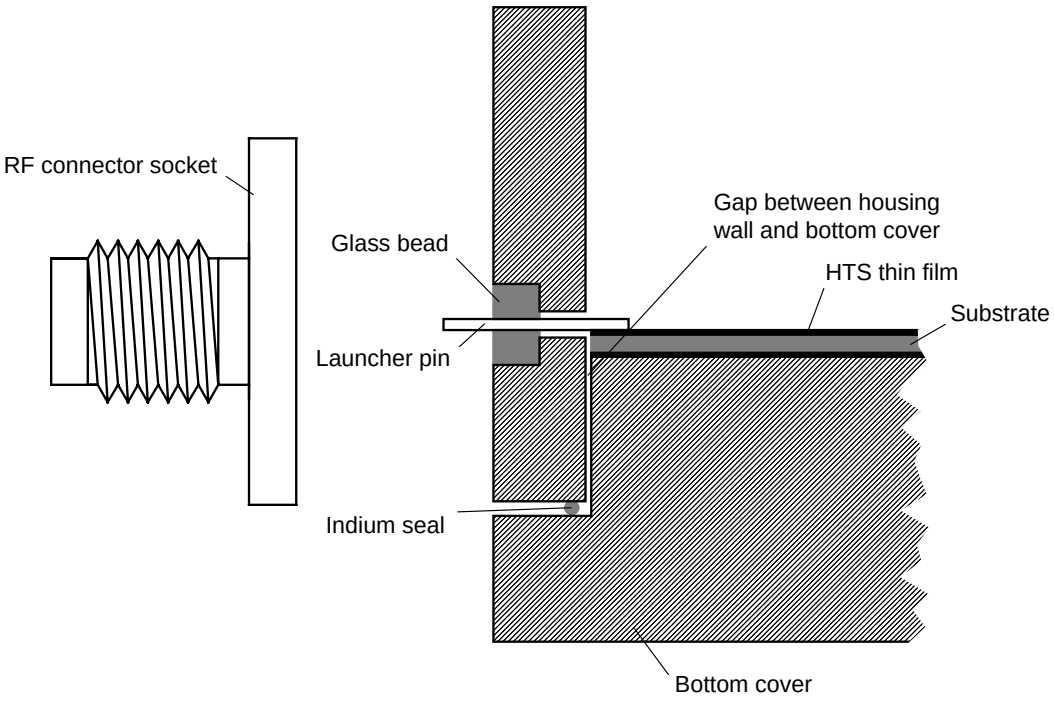


Figure 9.2 The design of a hermetic microwave connection based on housing with removable bottom cover.

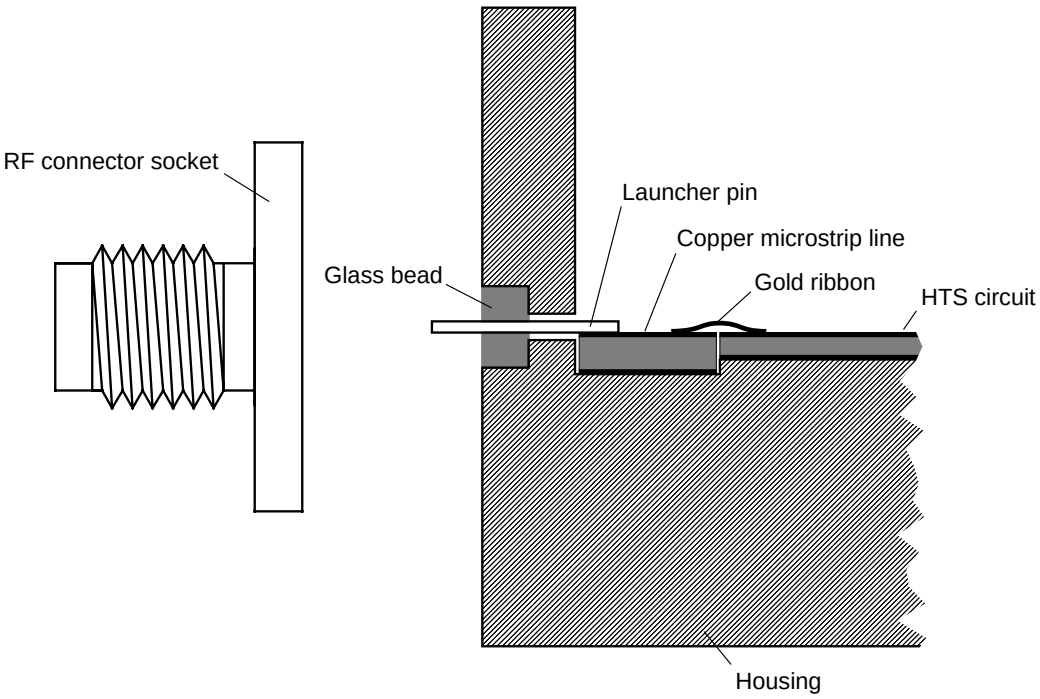


Figure 9.3 The design of the hermetic microwave connection with copper microstrip line transition.

was used as a transition from the launcher pin to the HTS microstrip circuit. The HTS circuit was attached to the housing with silver paste or silver loaded epoxy after the glass bead and the launcher pin had already been soldered. Gold ribbon was bonded to the copper microstrip line and the gold coated portion of the HTS circuit (see figure 9.4) by resistive welding with a ribbon bonding machine. The procedure for assembling such a microwave connection is described in appendix 5. The design and photograph of a housing based on such a connection design is shown in figures 9.5 and 9.6 respectively.

Another design that had satisfactory microwave performance and reliability is illustrated in figure 9.7. This method used the proprietary K-connector with a high precision sliding contact. In this method, the pin on the glass bead does not protrude beyond the hole on the housing and the substrate can be attached to the housing after the glass bead had been soldered. A gold ribbon was first bonded to the tab on the sliding contact. The sliding contact was then inserted into the launcher pin, and the free end of the ribbon was then bonded to the gold plated region on the HTS circuit. The procedure for assembling such a microwave connection is described in appendix 6. The dimension and photograph of a housing based on such a connection design is shown in figures 9.8 and 9.9 respectively. A hermetic microwave connection using the K connector without the sliding contact but with copper microstrip line transition can also be implemented, as shown in figure 9.10.

The advantages the K connector with the sliding contact have over the copper microstrip line transition are better performance especially at higher frequency, smaller cavity dimension and therefore higher cavity resonant frequency, quicker and easier packaging, and that the housing can be easily reused. In the copper microstrip line transition, the gold ribbon has to be torn off the copper microstrip line when

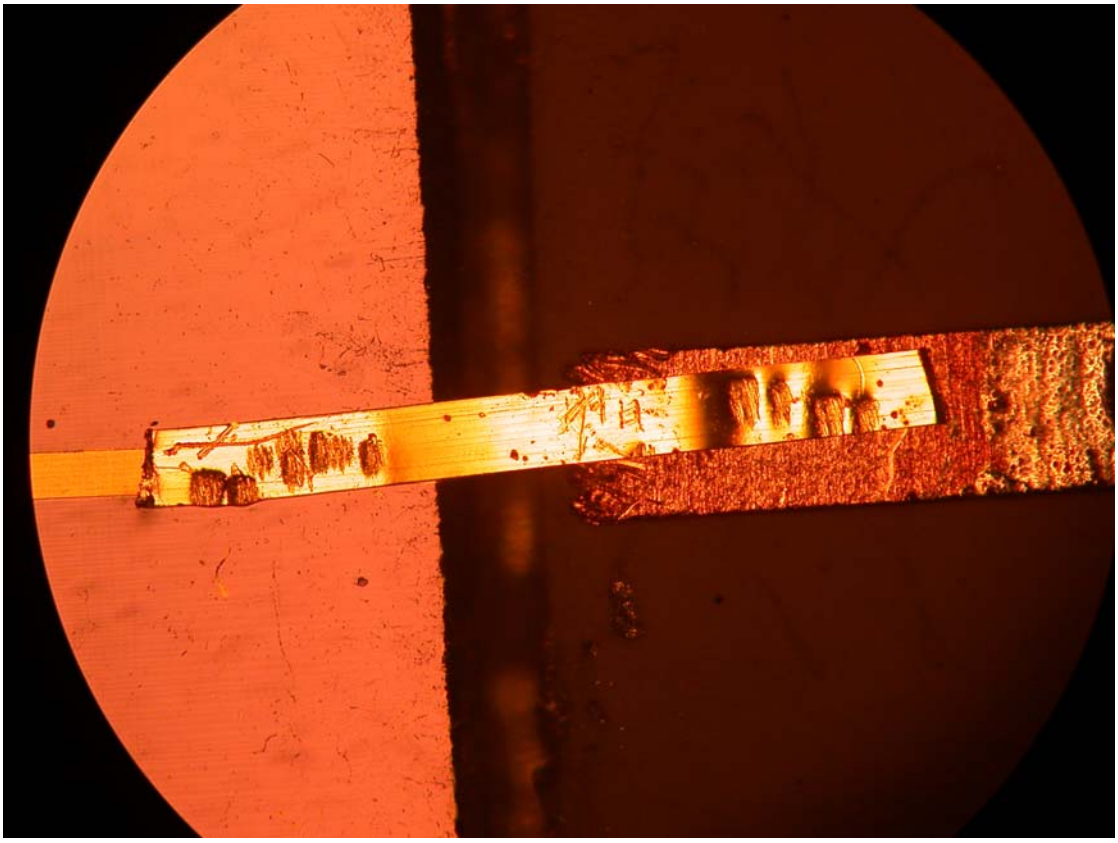

Figure 9.4 The photograph of a transition between gold/HTS microstrip line and copper microstrip line using resistive welded gold ribbon. The gold ribbon is 0.254 mm wide, whereas the gold/HTS microstrip line on the left side is 0.17 mm wide and the copper microstrip line on the right side is 0.6 mm wide.

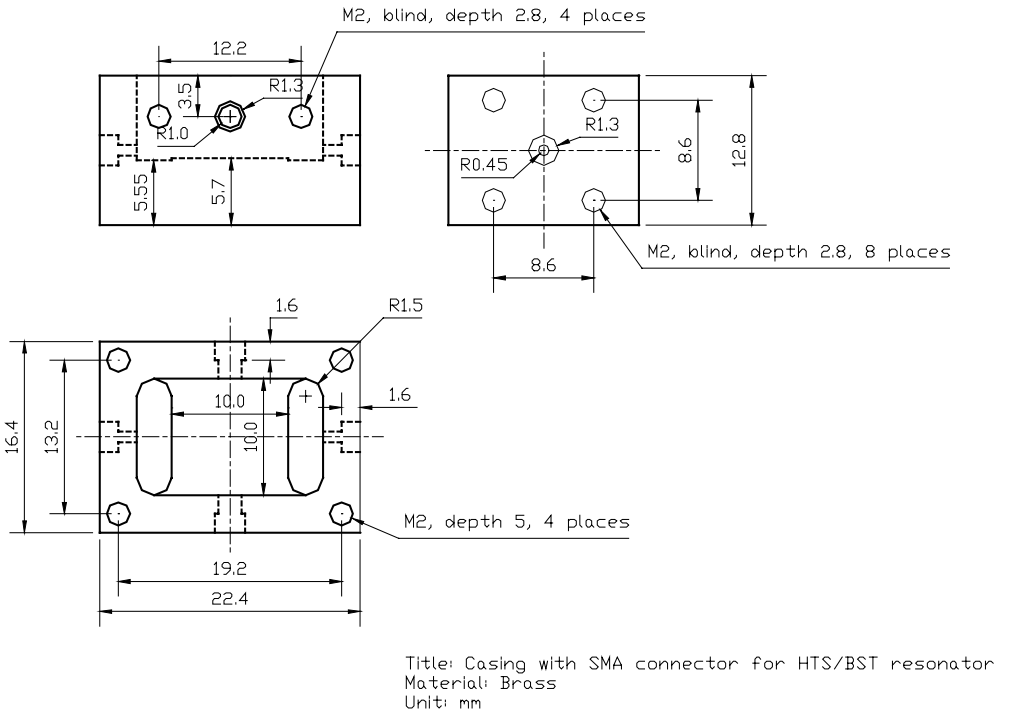


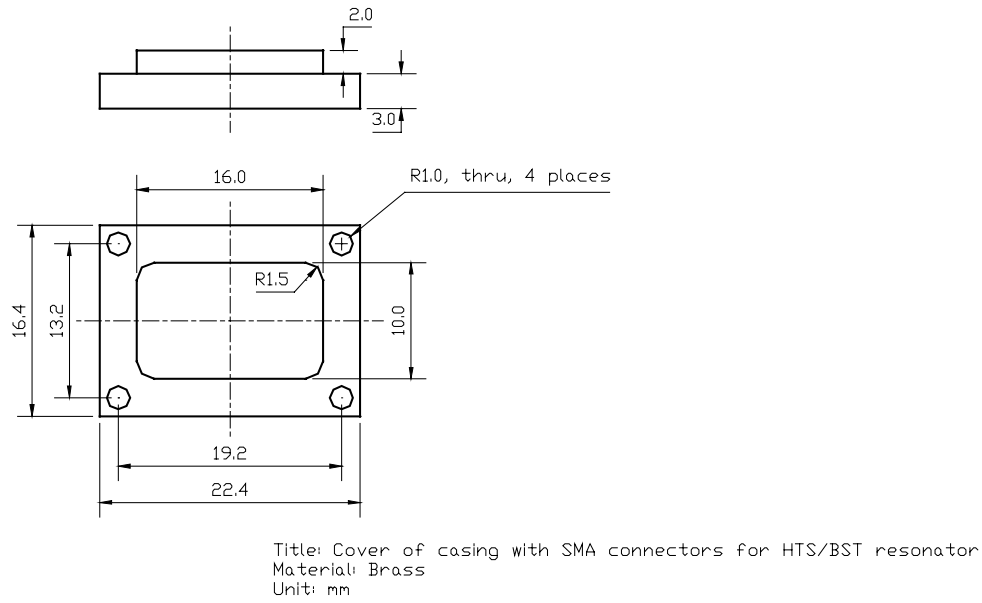


Figure 9.5 The design of a housing with hermetic SMA connection and copper microstrip line transition.

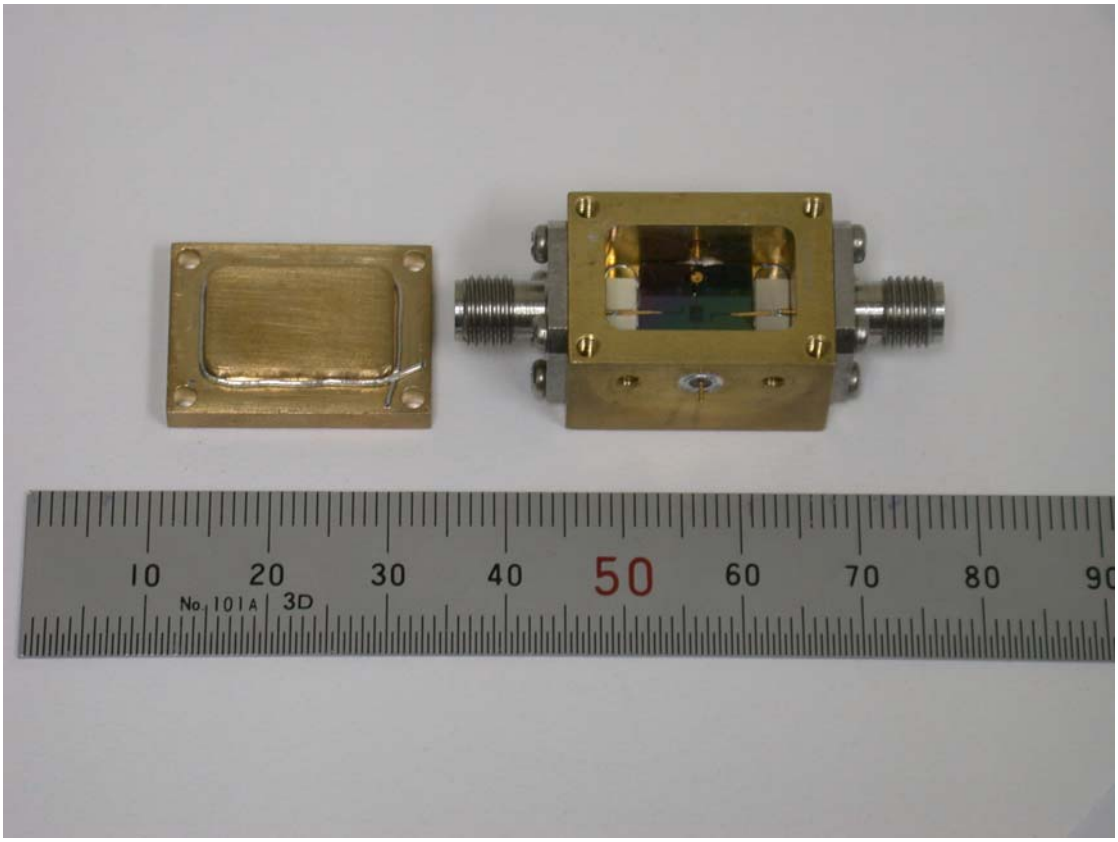


Figure 9.6 The photograph of a housing with hermetic SMA connection and copper microstrip line transition.

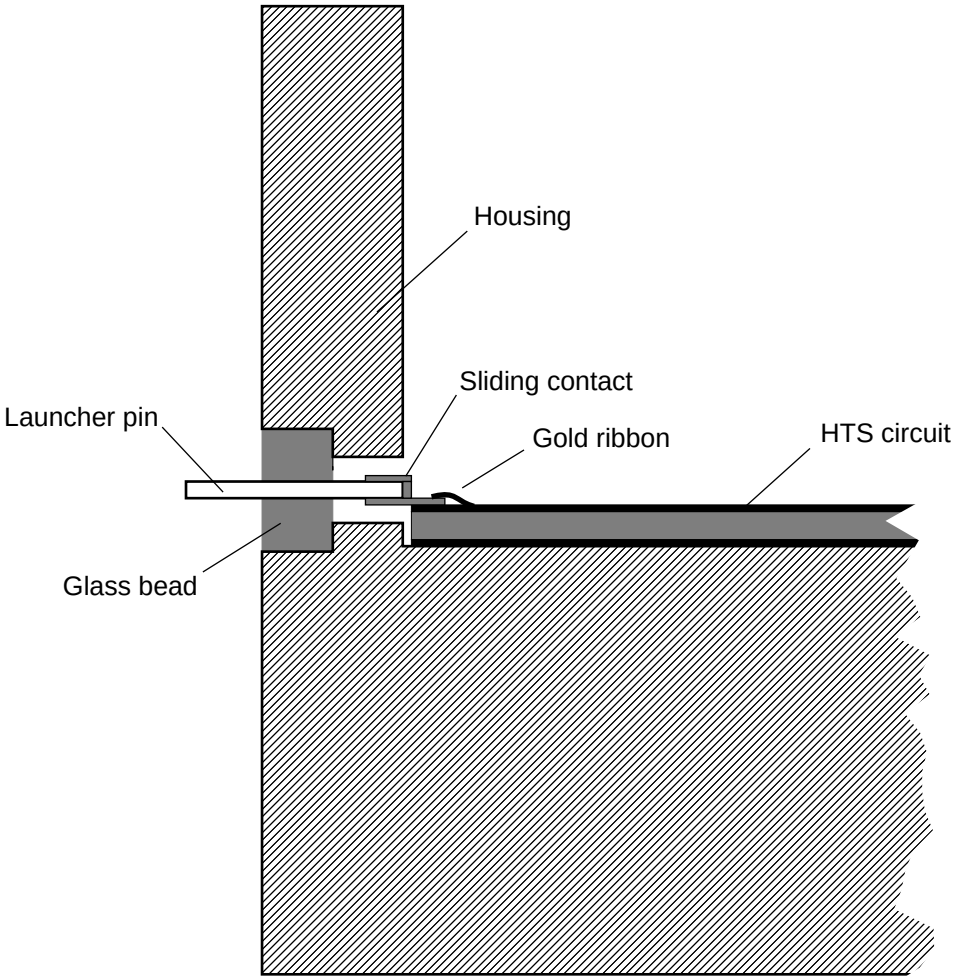


Figure 9.7 The design of a hermetic microwave connection with K connector and sliding contact.

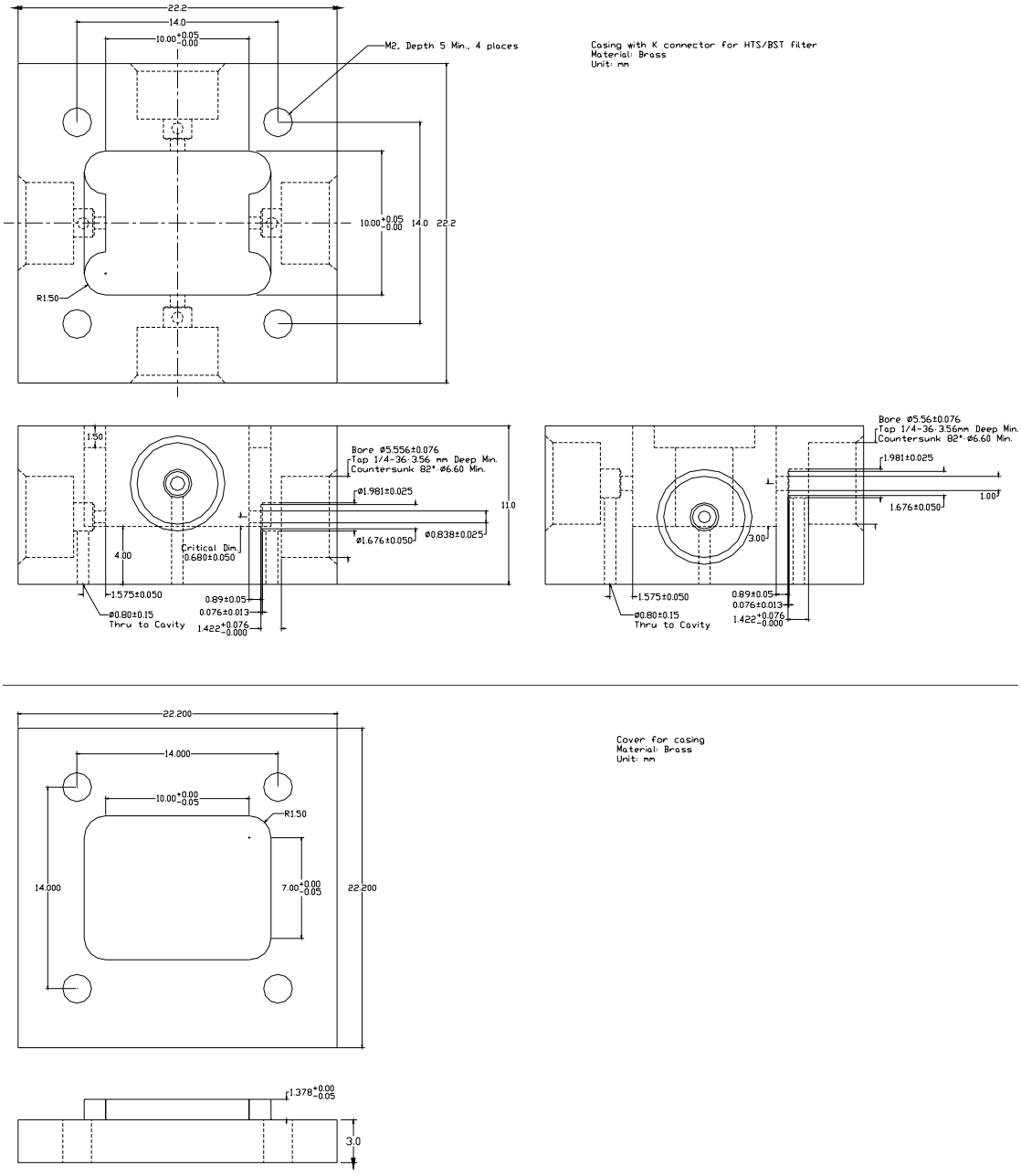


Figure 9.8 The design of a housing with hermetic K connector and sliding contact.

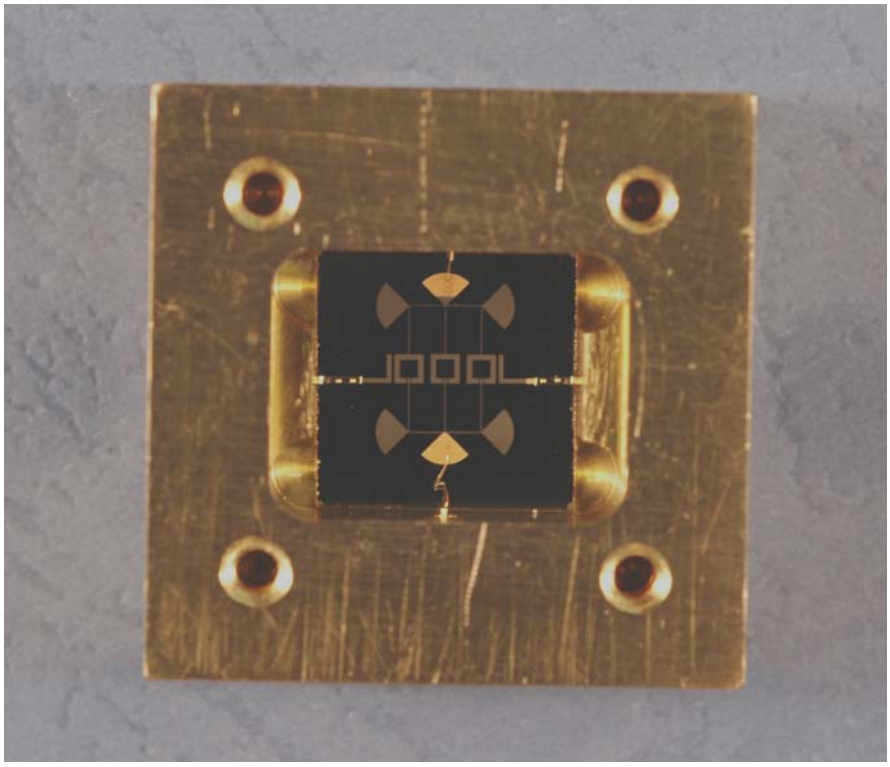

Figure 9.9 The photograph of a housing with hermetic K connector and sliding contact. The rf connector sockets had not been installed in this photograph.

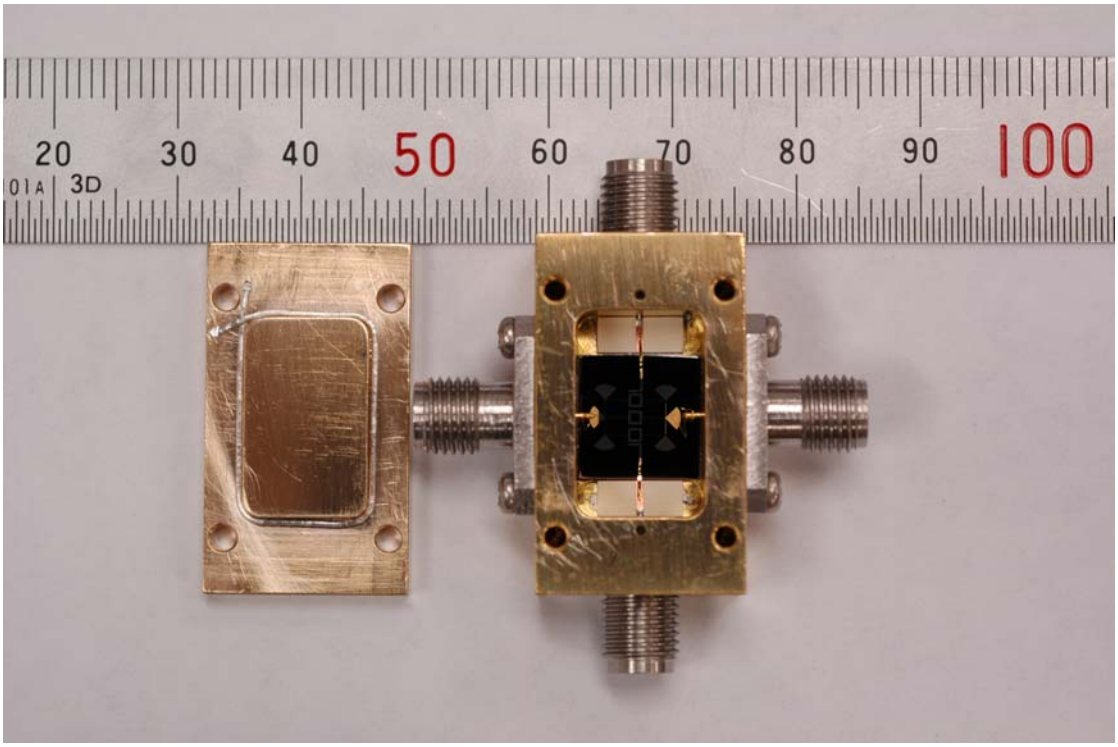


Figure 9.10 The photograph of a housing with hermetic microwave connection using K connector and copper microstrip transition line. The dc connection was based on hermetic SMA connector.

reusing the housing. The copper microstrip line is very likely to be delaminated when the gold ribbon is been torn off. For the K connector with the sliding contact method, the sliding contact is simply pull off the launcher pin and replaced with a new sliding contact when installing a new HTS circuit.

## 9.7 Hermetic dc feedthrough

The hermetic dc feedthrough, if required as in the case of tunable ferroelectric device, is implemented similarly to the microwave connection; i.e. by soldering the hermetic glass bead to the housing. The diameter of the hole for the glass bead pin can be made larger so that a higher dc voltage can be applied without electrical arcing. The launcher pin of the glass bead or the sliding contact was connected to the gold/HTS dc contact pad by wire bonding with 0.05 mm diameter gold wire.

References


[1] E. Gaganidze, T. Kasser, and J. Halbritter, "Corrosion and corrosion protection of epitaxial $YB_2CU_3O_{7-\delta}$ films quantified by studies of surface resistance $R_s(T, H_{rf})$ as a function of temperature and radio-frequency magnetic field", *Superconductor Science & Technology*, vol. 17, no. 4, pp. 601-607, 2004.

[2] A. G. Zaitsev, R. Schneider, J. Geerk, G. Linker, F. Ratzel, and R. Smithey, "Effective microwave surface resistance of gold-contacted $YBa_2Cu_3O_{7-x}$ thin films", *Applied Physics Letters*, vol. 75, no. 26, pp. 4165-4167, 1999.

[3] R. Schneider, A. G. Zaitsev, J. Geerk, G. Linker, F. Ratzel, and R. Smithey, "Increased quality factor in superconducting microstrip resonators by selective removal of the gold contact layer", *Superconductor Science & Technology*, vol. 15, no. 2, pp. 212-216, 2002.

[4] I. Shih and C. X. Qiu, "Chemical Etching of Y-Cu-Ba-O Thin-Films", *Applied Physics Letters*, vol. 52, no. 18, pp. 1523-1524, 1988.

[5] K. L. Agarwal and J. Betterton, "On low temperature indium seals", *Cryogenics*, vol. 14, no. 9, p. 520, Sept.1974.

[6] G. Caley and P. J. Gavin, "Rapidly demountable indium sealed couplings for use at helium temperatures", *Cryogenics*, vol. 14, no. 4, p. 226, Apr.1974.

[7] U. Hochuli and P. Haldemann, "Indium Sealing Techniques", *Review of Scientific Instruments*, vol. 43, no. 8, pp. 1088-1089, Aug.1972.

[8] C. C. Lim, "Indium seals for low-temperature and moderate-pressure applications", *Review of Scientific Instruments*, vol. 57, no. 1, pp. 108-114, Jan.1986.

[9] R. R. Turkington and R. F. Harris-Lowe, "Note on the design of simple indium O-ring seals", *Review of Scientific Instruments*, vol. 55, no. 5, pp. 803-805, 1984.

[10] D. M. Pozar, *Microwave Engineering*, 2nd Ed., John Wiley & Sons Inc., 1998.

[11] K. C. Gupta, R. Garg, I. Bahl, and P. Bhartia, *Microstrip Lines and Slotlines*, 2nd Ed., Artech House, 1996.

# CHAPTER 10:
# CONCLUSION

In this thesis, the fabrication and characterization of high $T_c$ superconductor (HTS) $YBa_2Cu_3O_{7-\delta}$ (YBCO) and ferroelectric $Ba_{0.1}Sr_{0.9}TiO_3$ thin films, and the designs and fabrication of passive microwave devices based on these thin films were examined.

The introductory materials of chapter 1 gave a brief review on superconductivity, its microwave applications, and the properties of the YBCO thin film and $LaAlO_3$ substrate used in this thesis. Chapter 2 described the pulsed laser deposition (PLD) technique and the fabrication procedures used to produce the YBCO thin films. Chapter 3 reviewed the techniques used to characterize the YBCO thin film and the typical characterization results. Chapter 4 reviewed the characteristics of microwave resonator and introduced the microstrip dual-spiral resonators. In chapter 5, the inter-resonator coupling of the dual-spiral resonators and the application of the dual-spiral resonators in cross-coupled filter were examined. Chapter 6 gave a brief introduction on the ferroelectric $Ba_{0.1}Sr_{0.9}TiO_3$ thin films and described the fabrication of $Ba_{0.1}Sr_{0.9}TiO_3$ thin films and multilayer YBCO/ $Ba_{0.1}Sr_{0.9}TiO_3$ thin films. Chapter 7 presented a method developed for nondestructive measurement of the complex permittivity of ferroelectric thin film at microwave frequency. In chapter 8, a fabrication process for the production of patterned ferroelectric thin films was described and the work on the tunable resonators and filter was presented. Chapter 9 described procedures for fabricating the microwave devices and the packaging of the microwave devices.

The major original contributions of this thesis are:

1. The study on dual-spiral resonators for the development of miniaturized resonator with high quality factor.
2. The design and demonstration of a highly-compact cascaded quadruplet cross-coupled bandpass filter using the dual-spiral resonators.
3. The development of a non-destructive characterization method for measuring the complex permittivity of ferroelectric thin film at microwave frequencies.
4. The development of a fabrication process for patterned ferroelectric thin film which is suitable for the production of tunable planar HTS/ferroelectric microwave devices.
5. The design and fabrication of tunable resonator and filter using the patterned ferroelectric thin films and YBCO thin films.
6. The development of packaging for microstrip HTS microwave devices.

## List of publications by author


[1] C. Y. Tan and C. K. Ong, "Planar tunable HTS microwave filter with patterned ferroelectric thin film", *Superconductor Science & Technology*, vol. 19, no. 2, pp. 212-216, 2006.

[2] C. Y. Tan, L. F. Chen, K. B. Chong, and C. K. Ong, "Nondestructive microwave permittivity characterization of ferroelectric thin film using microstrip dual resonator", *Review of Scientific Instruments*, vol. 75, no. 1, pp. 136-140, 2004.

[3] C. Y. Tan, L. F. Chen, J. Lu, X. S. Rao, and C. K. Ong, "Cross-coupled dual-spiral high-temperature superconducting filter", *IEEE Microwave and Wireless Components Letters*, vol. 13, no. 6, pp. 247-249, 2003

[4] Y. Liu, L. F. Chen, C. Y. Tan, H. J. Liu, and C. K. Ong, "Broadband complex permeability characterization of magnetic thin films using shorted microstrip transmission-line perturbation", *Review of Scientific Instruments*, vol. 76, no. 6 2005.

[5] Y. S. Tan, X. S. Rao, L. F. Chen, C. Y. Tan and C. K. Ong, "Simulation, fabrication and testing of a left-handed microstrip coupler", *Microwave and Optical Technology Letters*, vol. 45, no. 3, pp. 255-258, 2005.

[6] Y. B. Zheng, S. J. Wang, A. C. H. Huan, C. Y. Tan, L. Yan, and C. K. Ong, "$Al_2O_3$-incorporation effect on the band structure of $Ba_{0.5}Sr_{0.5}TiO_3$ thin films", *Applied Physics Letters*, vol. 86, no. 11 2005.

[7] L. Yan, L. B. Kong, L. F. Chen, K. B. Chong, C. Y. Tan, and C. K. Ong, "$Ba_{0.5}Sr_{0.5}TiO_3$-$Bi_{1.5}Zn_{1.0}Nb_{1.5}O_7$ composite thin films with promising microwave dielectric properties for microwave device applications", *Applied Physics Letters*, vol. 85, no. 16, pp. 3522-3524, 2004.

[8] L. Yan, L. F. Chen, C. Y. Tan, C. K. Ong, M. A. Rahman, and T. Osipowicz, "$Ba_{0.1}Sr_{0.9}TiO_3$-$BaTi_4O_9$ composite thin films with improved microwave dielectric properties", *European Physical Journal B*, vol. 41, no. 2, pp. 201-205, 2004.

[9] L. Yan, L. B. Kong, T. Yang, W. C. Goh, C. Y. Tan, C. K. Ong, M. A. Rahman, T. Osipowicz, and M. Q. Ren, "Enhanced low field magnetoresistance of $Al_2O_3$-$La_{0.7}Sr_{0.3}MnO_3$ composite thin films via a pulsed laser deposition", *Journal of Applied Physics*, vol. 96, no. 3, pp. 1568-1571, 2004.

[10] K. B. Chong, L. B. Kong, L. F. Chen, L. Yan, C. Y. Tan, T. Yang, C. K. Ong, and T. Osipowicz, "Improvement of dielectric loss tangent of $Al_2O_3$ doped $Ba_{0.5}Sr_{0.5}TiO_3$ thin films for tunable microwave devices", *Journal of Applied Physics*, vol. 95, no. 3, pp. 1416-1419, 2004.

[11] X. S. Rao, L. F. Chen, C. Y. Tan, J. Lu, and C. K. Ong, "Design of one-dimensional microstrip bandstop filters with continuous patterns based on Fourier transform", *Electronics Letters*, vol. 39, no. 1, pp. 64-65, 2003.

[12] J. Lu, C. Y. Tan, and C. K. Ong, "Resonator structure with high etching error tolerance for application in HTS filters", *Superconductor Science & Technology*, vol. 15, no. 3, pp. 327-329, 2002.

[13] B. B. Jin, C. K. Ong, X. S. Rao, and C. Y. Tan, "An anomalous weak link model for microwave surface impedance of $YBa_2Cu_3O_{7-\delta}$ films in a weak dc magnetic field", *Superconductor Science & Technology*, vol. 14, no. 1, pp. 1-5, 2001.

[14] L. F. Chen, C. Y. Tan, J. Lu, C. K. Ong, and B. T. G. Tan, "High-temperature superconducting dual-spiral resonators and their application in filter miniaturization", *Superconductor Science & Technology*, vol. 13, no. 4, pp. 368-372, 2000.

[15] B. B. Jin, X. S. Rao, C. Y. Tan, and C. K. Ong, "The anomalous unloaded quality factor behavior of high $T_c$ superconducting microstrip resonator in weak dc magnetic field", *Journal of Superconductivity*, vol. 13, no. 1, pp. 85-88, 2000.

[16] X. S. Rao, C. K. Ong, B. B. Jin, C. Y. Tan, S. Y. Xu, P. Chen, J. Li, and Y. P. Feng, "Anomalous microwave response of high-temperature superconducting thin-film microstrip resonator in weak dc magnetic fields", *Physica C*, vol. 328, no. 1-2, pp. 60-66, 1999.

[17] C. K. Ong, L. F. Chen, J. Lu, C. Y. Tan, and B. T. G. Tan, "High-temperature superconducting bandpass spiral filter", *IEEE Microwave and Guided Wave Letters*, vol. 9, no. 10, pp. 407-409, 1999.

[18] B. B. Jin, X. S. Rao, C. Y. Tan, and C. K. Ong, "A phenomenological description for unusual surface impedance behaviors of high-$T_c$ thin film in weak DC magnetic field", *Physica C*, vol. 316, no. 3-4, pp. 224-228, 1999.

[19] L. Jian, C. Y. Tan, C. K. Ong, and C. S. Teck, "RF tunable attenuator and modulator using high $T_c$ superconducting filter", *Electronics Letters*, vol. 35, no. 1, pp. 55-56, 1999.

# APPENDIX 1:
# PROCEDURE FOR PULSED LASER DEPOSITION OF YBCO THIN FILM

**Precautions:**

- Turn on the "Laser in operation" warning light and wear the laser safety goggles whenever the laser is turned on. Do not operate the laser when there are people not wearing laser safety goggles in the room.

- Wear clean powder-free latex or PVC gloves when handling anything in or will be going into the vacuum chamber. This is to avoid out-gassing from fingerprints.

1. Open the valve on the oxygen cylinder and set the regulator output pressure at 2 bar.

2. Switch on the vacuum gauge.

3. If the chamber had been previously pumped down, vent the vacuum chamber by opening the variable leak valve for the oxygen input. Fully close the variable leak valve when pressure within the chamber and the surrounding has equalized.

4. Open the vacuum chamber and load the cleaned substrates onto the heater with a pair of tweezers.

5. Close the chamber and fully open the gate valve, marked in figure 2.2 as (i).

6. Switch on the rotary vane pump.

7. When the pressure in the chamber is less than 1 mbar, switch on the turbo-molecular pump.

8. When the pressure of the chamber is less than $1\times10^{-5}$ mbar, turn on the temperature controller and SCR power controller. Set the temperature controller to ramp up the temperature of the heater ($T_h$) to 200 °C at rate of 1 °C/s.

9. When $T_h$ is at 200 °C, turn on the cooling fan of the chamber, cooling water supply and the motor driving the rotation of the YBCO target.

10. Half close the gate valve. Open and adjust the variable leak valve so that oxygen pressure is at 0.2 mbar.

11. Set the temperature controller to ramp up $T_h$ to 860 °C at rate of 1 °C/s.

12. Turn on the laser. The laser will take about 8 minutes to warm up before operation is possible.

13. When $T_h$ is at 860 °C, turn on the motor driving the scanning mirror.

14. Set the laser to constant energy mode with per pulse energy of 260 mJ and pulse repetition rate of 5 Hz.

15. Deposition duration of 30 minutes is required when fabricating YBCO thin film with thickness of 500 nm.

16. At the end of the deposition period, stop the laser and the motor driving the mirror rotation.

17. Set the temperature controller to ramp down $T_h$ to 580 °C at rate of 1 °C/s.

18. When $T_h$ is at 580 °C, fully close the gate valve and open the variable leak valve to increase oxygen pressure to 1 bar. When the pressure is at 1 bar, shut off the variable leak valve.

19. Turn off the turbo-molecular pump. Wait until the turbo-molecular pump has automatically vented before turning off the rotary vane pump.

20. Anneal the YBCO thin film at $T_h$ = 580 °C and oxygen pressure of 1 bar for 30 minutes.

21. After annealing for 30 minutes, set the temperature to decrease to room temperature at a rate of 1 °C/s. Below 400 °C, the actual temperature drop will

be slower as there is no active cooling mechanism and the natural heat dissipation from chamber is lower than that required for 1 °C/s temperature drop.

22. When $T_h$ has dropped to room temperature, turn off the target rotation motor, chamber cooling fan and cooling water.

23. The substrate can now be removed from the chamber. If deposition of YBCO thin film on both sides of the substrate is required, flip the substrate over and repeat the fabrication procedure from step 5.

24. Turn off the laser.

25. Open the gate valve and pump down the vacuum chamber to less than 1 mbar using the rotary vane pump. When pressure of less than 1 mbar is attained, closed the gate valve and turn off the rotary vane pump.

26. Turn off the vacuum gauge.

27. Close the valve on the oxygen cylinder.

## APPENDIX 2:
## PROCEDURE FOR DEPOSITION OF GOLD FILM

1. Clean the substrate by one minute immersion in acetone ultrasonic bath, followed by one minute immersion in high purity ethanol ultrasonic bath. Blow dried the substrate with compressed nitrogen gas immediately upon removal from ethanol.

2. Visually inspect the surface of the substrate for the presence of particles e.g. dusts. If any particle is present, use compressed nitrogen gas to blow it off the substrate.

3. Place and align the substrate on the copper aperture mask.

4. Carefully load mask and substrate into the vacuum chamber of the ion sputtering unit (JFC-1100[1]) and inspect the alignment of the mask. If the alignment is correct, replace the bell jar of the vacuum chamber.

5. Set the controls of the sputtering unit to the following: power at off, HV switch at off, HV control at 0 and Vacuum control at 10.

6. Switch on the power.

7. Allow the vacuum chamber to pump down for 3 minutes.

8. Set the HV switch to DC. Gradually turn the HV control knob clockwise until the voltmeter indicates a reading of 500 V. If the ammeter reading is less than 2 mA, continue to step 9. If the ammeter reading is 2 mA or more, the vacuum is too low. Set the voltage back to 0 V and turn off the HV switch. Continue pumping for a longer period before repeating step 8.

[1] Jeol, Tokyo, Japan

9. Rotate the vacuum knob and HV control knob clockwise until the ammeter and the voltmeter indicates 10 mA and 1200 V respectively.

10. Allow the deposition to continue for nine minutes to obtain gold film of about 100 nm thick.

11. After nine minutes, turn the HV control knob to 0 and turn the HV switch to off.

12. Turn off the power and turn the vacuum knob fully clockwise to vent the vacuum chamber.

13. When pressure in the chamber has equalized, the bell jar can be removed and the gold coated substrate can be retrieved.

# APPENDIX 3:
# PROCEDURE FOR PHOTOLITHOGRAPHY AND WET ETCHING OF SUBSTRATE WITH DOUBLE-SIDED YBCO THIN FILM

The following procedure is carried out in a darkroom with no UV light source such as white fluorescent lamp.

1. Clean the substrate by one minute immersion in acetone ultrasonic bath followed by one minute immersion in high purity ethanol ultrasonic bath. Blow dried the substrate with compressed nitrogen gas immediately upon removal from ethanol.

2. Load the substrate onto the spin coater (P6204[1]).

3. Visually inspect the surface of the substrate for the presence of particles e.g. dusts. If any particle is present, use compressed nitrogen gas to blow it off the substrate.

4. Apply a few drops of photoresist (S1813[2]) onto the substrate. The photoresist should nearly cover the substrate surface but not overflow the edge. Spin the substrate at 6000 RPM for 60 seconds.

5. Remove the photoresist coated substrate from the spin coater and bake dry the photoresist at 120 °C for 5 minutes in a preheated oven.

6. Coat the second side of the substrate with photoresist by flipping the substrate over and repeating steps 2 to 5.

[1] Specialty Coating System Inc., Indiana, USA
[2] Shipley Co. Inc., Massachusetts, USA

7. Load the substrate onto the mask aligner (Q-2001CT[3]). Use the microscrope on the mask aligner to check for the presence of defects like voids, bubbles or particles on the photoresist layer. If the photoresist layer contains any defect near or within the boundary of the region with device pattern, rinse off the photoresist with running acetone and repeat the procedure from step 1.

8. Load the soft mask onto the mask aligner. The printed side of the mask should be in contact with the photoresist. Check for the presence of particles on the mask by using the microscope on the mask aligner. If there is any particle, blow it off with compressed nitrogen gas.

9. Align the mask and substrate.

10. When the mask and substrate are aligned and in contact, expose the photoresist to UV light for 24 seconds. The UV light source on the mask aligner should be set to an output power of 250 W (note that the UV lamp should be allowed to warm up for at least 7 minutes before exposure to obtain the required intensity).

11. Remove the substrate from the mask aligner. Immerse the substrate in the photoresist developer solution (Microposit developer[2]) for 30 seconds to remove the exposed photoresist.

12. Thoroughly rinse the substrate with distilled water.

13. Remove the edge bead (if any) by wiping with a fine cotton swab soaked with acetone.

14. Etch away the unwanted region of the gold film by immersing the substrate into a KI (10 g), $I_2$ (5 g) and $H_2O$ (500g) mixture for 20 seconds.

15. Thoroughly rinse the substrate with distilled water.

[3] Quintel Corp., California, USA

16. Inspect the gold pattern; if there are unwanted gold remaining on the substrate, repeat from step 14 with etching interval of five seconds.

17. Etch away the unwanted region of the YBCO thin film by immersing and constant agitating the substrate in phosphoric acid (1 % concentration by volume) for 60 seconds.

18. Thoroughly rinse the substrate with distilled water.

19. Inspect the YBCO pattern; if there are unwanted YBCO remaining on the substrate, repeat from step 17 with etching interval of five seconds.

20. Remove the remaining photoresist by immersion in acetone ultrasonic bath for 30 seconds. Further rinse the substrate with running acetone, follow by rinsing with running high purity ethanol. Blow dried the substrate with compressed nitrogen gas immediately upon removal from ethanol.

## APPENDIX 4:
## PROCEDURE FOR PREPARING INDIUM WIRE SEAL

1. Cut the high purity, 0.5 mm diameter indium wire (IN005120[1]) to the suitable length. The length of the indium wire should be the perimeter of the seal with an additional 2 mm. The additional 2 mm is for the two ends of the indium wire to overlap when forming the seal.

2. Immerse the indium wire in acetone ultrasonic bath for one minute to remove organic contaminants on the surface of the indium.

3. Thoroughly rinse the indium wire with running distilled water.

4. Etch away the surface indium oxide on the indium wire by immersing the indium wire in 10 % (by volume) hydrochloric acid for about two minutes. The surface of the indium wire should appear bright and shiny when the surface indium oxide has been etched away.

5. Thoroughly rinse the indium wire with running distilled water.

6. Rinse off the water on the indium wire with acetone.

7. Blow dry the indium wire with compressed nitrogen gas. Note that the indium wire should be used immediately (within half an hour), before the indium is significantly oxidized again.

8. Place the indium wire around the cover of the housing with the two ends overlapping as in figure 9.10. Alternatively, an O-ring type of seal can be formed by cutting the indium wire with a clean knife to form beveled ends. The two freshly cut beveled ends will stick together readily.

[1] Goodfellow Cambridge Ltd., Huntingdon, UK

# APPENDIX 5:
# PROCEDURE FOR ASSEMBLING HTS MICROSTRIP DEVICE IN HOUSING WITH COPPER MICROSTRIP LINE TRANSITION AND SMA CONNECTOR

1. Apply a small amount of solder paste (149-968[1]) onto the regions of the housing where the two transition copper microstrip lines are to be positioned then place the copper microstrip lines into the housing. The two pieces of the 50 Ω characteristic impedance transition copper microstrip line are typically fabricated using 0.635 mm thick TMM10i substrate[2] with double-sided 17.5 μm thick copper plating.

2. Heat the housing on a hot plate set to 210 °C and wait for 10 seconds after the solder has melted before allowing the housing to cool down.

3. Insert the hermetic glass bead (PE1001-2[3]) into the hole on the housing. Apply a small amount of solder paste on the rim of the hole holding the hermetic glass bead. Melt the solder paste using a hot-air gun.

4. Solder the launcher pin of the glass bead to the copper microstrip line.

5. Clean the housing using isopropyl alcohol ultrasonic bath to remove the soldering grease and flux residue.

6. Apply a thin layer of silver conductive paint (186-3600[4]) onto the region in the housing where the HTS microstrip circuit is to be positioned, then insert the

[1] Farnell Components Pte Ltd, Tai Seng Drive, Singapore
[2] Rogers Corp., Connecticut, USA
[3] Pasternack Enterprises, California, USA
[4] RS Components Pte Ltd, Tech Park Crescent, Singapore

HTS circuit into the housing. Allow the silver paint to dry at room temperature for one day.

7. Use a piece of 3 mm × 10 mil × 1 mil gold ribbon (M8S2R1-02307[5]) to bridge the copper microstrip line and the gold plated rf input/output on the HTS circuit. The bonding of the ribbon can be done using the Model 50F[6] ribbon bonding machine with the UTM111L Unitip[6] electrode. Set the bonding machine to voltage feedback mode and the welding force at 270 g. For bonding on the copper microstrip line, use pulse duration of 15 ms and pulse amplitude of 0.65 V. For bonding on the gold/HTS circuit, use pulse duration of 10 ms and pulse amplitude of 0.6 V.

8. Prepare the indium wire seal using the procedure described in appendix 4. Place the housing, its cover and the indium wire seal in the helium packaging chamber. Purge and refill the chamber with helium gas until the humidity is at less than 1 %. Check that the indium wire seal is seated properly between the housing and its cover, and then secured the cover with screws.

[5] Kulicke & Soffa, Pennsylvania, USA
[6] Miyachi Unitek Corp., California, USA

## APPENDIX 6:
## PROCEDURE FOR ASSEMBLING HTS MICROSTRIP DEVICE IN HOUSING WITH K CONNECTOR AND SLIDING CONTACT

1. Apply a small amount of soldering grease to the edge of the hermetic glass beads (K100B[1]). Insert the greased glass beads into the holes on the housing. Secure the glass beads using the glass bead holding fixtures (01-103[1]).

2. Insert a length of solder wire (561-101[2]) into each of the soldering access hole on the housing. Cut the solder wire such that its top end is flush with the top of the solder access hole.

3. Heat the housing on a hot plate set to 210 °C and wait for 15 seconds after the solder has melted before allowing the housing to cool down.

4. Remove the glass bead holding fixtures and clean the housing by isopropyl alcohol ultrasonic bath to remove the grease and flux residue.

5. Screw in the K connector sparkplug assembly (K102F[1]) into the tapped mounting hole with the K connector torque tool kit (01-105A[1]).

6. Apply a thin layer of silver conductive paint (186-3600[2]) on the region in the casing where the HTS microstrip circuit is to be positioned, then insert the HTS circuit into the housing. Allow the silver paint to dry at room temperature for one day.

7. Bond a 1.5 mm × 10 mil × 1 mil gold ribbon[5] to the tab of the sliding contact using the ribbon bonding machine (Model 50F [3] with UTM111L Unitip

[1] Anritsu Corp., Tokyo, Japan
[2] RS Components Pte Ltd, Tech Park Crescent, Singapore
[3] Miyachi Unitek Corp., California, USA

electrode[3]). Use the following settings for the bonding: welding force at 270 g, voltage feedback mode, pulse duration of 10 ms and pulse amplitude at 0.6 V.

8. Place the sliding contact onto the substrate with the sleeve-end facing the pin of the glass bead. Gently push the sliding contact onto the conductor pin of the glass bead with the tip of a small screwdriver.

9. Bond the other end of the gold ribbon to the gold plated input/output on the HTS circuit using the settings in step 7.

10. Prepare the indium wire seal using the procedure described in appendix 4. Place the housing, its cover and the indium wire seal in the helium packaging chamber. Purge and refill the chamber with helium gas until the humidity is at less than 1 %. Check that the indium wire seal is seated properly between the housing and its cover, and then secured the cover with screws.